UNIVESITAT POLITÈCNICA DE

CATALUNYA

Escola Tècnica Superior d'Enginyers de Camins, Canals i Ports de Barcelona

THERMO-HYDRO-MECHANICAL ANALYSIS OF JOINTS

A THEORETICAL AND EXPERIMENTAL STUDY

Ph.D, THESIS

Presented by:

Maria Teresa Zandarin Iragorre

Supervised by:

Eduardo Alonso Pérez de Ágreda

Sebastià Olivella

Barcelona, 2010

ABSTRACT

The thesis presents numerical and experimental studies on joints.
A formulation for the coupled analysis of thermo- hydro- mechanical problems in joints is presented. The work involves the establishment of equilibrium and mass and energy balance equations. Balance equations were formulated taking into account two phases: water and air.

Once the joint element was implemented in Code_Bright computer code, it was then used to study some cases. The numerical simulation of hydraulic shear tests of roughness granite joints is presented. This allowed evaluating the coupling between permeability and the geometry of the opening of the joint. Then, a thermo-hydro-mechanical simulation of a large-scale nuclear waste repository was performed considering the joint element to model the interface between canister and bentonite. This example allowed evaluating the behaviour of the joint element when coupled to continuum elements. Then, other examples show how hydro-mechanical coupling affects the permeability and saturation of the joints and adjacent material. Finally, the gas flow through joints was also investigated.

The experimental investigation focused on the effects of suction on the mechanical behaviour of rock joints. Laboratory tests were performed in a direct shear cell equipped with suction control. Suction was monitored using a vapour forced convection circuit controlled by an air pump that was connected to the shear cell. Once equilibrium conditions are achieved, the rock specimen is assumed to reach the Relative Humidity imposed by the flowing air at a given vapour concentration. Artificial joints of Lilla claystone were prepared. Joint roughness of varying intensity was created by carving the surfaces in contact in such a manner that rock ridges of different tip angles formed. These angles ranged from 0º (smooth joint) to 45º (very rough joint profile). The geometric profiles of the two surfaces in contact were initially positioned in a “matching” situation. Several tests were performed for different values of suction (200, 100 and 20 MPa) and for different values of vertical stress (30, 60 and 150 kPa).
A constitutive model including the effects of suction and joint roughness is proposed to simulate the unsaturated behaviour of rock joints.
The new constitutive law was incorporated in the code and experimental data were numerically simulated.

ACNOWLEDGEMENTS

I would like to express my gratitude to my supervisors Professor Eduardo Alonso and Professor Sebastià Olivella for their dedication to my work and for always being ready to answer any of the questions or comments I posed.

I would also like to acknowledge Professor Antonio Gens's interest in my work and his support in the publication of the results.

My sincere appreciation to Mr. Tomás Peréz for his cooperation in the laboratory work.

I am specially thankful to my mother and my aunt, who from the distance have supported me at all times.

I would finally like to thank the Agencia Española de Cooperación Internacional para el Desarrollo for granting me the FPI scholarship that has made this thesis possible.

TABLE OF CONTENTS

CHAPTER 1

Introduction

1.1. Motivation and objective

This thesis was originally motivated by the need to model interfaces present in nuclear waste repositories. These interfaces can be located between blocks of the engineering barrier (bentonite blocks placed around the canister, which contain radioactive waste and prevent the contamination of the rock mass), between the bentonite and the canister or between the bentonite and the rock. Furthermore these interfaces can be rock joints within the rock mass. As a consequence, an European project, named THERESA, was developed to study interfaces between buffer-canister and buffer-rock.

Moreover, engineering facilities in rock mass cause deformations in intact rock and rock joints as a result of stress changes. Examples of these facilities are repositories of radioactive waste, dam foundations, tunnel excavations, geothermal energy plants, and oil and gas production plants. The major deformation occurs in joints as normal and shear displacements due to their lower strength if compared with the rock matrix. These displacements cause changes in the joint opening leading thus to a variation of the fluid flow through the joints.

There are many references in the literature on the experimental and theoretical study of the mechanical and hydro-mechanical behaviour of rock joints, and on two-phase flow through rock joints. These studies consider the effect of the changes in the opening on the hydraulic conductivity and on the capillary pressure. They also introduce the effect of this aperture changes on stress state of joints and vice versa.

Nevertheless, the effect of the degree of saturation (suction) on the mechanical strength of rock joints and on the degradation of their roughness has not been reported. Temperature induced effects considered in the analytical formulation proposed.
A reference general thermo-hydro-mechanical finite element program for some of the developments described in this thesis is Code-Bright (Olivella, 1995 and DIT-UPC, 2000)

developed in the Department of Geotechnical Engineering and Geosciences of the Technical University of Catalonia.

Therefore, in this context, the objectives of this thesis were:

1. To implement a coupled thermo-hydro-mechanical formulation for interfaces in Code_Bright.
2. To perform an experimental program of direct shear test on rock joints with different suction and different asperity roughness.
3. To propose a new mechanical constitutive law considering the effect of suction and asperity roughness.
4. To implement this new constitutive law in Code_Bright and numerically simulate the experimental results.
5. To use the implemented formulation to model a large-scale test of the nuclear waste repository, and to compare the test and model results.

1.2. Organization and scope

A review of the hydro-mechanical behaviour of rock joints is presented in Chapter 2. An overview of the experimental results from the normal, shear, and hydro-mechanical tests performed on rough joints is presented. Additionally, the existent constitutive laws to mathematically model the hydro-mechanical behaviour of rock joints are described.

The coupled thermo-hydro-mechanical formulation of the interface element with double nodes implemented in Code_Brigth is explained in Chapter 3. The mechanical problem is formulated by means of the equation of stress equilibrium. The effective stresses are considered to be applied in the mid-plane and related to the relative normal and tangential displacements in the mid plane of the element by the mechanical constitutive law. The mechanical constitutive law is developed within the elastic-viscoplastic framework. The hydraulic problem is solved with the mass balance equation (water and air). The hydraulic constitutive law depends on the interface aperture. The balance of internal energy is established assuming thermal equilibrium between

phases. Some general aspects of the constitutive theory are also presented. Finally, hydro-mechanical tests are modelled to validate and verify the implementation of interfaces.

The test program performed on rock joints with different asperity roughness and different suctions is explained in Chapter 4. A description of the direct shear cell and of the improvements on the equipment is presented. Likewise the geotechnical characterization of the rock used to construct the rock joints samples is given. Moreover a detailed description of the preparation of the samples is explained taking into account the joint construction, the measurement of the joint profile and the technique used to equilibrate the relative humidity of the samples. Then, the shear test protocol is described. Finally, the chapter describes the shear test and profilometry results.

The direct shear test results are analyzed in Chapter 5. A new mechanical model for rock joints is formulated, based on the changes of strength parameters with asperity roughness and suction. This model was implemented in Code_Bright, and was then used to numerically simulate the tests. Finally, the model results are plotted against experimental results and discussed.

Within the framework of the European project THERESA, the numerical thermo-hydro-mechanical simulation of a large-scale in situ test of a nuclear waste repository was performed. A description of the geometry, protocol and materials of the test is given in Chapter 6. The geometry and the materials considered in the finite element model are presented. The thermo-hydro-mechanical formulation of interfaces described in Chapter 3 was used to model the interface located between the buffer and the canister in the nuclear waste repository. The buffer made of bentonite and pellets was modelled using the Barcelona Basic Model. In this case the interface element is adjacent to an expansive material. In the end, the numerical results were compared with the experimental data available.

Chapter 7 presents a sensitivity analysis of the interface properties. This analysis allows investigating the effects on the adjacent bentonite. This chapter also describes the analysis of the gas flow through interfaces.

Finally, in Chapter 8 the conclusions of the work are brought to light as well as a recommendation for further research. The thesis closes with a list of references.

CHAPTER 2

Hydro-mechanical behaviour of rock joints

2.1. Introduction

In order to determine the structural stability of a massive rock, it is necessary to determine the presence of discontinuities and their geotechnical characteristics. Generally, the orientation and dip of discontinuities are measure in situ and their hydro-mechanical characterization performed in the laboratory. Once the strength and hydraulic parameters of the joints are determined, it is possible to predict their behaviour using some of the mathematical models proposed.

This chapter presents a summary of the state-of-the-art on rock joints. It includes a description of the geometrical, mechanical and hydraulic properties of rock joints. It also describes the damage of the asperity roughness of the joints walls and their influence on strength and permeability. Furthermore, a brief overview of scale effects is included.

Finally, the mathematical model proposed to predict the hydro-mechanical behaviour and damage of joints is explained.

2.2. Characteristics of rock joints

The discontinuities existing in the rock mass are the result of the formation of the rock mass and subsequent movements in the crust of the earth. According to Jennings & Robertson (1969), two sets of discontinuities could be defined as major and minor or secondary. Major discontinuities include bedding planes, faults, contacts and dykes, while minor are joints of limited length, i.e. cross joints in sedimentary rocks.

Taking into account their origin, joints can be classified as: bedding planes, which are associated with sedimentary rocks and appear when there is a change in the characteristics of the deposited material; stress relief joints, which form as a result of erosion of weathered rock; tension joints,

which are the result of cooling and crystallization of igneous rock; and faults, defined as a plane of shear failure that exhibits obvious signs of differential movement of the rock mass on either side of the plane. Usually, faults are linked to the movement of tectonic plates.

A joint consists of two planes separated by a specific opening. The characteristics of the plane surfaces depend on the geological history of the rock mass, which involves mechanical, hydraulic, depositional, chemical and many other processes.

The geometry of the joint can be described by the aperture (separation between the two joint wall surfaces), roughness (surface height distribution or shape of the surfaces), contact area (area where the surfaces are in contact, and can transfer stresses), matedness (how well matched surfaces are), spatial correlation (how abruptly or slowly aperture changes), tortuosity (forced bending of stream lines due to variations in joint aperture), and channelling (differences in flow velocity along a certain path, due to variations in joint aperture). The void structure of discontinuities has a great importance on its hydro-mechanical behaviour (Hakami, 1995).

2.3. Joint Roughness Coefficient (JRC).

Barton, (1973) proposed an empirical coefficient to measure the rugosity named JRC. Even though the determination of JRC is done by visually comparing the joint surface to a table proposed by Barton (Fig. 2.1), this parameter is extensively used to model the mechanical and hydro-mechanical behaviour of rock joints.

Barton & Bandis (1990) proposed to scale the JRC with the amplitude of asperities and the length of the joint as:

$$JRC_n = JRC_0 \left(\frac{L_n}{L_0} \right)^{0.02\,JRC_0} \qquad 2.1$$

where L_n is the in situ block size and L_0 is the lab-scale sample length.

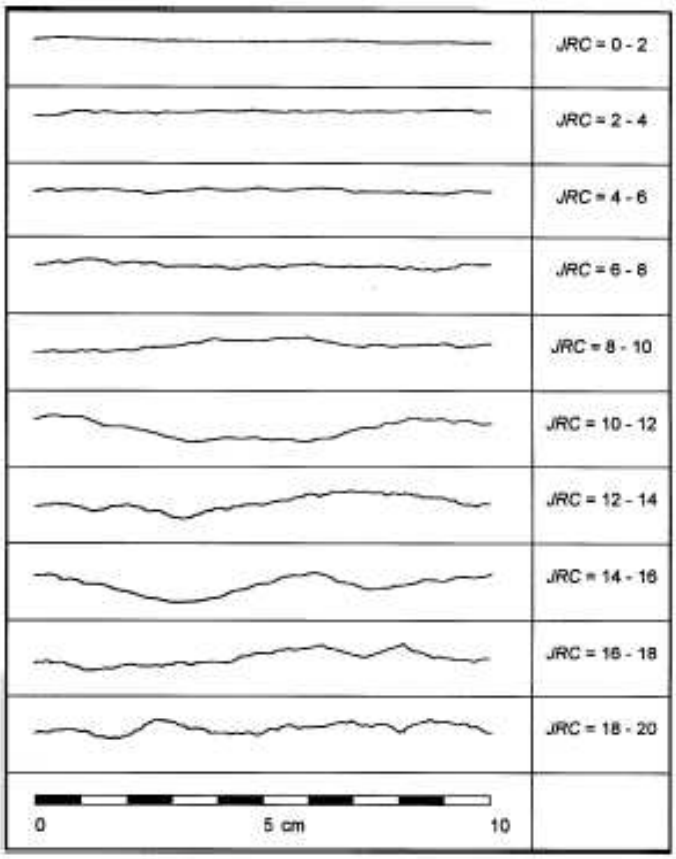

Figure 2.1: Laboratory scale joint roughness profile with its measured JRC values, (after Barton & Choubey, 1977).

2.4. Joint wall compression strength (JCS).

The JCS is determined using a Schmidt hammer (Barton & Choubey, 1977). The Schmidt hammer is a simple device that records the rebound of a spring loaded plunger after its impact to a surface. It is suitable for measuring JCS values down to about 20MPa and up to at least 300MPa. A reasonable correlation between the rebounded number and the unconfined compressive strength (σ_c) of the rock was proposed by Barton & Choubey (Fig. 2.2). The importance of the parameter is accentuated if the joint walls are weathered, in which case the JCS value may be a small fraction of σ_c. Likewise, the ratio JCS/σ_c controls the amount of asperity damage for a given joint roughness.

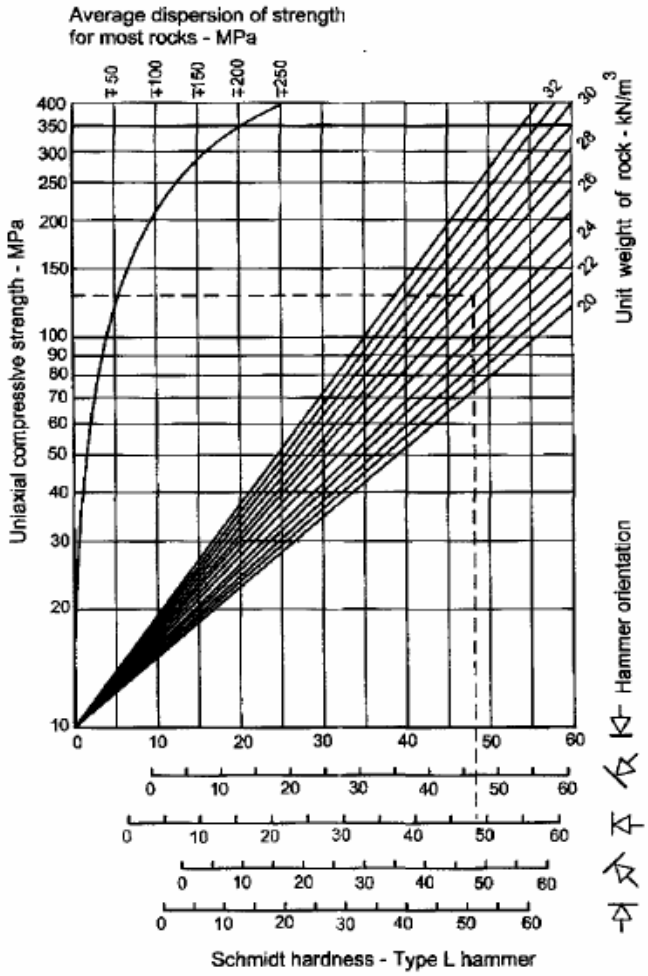

Figure 2.2: The relationship between the Schmidt hardness and the uniaxial compression strength of the rock (Barton & Choubey, 1977).

2.5. Description of the mechanical behaviour of rock joints

The stress-displacement curves obtained from normal and shear experiments performed on rock joints are highly no-linear (Figs. 2.3 and 2.4). This non-linear behaviour depends on initial geometry of the joint, and on the strength and deformability of the adjacent material.

2.5.1 Normal compressive stress test

Typical tests consist in applying a normal compressive stress to reach a given value and then remove the stress. In this case, a single curve is plotted, which represent normal stress vs. normal relative displacement (Fig. 2.3). At low normal stress values only a few of the surfaces are in contact and the interface closes easily. As normal stress increases, so does the contact area reducing the void space. Hence, the normal stiffness increases with displacement until a limiting closing value is attained. At this point the interface is not able to close any more and the limiting compressive stress is reached. Figure 2.3 shows the results obtained by Bandis (1983) for three different cases: a) intact rock, b) interlocked joint and c) a mismatched joint. For the intact rock the relationship between stress and displacement is quasi linear elastic. On specimens crossed by a joint present a non-linear plastic behaviour. Note also in the figure that the non linearity and the hysteretic behaviour depend on the area of the contact zones; these phenomena are larger for mismatched joints.

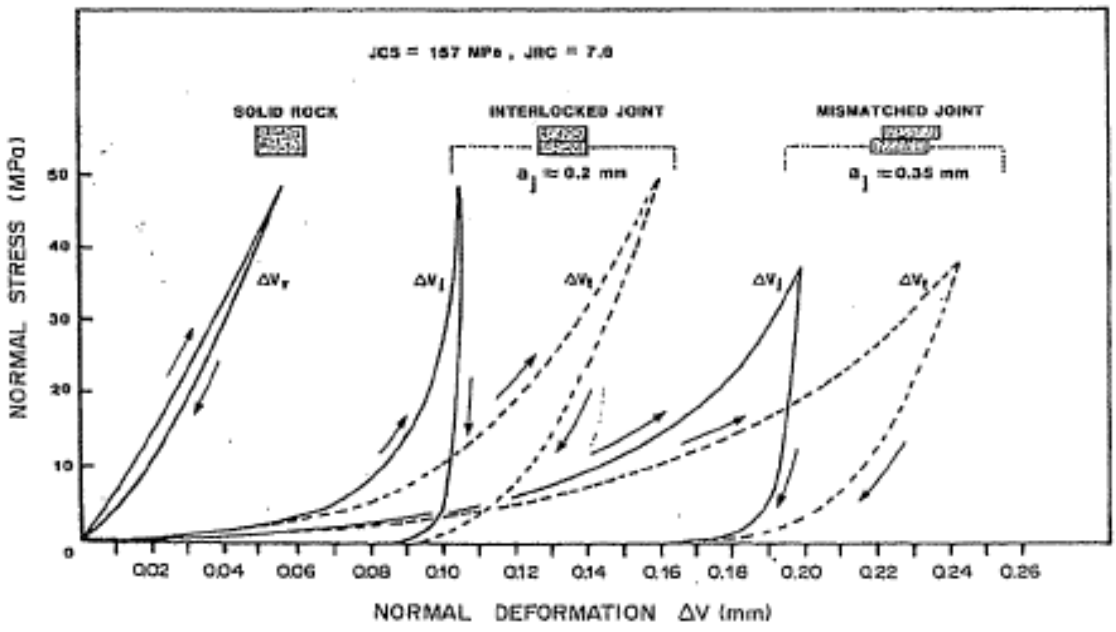

Figure 2.3: Normal stress vs. normal displacements. a) Intact rock, b) interlocked joint, c) mismatched joint (Bandis et al., 1983).

The behaviour of fresh joints and weathered joints subjected to cyclic normal stress was also studied by Bandis et al. (1983). Figure 2.3 shows that the fresh joint presented a lower plastic displacement than the weathered joint. Likewise, the hysteretic behaviour is more pronounced in weathered joints.

2.5.2. Shear stress test

There are several protocols to carry out shear testing depending on how the stress is applied. It is possible to perform tests applying a constant normal force (F_n); a constant normal stress (CNS); a constant normal stiffness (CNK, $\frac{d\sigma_n}{du} = c$); maintaining a constant volume or imposing a dilatancy. Nevertheless, the tests are generally performed applying a constant normal stress or a constant normal stiffness.

Given that shear stress at constant normal stress is the most commonly used test, the experimental program of this thesis also resorted to it.
The test begins applying a normal compressive stress that remains constant while the shear relative displacement is prescribed. Two different curves are obtained from this test: a) shear stress vs. shear relative displacement and b) normal vs. shear displacement (Fig. 2.4). Shear stress rapidly increased up to a peak, followed by a gradual decrease down to a residual value. This loss is related to the wearing of roughness. The figure also shows that a minimal dilation occurs during the initially elastic deformation of the joint and after a rapid increase is observed, when the opposite asperities begin to ride over each other (Pt. 2-Fig. 7.b). At this point the roughness is sufficiently damaged to allow one surface to slide over the other and for dilatancy to increase although at a progressively decreasing rate (Pt. 4-Fig. 7.b). At the end, shear displacement is attained at constant shear stress without a significant increase in dilatancy. Large dilation occurs under low confining stresses. Nevertheless, under higher confining stresses, asperities are crush due to higher frictional forces and dilation decreases (Barton, 1976).

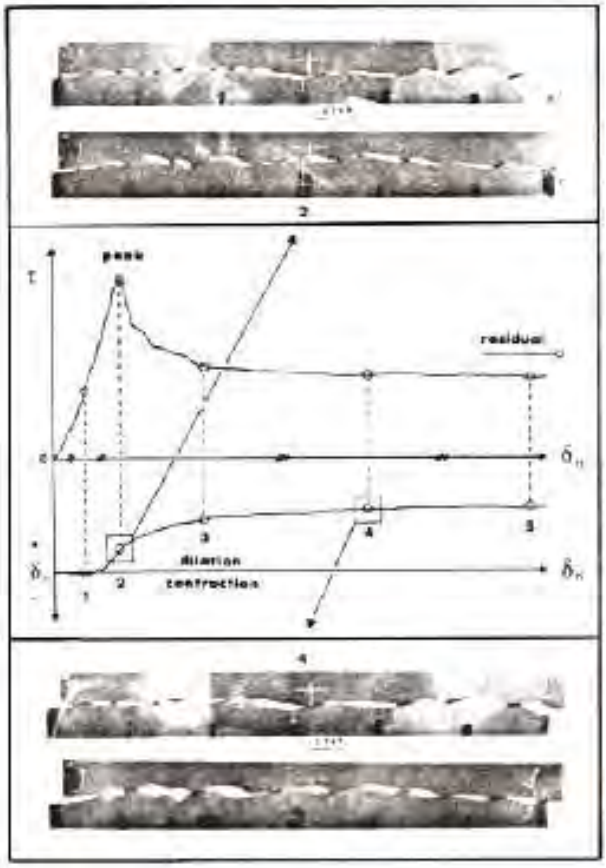

Figure 2.4: Shear test plots. a) Shear stress vs. shear displacement, b) normal vs. shear displacement (Barton, 1976).

2.6. Description of the hydraulic behaviour of rock joints

The fluid flow through joints has always been analyzed as a laminar flow between two smooth and parallel plates separated by a specific hydraulic aperture (e). An empirical relationship between the hydraulic aperture and the geometrical aperture (E) for different values of joint roughness was developed by Barton et al., (1985)(Fig. 2.5):

$$e = \frac{E^2}{JRC^{2.5}} \qquad 2.2$$

The figure shows that this relationship is highly non-linear due to the roughness. The measurement of the geometrical aperture is also a matter of discussion, but is widely used to measure it normal to the orientation of the axis. This measurement is also considered to be constant over a segment.

Further to these hypotheses, the cubic law is used to calculate the permeability of the joints:

$$k = \frac{\rho g}{\mu} \frac{e^3}{12} \qquad 2.3$$

where ρ is the fluid density, g is the gravity and μ is the fluid viscosity.

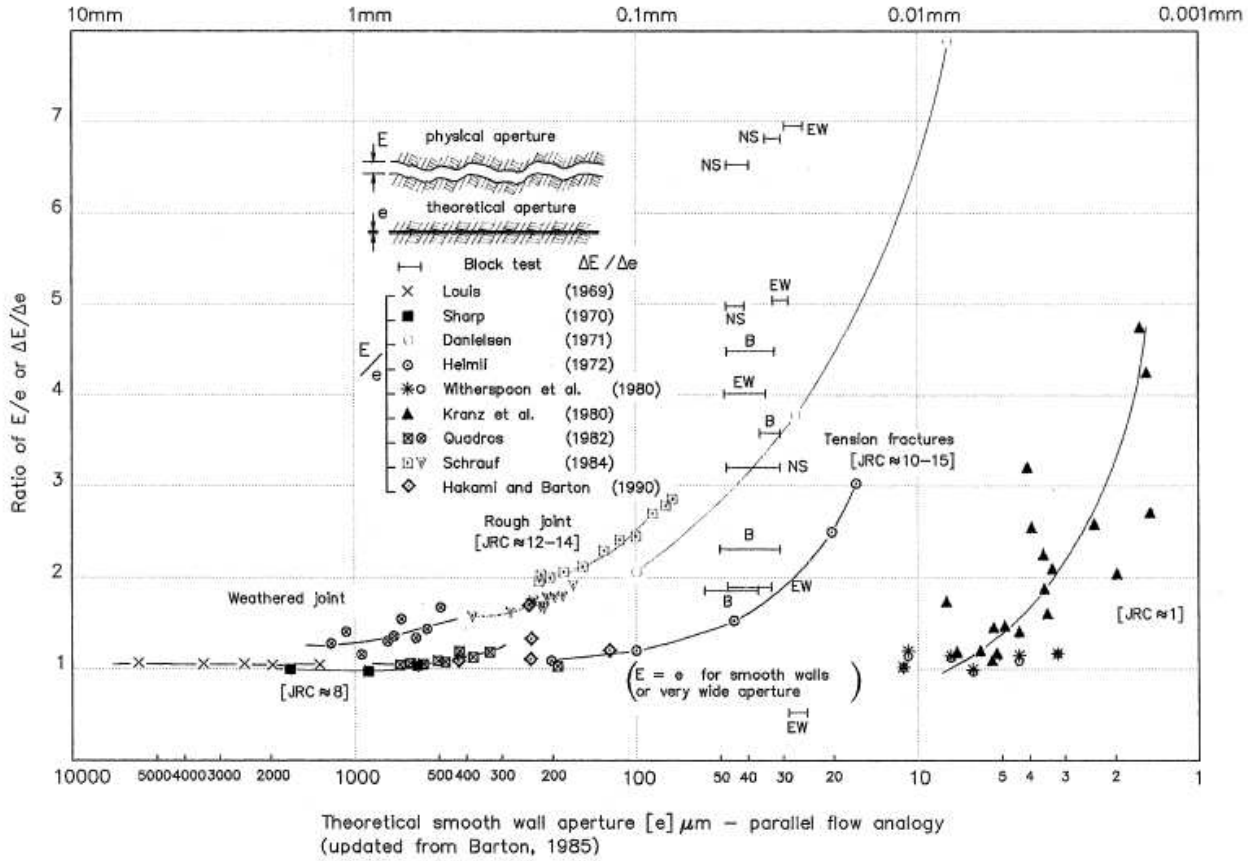

Figure 2.5: Comparison of the real mechanics aperture (E) with the theoretical smooth wall conducting aperture (e) (Barton et al., 1985).

2.7. Description of hydromechanical behaviour of rock joints

The hydro-mechanical behaviour associated with normal stress has been extensively studied. Figure 2.6 shows the experimental results obtained by Hans et al. (2002). It is observed that transmissibility decreased as normal stress increased. This decrease is due to the reduction of the void space between the discontinuous walls, the increase of the contact area and the tortuosity. When the compression on the discontinuity is released, a non reversible behaviour can be observed, i.e. the transmissivity at zero stress is lower than the initial transmissivity.

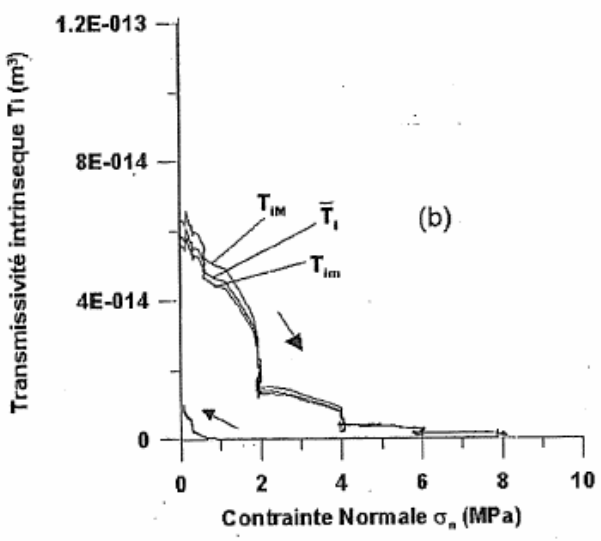

Figure 2.6: Transmissivity evolution with compression stress. Tests results obtained by Hans, (2002).

Thus, when a shear stress is applied before the shear stress reaches a peak, transmissivity decreases, thereafter increasing considerably (approximately two orders of magnitude). The increment of transmissivity is directly related to joint dilatancy (Fig. 2.7)(Lee et al., 2001). The figure also shows that, even thought dilatancy increases continuously, joint permeability reaches a constant value. This is a consequence of the gouge material generated by the asperity breakage. The roughness degradation depends on the strength of asperities, the applied normal stress and the shear stiffness. This was also measured by Olsson & Barton (2001), who performed shear stress test at different normal stresses (2 and 4 MPa) and stiffness (0, 37 and 75 KN/mm)(Fig.

2.7). Note that higher normal stresses and higher normal stiffness reduce dilatancy and induce lower increments of transmissivity.

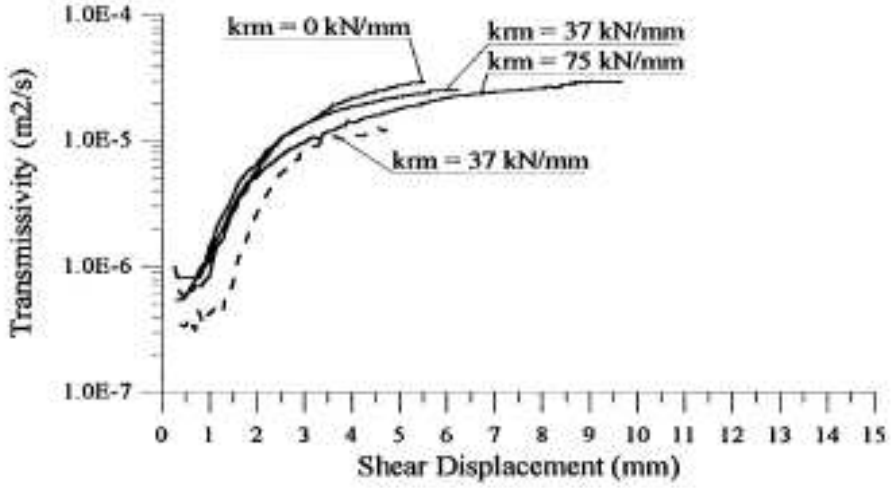

Figure 2.7: Shear stress tests performed at different constant normal stiffness (krm =0 , 37 and 75 KN/mm)(Olsson & Barton, 2001).

2.8. Scale effects

There is a recurring problem when laboratory results are extrapolated to apply them to “in-situ” problems. Given that the JRC coefficient depends on the length of joint, Bandis et al. (1981) observed a similar effect when joints of different lengths underwent shear stress tests. Figure 2.8 shows that the peak shear stress and dilatancy augment as joint block length decreases.

Scale effects were also detected in joint transmissivity during hydro-mechanical tests. Raven & Gale (1985) measured the transmissivity of joint samples with diameters that ranged from 10 cm to 29.4 cm. This is explained by the increment of contact points with regard to the diameter of the sample (Fig. 2.9).

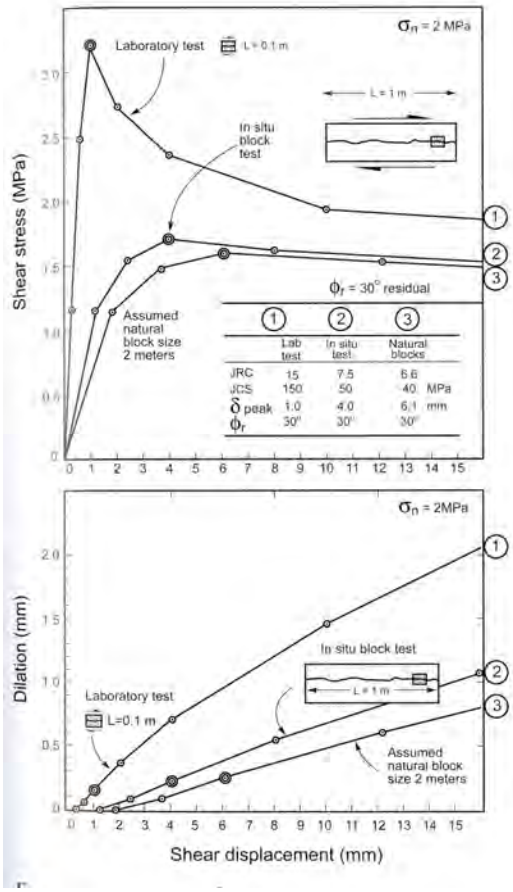

Figure 2.8: Example of manually calculated shear stress displacement-dilation curve for different block sizes, using the JRC_{mob} concept from Barton (1982).

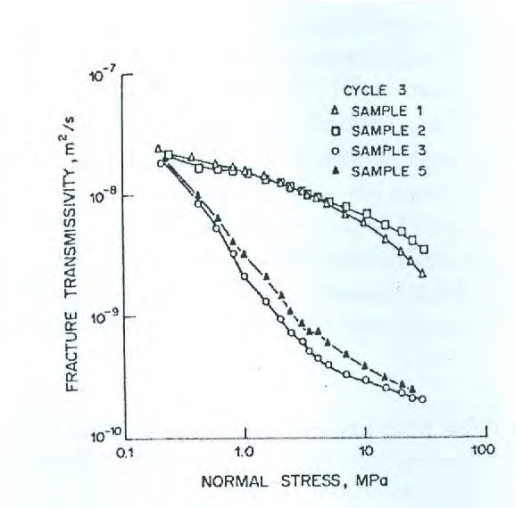

Figure 2.9: Evolution of transmissivity versus normal stress for different sample sizes. Sample 1 = 10 cm, Sample 2 = 15 cm, Sample 3 = 19.3 cm, Sample 5 = 29.4 cm (Raven & Gale, 1985).

2.9. Mechanical Models

The mechanical behaviour of joints could be modelled considering two theories, one developed for pre-existing joints and another based on fracture mechanics, which enable modelling the initiation and propagation of joints. In general, the group of pre-existing joints includes most geological discontinuities, such as rock joints, faults, as well as interfaces between soil and structure, i.e. rock-concrete or soil-concrete contacts in foundations. Fracture mechanics are used to describe the quasi-brittle behaviour of concrete and rocks. In this case the cracks begin in a zone where the materials show micro-cracking (fracture cohesive zone). As micro-cracks nucleate, stress increases up to a maximum value. At a point close to this maximum value, the coalescence between micro cracks is lost and they connect, leading to macro-cracks or fractures and causing a sudden drop in stress. The following sections present the models used for the different theories.

2.9.1. Pre-existing joints

For pre-existing joints several empirical strength criteria were formulated to describe the non-linear behaviour of rock joints.

Barton (1973) proposed the following simple expression relating shearing stress to normal stress at failure:

$$\tau = \sigma_n \tan\left(\phi_B + d_n + s_n\right) \qquad 2.4$$

where Φ_B is the basic angle friction; d_n, the peak dilatation angle, and s_n, the contribution of the intact material (asperities).

This expression implies that the angle of the total shearing resistance is the sum of the three components above mentioned. The experimental data reported in literature suggest that most rocks have a basic angle Φ_B that ranges from 25º to 35º. The peak dilatation angle is a geometrical component that depends on the rock roughness and reduces with an increase in

normal stress level. Furthermore, the component due to partial or total failure of asperity is expressed by s_n, which initially increases with an increasing stress level.

Later, Barton & Choubey (1977) proposed an empirical logarithmic criterion, which is widely accepted in literature and practice. Their proposal consisted in predicting the peak angle of the shear strength of rough joints as a finction of the joint wall compressive stress (JCS) and joint roughness coefficient (JRC). The expression for the shear strength is:

$$\tau = \sigma_n \tan\left(JRC \log\left(\frac{JCS}{\sigma_n} \right) + \phi_r \right) \qquad 2.5$$

where ϕ_r is the residual friction angle.

Later Olsson & Barton (2001) modified expression 2.5 to improve the hydraulic behaviour of the joint:

$$\tau = \sigma_n \tan\left(JRC_{mob} \log\left(\frac{JCS}{\sigma_n} \right) + \phi_r \right) \qquad 2.6$$

where JRC_{mob} is a coefficient that considers the degradation of asperities during shear straining. One of the main aspects of the model is that roughness decrease after reach the peak strength when JRC_{mob}/JRC equals 1.0. The residual strength is attained after a large shear displacement (Fig. 2.10), and that dilatancy is calculated as:

$$d_{nmob} = \frac{1}{M} JRC_{mob} \log\left(\frac{JCS}{\sigma_n} \right) \qquad 2.7$$

where M is a damage coefficient. Dilation begins when the rate between shear displacement u_s and peak shear displacements u_{sp} is 0.3. It is at this point that roughness is mobilized. Then, dilatancy decreases following the reduction of roughness ($u_s > u_{sp}$).

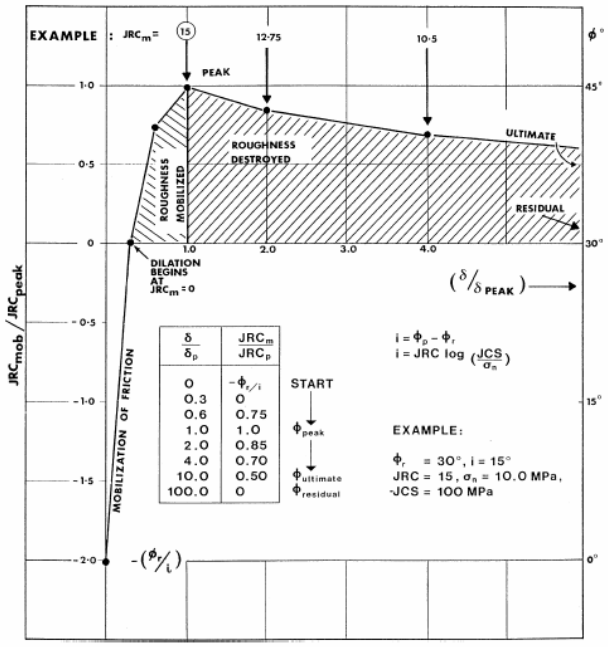

Figure 2.10: Barton (1982)'s JRC_{mob} concept Shear strength development for rock joints expressed as dimensionless JRC_{mob}/JRC_{peak} and reduction of this fraction with a dimensionless δ/δ_{peak} displacement.

Gens et al. (1990) proposed an elasto-plastic model to describe the mechanical behaviour of pre-existing joints. For the elastic formulation it is necessary to define a normal and a tangential stiffness. As for the plastic formulation, it is necessary to define a yield surface, a hardening law and flow rule.

In case of elastic behaviour, a constant tangential stiffness is assumed, whereas the value of normal elastic stiffness depends on the loading conditions and interface opening (see Fig. 2.11).

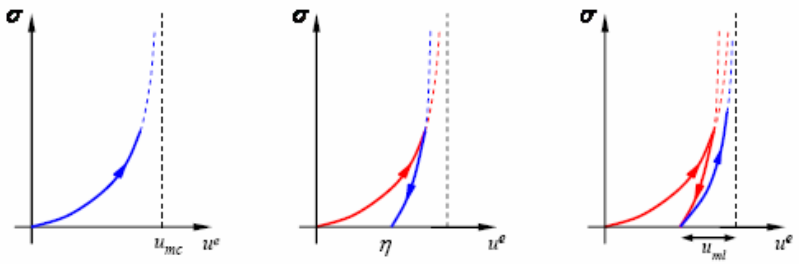

Figure 2.11: Normal stress vs. aperture for first loading, unloading and reloading respectively (Gens et al., 1990).

The mathematical expressions are:

$$\textit{First Loading} \quad \sigma = m\frac{u^e}{u_{mc} - u^e}$$

$$\textit{Unloading} \quad \sigma = m\frac{u^e - \eta}{u_{ml} - \left(u^e - \eta\right)} \qquad 2.8$$

$$\textit{Reloading} \quad \sigma = m\frac{u^e - \eta}{u_{mc} - u^e}$$

where u^e is the elastic normal relative displacement, u_{mc} is the maximum closure value, m is a constant, η is the value of u^e attained at unloading when $\sigma = 0$, and u_{ml} is a model parameter ($u_{ml} < u_{mc}$) that represents the asymptotic aperture after unloading and measured with regards to η.

The plastic behaviour is defined by a hyperbolic yield surface:

$$F \equiv \tau_1^2 + \tau_2^2 - B^2\left(\sigma^2 + 2a\sigma\right) \qquad 2.9$$

where τ_1 and τ_2 are the two components of the tangential stress in a set of orthogonal axes contained in the discontinuity plane, σ is the normal stress and *a* and *B* are constants (Fig. 2.12). Constant *B* is the slope of the asymptote when σ tends to infinity. It can therefore be expressed in terms of the tangent of the friction angle. Constant *a* is the distance between the origin and the σ-axis intercept of the asymptote. The comparison with experimental results suggests that $\tan\Phi'$ may correspond to a basic friction angle, whereas *a* would be a measure of the degree of roughness.

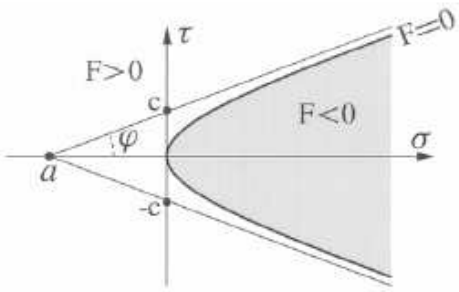

Figure 2.12: Yield surface for elasto-plasto behaviour of joints under shear stress (Gens et al., 1990).

Hardening law: The variation of hardening parameters, tanΦ and a, produces the corresponding family of yield surfaces, and it is controlled by a single internal variable ξ that depends on dv^p_1 and dv^p_2, which are the plastic tangential relative displacements. The variation of hardening parameters *a* and tanΦ with ξ follows a second degree parabola in the pre-peak range, and a third degree polynomial, after the peak. Residual conditions are attained at a residual value of ξ (Fig. 1.13).

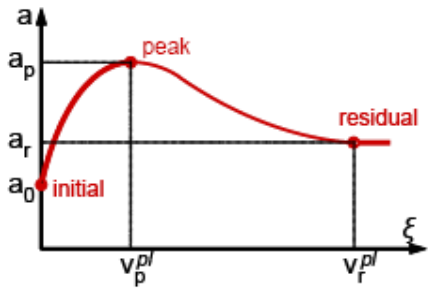

Figure 2.13: Evolution of hardening parameters (Gens et al., 1990).

In case that a better fit is required, a modification of the hardening law is used so that the polynomials are made to depend on a function $f(\xi)$ instead of ξ itself. This function is represented as follows:

$$f(\xi) = \frac{\xi e^c}{1 + (e^c - 1)\xi} \qquad 2.10$$

where c is a constant that controls the initial plastic tangent stiffness. If c is made equal to zero the original polynomial expressions are recovered.

Plastic potential: The expression adopted for the derivatives of plastic potential Q are:

$$\frac{\partial Q}{\partial \tau_1} = \tau_1 ; \quad \frac{\partial Q}{\partial \tau_2} = \tau_2 ; \quad \frac{\partial Q}{\partial \sigma} = -\sqrt{(\tau_1)^2 + (\tau_2)^2} \tan i \qquad 2.11$$

where i is the dilatancy angle. It is assumed that i varies with ξ in the same way as the hardening parameters. However, the initial and final (residual) values of the dilatancy angle are always expected to be equal to zero. The variation of the peak angle of dilatancy, i_p with the normal stress level is given by:

$$\tan i_p = i_p^0 \left(1 - \frac{\sigma}{q_u}\right)^4 \qquad 2.12$$

where i^0_p is the peak dilatancy angle for an applied compression equal to zero, and q_u is the unconfined compression strength of the rock.

2.9.2. Model based on fracture mechanics

A simple but general model for normal/shear cracking in quasi-brittle materials was developed by Carol et al. (1997). A crack surface in stress space determines crack initiation under pure tension, shear-tension, or shear-compression loading. Its evolution is determined by two independent fracture energy parameters. One of the energy parameters was measured when a material broke as a consequence of applying a normal tension stress over it (Mode I from fracture mechanics theory). The other energy parameter is obtained when the crack of the material is due to a shear stress under high compression, which implies a dilatancy equal to zero

(Mode IIa from fracture mechanics theory). This constitutive law is completely defined by a cracking surface, softening laws and plastic potential surface.

Cracking surface: A crack is assumed to start when stresses reach the cracking surface (Fig. 2.14 a), which is considered to be hyperbolic with the following expression:

$$F \equiv \sigma_T{}^2 - \left(c - \sigma_N \tan\phi\right)^2 + \left(c - \chi \tan\phi\right)^2 \qquad 2.13$$

where tanΦ, c, and χ are model parameters representing the slope, the cohesion of the asymptote and the tensile strength of the interface respectively. This curve will result in a smooth transition between two limit states: Mode I and Mode IIa loading conditions (Fig. 2.14 b).

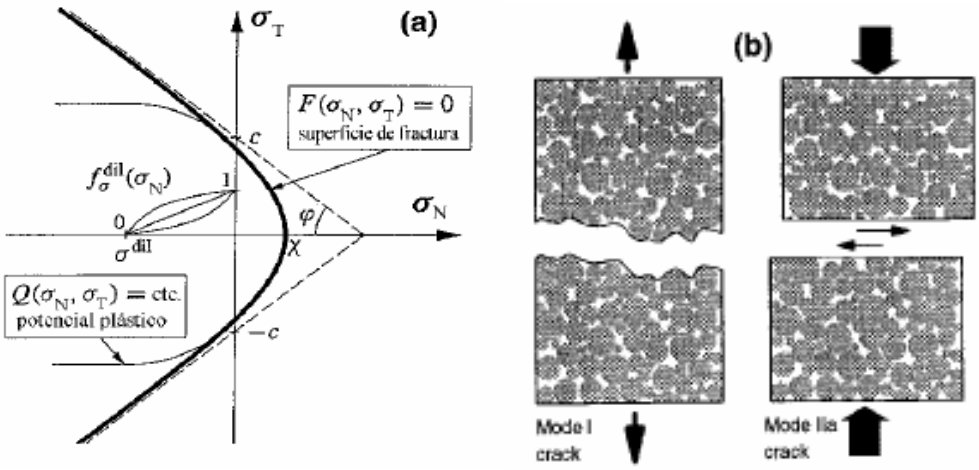

Fig. 2.14: a) Cracking and plastic potential surface; b) modes of fracture (Carol, et al., 1997).

Softening laws: The shrinkage of the cracking surface for both modes is achieved by the evolution of parameters tanΦ, c, and χ as a function of the work spent on fracture processes during the formation of the crack.

$$dW^{cr} = \sigma_N du_N^{cr} - \sigma_T du_T^{cr} \quad \sigma_N \geq 0 \quad (tension)$$

$$dW^{cr} = \sigma_T du_T^{cr} \left(1 - \left|\frac{\sigma_N \tan\phi}{\sigma_T}\right|\right) \quad \sigma_N < 0 \quad (compression) \qquad 2.14$$

where dW^{cr} is the increment of work spent on fracture processes, and du_N^{cr} and du_T^{cr} are the increments of the normal and tangential displacement of the crack respectively.

The variation of tanΦ, c, and χ is assumed to be linear in terms of the intermediate scaling function f, defined as:

$$f(\xi) = \frac{\xi e^{-\alpha}}{1 + \left(e^{-\alpha} - 1\right)\xi}$$

$$\xi = \frac{W^{cr}}{G_f^I} \quad ; \quad \alpha = \alpha_\chi \qquad 2.15$$

$$\xi = \frac{W^{cr}}{G_f^{IIa}} \quad ; \quad \alpha = \alpha_\phi \quad ; \quad \alpha = \alpha_c$$

where Gf^I is the fracture energy dissipated by Mode I and Gf^{IIa} is the fracture energy dissipated by Mode IIa of the fracture. The values of α define the different evolution of parameters Φ, c, and χ (see Fig. 2.15 b and c).

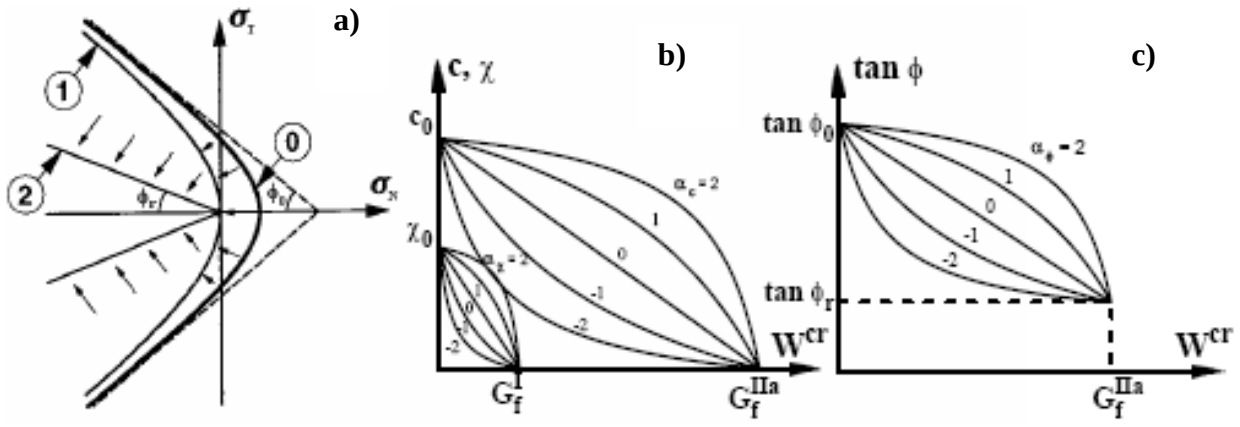

Figure 2.15: a) Evolution of cracking surface; b) softening law of c and χ; c) softening law of tanΦ (Carol et al., 1997).

Plastic potential surface and dilatancy: Initially, the potential surface coincides with the cracking surface in tension, while in compression the rule is non-associated, with dilatancy vanishing for compression intensity approaching value σ^{dil} (compression strength of the material), which is an additional parameter of the model. The amount of dilatancy must also decrease with the increasing degradation of the crack surface, so that it vanishes completely for the residual friction state given by $c = 0$ (Fig. 2.15 a). The following expressions describe all these effects:

$$\mathbf{Q} = \mathbf{A} \bullet \mathbf{n}$$

$$\mathbf{A} = \begin{bmatrix} f_\sigma^{dil} f_c^{dil} & 0 \\ 0 & 1 \end{bmatrix} \qquad 2.16$$

$$\mathbf{n} = \frac{\partial F}{\partial \boldsymbol{\sigma}} = \left[2\tan\phi\left(c - \sigma'_n \tan\phi\right) \quad , \quad 2\tau \right]^T$$

where $f\sigma^{dil}$ and fc^{dil} are calculated by:

$$f(\xi) = \frac{\xi e^{-\alpha}}{1+\left(e^{-\alpha}-1\right)\xi}$$

$$\xi = \frac{|\sigma_N|}{\sigma^{dil}} \quad ; \quad \alpha = \alpha_\sigma^{dil} \qquad 2.17$$

$$\xi = \frac{c}{c_0} \quad ; \quad \alpha = \alpha_c^{dil}$$

where the values of the α define the different evolutions of parameters $f\sigma^{dil}$ and fc^{dil}.

2.10. Effect of moisture content

Barton (1973) detected that the saturation of a rock joint causes a reduction in Φ_b, Φ_r, σ_c, tensile strength σ_t and JCS. The studies showed in general terms that moisture (when comparing wet to dry) caused a reduction of 1º to 3º in Φ_b and Φ_r. Examples of the effect of saturation compared to dry conditions on Φ_b are shown in Table 2.1. The water saturation, also led to a reduction of 20 to 40% in σ_c and σ_t. This reduction in σ_c implies a decrease in JCS.

Table 2.1: Basic friction angle for dry and wet rock joint (after Barton, 1973).

Rock type (flat, smooth, non-polished surface)	$\Phi_{b\ dry}$ (º)	$\Phi_{b\ wet}$ (º)
Sandstone	26-35	25-33
Siltstone	31-33	27-31
Limestone	31-37	27-35

2.11. Hydraulic Models

The permeability of joints is influenced by the magnitude of the applied normal stress and by the dilatancy caused by shear stress. The models suggested to reproduce the variation of permeability with its stress state are described below.

Gangi (1978), Gale (1982) and Swan (1983) proposed the equations 2.17, 2.18 and 2.19, respectively, to calculate permeability as a function of normal stress:

$$k = k_0 \left[1 - \left(\frac{\sigma'_n}{D} \right)^{\frac{1}{n}} \right]^2 \qquad 2.17$$

$$k = \beta_0 \sigma'^{\,a}_n \qquad 2.18$$

$$k = k_0 \left(C + M \ln \sigma'_n \right)^2 \qquad 2.19$$

where k_0 is the initial permeability, and D, n, β, a, C and M are model parameters.

These models were used by Lee & Cho (2002) to fit experimental fracture permeability, which was calculated by determining the hydraulic aperture proposed by Barton, 1985 in Equation 1.1. Figure 2.16 shows a comparison of the permeability fitting calculated with the models above suggested. From the results it is possible to deduce that fracture permeability decreases proportionally to the negative power of applied normal stress.

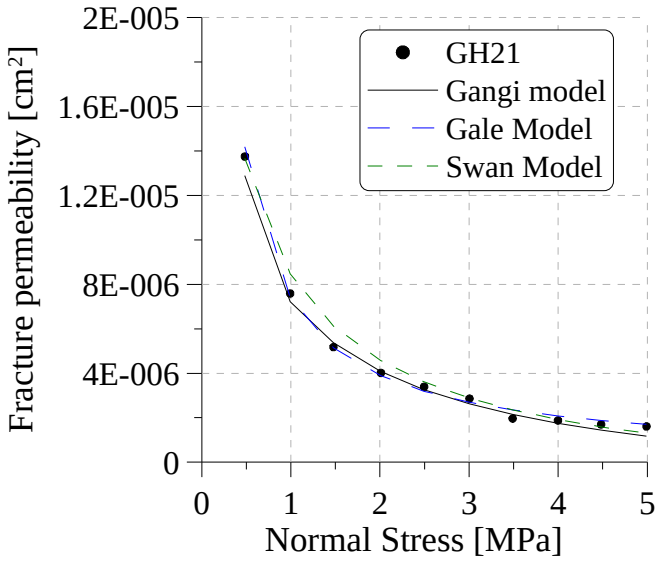

Figure 2.16: Normal stress vs. fracture permeability data with regards to several hydraulic models (Lee & Cho, 2002).

Olsson & Barton (2001) proposed a model that bears in mind the changes of permeability with dilatancy during shear tests. The value of the hydraulic aperture before the peak is calculated by:

$$e = \frac{E^2}{JRC_0^{2.5}} \qquad u_s \le 0.75 u_{sp} \tag{2.20}$$

while the aperture after the peak is calculated by:

$$e = E^{0.5}\ JRC_{mob} \tag{2.21}$$

where JRC_{mob} is the mobilized value of roughness. This value is dependent on the strength on the discontinuity surface, on the applied normal stress and on the magnitude of shear displacement. Tests and model results are compared in Figure 2.17. The figure shows that this improved model reproduced the tests results better.

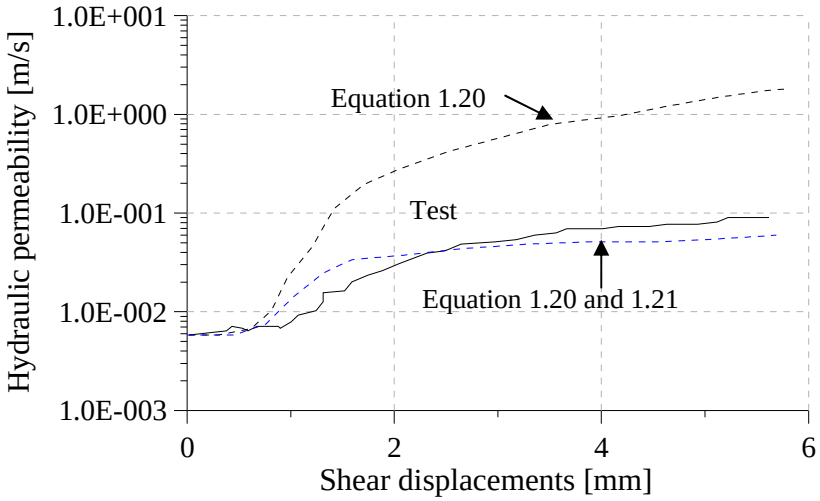

Figure 2.17: Hydraulic conductivity vs. shear displacements for predicted (calculated with Eqs. 1.20 (dash line), 1.20 and 1.21) and performed CNL shear tests (Olsson & Barton, 2001).

2.12. Damage of roughness models

The joint roughness changes continuously with shearing due to the wearing, grinding, breaking and crushing of asperities. Sheared laboratory samples prove that damage depends on the geometry of asperity (including size and shape), the mechanical properties of the rock, shear direction and applied normal stress and shear displacements. Hydraulic tests under shear stress also showed fracture permeability changes with roughness damage. The inclined asperity areas opposite to shear direction are detached causing voids perpendicular to the shearing direction. This gouge material causes the obstruction of the fracture, thus decreasing its permeability.

Different asperity degradation laws are briefly described below:

Barton & Choubey (1977) proposed the following damaged coefficient:

$$M = \frac{JRC}{d_{n0}} \log\left(\frac{JCS}{\sigma_n}\right) \text{ with } 1 \le M \le 2 \qquad 2.22$$

Plesha (1987) suggested an exponential law for asperity angle degradation α based on experimental results:

$$\alpha = \alpha_0 \exp\left(-cW_p\right) \tag{2.23}$$

where α_0 is the initial asperity angle; c is a damage coefficient determined experimentally; W_p is the plastic work or energy dissipation during frictional sliding.

Lee et al. (2002) proposed an extended version of Plesha´s model introducing forward (F) and backward (B) shear displacements and considering a first and second (1 and 2) order roughness effect:

$$\begin{aligned} \alpha_F &= \alpha_{0F1} \exp\left(-c_1 W_p\right) + \alpha_{0F2} \exp\left(-c_2 W_p\right) \\ \alpha_B &= \alpha_{0B1} \exp\left(-c_1 W_p\right) + \alpha_{0B2} \exp\left(-c_2 W_p\right) \end{aligned} \tag{2.24}$$

More recently Belem et al. (2007) proposed two generalized degradation roughness models for the two different kinds of rock joint tests CNS and CNK (mentioned in Section 3.2). The models are based on the following surface roughness descriptive parameters: anisotropy (k_a); roughness mean angle (θ_s); specific roughness asperity, which evaluates the evolution of roughness during shearing (SR_s); degree of relative surface roughness to describe the possible evolution of surface roughness from the initial state (DR_r) and the surface roughness amplitude (a_0). These parameters were calculated from the statistical analysis of the topography of joint walls measured prior and after shear testing using a 3D profilometer. The expressions of the model proposed are:

$$\begin{aligned} &Dw = 1 - \left(1 - \frac{\sigma_{n0}}{\sigma_c}\right) \exp\left(-\beta_d \frac{\sigma_{n0} + k_n u_{s0} \tan\left(\delta_{\text{ave}}\right)}{\sigma_c}\right) \qquad \beta_d = \frac{3k_a{}^3}{8DR_r \tan\theta_s} \log\left(\frac{u_{s-tot}}{a_0 k_a}\right) \\ &Dw = \left(\alpha_0 - k_a\right) \sqrt{\tan\theta_s} \exp\left(-\chi \frac{\sigma_{n0} + k_n u_{s0} \tan\left(\delta_{\text{ave}}\right)}{\sigma_c}\right) \quad \chi = \frac{7k_a{}^3}{15DR_r \tan\theta_s} \log\left(\frac{u_{s-tot}}{a_0 k_a}\right) \end{aligned} \tag{2.25}$$

where σ_{n0} is the initial normal stress; σ_c is the uniaxial compression stress; k_n is the normal stiffness; α_0 is a correction factor, and δ_{ave} is the average dilation angle.

2.13. Concluding Remarks

From mechanical, hydraulic and hydromechanical tests results it is possible to conclude that rock joint behaviour heavily depends on their geometric properties, such as the level of stress applied on the joint. As far as geometrical properties are concerned, it is proved that the wall roughness has a strong influence on strength and dilatancy. Therefore, joint permeability is also affected by normal stress level, dilatancy and damage to the roughness of joint walls. The degradation of roughness affects both residual strength and permeability.

There are several mathematical models to predict the behaviour of joints. The development of numerical models depends on the progress made in testing and on the reliability of data. Moreover, Barton, 1973 considered the effect of moisture determining the model parameters for the rock joint in a wet or dry state.

Recently models of roughness degradation of the rock joint wall have been incorporated to mechanical models. This improvement was made possible thanks to advance techniques that measure the topography of the surface. In general, all hydro-mechanical models satisfactorily predict the main characteristic of rock joint behaviour, i.e. the increase of normal stiffness with joint closure; the softening of shear strength; the rate of change of dilatancy with shear displacements, and, regarding the evolution of the mechanical joint opening with its hydraulic aperture, the prediction of permeability changes.

CHAPTER 3

Coupled Thermo-Hydro-Mechanical Formulation of Joint Elements with double nodes

Implementation in Code_Bright

3.1. Introduction

This chapter presents a finite element formulation for the coupled thermo-hydro-mechanical behaviour of joint elements with double nodes. The formulation is based on works by Goodman et al. (1968) and Segura (2008). The coupling is achieved by the effective stress principle. Changes in stress cause changes in joint openings that affect longitudinal conductivity, as well as the storage capacity of the joint.

The mechanical behaviour of the joint is described using a constitutive law for pre-existing discontinuities. This law includes elastic and visco-plastic relative displacements. In particular, the elastic normal stiffness increases as the joint is closed. The visco-plastic formulation allows considering the variation of the displacement rate with time, and the softening of the shear stress due to degradation of the parameters of the hyperbolic yield surface defined.

The diffusion model considers advective and non-advective fluxes along joint elements. The transversal advective flux is calculated considering a pressure drop between the two sides of the joint (Segura, 2008). The longitudinal advective flux is calculated using Darcy's law with a longitudinal permeability dependant on joint opening. The non-advective flux (vapour diffusivity) is calculated by means of Fick's law.

There is also the possibility that the joint be, could become, unsaturated. A retention curve based on van Genutchen (1980)'s model, is defined for the joint. The air entry

pressure depends on joint opening (Olivella & Alonso, 2008; Alonso et al., 2006).

Heat conduction through the joint element is calculated by Fourier's law.

The finite element formulation, as well as the mechanical and hydraulic constitutive models described in this chapter, were implemented in Code_Bright (DIT-UPC, 2000; Olivella et al., 1995).

Finally, the validation of models and verification of the implementation is carried out simulating hydro-mechanical tests on rough granite joints reported by Lee & Cho (2002).

3.2. Mechanical problem

The mechanical behaviour of joint elements is defined by the relation between stress and relative displacements of the joint element mid-plane (Fig. 3.1). Then, the mid-plane relative displacements are interpolated using the nodal displacements and shape functions.

$$\mathbf{w}_{mp} = \begin{bmatrix} u_n \\ u_s \end{bmatrix}_{mp} = \mathbf{r}\, \mathbf{N}^{u}_{mp} \begin{bmatrix} -\mathbf{I}_4 & \mathbf{I}_4 \end{bmatrix} \mathbf{u}_j \qquad 3.1$$

where u_n and u_s are the normal and tangential relative displacements of the element's mid-plane (see Fig. 2.1b); $\mathbf{r}$ is the rotation matrix that transforms the relative displacements in the local orthogonal coordinate system into the global coordinate system; $\mathbf{N}_{mp}^{u}$ is a matrix of shape functions; $\mathbf{I}_4$ is an identity matrix of the 4th order, and $\mathbf{u}_j$ is the vector of nodal displacements.
The stress tensor of the mid-plane is calculated by:

$$\boldsymbol{\sigma}'_{mp} = \begin{bmatrix} \sigma' \\ \tau \end{bmatrix}_{mp} = \mathbf{D}\, \mathbf{w}_{mp} \qquad 3.2$$

where σ'_{mp} is the net effective stress at the element's mid-plane and it is defined as $\sigma'_{mp} = \sigma_{mp} - \max\{P_{gmp}; P_{lmp}\}$ (where σ_{mp} is the total mean stress; P_{gmp} is the gas pressure, and P_{lmp} is the liquid pressure in the element's mid-plane); τ is the tangential stress at mid-plane; **D** is the stiffness matrix, which relates relative displacements to the stress state (see Fig. 3.1a and b).

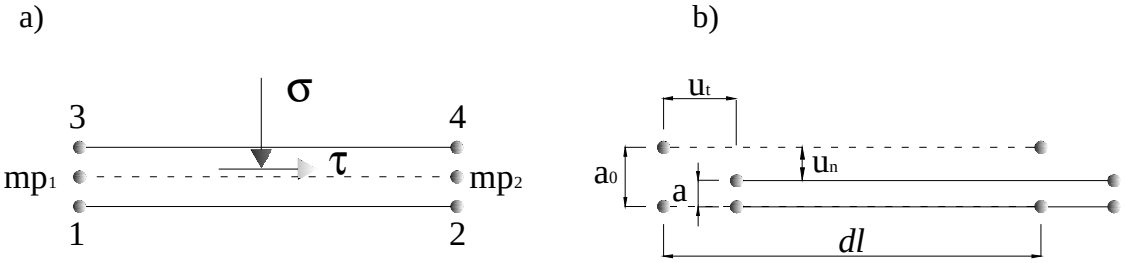

Figure 3.1: Joint element with double nodes. a) Stress state at the mid-plane of the joint element. b) Relative displacement defined at mid plane.

3.3. Mass and energy balance equation

In order to explain the numerical treatment of mass and energy balance equations, the water mass balance equation is used as an example. For the rest of mass balance and energy balance equations, the treatment is identical (DIT-UPC, 2000; Olivella et al., 1995).

3.3.1 Water mass balance equation

The water mass balance equation for a differential volume of joint is:

$$\frac{\partial\left(\theta_l^w S_l + \theta_g^w S_g\right)}{\partial t}\mathrm{a}\, dl + \left(\theta_l^w S_l + \theta_g^w S_g\right)\frac{d\mathrm{a}}{dt}\, dl + \left[\mathrm{j}'^{w}_{l}\right]_{mp} + \left[\mathrm{j}'^{w}_{g}\right]_{mp} = f^{w} \qquad 3.3$$

where the first term of Equation 3.3 considers the storage rate of mass at constant joint volume. The second term is the storage rate caused by changes of joint opening, the third is the liquid flux at mid plane, and the fourth is the vapour flux at mid plane. The fluxes at mid plane can be

calculated interpolating the leak-off at boundaries (see Fig. 3.2 and Eq. 3.4). The divergence term in the continuous balance equation was substituted by the incremental form.

$$\left[j_l^{'w} \right]_{mp} = \left[\theta_l^w q_{lt} dl + i_{lt}^w dl \right]_0^a + \left[\theta_l^w q_{ll} a + i_{ll}^w a \right]_0^{dl}$$

3.4

$$\left[j_g^{'w} \right]_{mp} = \left[\theta_g^w q_{gt} dl + i_{gt}^w dl \right]_0^a + \left[\theta_g^w q_{gl} a + i_{gl}^w a \right]_0^{dl}$$

In Equation 3.4 a is the opening of the joint; dl is the discrete length of the element, q_{lt} and q_{ll} are the advective and i_{lt} and i_{ll} are the non-advective transversal and longitudinal fluxes at the boundaries of the element; θ_l^w is the mass of liquid phase (water); θ_g^w is the mass of gas phase (vapour); S_l is the degree of saturation of liquid; S_g is the degree of saturation of gas, and f^w is an external supply of water.

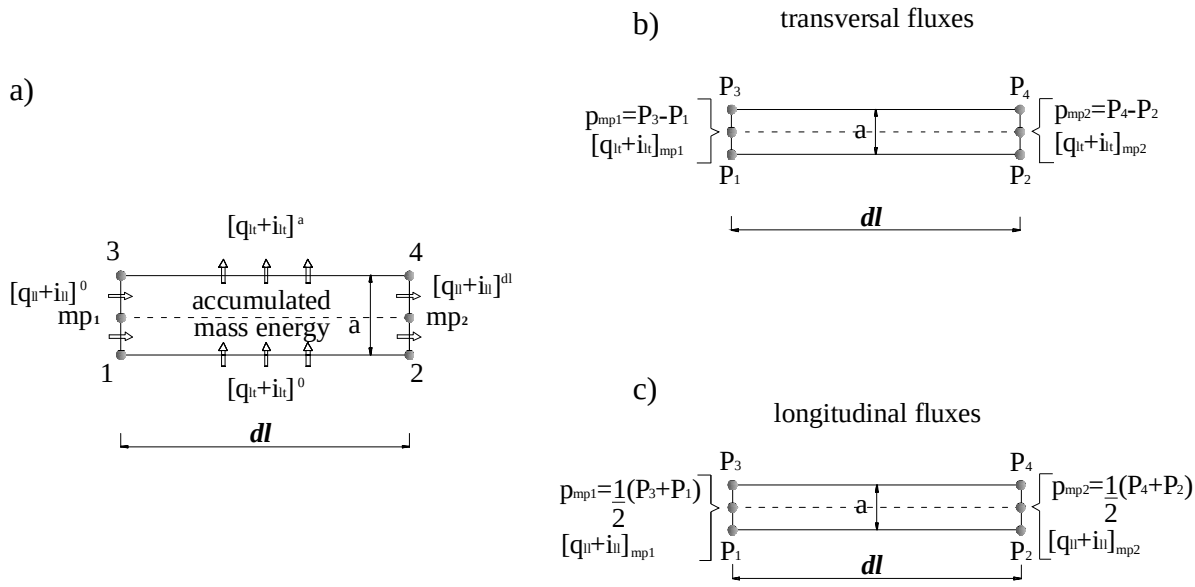

Figure 3.2: a) Schematic view of the mass balance of a joint element. b) Transversal fluxes at the joint's mid-plane are calculated considering a drop of pressure between joint boundaries. c) Longitudinal fluxes at mid-plane are calculated considering the average pressure of nodal pressures.

3.3.2. Air mass balance equation

The air mass balance equation considers the dry air and water vapour in the gas phase, whose expression is:

$$\frac{\partial\left(\theta_l^a S_l + \theta_g^a S_g\right)}{\partial t}\mathrm{a}\, dl + \left(\theta_l^a S_l + \theta_g^a S_g\right)\frac{d\mathrm{a}}{dt}\, dl + \left[\mathrm{j}'^{a}_{l}\right]_{mp} + \left[\mathrm{j}'^{a}_{g}\right]_{mp} = f^{a} \qquad 3.5$$

where θ_l^a is the mass of air dissolved in the liquid phase, θ_g^a is the mass of gas phase (dry air), j'^{a}_{l} is the air dissolved fluxes at mid plane, j'^{a}_{g} is the gas flux at mid plane, and f^a is an external supply of air.

3.3.3 Internal energy balance for the element

The internal energy balance for the element is expressed by:

$$\frac{\partial\left(E_l\rho_l S_l + E_g\rho_g S_g\right)}{\partial t}\mathrm{a}\, dl + \left(E_l\rho_l S_l + E_g\rho_g S_g\right)\frac{d\mathrm{a}}{dt}\, dl + \left[\mathrm{i}_c\right]_{mp} + \left[\mathrm{j}_{El}\right]_{mp} + \left[\mathrm{j}_{Eg}\right]_{mp} = f^{E} \qquad 3.6$$

where the energy of the liquid and gas phases is calculated by:

$$\begin{aligned} E_l\rho_l &= \left(E_l^w\omega_l^w + E_l^a\omega_l^a\right)\rho_l = E_l^w\theta_l^w + E_l^a\theta_l^a \\ E_g\rho_g &= \left(E_g^w\omega_g^w + E_g^a\omega_g^a\right)\rho_g = E_g^w\theta_g^w + E_g^a\theta_g^a \end{aligned} \qquad 3.7$$

where E_l^w and E_g^w are the internal energy of water in liquid and gas phase, respectively, per unit of mass of water; ω_l^w and ω_g^w are the mass fraction of water in liquid and gas phase respectively; E_l^a and E_g^a are the internal energy of air in liquid and gas phase per unit of mass of air; ω_l^a and ω_g^a are the mass fraction of air in liquid and gas phase, respectively.

The conduction of heat at the joint's mid-plane is calculated by:

$$\left[\mathrm{i}_c\right]_{mp} = \left[i_{ct} dl\right]_0^{\mathrm{a}} + \left[i_{cl}\,\mathrm{a}\right]_0^{\mathrm{dl}} \qquad 3.8$$

where $[i_c]_{mp}$ is the heat flux at the joint's mid-plane, i_{ct} is the transversal heat flux, and i_{cl} is the longitudinal heat flux at the element boundaries.

The energy fluxes are calculated considering the advective fluxes as:

$$\begin{aligned} \left[\mathrm{j}_{El}\right]_{mp} &= \left[\mathrm{j}'^{w}_{l}\right]_{mp} E_l^w + \left[\mathrm{j}'^{a}_{l}\right]_{mp} E_l^a \\ \left[\mathrm{j}_{Eg}\right]_{mp} &= \left[\mathrm{j}'^{w}_{g}\right]_{mp} E_g^w + \left[\mathrm{j}'^{a}_{g}\right]_{mp} E_g^a \end{aligned} \qquad 3.9$$

Equations 3.2, 3.3, 3.5 and 3.6 are solved simultaneously; this means that the unknown's vector for each node is u_n, u_s, P_l, P_g, T.

3.4. Constitutive Models

This section describes the mechanical, hydraulic and thermal constitutive laws adopted to simulate the behaviour of joints.

The mechanical law considers elastic and visco-plastic displacements.

The hydraulic law takes into account the advective and nonadvective fluxes. The intrinsic permeability of joints depends on their opening and JRC (Joint Roughness Coefficient). Furthermore, the air entry pressure in water retention curve also changes with joint opening.

The thermal law defines the heat conduction through the joint.

3.4.1 Mechanical model based on elasto-viscoplastic formulation

The elastic formulation proposed allows the treatment of elastic normal stiffness dependant on the joint opening Gens (1990).

The viscoplastic formulation based on Perzyna (1963), Zienkiewicz & Cormeau (1974), Lorefice et al. (2008) allows the treatment of non-associated plasticity and softening behaviour of joints

subjected to shear displacements. More over, using viscoplasticity enables considering the variation of the displacement with time.

Total displacements **w** are calculated by adding reversible elastic displacements, $\mathbf{w}^e$, to viscoplastic displacements $\mathbf{w}^{vp}$, which are zero when stresses are below a threshold value (the yield surface):

$$\mathbf{w} = \mathbf{w}^e + \mathbf{w}^{vp} \tag{3.10}$$

Displacements are represented by a two-element vector in the two-dimensional case which consists in:

$$\mathbf{w}^T = \left[u_n, u_s\right] \tag{3.11}$$

3.4.1.1 Elastic behaviour

The elastic behaviour of the joint relates the normal effective stress (σ') and the tangential stresses (τ) to the normal (u_n) and the tangential (u_s) displacement of the joint element using normal (K_n) and tangential stiffness (K_s), respectively. Normal stiffness depends on the opening of the joint, as shown in Equation 3.13 (see Fig. 3.3).

$$\begin{Bmatrix} \sigma' \\ \tau \end{Bmatrix} = \begin{bmatrix} K_n & 0 \\ 0 & K_s \end{bmatrix} \begin{Bmatrix} u_n \\ u_s \end{Bmatrix} \tag{3.12}$$

$$K_n = \frac{m}{\mathrm{a} - \mathrm{a}_{\min}} \tag{3.13}$$

where *m* is a parameter of the model; a is the opening of the element, and a_{min} is the minimum opening of the element (at this opening the element is closed).

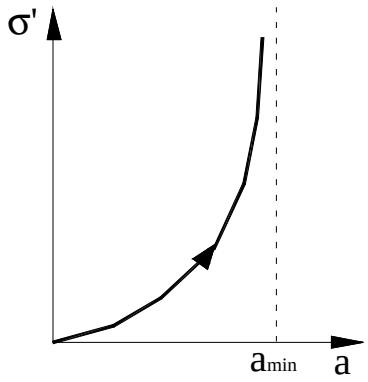

Figure 3.3: Elastic constitutive law of the joint element. Normal stiffness depends on joint opening.

3.4.1.2 Visco-plastic behaviour

The visco-plastic behaviour of joints was developed taking into account the formulations proposed by Gens et al. (1990) and Carol et al. (1997). According to these theories, it is necessary to define a yield surface, a plastic potential and a softening law to mathematically model the behaviour of a joint.

Visco-plastic displacements occurred when the stress state of the joint reached a failure condition. This condition depends on a previously defined yield surface. In this study a hyperbolic yield surface (Fig. 3.4) based on Gens et al. (1990) was adopted.

$$F \equiv \tau^2 - \left(c' - \sigma' \tan\phi'\right)^2 \qquad 3.14$$

where τ is the shear stress; c' is the effective cohesion; σ'is the net normal stress and tanΦ' is the tangent of internal friction effective angle.

Strength parameters c and tanΦ' are the value of interception between the asymptote of the failure surface with shear stress axis and the slope of the asymptote respectively. The variation of these parameters produces the corresponding family of yield surfaces.

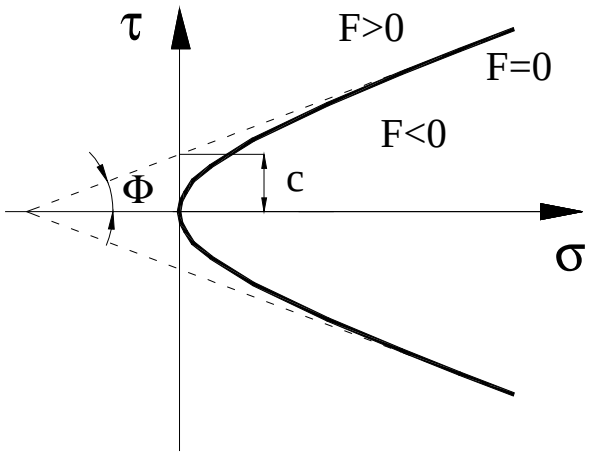

Figure 3.4: Hyperbolic failure surface and strength parameters.

3.4.1.3 Softening law

The strain-softening behaviour of the joint under shear straining is modelled considering the degradation of the strength parameters defined in Equations 3.15 and 3.16. The degradation of parameters c' and tanΦ' is considered to be linear and dependant on viscoplastic shear displacements. This is based on the slip weakening model introduced by Palmer & Rice (1973). In this way the cohesion drops from value c' to zero, while tangent of friction angle decays from peak (intact material) to residual values as a function of critical visco-plastic shear displacement (u^*). Two different u^* values can be used to define the decrease in cohesion ($u^*_{c'}$) and friction angle ($u^*_{\tan\Phi'}$) (see Fig. 3.5a, b and c). Therefore, the mathematical expressions will be:

$$c' = c'_0 \left(1 - \frac{u_s^{vp}}{u_c^*} \right) \qquad 3.15$$

where c' is the effective cohesion that corresponds to visco-plastic shear displacement u_s^{vp}; c'_0 is the initial value for effective cohesion; u^*_c is the critical value for shear displacement when c' equals zero.

$$\tan\phi' = \tan\phi'_0 - \left(\tan\phi'_0 - \tan\phi'_{res}\right)\frac{u_s^{vp}}{u_\phi^*} \qquad 3.16$$

where tanΦ' is the tangent of the internal friction effective angle, which corresponds to visco-plastic shear displacement u_s^{vp}; $\tan\Phi'_0$ is the tangent of the internal friction effective peak angle; $\tan\Phi'_{res}$ is the tangent of internal friction effective residual angle, and u^*_Φ is the critical value of shear displacement when tanΦ' equals $\tan\Phi'_{res}$.

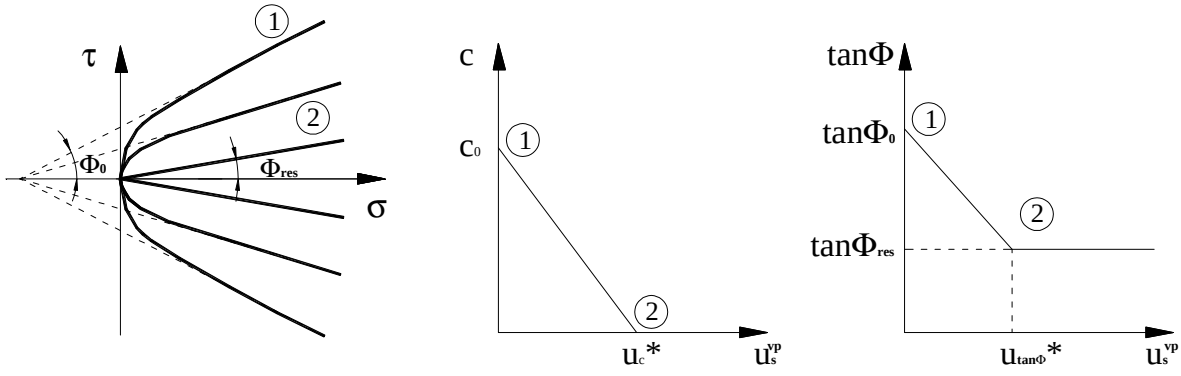

Figure 3.5: a) Evolution of the failure surface due to softening of the strength parameters. b) Softening law of cohesion. c) Softening law of tanΦ.

3.4.1.3 Visco-plastic displacements

If F < 0, the element is inside the elastic region. If F ≥ 0, the displacements of the element has a visco-plastic component. Viscoplastic displacements are calculated by:

$$\frac{d\dot{\mathbf{w}}^{vp}}{dt} = \Gamma < \phi\left(\frac{F}{F_0}\right) > \frac{\partial G}{\partial \boldsymbol{\sigma}} \qquad 3.17$$

where Γ is a fluidity parameter. In order to ensure that there is no viscoplastic flow inside the yield surface, the following consistency conditions should be met:

$$<\phi\left(\frac{F}{F_0}\right)>=0 \qquad if\ F<0$$

$$<\phi\left(\frac{F}{F_0}\right)>=\phi(F) \qquad if\ F\geq 0 \qquad 3.18$$

where F_0 can be any convenient value of F that renders the above expressions non-dimensional. In this study the value considered for F_0 is 1.
Consequently, the visco-plastic displacement rate is given by a power law for Φ:

$$\Delta u_n^{vp} = \Gamma F^N \frac{\partial G}{\partial \sigma}\Delta t$$

$$\Delta u_s^{vp} = \Gamma F^N \frac{\partial G}{\partial \tau}\Delta t \qquad 3.19$$

3.4.1.4 Plastic potential surface and dilatancy

Since the visco-plastic displacements are given by a vector normal to the plastic potential G surface, in order to calculate the direction of displacements, it is necessary to define the derivative of G with respect to stresses:

$$\frac{\partial G}{\partial \boldsymbol{\sigma}} = \left[2\tan\phi'\left(c'-\sigma'\tan\phi'\right) f_\sigma^{dil} f_c^{dil} \quad , \quad 2\tau\right]^T \qquad 3.20$$

Equation 3.20 provides a non-associated flow rule, because of the inclusion of both parameters f_σ^{dil} and f_c^{dil}, which consider the dilatant behaviour of the joint with shear stresses (Lopez., 1999). The amount of dilatancy depends on the level of the normal stress and on the degradation of the joint surface. The following expressions describe these effects:

$$f_{\sigma}^{dil} = \left(1 - \frac{|\sigma'|}{q_u}\right) \exp\left(-\beta_d \frac{|\sigma'|}{q_u}\right)$$

3.21

$$f_{c}^{dil} = \frac{c'}{c_0'}$$

where q_u is the compression strength of the material at which dilatancy vanishes; β_d is a model parameter; c' is the cohesion value that corresponds to visco-plastic shear displacement u_s^{vp}, and $c_{0'}$ is the initial value of cohesion.

Further to this, the tangent visco-plastic compliance matrix is calculated by:

$$C^{vp} = \begin{bmatrix} \frac{\partial \Delta u_n^{vp}}{\partial \sigma} & \frac{\partial \Delta u_n^{vp}}{\partial \tau} \\ \frac{\partial \Delta u_s^{vp}}{\partial \sigma} & \frac{\partial \Delta u_s^{vp}}{\partial \tau} \end{bmatrix}$$

$$\frac{\partial \Delta u_n^{vp}}{\partial \sigma} = \Gamma N F^{N-1} f_{\sigma}^{dil} f_{c}^{dil} \left[2 \tan\phi' \left(c' - \sigma' \tan\phi'\right)\right]^2 \Delta t + \\ + \Gamma F^{N} \left[-2 \tan^2 \phi' f_{\sigma}^{dil} f_{c}^{dil}\right] \Delta t$$

3.22

$$\frac{\partial \Delta u_n^{vp}}{\partial \tau} = \Gamma N F^{N-1} 2\tau f_{\sigma}^{dil} f_{c}^{dil} \left[2 \tan\phi' \left(c' - \sigma' \tan\phi'\right)\right] \Delta t$$

$$\frac{\partial \Delta u_s^{vp}}{\partial \sigma} = \Gamma N F^{N-1} 2\tau \left[2 \tan\phi' \left(c' - \sigma' \tan\phi'\right)\right] \Delta t$$

$$\frac{\partial \Delta u_s^{vp}}{\partial \tau} = \Gamma N F^{N-1} 2\tau \Delta t + \Gamma F^{N} 2 \Delta t$$

Finally, the elasto-viscoplastic mechanical model of the joint is expressed by the tangent stiffness matrix:

$$\mathbf{D}^{evp} = \left[\mathbf{C}^{e} + \mathbf{C}^{vp} \right]^{-1} \qquad 3.23$$

This matrix is represented by **D** in Equations 3.2.

3.4.2. Hydraulic model

The horizontal advective flux flow through the joint is calculated considering a tangential intrinsic permeability and the pressure drop between joint surfaces. Furthermore, the longitudinal advective flow is calculated using a longitudinal intrinsic permeability and the generalization of Darcy's law. Therefore, it is necessary to define the longitudinal and transversal intrinsic permeabilities of the joint. Likewise, in the case of joints under unsaturated conditions, the water retention curve should be calculated.

3.4.2.1. Advective fluxes

The equation for liquid fluxes is developed below. It is applied to gas and energy fluxes.
The transversal flux is calculated considering a transversal permeability and a transversal fluid pressure drop $\breve{p}_{mp}$ between the joint element boundaries (Segura, 2008).

$$q_{lt} = \frac{k_{lt} k_{rlt}}{\mu_l} \breve{p}_{mp} \qquad 3.24$$

where k_{lt} is the transversal intrinsic permeability for the liquid; k_{rlt} is the transversal relative permeability for the liquid, and μ_l is the dynamic viscosity of the liquid.

A generalized Darcy's law is used to calculate the longitudinal flux

$$q_{ll} = -\frac{k_{ll} k_{rll}}{\mu_l}\left(\frac{\partial p_{mp}}{\partial l} - \rho \mathbf{g}\right) \qquad 3.25$$

where k_{ll} is the longitudinal intrinsic permeability for liquid, k_{rll} is the longitudinal relative permeability for the liquid, μ_l is the dynamic viscosity of the liquid and **g** is the gravity vector.

3.4.2.2 Nonadvective fluxes

The Nonadvective flux (vapour diffusivity) is calculated by Fick's law:

$$\mathbf{i}_g^w = -\tau \rho_g S_g D_g^w \mathbf{I} \nabla \omega_g^w \qquad 3.26$$

where τ is the tortuosity; D_g^w is the molecular diffusion coefficient, which depends of temperature and gas pressure; **I** is the identity matrix, and ω_g^w is the mass fraction of vapour in the gas phase.

3.4.2.3 Intrinsic Permeability

The longitudinal fluid flow through joints has always been analyzed as a laminar flow between two smooth and parallel plates separated by a specific hydraulic opening (*e*). Based on this hypothesis, the hydraulic conductivity of the joint is calculated by the following cubic law:

$$K_l = \frac{\rho g}{\mu}\frac{e^3}{12} \qquad 3.27$$

where ρ is the fluid density; g is the gravity, and μ is the fluid viscosity.

Therefore the equation of intrinsic permeability is:

$$k_l = \frac{e^2}{12} \tag{3.28}$$

The joint hydraulic opening (e) depends on its geometrical aperture (E) for different values of joint roughness, as stated in Barton (1985)'s law (Fig. 2.5-Ch. 2). The figure shows that this relationship is highly non-linear due to roughness. Should Barton's expression of longitudinal intrinsic permeability be substituted in Eq. 3.36, then:

$$k_l = \left[\frac{\mathrm{a}^2}{JRC^{2.5}} \right]^2 \frac{1}{12} \tag{3.29}$$

Transversal intrinsic permeability k_t is considered to be equal to the continuum media.

3.4.2.4. Water retention curve

The degree of saturation of joints is calculated using the standard retention curve of van Genuchten (van Genuchten, 1980):

$$S_l = \left[1 + \left(\frac{\Psi}{P} \right)^{\frac{1}{1-\lambda}} \right]^{-\lambda} \tag{3.30}$$

where S_l is the liquid degree of saturation; $\Psi = P_g - P_l$ is the current suction; λ is a model parameter, and P is the air entry pressure necessary to desaturate joints.

The variation in the joint opening also causes changes in air entry pressure (Olivella & Alonso, 2008). The air entry pressure necessary to desaturate the joint depends on its hydraulic opening, that is:

$$P_0 = \sigma\left(\frac{1}{r_1}+\frac{1}{r_2}\right)=\frac{2\sigma}{e} \qquad 3.31$$

which is obtained when $(1/r_1) = 0$ and $r_2 = e/2$. In this case the wetting angle was assumed to equal zero. If Equation 3.31 is combined by means Equation 3.28, the capillary pressure necessary to start desaturation is obtained as:

$$P = P_0 \frac{\sqrt{k_{l0}}}{\sqrt{k_l}} \qquad 3.32$$

P can be scaled with the surface tension calculated at different temperatures:

$$P = P_0 \frac{\sqrt{k_{l0}}}{\sqrt{k_l}} \frac{\sigma}{\sigma_0} \qquad 3.33$$

3.4.2.5 Relative permeability

Relative permeability is calculated by:

$$k_{rl} = AS_l^{\,n} \qquad 3.34$$

where A = 1.0 and n = 3.

3.4.3 Thermal model

The heat conduction is given by Fourier's law:

$$i_c = -\lambda \nabla T \qquad 3.35$$

where λ is the thermal conductivity and ∇T is the change in temperature.

3.5. Discretization of the equations

The finite element method is used for spatial discretization while finite differences are used for time discretization.

The weighted residual method is applied to obtain the discrete form of stress equilibrium and mass and energy balance equations.

3.5.1. Stress equilibrium equation

Note that the discrete form of stress equilibrium (forces) can be directly established for the joint element. Therefore, the integration to average residuals gives:

$$\begin{bmatrix}-\mathbf{I}_4\\ \mathbf{I}_4\end{bmatrix}\int_{lmp}\mathbf{N}^u_{mp}\,\mathbf{r}^T\,\mathbf{D}\,\mathbf{r}\,\mathbf{N}^u_{mp}\begin{bmatrix}-\mathbf{I}_4 & \mathbf{I}_4\end{bmatrix}\mathbf{u}_j dl+\begin{bmatrix}-\mathbf{I}_4\\ \mathbf{I}_4\end{bmatrix}\int_{lmp}\mathbf{N}^u_{mp}\,\mathbf{r}^T\,\mathbf{m}\,\mathbf{N}^p_{mp}\,\frac{1}{2}\begin{bmatrix}\mathbf{I}_2 & \mathbf{I}_2\end{bmatrix}P_j dl-\mathbf{b}=0 \qquad 3.36$$

where **b** is the vector of the external forces.

3.5.2 Mass and energy balance equation

In order to explain the numerical treatment of mass and energy balance equations, the water mass balance equation is used as an example:

- Storage changes of mass or energy at constant joint opening:

$$\frac{1}{2}\begin{bmatrix}\mathbf{I}_2\\ \mathbf{I}_2\end{bmatrix}\left[\int_{lmp}\mathbf{N}^p_{mp}\,\frac{\partial\left(\theta_l^w S_l+\theta_g^w S_g^w\right)}{\partial t}\,\mathrm{a}\,dl\right]=\frac{1}{2}\begin{bmatrix}\mathbf{I}_2\\ \mathbf{I}_2\end{bmatrix}\left[\int_{lmp}\mathbf{N}^p_{mp}\mathrm{a}\,\frac{\Delta\left(\theta_l^w S_l+\theta_g^w S_g^w\right)}{\Delta t}dl\right]=\begin{bmatrix}\mathbf{I}_4\end{bmatrix}\frac{\Delta\left(\theta_l^w S_l+\theta_g^w S_g^w\right)}{\Delta t}\frac{\mathrm{a}l}{4} \qquad 3.37$$

– Storage change cause by changes in the joint opening:

$$\frac{1}{2}\begin{bmatrix}\mathbf{I}_2\\ \mathbf{I}_2\end{bmatrix}\left[\int_{lmp}\mathbf{N}_{mp}^{p\ T}\left(\theta_l^w S_l+\theta_g^w S_g\right)\mathbf{m}^T\mathbf{r}\mathbf{N}_{mp}^{u}\left[-\mathbf{I}_4 \quad \mathbf{I}_4\right]\frac{du}{dt}dl\right]= \\ \frac{1}{2}\begin{bmatrix}\mathbf{I}_2\\ \mathbf{I}_2\end{bmatrix}\left[\int_{lmp}\mathbf{N}_{mp}^{p\ T}\left(\theta_l^w S_l+\theta_g^w S_g\right)\mathbf{m}^T\mathbf{r}\mathbf{N}_{mp}^{u}dl\right]\left[-\mathbf{I}_4 \quad \mathbf{I}_4\right]\frac{\Delta u}{\Delta t} \tag{3.38}$$

– Advective flux due to phase motion:

In the case of transversal fluxes, nodal liquid pressures $\mathbf{P}l_j$ are interpolated to the joint's mid-plane with regards to the pressure drop:

$$\breve{p}_{mp}=N_{mp}^{p}\left[\mathbf{I}_2 \quad -\mathbf{I}_2\right]\mathbf{P}l_j \tag{3.39}$$

The discretized expression for the transversal advective flux (for instance, in case the liquid flux is replaced by Eq. 3.24) is:

$$\begin{bmatrix}\mathbf{I}_2\\ -\mathbf{I}_2\end{bmatrix}\left[\int_{lmp}\mathbf{N}_{mp}^{p\ T}\theta_l^w q_{lt}\,dl\right]=\begin{bmatrix}\mathbf{I}_2\\ -\mathbf{I}_2\end{bmatrix}\left[\int_{lmp}\mathbf{N}_{mp}^{p\ T}k_{lt}\left(\frac{k_{rlt}\theta_l^w}{\mu_l}\right)\mathbf{N}_{mp}^{p}\,dl\right]\left[\mathbf{I}_2 \quad -\mathbf{I}_2\right]\mathbf{P}l_j \tag{3.40}$$

In the case of longitudinal fluxes, the liquid pressure at mid-plane is calculated considering the average liquid pressure of the nodal liquid pressure:

$$p_{mp}=N_{mp}^{p}\frac{1}{2}\left[\mathbf{I}_2 \quad \mathbf{I}_2\right]\mathbf{P}l_j \tag{3.41}$$

The discretized expression for the longitudinal advective fluxes (in this case the flux is calculated by Eq. 3.25) is:

$$\frac{1}{2}\begin{bmatrix}\mathbf{I}_2\\ \mathbf{I}_2\end{bmatrix}\left[\int_{lmp}\frac{\partial \mathbf{N}_{mp}^{p\ T}}{\partial_l}\frac{k_{ll}k_{rll}}{\mu_l}\left(\frac{\partial p_{mp}^{p}}{\partial_l}-\rho_l\mathbf{g}\right)dl\right]=$$

$$\frac{1}{2}\begin{bmatrix}\mathbf{I}_2\\ \mathbf{I}_2\end{bmatrix}\left[\int_{lmp}\frac{\partial \mathbf{N}_{mp}^{p\ T}}{\partial_l}k_{ll}\left(\frac{k_{rll}\theta_l^w}{\mu_l}\right)\frac{\partial \mathbf{N}_{mp}^{p}}{\partial_l}dl\right]\frac{1}{2}\begin{bmatrix}\mathbf{I}_2 & \mathbf{I}_2\end{bmatrix}\mathbf{P}l_j+\frac{1}{2}\begin{bmatrix}\mathbf{I}_2\\ \mathbf{I}_2\end{bmatrix}\left[\int_{lmp}\frac{\partial \mathbf{N}_{mp}^{p\ T}}{\partial_l}k_{ll}\left(\frac{k_{rll}\theta_l^w\rho_l}{\mu_l}\right)\mathbf{g}\,dl\right] \qquad 3.42$$

The discretized equations for non-advective fluxes and heat conduction are analogous to advective fluxes, although diffusion and transversal heat conduction are greater than in the case of them being longitudinal.

3.6. Model validation. Comparison with a hydraulic shear tests on rough fractures (Lee & Cho, 2002)

The hydraulic shear tests were performed using granitic rock from Korea, whose mechanical properties are summarised in Table 3.1 (Lee & Cho, 2002). The intact rock block was sawed to obtain samples with a length of 160 mm and a width and height of 120 mm (Fig. 3.6). The fracture surfaces were created by a tensile fracture exerted by a splitter. The fracture opening was measured using a 3-D laser profilometer. The mean value of the opening was 0.65 mm.

Table 3.1: Physical and mechanical properties of intact rock.

Property [Hwangdeung granite]	**Value**
Specific gravity	2.72
Apparent porosity [%]	0.49
Uniaxial compressive strength [MPa]	151
Young's modulus [GPa]	54.1
Poisson's ratio	0.29
Brazilian tensile strength [MPa]	14

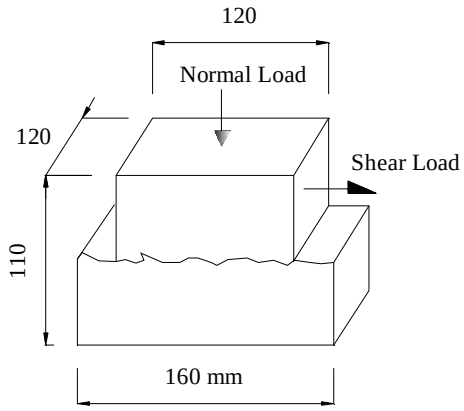

Figure 3.6: Dimension of joint specimens of Hwangdeung granite (Lee et al., 2001).

Shear hydraulic tests were performed maintaining constant normal stresses of 1, 2 and 3 MPa. The tangential displacement was applied at a rate of 5 mm/seg. The hydraulic pressure applied to the joint varied from 4.91 kPa to 19.64 kPa. For each stage of shear displacement of about 1 mm, hydraulic pressure was kept constant. When the fluid flow reached a steady state, the mean flow rate was calculated by measuring the amount of outflow during a period of 2 minutes. These measurements were also used to calculate the permeability of the joint.

The mechanical shear behaviour of the rock joint is shown in Figure 3.7a and b. The results obtained are characterized by a peak shear strength and a pronounced dilation, that greatly affected the hydraulic behaviour of rough fractures. Dilatancy increases rapidly before shear stress reaches its peak value. Dilatancy increases at low rate during the shear stress drop to reach residual values.

The permeability changes, with respect to the increments of shear displacements, are plotted in Figure 3.7c. Note that the fracture permeability changes slightly during the initial stage of shear loading. But, as dilation occurs close to peak strength, permeability increases dramatically, about two orders of magnitude. Thus, when shear displacements are about 7 mm, permeability reaches a constant value.

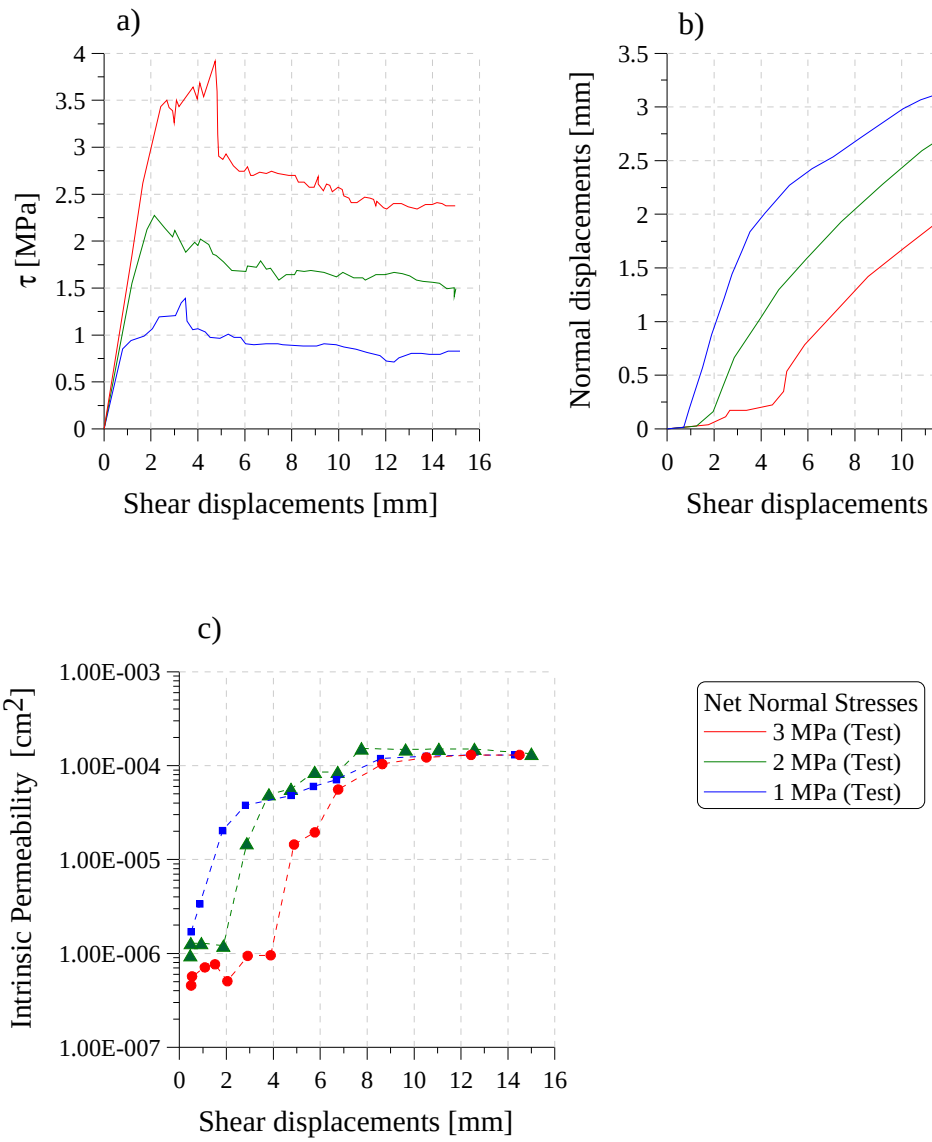

Figure 3.7: Test results from Lee & Cho (2002). a) Shear stress-shear displacement curve. b) Normal displacements vs. shear displacements. c) Intrinsic permeability vs. shear displacements.

3.6.1. Mathematical model

The tests described above were modelled using the coupled hydro-mechanical formulation and its implementation by means of a visco-plastic constitutive law in CODE_BRIGHT. The model is 120 mm high and 110 mm wide (Fig. 3.8). The continuum was discretized using 200 quadrilateral 4-node elements and the joint was discretized with 10 joint elements. The normal stress is applied at AB boundary, while shear rate displacements are applied at AC and BD

boundaries. Boundaries EG and FH are horizontally fixed and GH is vertically fixed. The water injection (P_l) on the joint was applied at CE boundary, while at DF a drainage boundary condition was considered (Fig. 3.8). The pressure at CE increased when shear displacement reached 1 mm. The joint is considered to be saturated ($S_l = 1$) during testing.

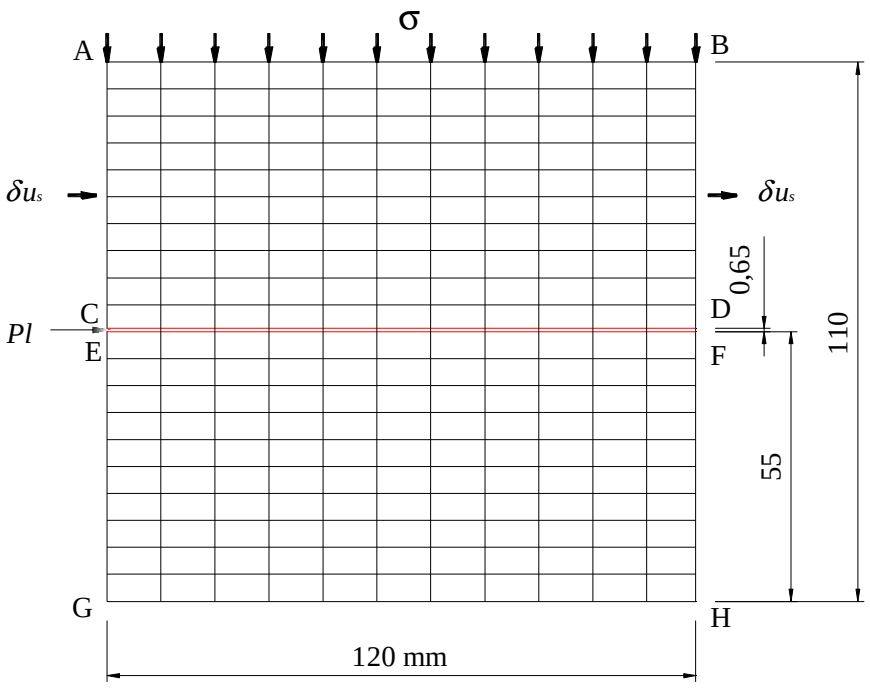

Figure 3.8: Discretized geometry and boundary conditions used for the hydro-mechanical simulation of the test performed by Lee & Cho (2002).

The mechanical and hydraulic parameters of the granite and joint are summarised in Table 3.2. The parameters of the joint were obtained by back-analysing the tests results.

Table 3.2: Hydro-mechanical parameters of the granite matrix and joint used in the numerical model.

Rock Matrix

Mechanical Properties	**Value**	**Unit**
Young's modulus [E]	54100	MPa
Poisson's ratio [υ]	0.29	
Porosity[n]	49.0	%
Hydraulic Properties	**Value**	**Unit**
Intrinsic permeability [k]	$1x10^{-16}$	m^2

Joint Rock

Mechanical Properties	**Value**	**Unit**
Initial normal stiffness parameter [m]	90	MPa
Tangential stiffness [K_s]	1500	MPa/m
Initial cohesion [c_0]	0.02	MPa
Initial friction angle [Φ_0]	47º	
Residual friction angle [Φ_{res}]	37º	
Initial opening [a_0]	0.65	mm
Minimum opening [a_{min}]	0.065	mm
Viscosity [Γ]	$1x10^{-4}$	s^{-1}
Stress power [N]	2.0	
Critical displacements of cohesion [u_c*]	15.0	mm
Critical displacements of tanΦ [$u_{tan\Phi}$*]	15.0	mm
Uniaxial compressive strength [q_u]	151	MPa
Model parameter [β_d]	40	
Joint Roughness Coefficient [JRC]	2.70	
Hydraulic Properties	**Value**	**Unit**
Hydraulic opening [*e*]	0.035	mm
Longitudinal intrinsic permeability [k_l]	$1x10^{-8}$	m^2
Transversal intrinsic permeability [k_t]	$1x10^{-16}$	m^2

3.6.2. Comparison between tests and numerical results

The results obtained from the simulation are compared to the tests results in Figure 3.9a, b and c. The mechanical behaviour of the joint is closely reproduced by the model. The numerical formulation is able to reproduce the increment of peak shear stress with normal stresses. Also, it is possible to capture how the shear strength decreases with displacements. Moreover, the figure also depicts the dilatancy of the joint (Fig. 3.9b).

The evolution of the intrinsic permeability of the joints is also simulated. Even though, permeabilities of the model increase continuously, the permeability of the tests for different normal stresses became almost the same. This is mainly caused by the gouge materials generated from the degradation of asperities during shearing. This effect is not considered in the model (Fig. 3.9c).

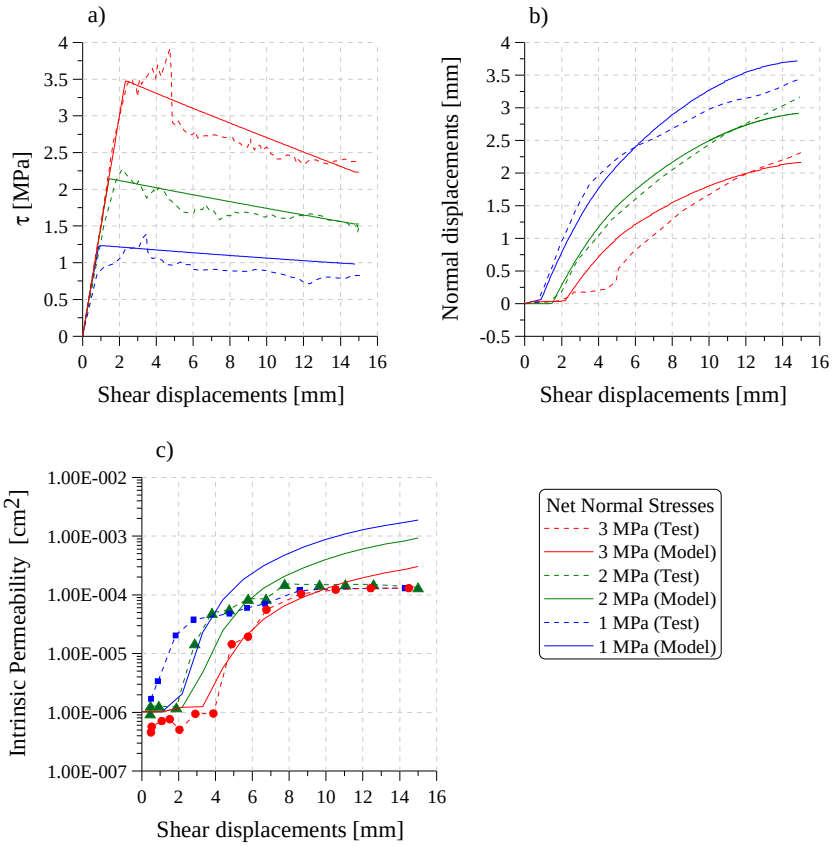

Figure 3.9: Comparison between experimental results obtained by Lee & Cho (2002), and results from the numerical simulation. a) Shear stress-shear displacements curve. b) Normal displacements vs. shear displacements and c) Intrinsic permeability vs. shear displacements.

3.7. Concluding remarks

A coupled hydro-mechanical formulation using a newly developed joint element was described. It is based on a number of previous developments on rock joints behavior.

A mechanical constitutive law proposed by Gens et al. (1990) was the starting point to model the elastic and plastic deformation of the joint. In the elastic law normal stiffness depends on the evolution of the joint element. Plastic behavior is defined by a hyperbolic failure surface and softening is based on a slip weakening model (Palmer and Rice, 1973). The equations developed were transformed into a viscoplastic formulation.

Darcy's law was adopted as the longitudinal hydraulic constitutive law. However, the transversal flux is calculated considering a pressure drop between joint surfaces (Segura, 2008). A retention curve with a capillary pressure dependant on joint aperture (Olivella & Alonso, 2008) is adopted to calculate the degree of saturation of the joint.

The finite element formulation and constitutive law were implemented in Code_Brigth.

Numerical simulation of hydro-mechanical tests on granite joints carried out by Lee & Cho (2002) was performed to validate the numerical tool. From the comparison between test and numerical results can be concluded that the formulation is capable to reproduce the main characteristics of coupled joint behavior. For instance, shear stress softening and dilatancy development with shear displacements are as well captured by the model as well as the increments of permeability with displacement.

CHAPTER 4

Direct Shear Testing with Suction Control on Rock Joints with different asperity roughness angle

4.1. Introduction

The main objective of the laboratory testing programme consisted in determining the effects of suction and roughness on the mechanical properties of rock joints.

Tests were carried out using a Direct Shear Cell with Suction Control. The equipment was originally developed by researchers of the Department of Geotechnical Engineering and Geosciences of the Technical University of Catalonia. Nevertheless, further refinements of the equipment were done to carry out tests with suction control. A vapour circuit was connected to the shear cell, and the data acquisition system was improved incorporating an analogue data acquisition device that allows automatically recording shear forces, vertical displacements, temperature and relative humidity.

The relative humidity of rock joints was changed using the vapour equilibrium technique. This technique consists in applying a water potential to the rock by migrating the water molecules in vapour phase from a reference system of known potential towards the rock pores until equilibrium is reached. The thermodynamic relationship between the total suction of the rock and the relative humidity of the reference is given by Kelvin's law (Fredlund & Rahardjo, 1993).

Artificial joints of Lilla claystones were prepared. Joint roughness of varying intensity was obtained by carving the surfaces in contact in such a manner that rock ridges of different tip angles were formed. These angles varied from 0º (smooth joint) to 45º (very rough joint profile). The geometric profiles of the two surfaces in contact were initially positioned in a "matching" situation. Several tests were performed for different values of suction (200, 100 and 20 MPa) and vertical stress (30, 60 and 150 kPa).

The following sections contain a description of the modifications done on the shear test cell; a summary of the mechanical properties and geology of Lilla claystones, and a description of the sample preparation and procedures followed during the test. Furthermore they present the result of the tests, their analysis and the model improvements proposed. Finally, a comparison of the tests and model results is presented and discussed.

4.2. Direct Shear Cell Apparatus with Suction Control by a Vapour Transfer Technique

The equipment is constituted by the shear cell, the forced convection vapour circuit and the data acquisition system. An overall view of the device is given in Figure 4.2a.

4.2.1. Direct Shear Cell

The shear cell is formed of the following main parts: A mobile base with a ceramic disc; an electrical motor that moves the push rod at different displacement rates; an air chamber that encloses a shear box with vertical load centering bushing, and the air pressure chamber containing a piston that applies the vertical load. A schematic draw of the cell is shown in Figure 4.2b.

The mobile base moves horizontally by means of a push rod. An electrical motor controls the displacement rate of the rod. The motor allows using three different displacement rates: slow, manual and fast. The slow displacement rate ranges from 0.005 to 0.100 mm/min, the manual displacement rate allows displacing the wheel 0.2 mm in every turn, and the fast displacement rate ranges from 0.100 to 2000 mm/min. The base slides through two metallic guides having bearings to reduced friction. The base has also a ceramic porous disc whereby the bottom of the sample is in contact with the air within the chamber (Fig. 4.2c).

The air chamber is a steel cylinder with an inner diameter of 220 mm and a thickness of 26.5 mm. At its base there is a piston, which is in contact with the shear box and load cell, and which transmits the shear load supported by the sample to the load cell. In order to change the relative

humidity of the sample placed inside the shear box, the air chamber is connected to the vapour circulation system by two pipe connections. The temperature and relative humidity of the air within the chamber is recorded by a humidity and temperature transmitter hosted in a small hermetic chamber added to the air chamber (Fig.4.2 d.)

The shear box consists of two pieces. The lower piece has a height of 10 mm and an inner hollow of 50 mm in diameter where the sample is placed. This piece is fixed to the mobile base holding the ceramic disk by means of four screws. The upper piece with a height of 21 mm slides over the lower fixed part. This part covers the entire sample and it hosts a metallic porous disc and the loading cap. The metallic porous disc has a diameter of 50 mm and is 10 mm high. The loading bushing has a special design that allows it to swing freely and to center the piston that applies the vertical load. This is possible because the piston end fits into the shaft of the loading bushing (Fig.4.2e.) (Escario & Saez, 1986)

The air pressure chamber consists of an upper lid with a valve connected to the air pressure. A lower piece holds the Bellofram seal and allows the passage of the load piston. Then the vertical load is applied by the diaphragm pressure acting on the piston. Maximum pressure is limited to 1 MPa. The air pressure is controlled by a throttle and measured by a manometer. The vertical displacements of the sample are measured with a LVDT placed on the horizontal extension of the piston (Fig.4.2f.). (Escario & Saez, 1986)

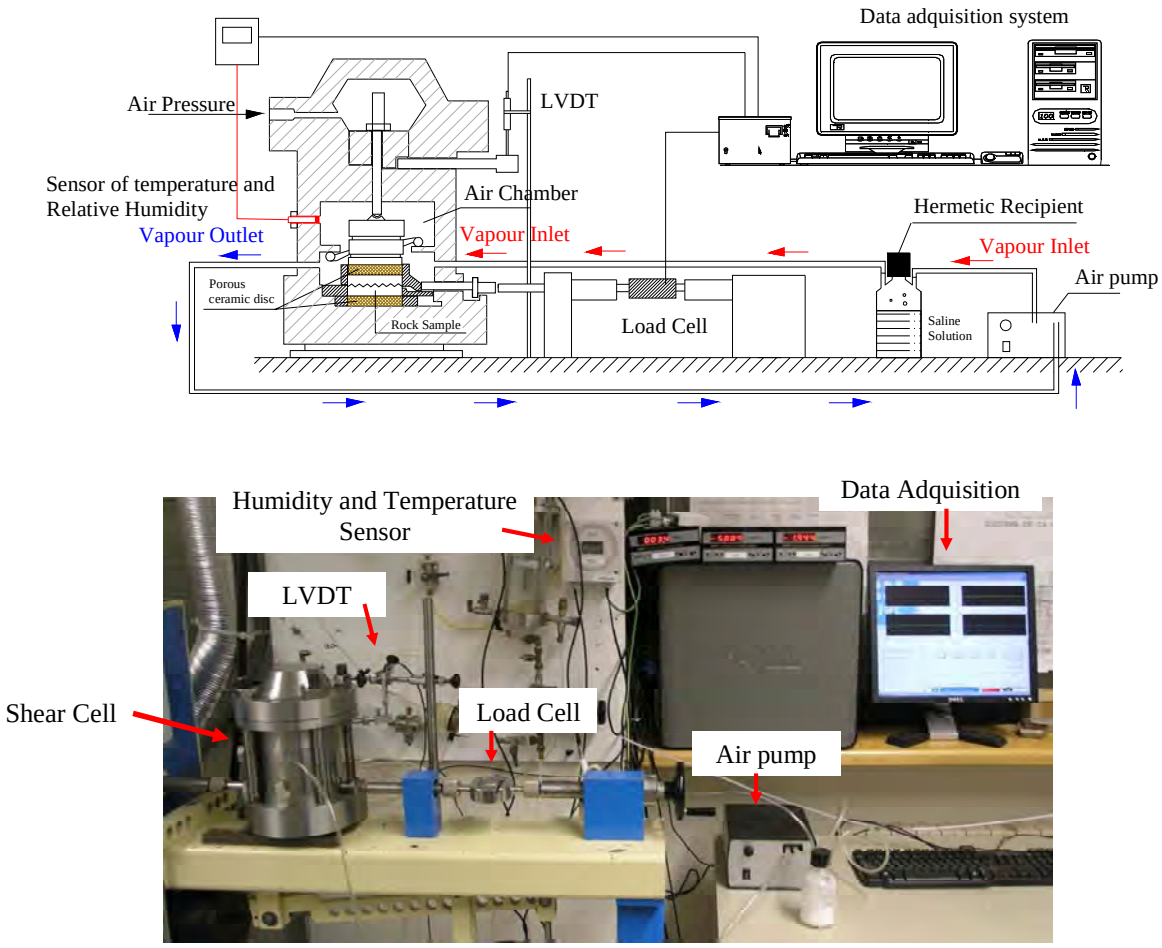

Figure 4.2a: Overall view of the direct shear tests device.

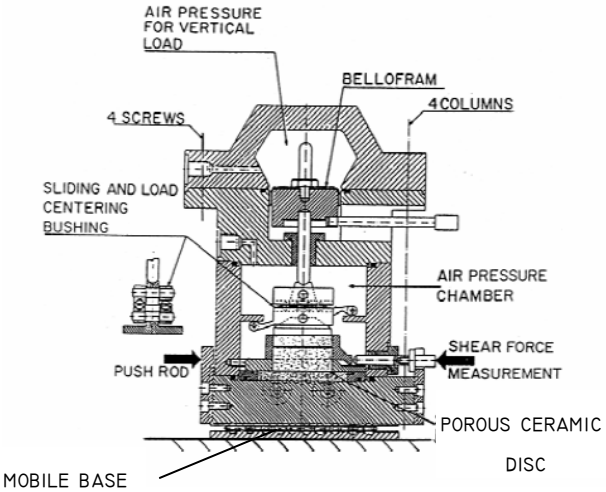

Figure 4.2b: Schematic view of the main parts of the shear cell.

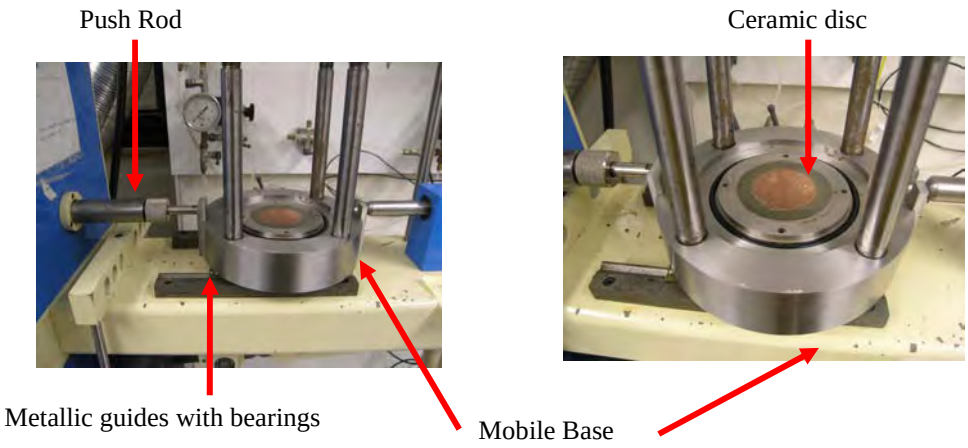

Figure 4.2c: Description of the mobile base of the shear cell.

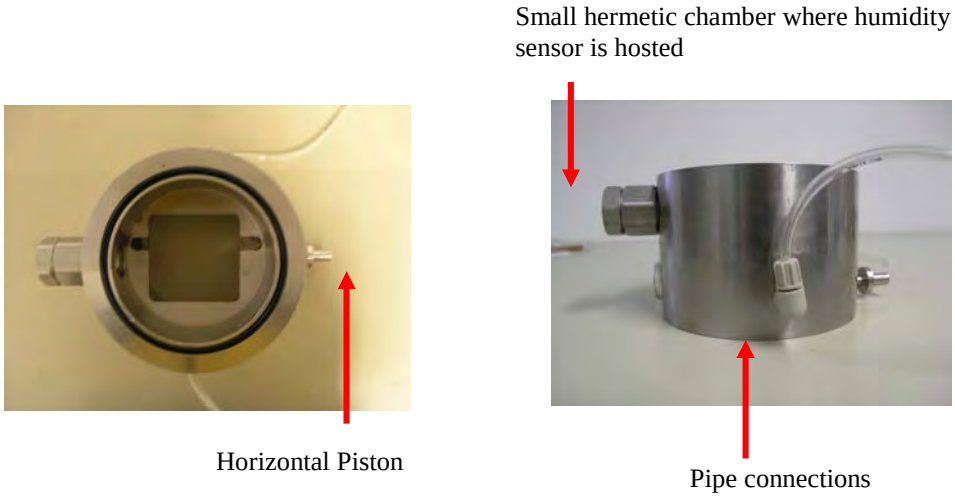

Figure 4.2d: Description of the air chamber in which the shear box is enclosed.

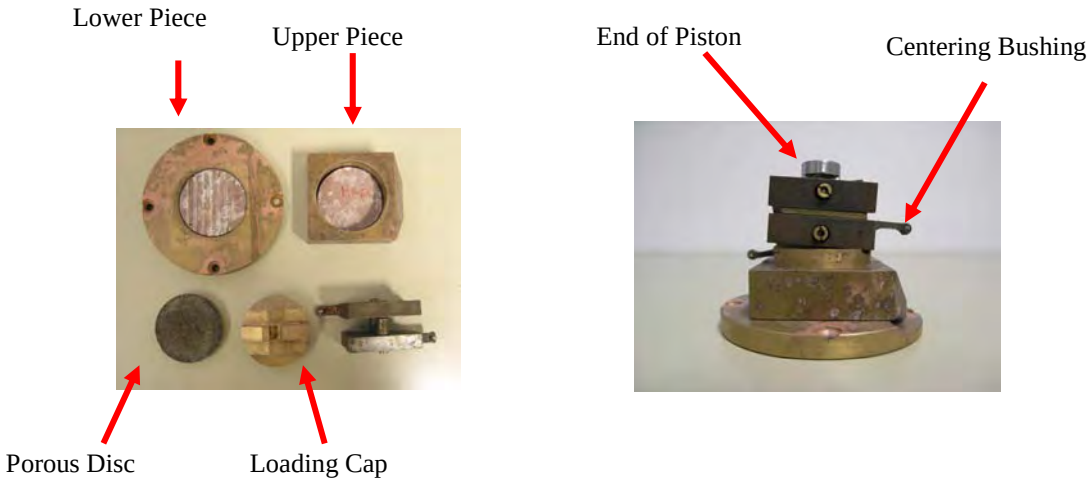

Figure 4.2e: Description of the shear box and the load centering bushing.

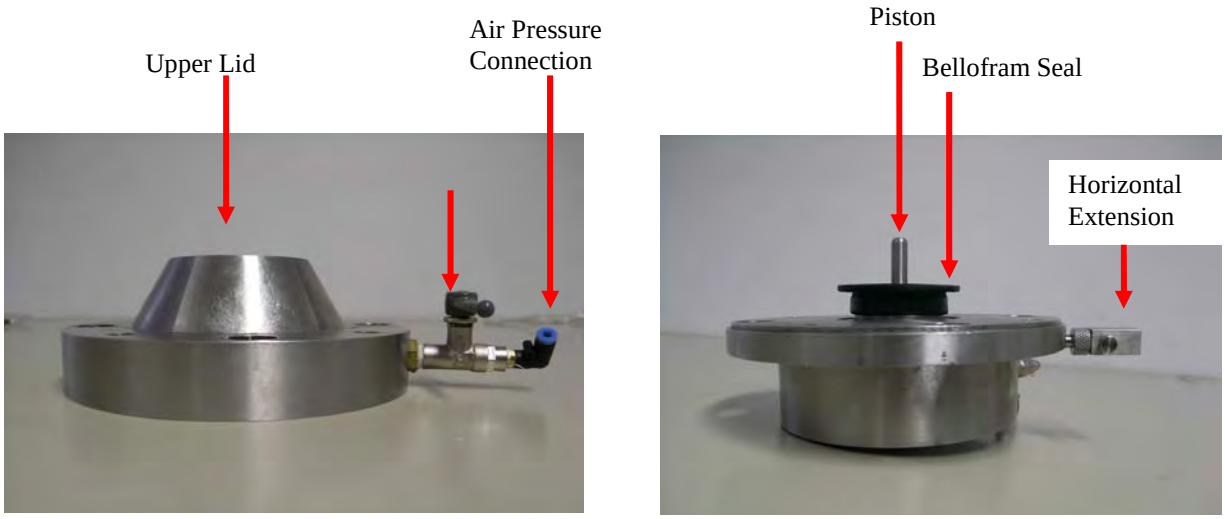

Figure 4.2f: Air pressure chamber view. Upper lid (left) and lower piece (right).

4.2.2. Vapour forced convection circuit system

The system consists of an air pump that impulses the vapour produced by a saline solution contained in a hermetic recipient. The system is closed and continuously impulses the vapour contained in the recipient towards the air chamber and then extracts the air from the chamber. This allows keeping constant the relative humidity of the air chamber and that of the sample during the test (Fig. 4.3).

Figure 4.3: Description of vapour forced convection circuit system.

4.2.3. Data measurement

Shear loads are measured by a load cell. The load cell has a nominal capacity of 500 kg. Both extremes of the load cell are attached to a steel stem. The left stem is in contact with the horizontal piston of the air chamber. The right stem is mobilized by a wheel. This allows positioning the left stem in contact with the horizontal piston. After that, the right stem is set using a security key (Fig. 4.4a).

Vertical displacements are measured by means of a Linear Variable Differential Transformer (LVDT) Displacement Transducer with a range of measure of ± 5 mm. The LVDT is fixed to a steal stem using a lug, and located over the horizontal extension of the vertical load piston (Fig. 4.4b).

A humidity and temperature transmitter is used to measure the relative humidity and temperature of the air at the chamber during the tests. This equipment is able to measure relative humidities from 0% to 100% and temperatures from 0º to 60ºC (Fig. 4.4c)
The measurement of the data was done automatically on a PC under Windows SO and through a multifunctional analog to digital, digital to analog and digital input/output board that uses a USB6009 data acquisition device. A digital program was designed with LabVIEW programming language to build data acquisition.

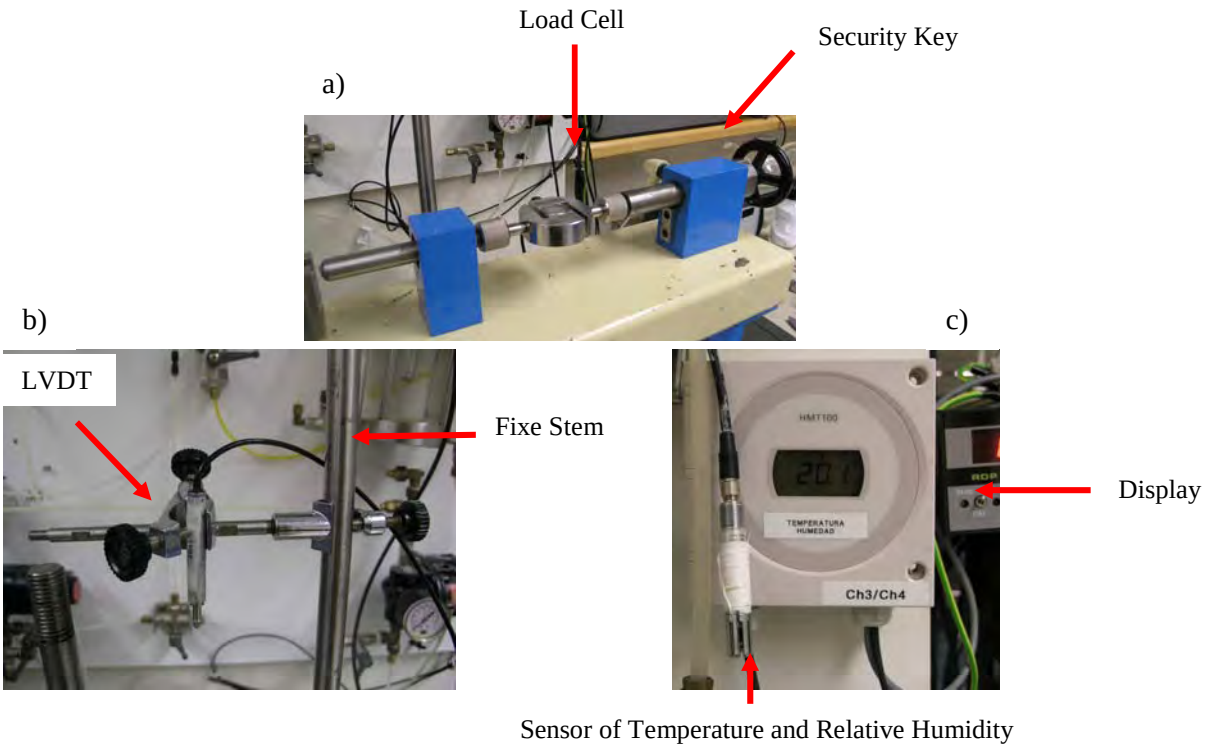

Figure 4.4: Description of data measuring a) Shear load cell. b) Normal displacement of samples using a LVDT displacement transducer. c) Humidity and temperature transmitter.

4.3. Characterization of the rock tested

The characterization of the rock was extracted from previous works by García-Castellanos et al., (2003), Berdugo (2007), Tarragó (2005) and Pineda et al.,(2010). The rock tested, called Lilla claystone, is a sulphate-bearing argillaceous rock located in the Lower Ebro Basin, in the northeast of Spain. These sulphate rocks, formed during the Tertiary Period, range from Early Eocene to Late Miocene in age. Lilla claystones have two main components: the host argillaceous matrix (composed by illite, paligorskite, dolomite and quartz), and the sulphated crystalline fraction (composed mainly of anhydrite and gypsum (Berdugo, 2007)).

4.3.1 Geotechnical Properties.

The density of the rock varies from 2.56 to 2.58 g/cm^3. The clay matrix has low plasticity, with high in situ moisture. Porosity varies from 0.09 to 1.1. Young modulus, E_0, varies from 26.5 to 28.5GPa and shear stiffness, G_0, varies from 11 to 12.5 GPa (Pineda et al., 2010). All data are summarized in Table 4.1.

Table 4.1: Geotechnical Properties of Lilla claystone.

Parameter	**Value**	**Units**
Density [ρ]	2.56 – 2.58	Mg/m^3
Porosity [n]	0.11	-
Water content [w]	3.2 – 4.1	%
Liquid Limit [LL]	23	%
Plasticity Index [IP]	5	%
Young Modulus [E_0]	26.5 – 28.5	GPa
Shear Modulus [G_0]	11 – 12.5	GPa
Uniaxial compressive strength [q_u]	20.0	MPa

4.3.2. Mineralogy

Crushed rock fractions with a particle size smaller than 20 μm were analyzed using X-Ray diffraction. The main mineral phases of the rock identified were dolomite, anhydrite, illite and paligorsquite (Fig. 4.5) (after Tarragó, 2005).

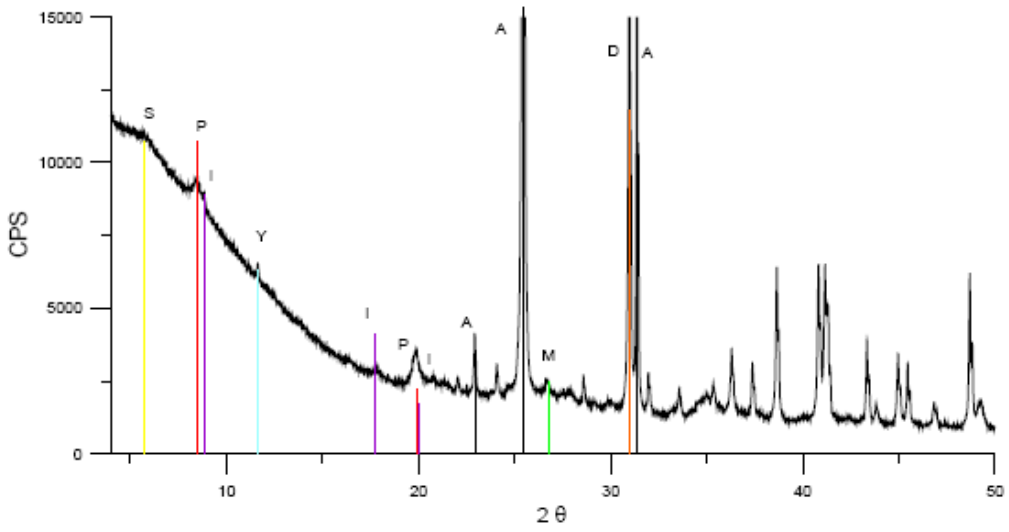

Fase 1: Dolomita	31.32 %
Fase 2: Anhidrita	44.32 %
Fase 3: Illita	15.85 %
Fase 4: Paligorsquita	8.51 %

Figure 4.5: Results of X-ray diffraction identifying the minerals in unaltereted Lilla claystones (after Tarragó, 2005).

4.3.3 Water retention properties

The water retention curve for unaltered Lilla claystone was determined by Pineda et al, (2010). The methodology followed consists in placing an intact sample of 15 mm in diameter and 10 mm in height in a wetting-drying cycle under unstressed conditions. The initial state of the sample was RH ~ 50% and T = 20º. The wetting and drying path was applied using the vapour equilibrium technique; while the wetting path used a hermetic vessel with distilled water. Air drying was used to induce a suction increase until a relative humidity of RH = 50% was attained. Suction was measured, after 24 hours of equalization, using a chilled-mirror dew-point psychrometer (measurements are plotted in black and grey in Fig. 4.6).

On the other hand, in this study also the suction and gravimetric water content was measured in this study six samples of unweathered Lilla claystone. The initial state of all samples was T = 20º and RH ~ 50% (laboratory conditions). These samples, in pairs, were subjected to different

relative humidity conditions using the vapour equilibrium technique. These conditions consisted in: drying path, placing the samples in a hermetic vessel with lithium chloride (RH ~ 20% at 20º); air drying, maintaining the samples at air laboratory condition; and wetting path, placing the samples in a hermetic vessel with distilled water (RH ~ 98% at 20º). Suction was measured after a fifteen-day equalization period, using a chilled-mirror dew-point psychrometer and the gravimetric content was determined after 24 hours of oven dry (measurements are indicated in blue and red in Fig. 4.6). This was done to determine a reference time of equalization to be used in the experimental program followed in this thesis.

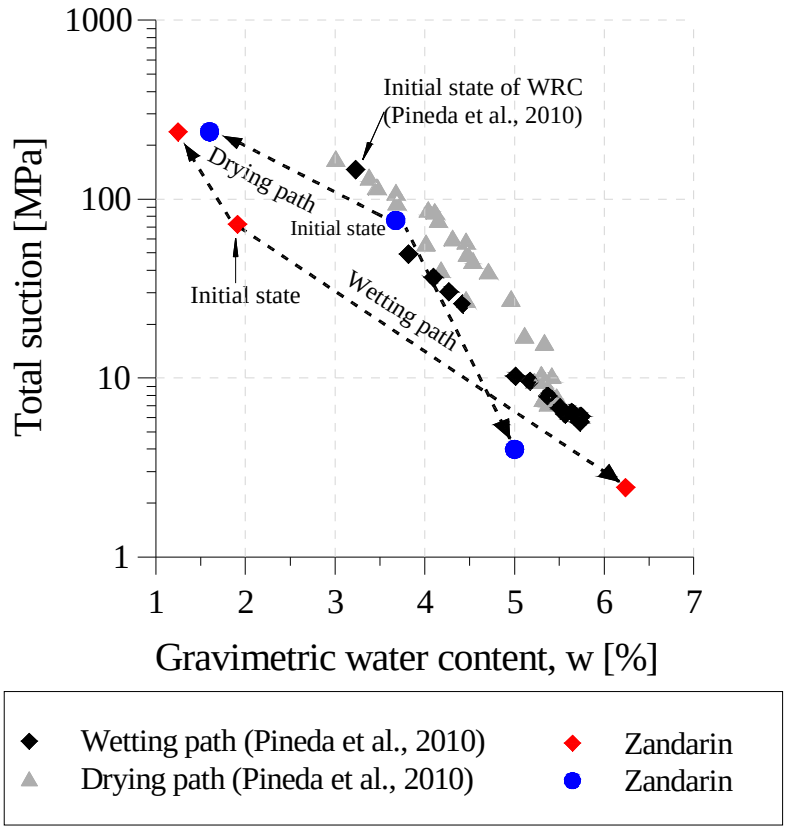

Figure 4.6: Water retention curve for unaltered Lilla claystone (after Pineda, et al., 2010) and equalization points used as reference for the experimental program performed in this thesis.

4.4. Direct Shear Test testing methodology

The testing methodology consisted in preparing the samples (carving joints with different geometrical angles), applying a wetting or drying cycle on the samples using the diffusion vapour equilibrium technique, and then performing the direct shear test.

4.4.1. Preparation of samples

The samples were extracted from borehole cores of Lilla claystone. Cores had a diameter of 110 mm and a length of 1 or 2 meters. The core was cut into pieces with a nominal length of 500 mm. Then, these pieces were drilled and cut in a machine to obtain samples of 50 mm in diameter and 12 mm in height. Then, the joints were carved with a diamond drill. The joints had different geometric angles, 15º, 30º, and 45º degrees respectively (refer to Figs. 4.7a and b) in order to obtained different asperity roughness angles.

4.4.2. Measurement of surface roughness

In order to obtain the topographical data of rock fracture surfaces, 2-D laser-scanning profiles of both sides of the joints were measured before and after the shear test. A laser and a LVDT were used to obtain the X-Y profile. The laser has a range of measure that varies from 25 to 30 mm, and a precision of 0.03%. The LVDT BS/50 model has a range of measure of +/-25 mm and a sensitivity of ± 0.05% mV/mm (Fig. 4.8). Data were collected by means of a PC computer that processed them in real time.

a)

b)

Figure 4.7: Sample construction. a) Drilling of borehole core and joint carving with the diamond drill. b) Rock joints with different geometric angles 0º, 15º, 30º and 45 degrees respectively.

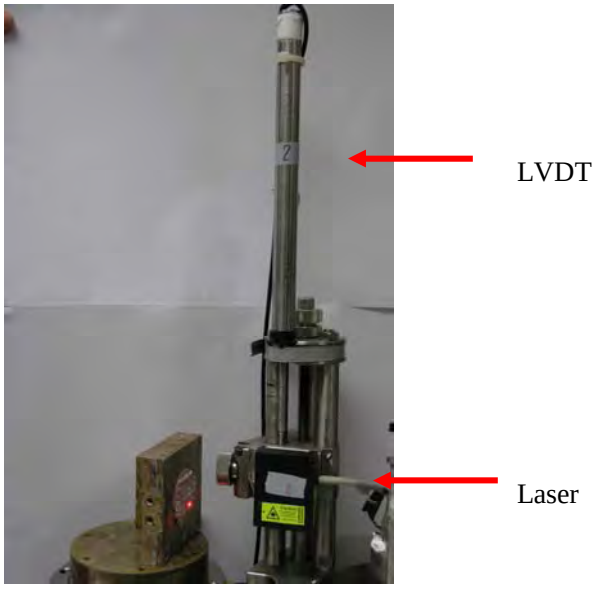

Figure 4.8: Laser and LVDT used to measure a 2D joint surface topography.

4.4.3. Equilibration with the Relative Humidity of the environment

Prior to shearing, each sample was equalized at the required suction. This suction was applied using the vapour transfer equilibrium technique, which consists in controlling the relative humidity of a closed air-vapour system. Then the soil water potential is applied to reach specimens by migrating the moist air from a reference system of known potential to the soil pores, until equilibrium is reached (Romero, 2001). The samples were placed in a desiccator with a solution whose concentration is known at a constant temperature of 20ºC. Some of the samples were dried with pure lithium chloride. The pure lithium chloride allows reducing RH to 20% (approximately a total suction of 200MPa). Other samples were wetted using distilled water. A quasi-saturation condition was obtained with RH ≅ 86% and a suction of 20 MPa (Fig. 4.9a). Other samples were exposed to laboratory room environment (RH ≅ 50% which corresponds to a suction of 100 MPa).

The equalization was considered to be complete when there was no significant change in the weight of samples (no changes in water content). Samples weights were measured; as well as a total suction on a small piece of rock using a dew-point psychrometer (WP4, Decagon Device).

This piece of rock was placed in the desiccator together with the samples, and its suction was used as a standard average value (Fig. 4.9b). This means that although the samples are not equal, it was assumed that the suction measured with WP4 is the suction of the joint. The samples reached equalization after fifteen days.

For this value of suction, and using the retention curve shown in Figure 4.6 and the porosity of the rock (Table 4.1), an average degree of saturation (S_l) of the samples is calculated. A value of S_l = 0.33 corresponds to samples with a suction of 200 MPa, of S_l = 0.82 for samples with a suction of 100 MPa and of S_l = 1.0 for samples with a suction of 20MPa

a) b)

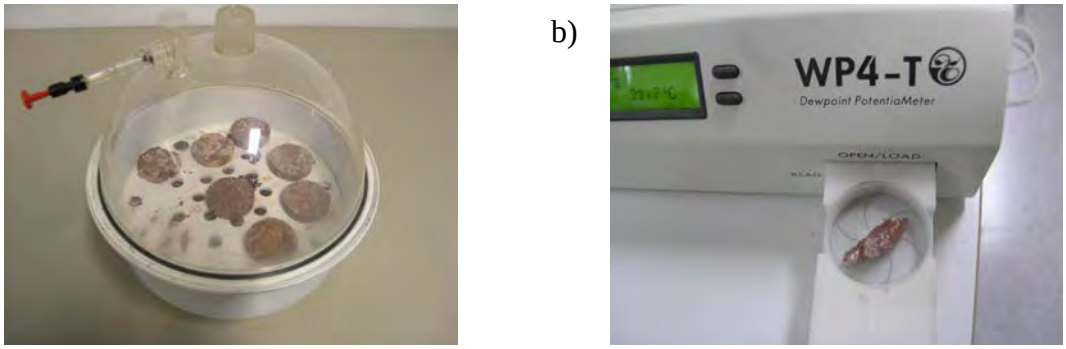

Figure 4.9: a) Samples within the desiccator. Application of the vapour diffusion transfer technique. b) Measurement of suction with a psycrometer. The suction measure of a small piece of rock is used as a standard.

4.4.4. Direct shear testing.

Shear testing consisted in placing the sample in the shear cell, and controlling that the joint is normal to the horizontal piston. Then the centering bushing was positioned and the piston was carefully inserted into its axis. After connecting the shear cell to the vapour system, the hygrometer was introduced into its chamber. Once the upper lid of the air chamber and the LVDT were properly fixed, the air pressure was applied. The pressure was controlled using a valve and a manometer. Three different values of air pressure (which defines the net normal stress) were applied, 30, 60 and 150 kPa respectively. Finally, the shear displacement is applied to the sample at a rate of 0.05 mm/min. The program allows users to specify the time interval at

which data were recorded, i.e. one second, in this case. The shear test finished when the residual shear stress was reached. The data obtained from the tests allows defining shear stress vs. shear displacements and normal displacements vs. shear displacements. These data are plotted and analyzed in the following section.

4.5. Tests results and discussion.

This section describes and discusses the results obtained from direct shear testing and from measuring surface roughness.

4.5.1. Results of direct shear tests.

The results of the tests are plotted in Figures 4.10 to 4.14 in terms of different asperity roughness angle of the joints (α_a = 0º, 5º, 15º, 30º and 45º) and the different normal stresses (30, 60 and 150 kPa). The left side of the figures shows the shear stress-shear displacement curves, while the right side shows the normal displacements-shear displacement curves. Each plot draws three curves which correspond to the different values of suction used in the tests. The red line corresponds to a suction of 200 MPa, the green line to 100 MPa and the blue line to 20 MPa. The normal and shear stresses calculated are the mean average value acting on the middle plane of the joint.

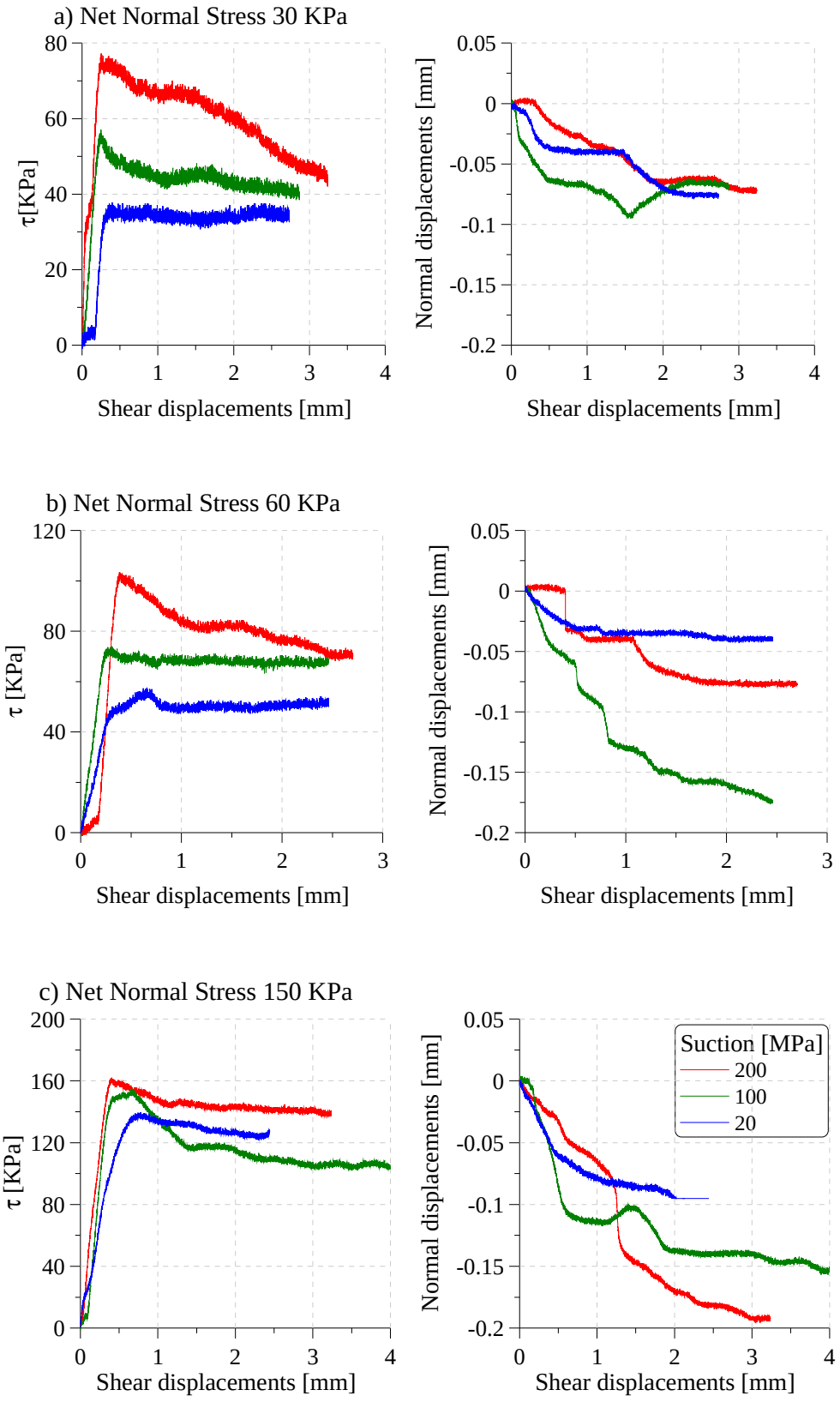

Figure 4.10: Shear test results for the joint with a roughness angle equal to 0º.

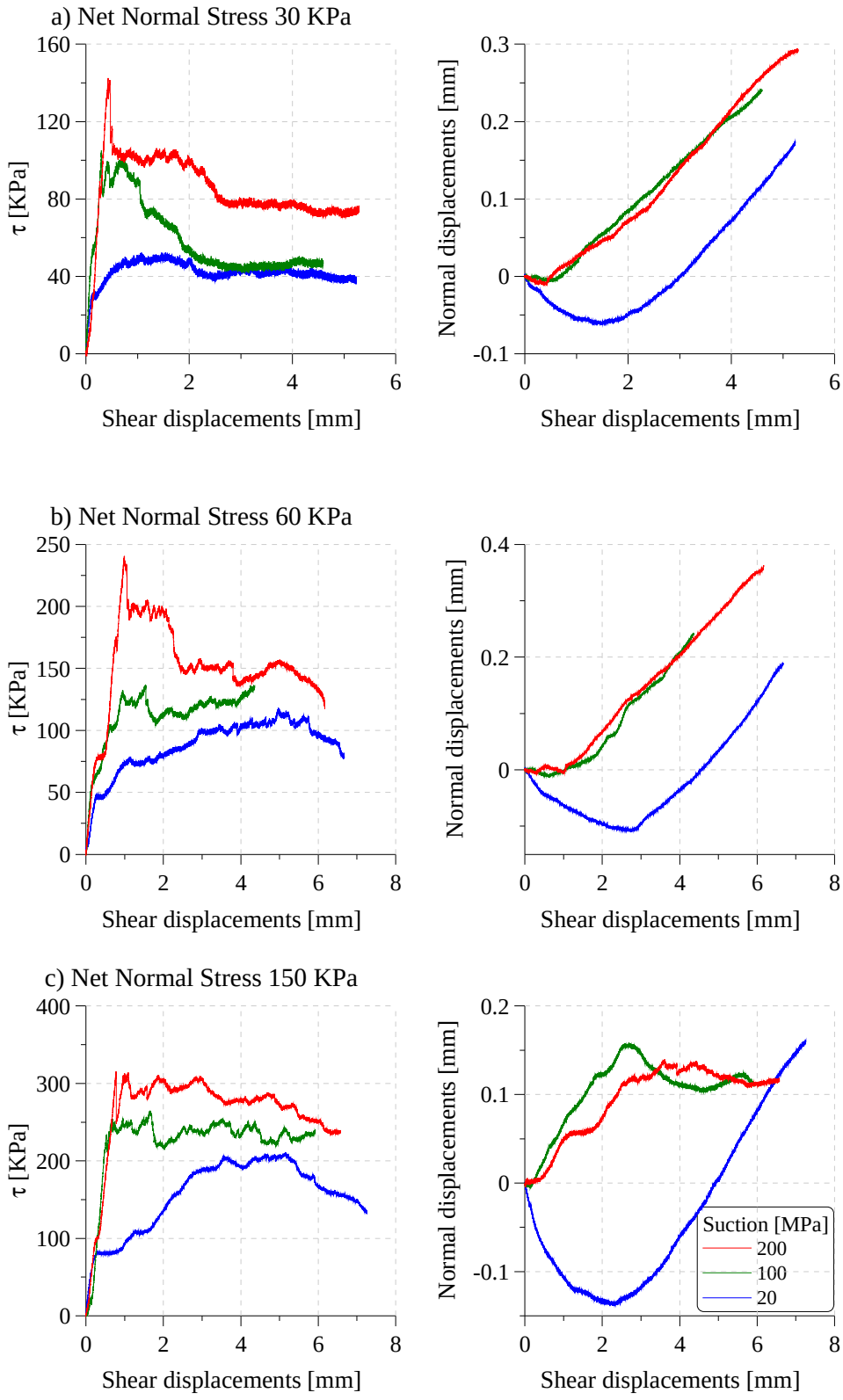

Figure 4.11: Shear test results for the joint with a roughness angle equal to 5º.

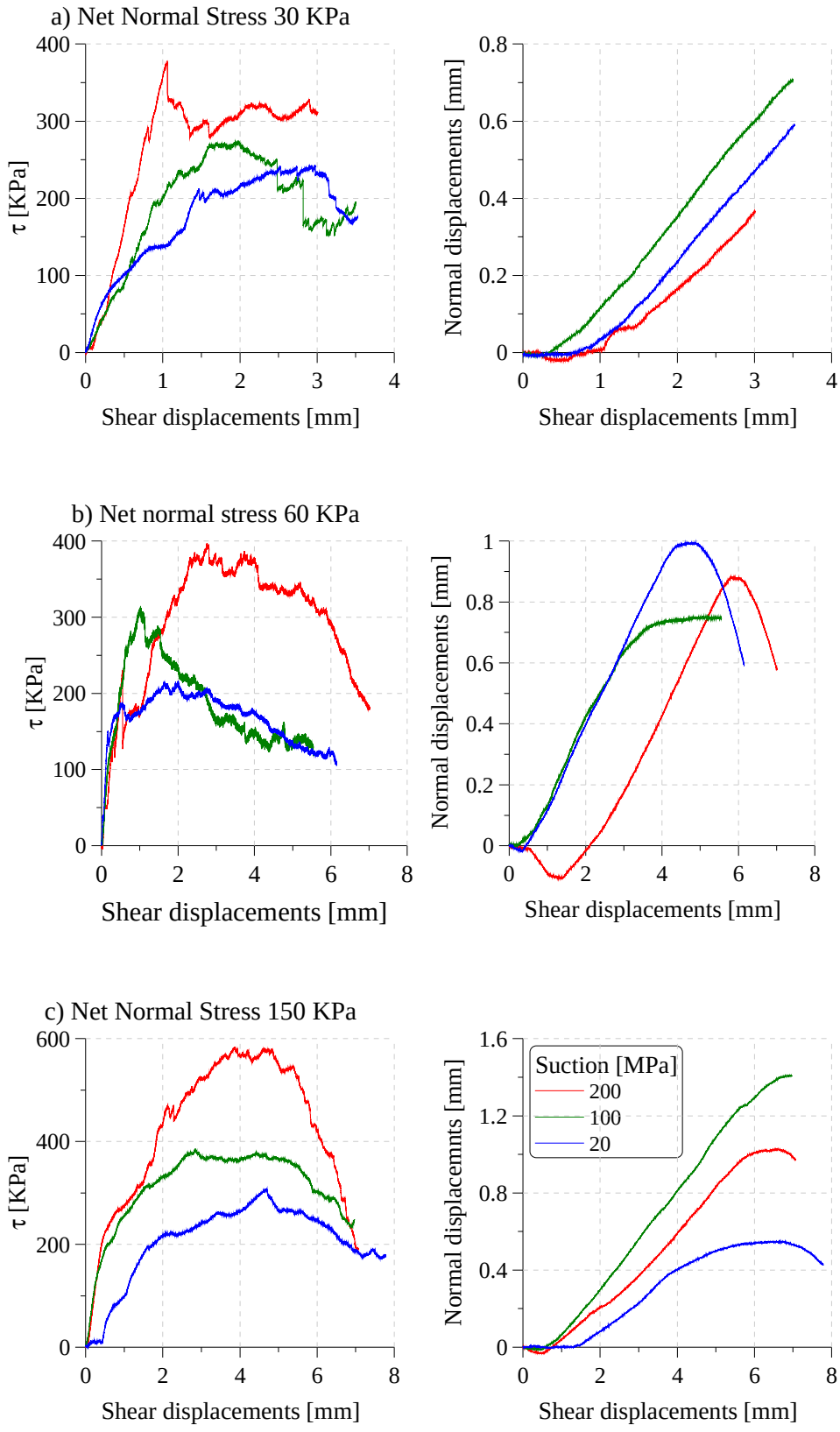

Figure 4.12: Shear test results for the joint with a roughness angle equal to 15º.

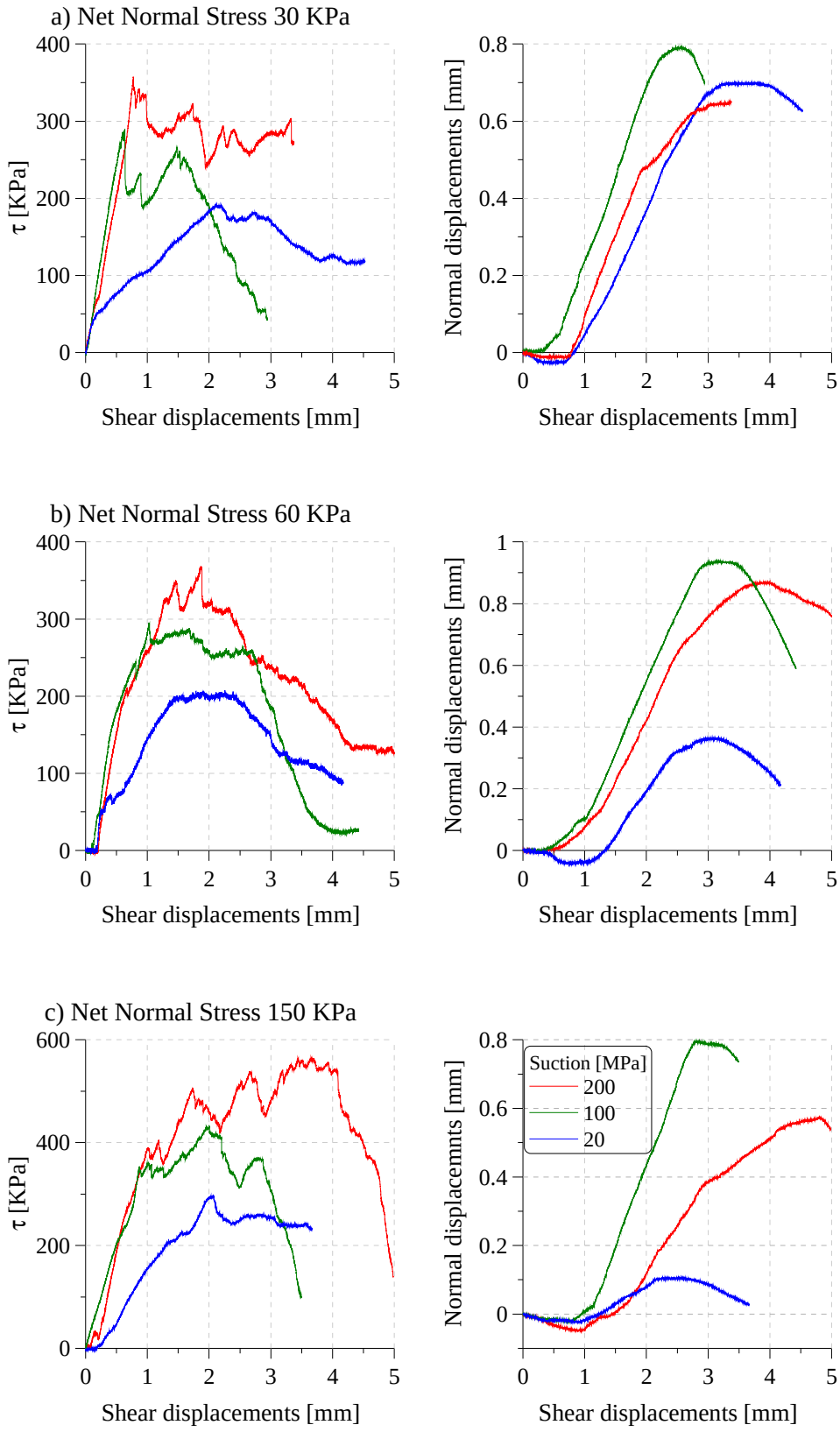

Figure 4.13: Shear test results for the joint with an asperity roughness angle equal to 30º.

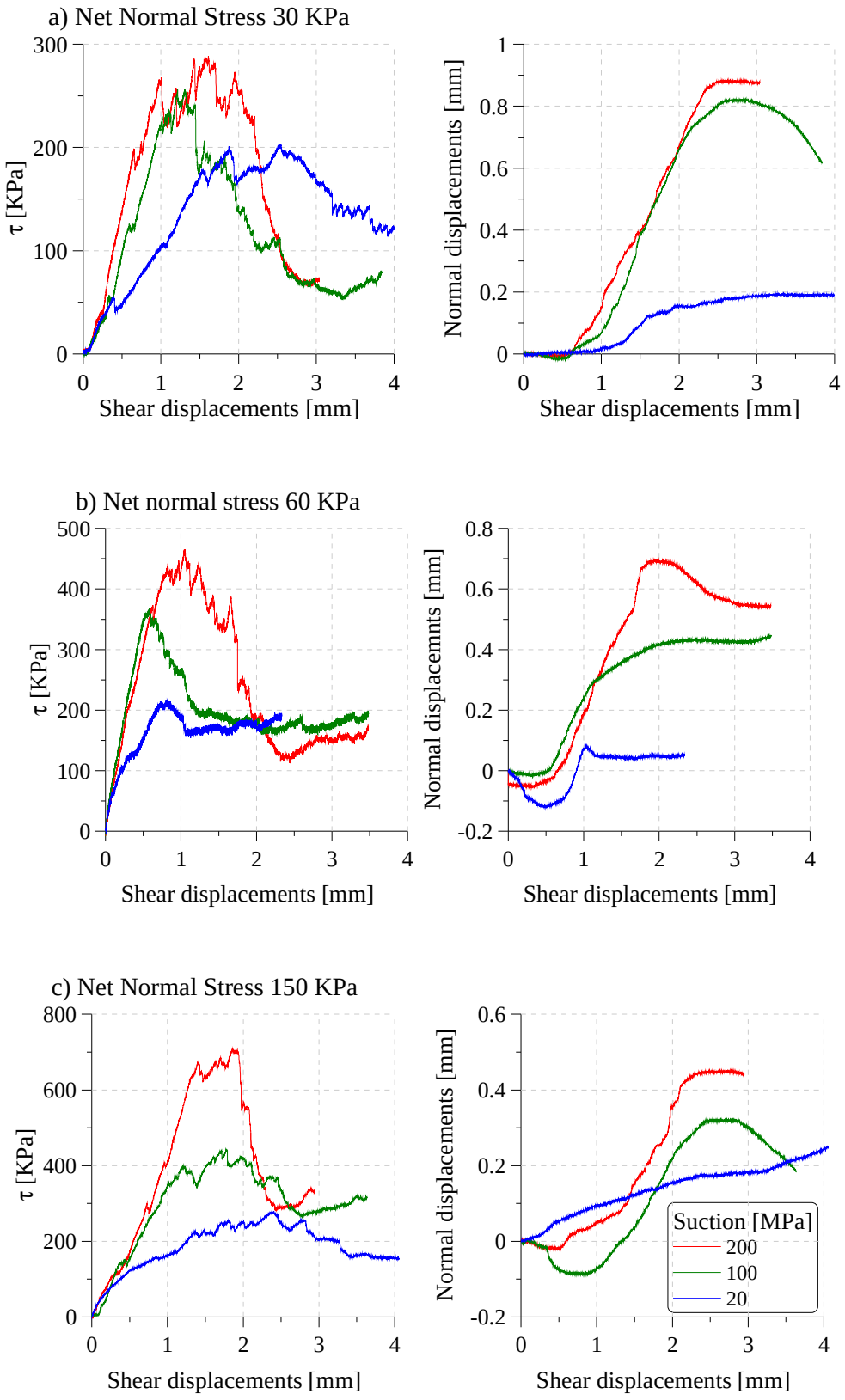

Figure 4.14: Shear test results for the joint with a roughness angle equal to 45º.

4.5.1.1 Shear strength

The shear stress vs. shear displacement plots show that the shear strength of joints depends on three variables: normal stress, suction and joint roughness angle. The effect of normal stress is well–known: the greater the normal stress, the greater the shear strength. This effect is explained by the increment in friction between two surfaces due to normal stress. The value of suction applied also affects peak and residual shear strength. The greater the suction, the greater the values of peak shear strength. However, the effect of suction on residual strength is not observed as clearly as in peak strength, because residual strength not only depends on suction, but also on the degradation of asperities. The degradation of asperities is influenced not only by suction but also by the irregular matching of asperities due to defects in joint construction and by the heterogeneity of the rock.

Rougher asperities are associated with higher shear strength. Roughness also affects the strength softening of the joint. In joints with higher asperity roughness, residual strength is attained at smaller displacements. For example, for joints with a roughness of 45º, residual strength is reached at a displacement of approximately 2.5 mm; while for a joint with a roughness of 15º, residual strength occurs at a displacement of 6 mm. Flat joints show a ductile behaviour, in which case the softening effect is neglected.

4.5.1.2 Normal displacements

The normal displacements recorded for the flat joint were negative. Therefore these joints present a contractive behaviour. Contraction increases with the increase in net normal stresses (Fig. 4.10a, b and c). For joints with a smooth angle of roughness α_a=5º, positive normal displacements showing a dilatant behaviour were recorded. For the rest of the samples, with α_a= 15º, 30º and 45º, normal displacements increase, implying thus increasing dilatancy. Nevertheless, comparing normal displacements for α_a= 15º, 30º and 45º it is noticed that dilatancy decreases with regards to α_a. This is explained by the fact that rougher asperities present more degradation and more extent affecting the whole surface of the joint.

It was also generally recorded that the greater the normal stress, the lower the dilatancy. However this trend was not always measured, e.g. in cases α_a = 15º and 30º (see Figs. 4.12 and 4.13a and b). It is thought that this anomalous behaviour is due to some irregularity of matching and to the heterogeneity of the rock which influence the degradation of asperities.

Figures also show the influence of suction on dilatancy. The joints with less suction (Ψ=20MPa, RH=86%) exhibit lower dilatancy, whereas if suction increases dilatancy increases. Since suction increases rock strength, the sliding of joint walls one over the other occurs without breakage. Even in the case of breakage, it is more likely that the gouge material with higher suction would roll over the joint surface. Under a lower suction, is easier to crush without rolling.

4.6. Rock joint surface damage

Figures 4.15 to 4.18 present photographs of the joint samples after testing for α_a = 5º, 15º, 30º and 45º respectively. The photographs are ordered from σ' = 30KPa to σ' = 60KPa to σ' = 150KPa with respect to the increment of net normal stress; and from left to right considering the increment in suction (20, 100 and 200 MPa).

The damage of rock joint surfaces was qualitatively measured by topographical profiles obtained before and after the shear tests. The topographical profiles were measured using the laser and LVDT described in Section 4.2. The profiles are plotted in Figures 4.19 to 4.21 for α_a = 5º; Figures 4.22 to 4.24 for α_a = 15º; Figures 4.25 to 4.27 for α_a = 30º; and Figures 4.28 to 4.30 for α_a = 45º. The profiles measured before the tests are drawn using a black dashed line.

Damage was quantitatively measured by determining the ratio of the gouge material weight generated during shear process vs. the initial specimen weight (Wg/Wi). The ratio Wg/Wi against net normal stress and for a suction equal 20, 100 and 200 MPa is shown in Figures 4.31a, b and c respectively.

Also the damage was related to the shear work (Fig. 4.32), to the dilatancy work (Fig. 4.33) and to the total work exerted on the joints (Fig. 4.34).

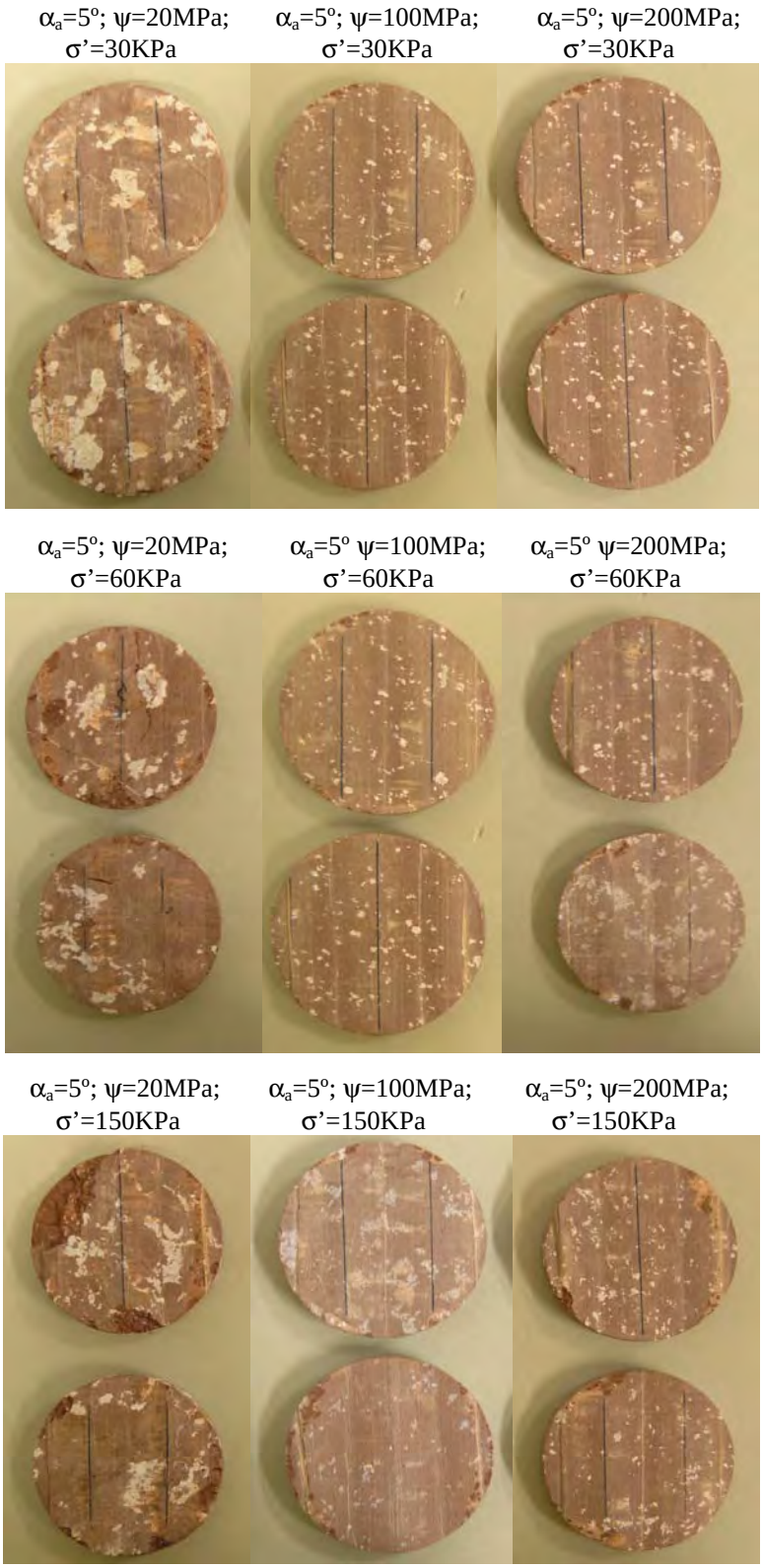

Figure 4.15: Photograph of rock joint surfaces after shear tests with α_a = 5°.

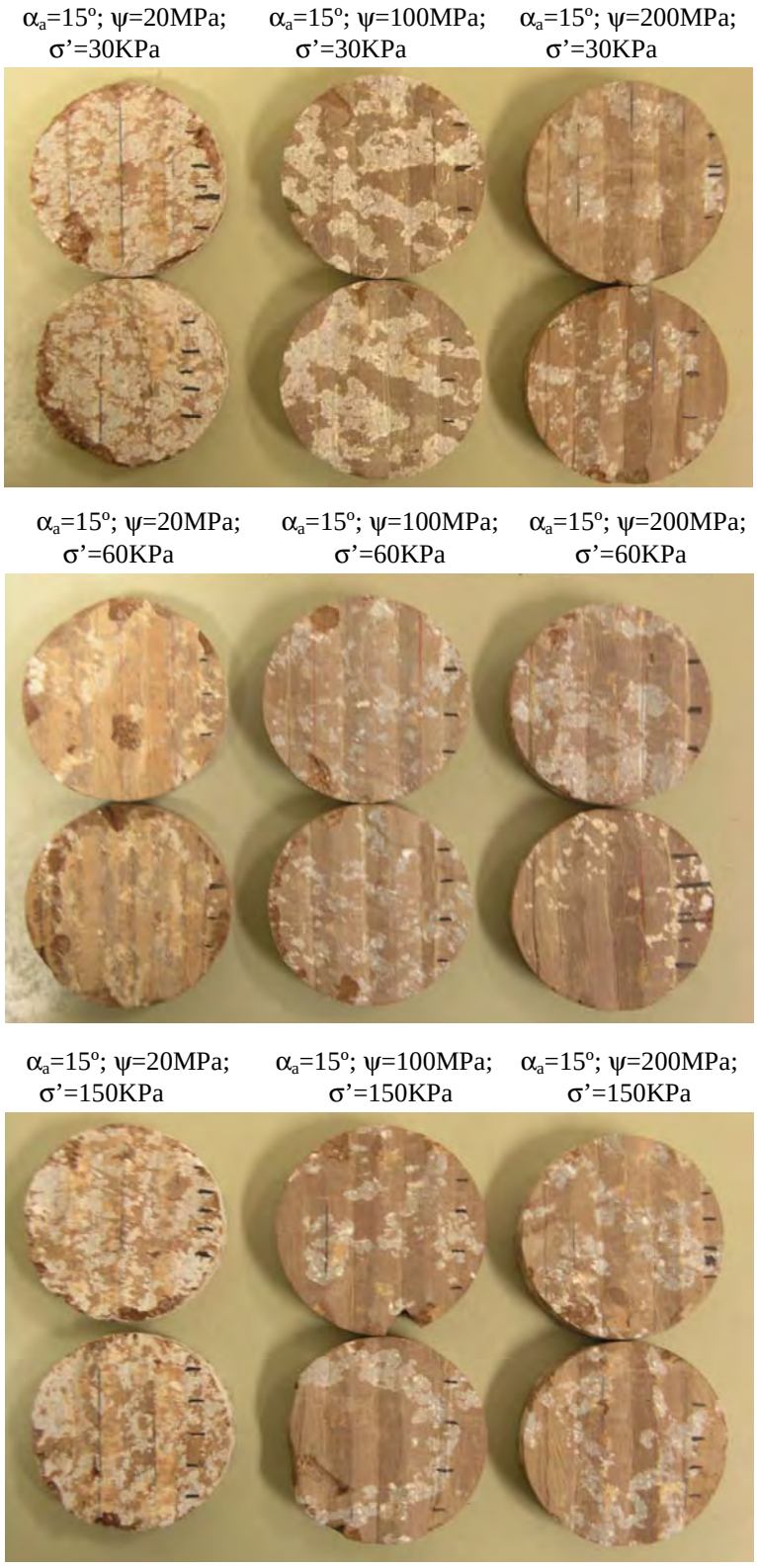

Figure 4.16: Photograph of rock joint surfaces after shear tests with α_a = 15º.

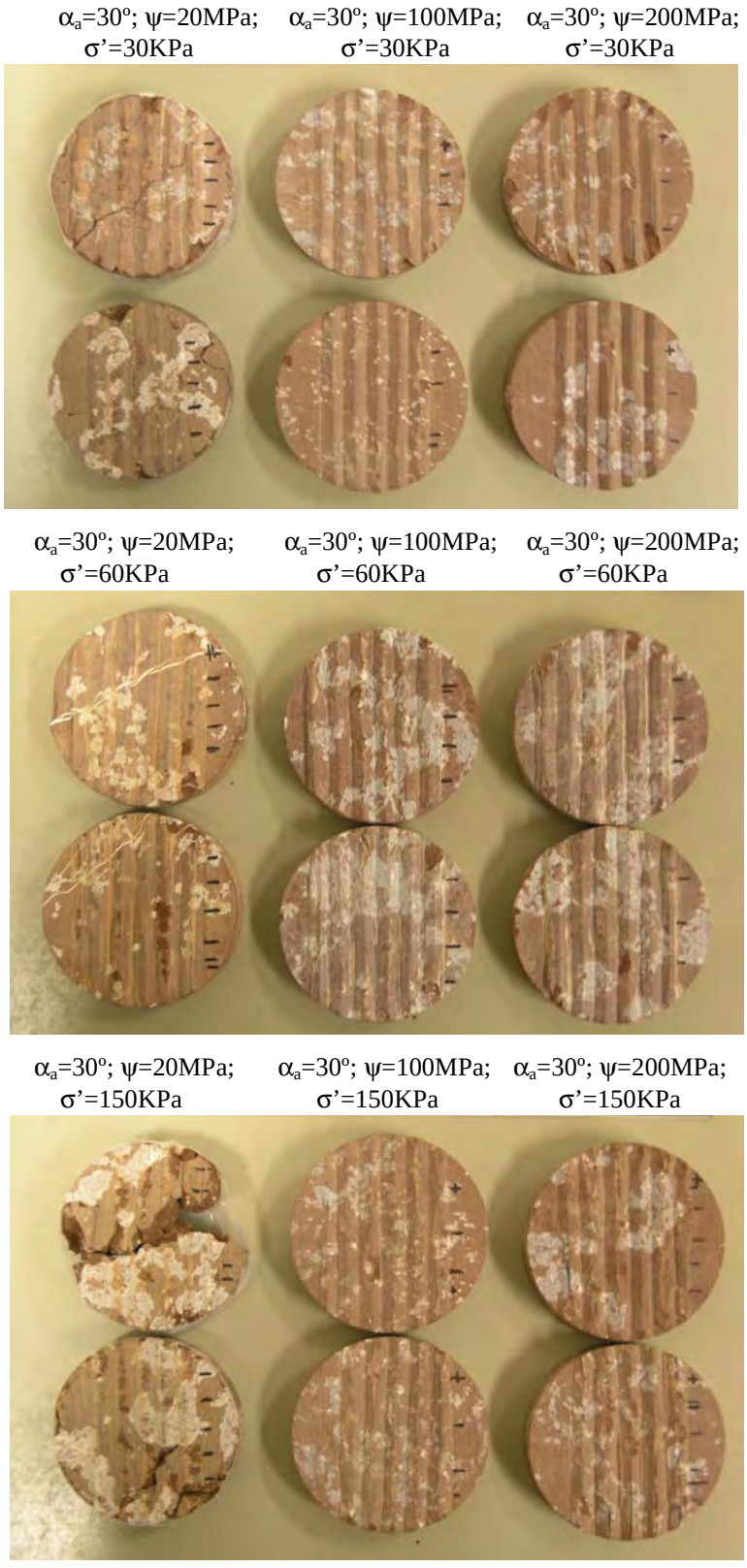

Figure 4.17: Photograph of rock joint surfaces after shear tests with α_a = 30º.

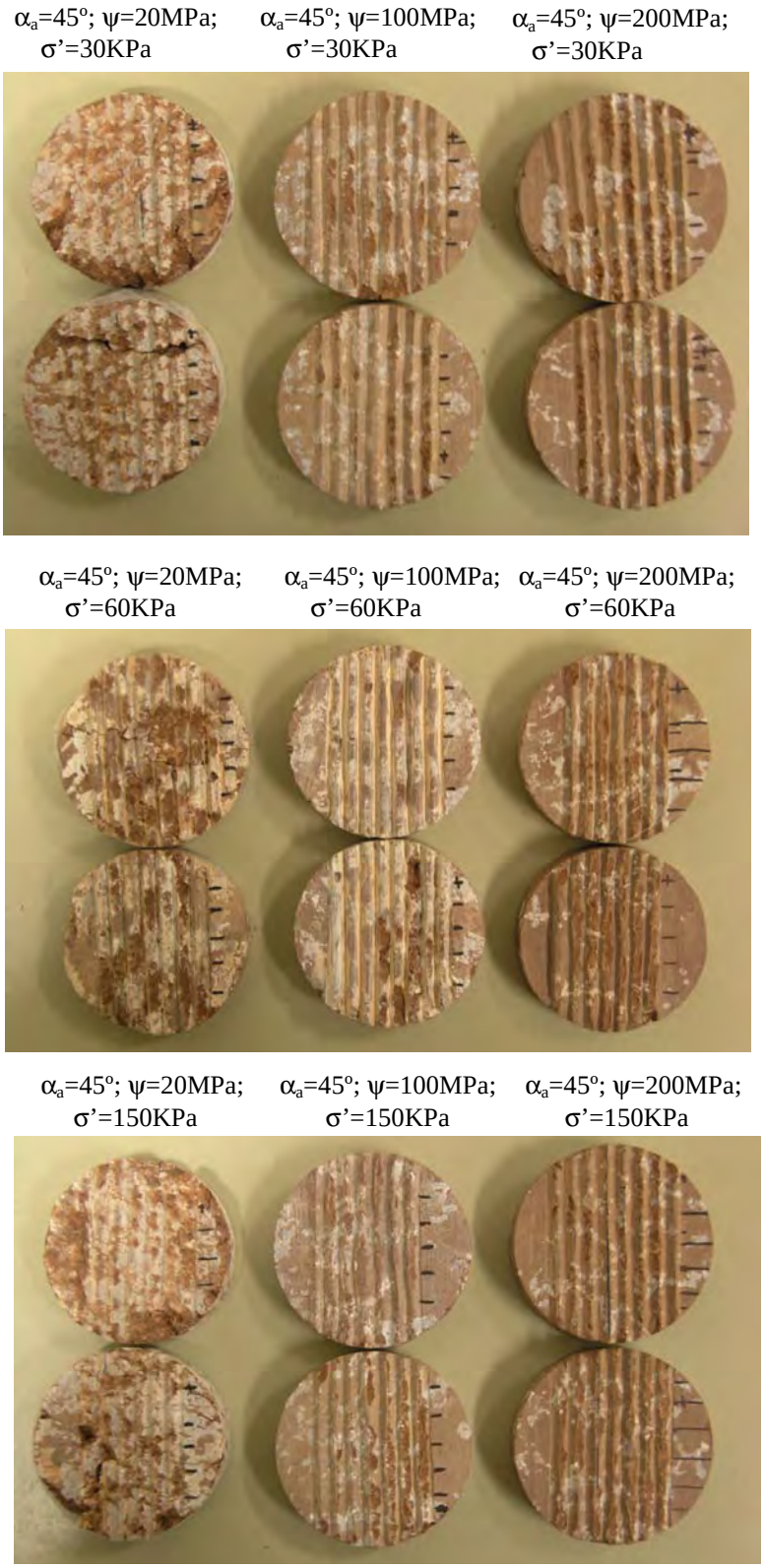

Figure 4.18: Photograph of rock joint surfaces after shear tests with α_a = 45°.

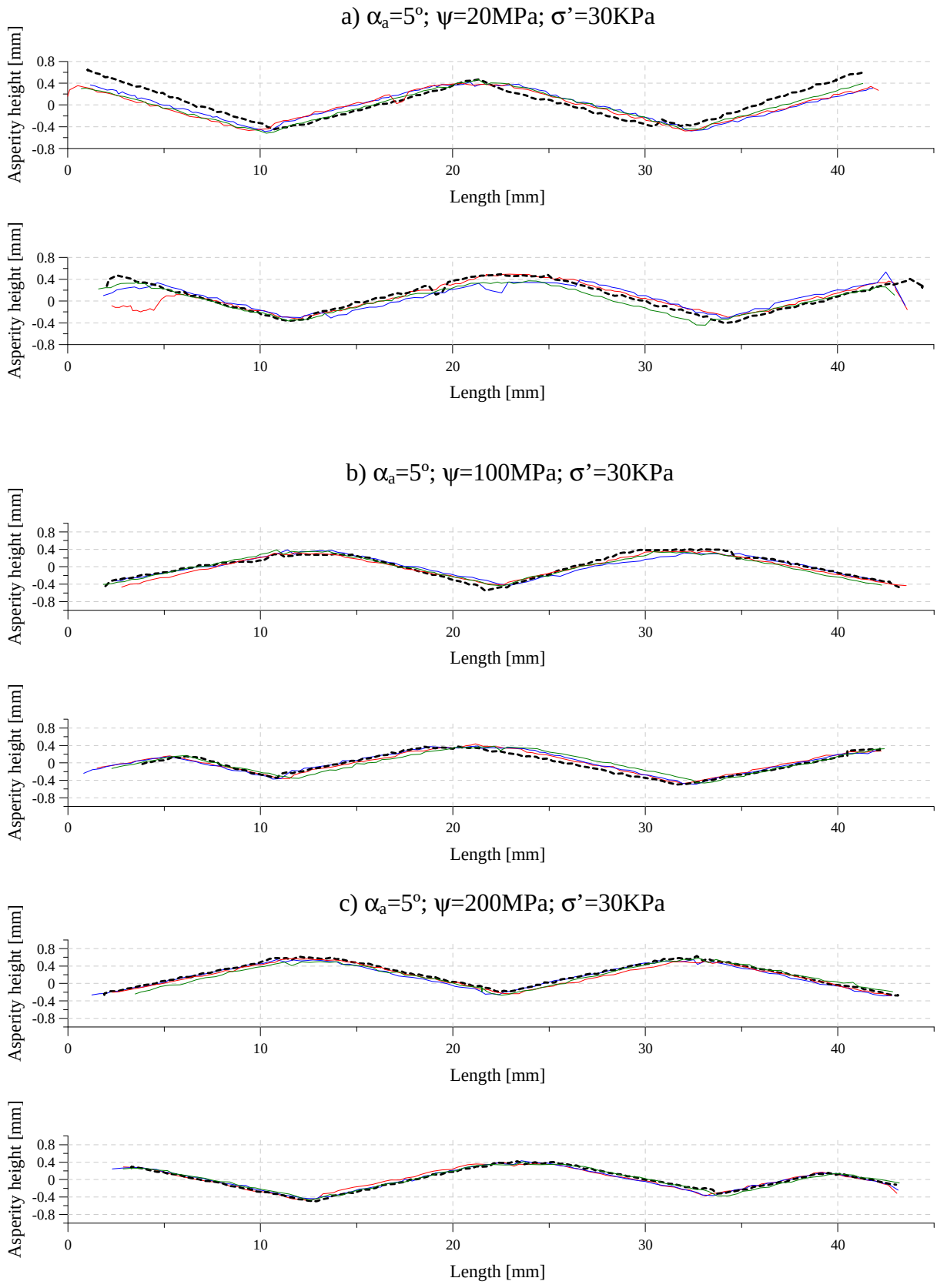

Figure 4.19: Topographical surface profile for rock joints with α_a = 5º and σ' = 30 kPa.

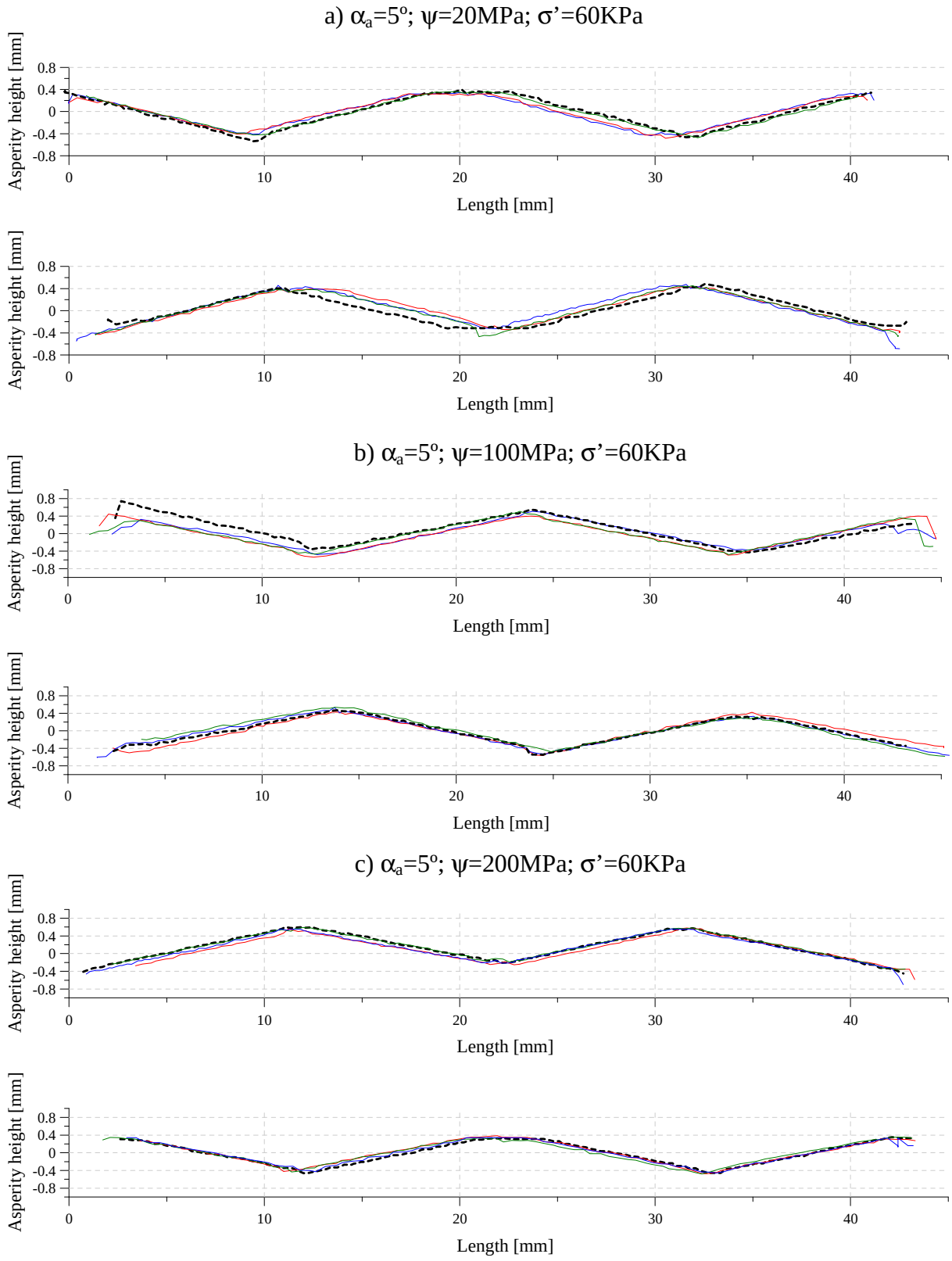

Figure 4.20: Topographical surface profile for rock joints with α_a = 5º and σ' = 60 kPa.

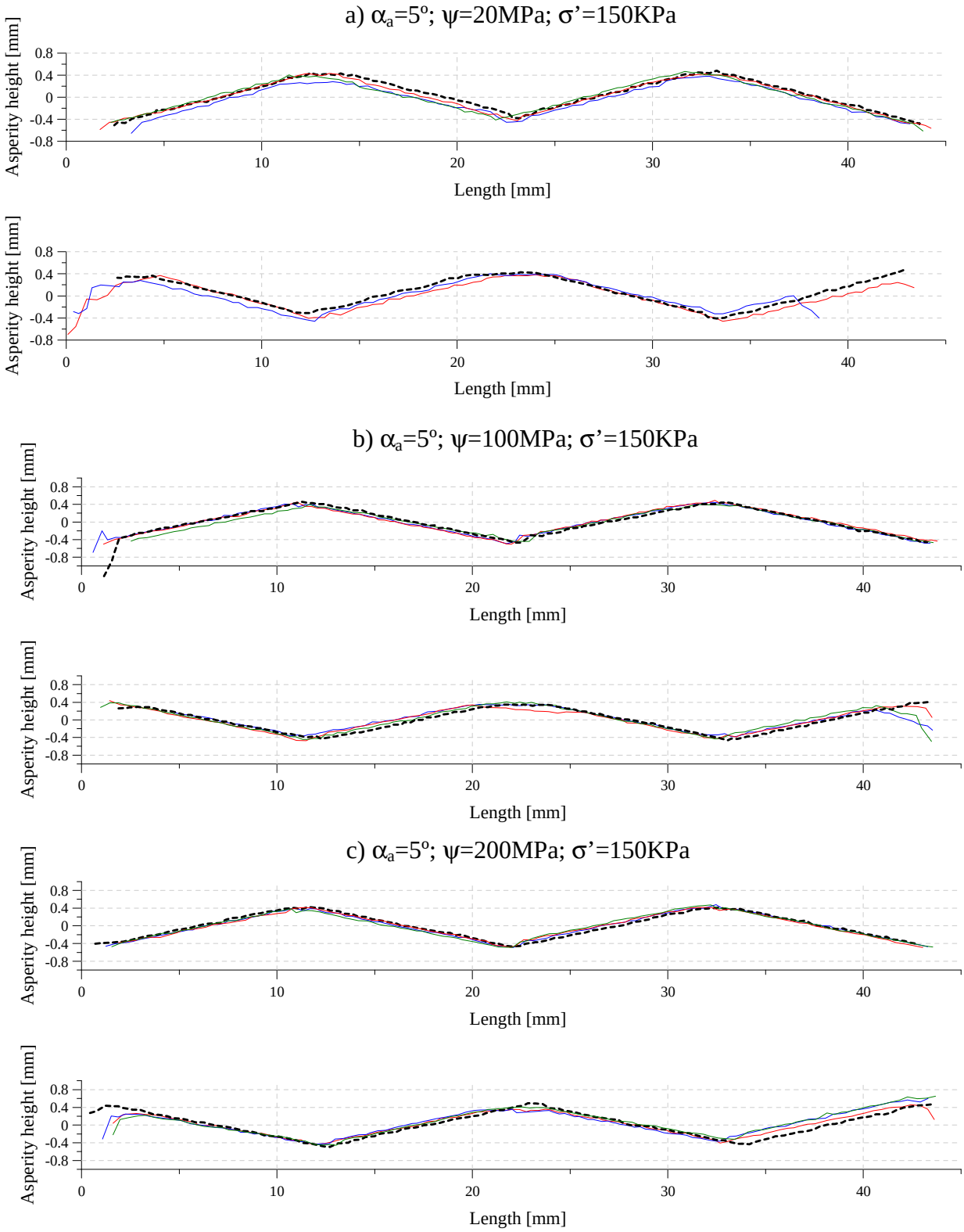

Figure 4.21: Topographical surface profile for rock joints with α_a = 5° and σ' = 150 kPa.

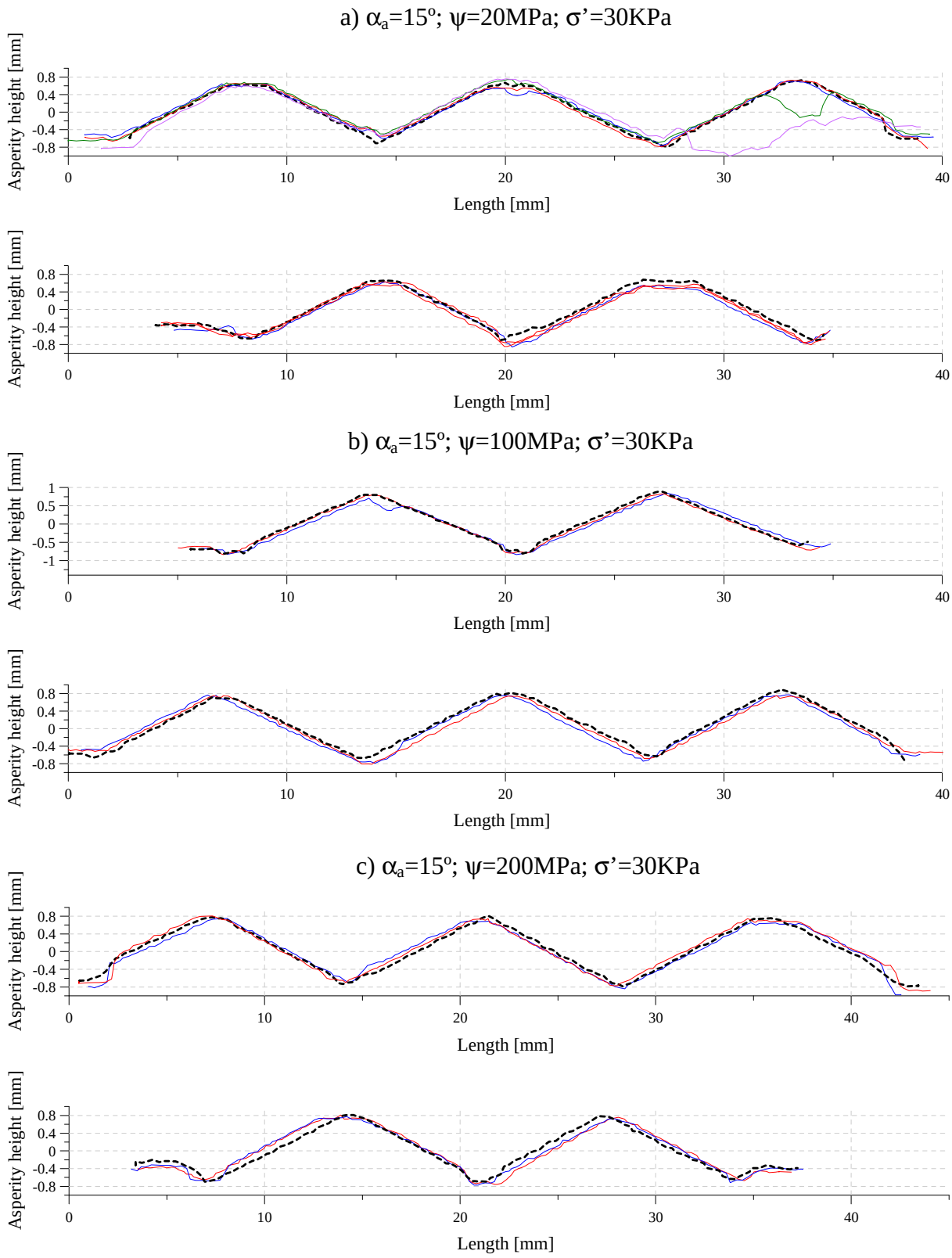

Figure 4.22: Topographical surface profile for rock joints with α_a = 15º and σ' = 30 kPa.

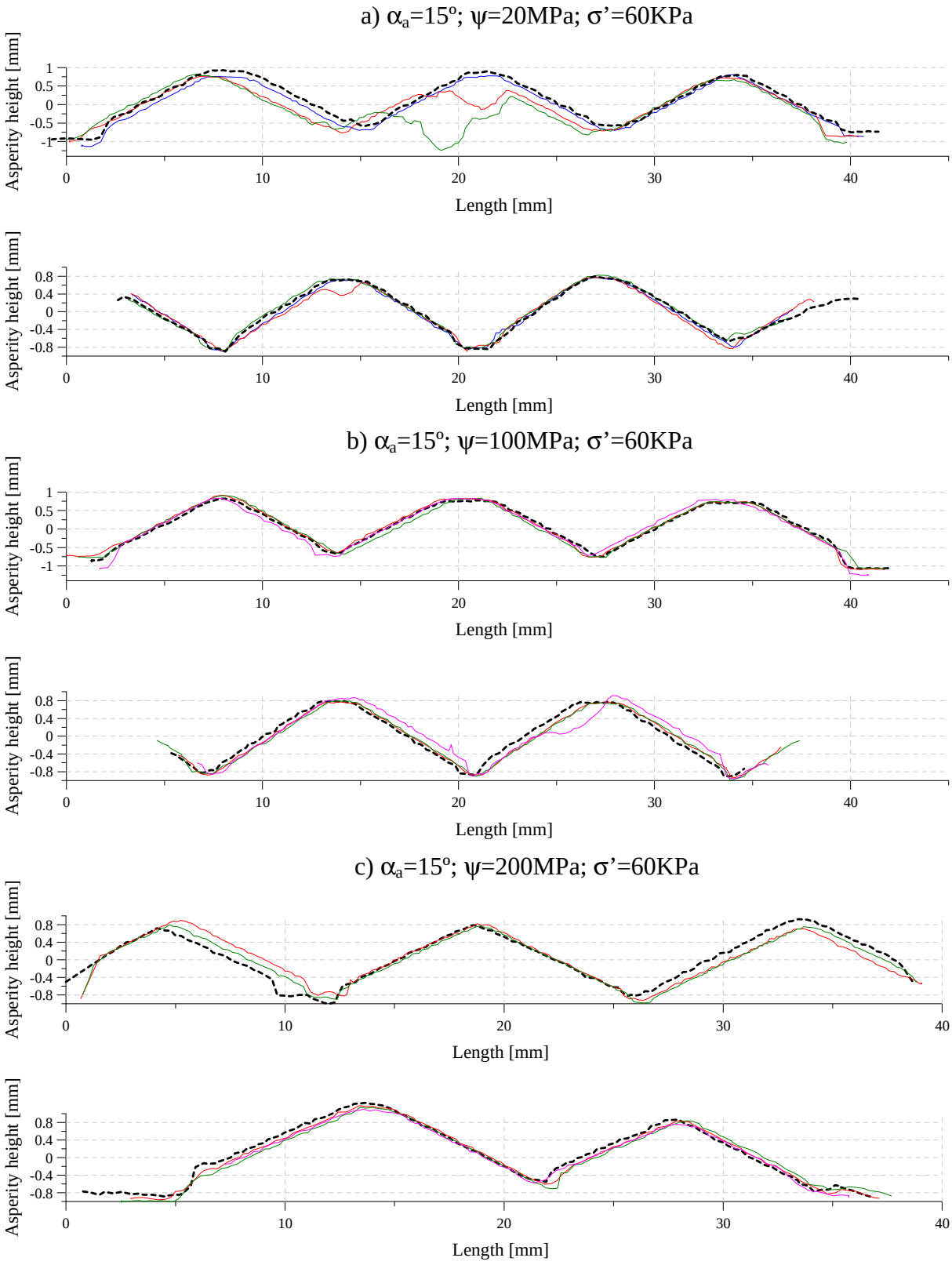

Figure 4.23: Topographical surface profile for rock joints with α_a = 15º and σ' = 60 kPa.

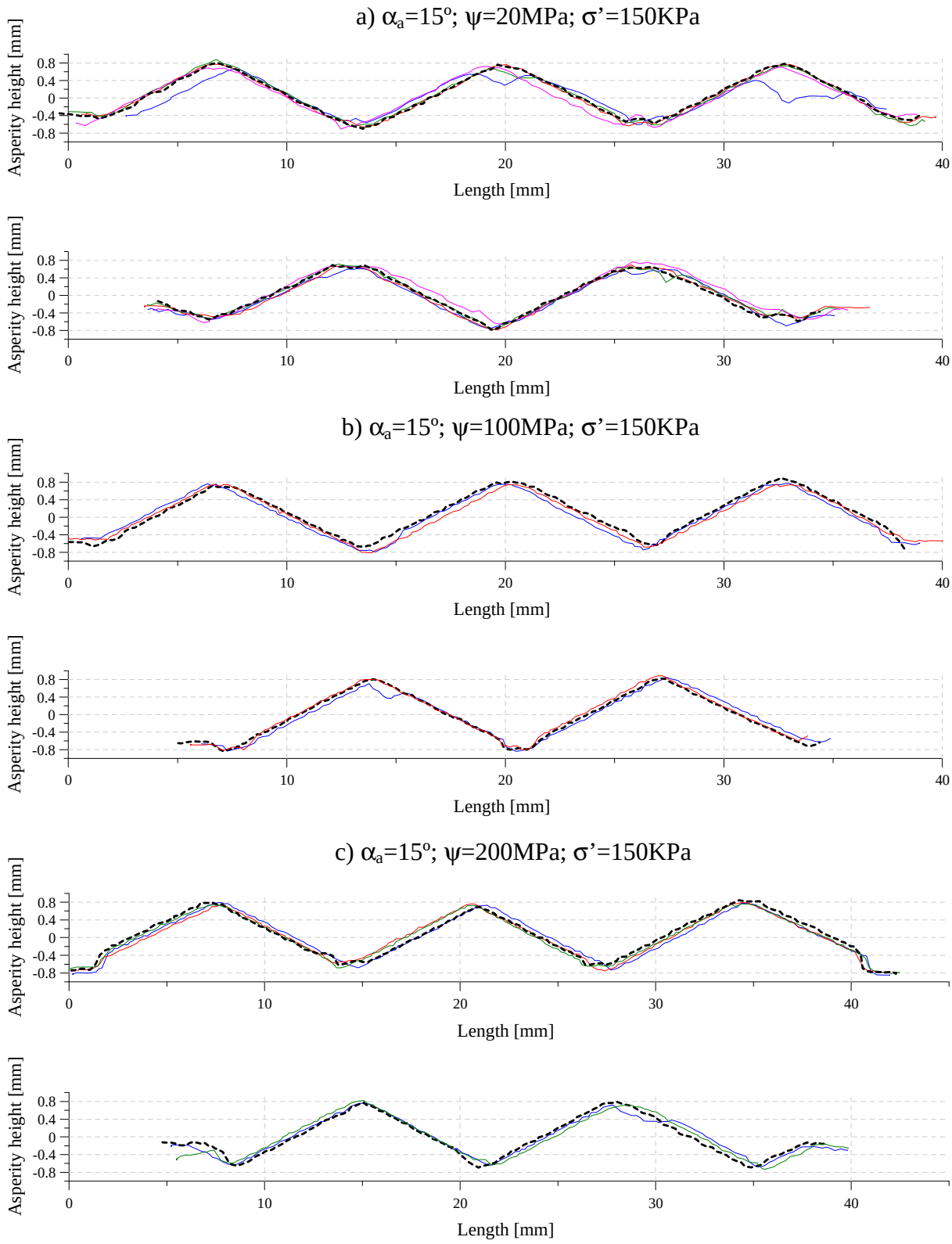

Figure 4.24: Topographical surface profile for rock joints with α_a = 15º and σ' = 150 kPa.

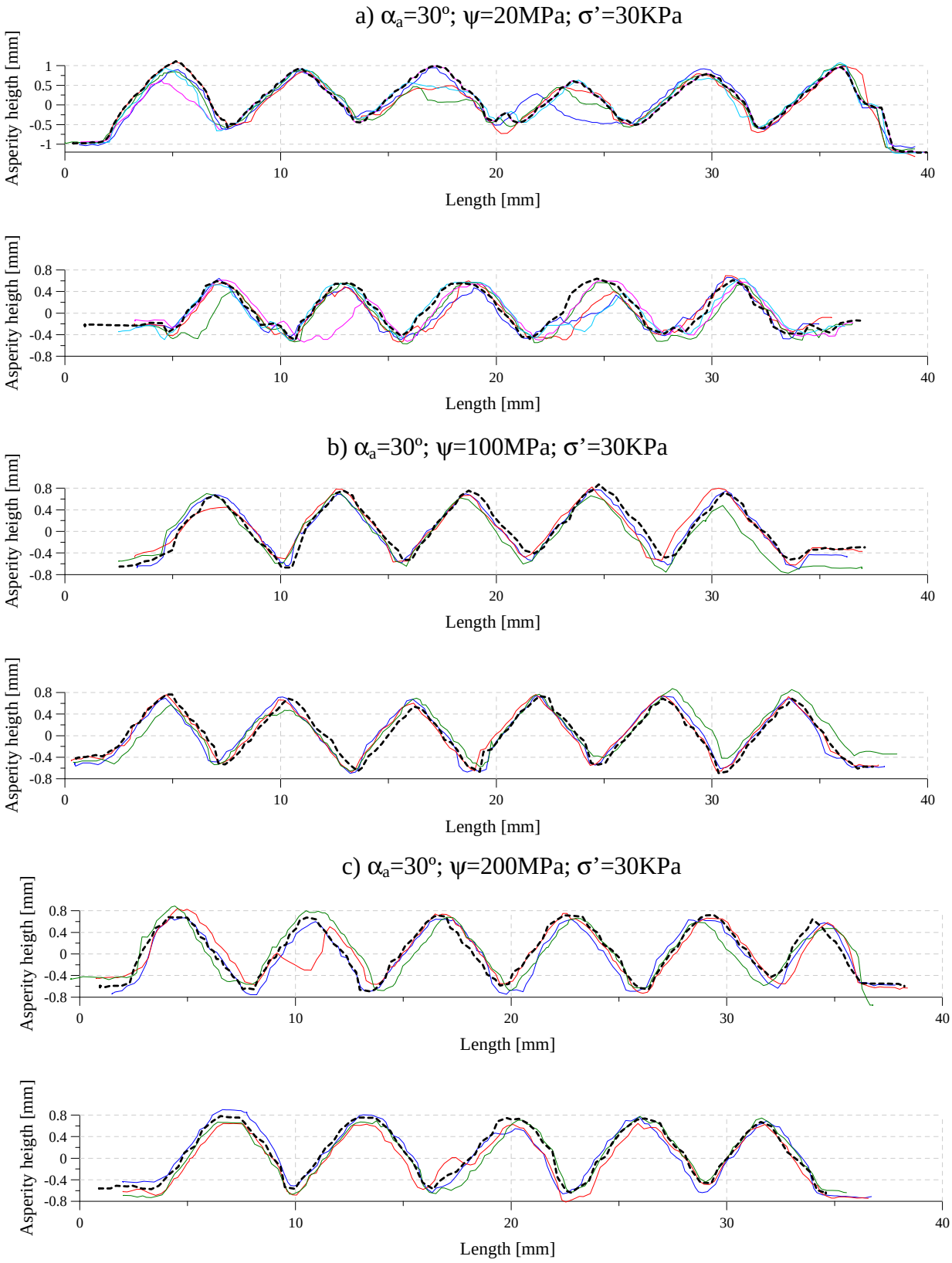

Figure 4.25: Topographical surface profile for rock joints with α_a = 30º and σ' = 30 kPa.

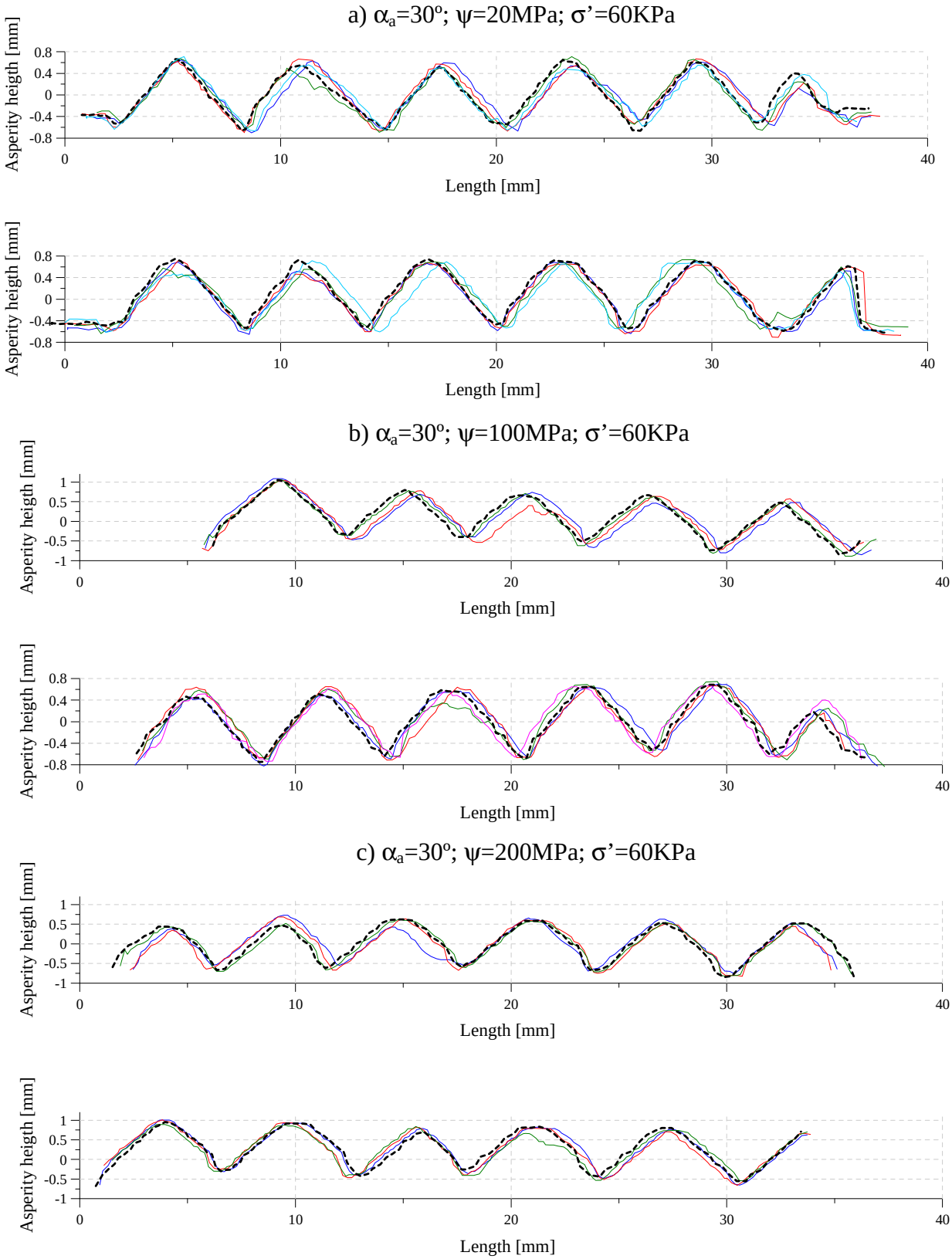

Figure 4.26: Topographical surface profile for rock joints with α_a = 30º and σ' = 60 kPa.

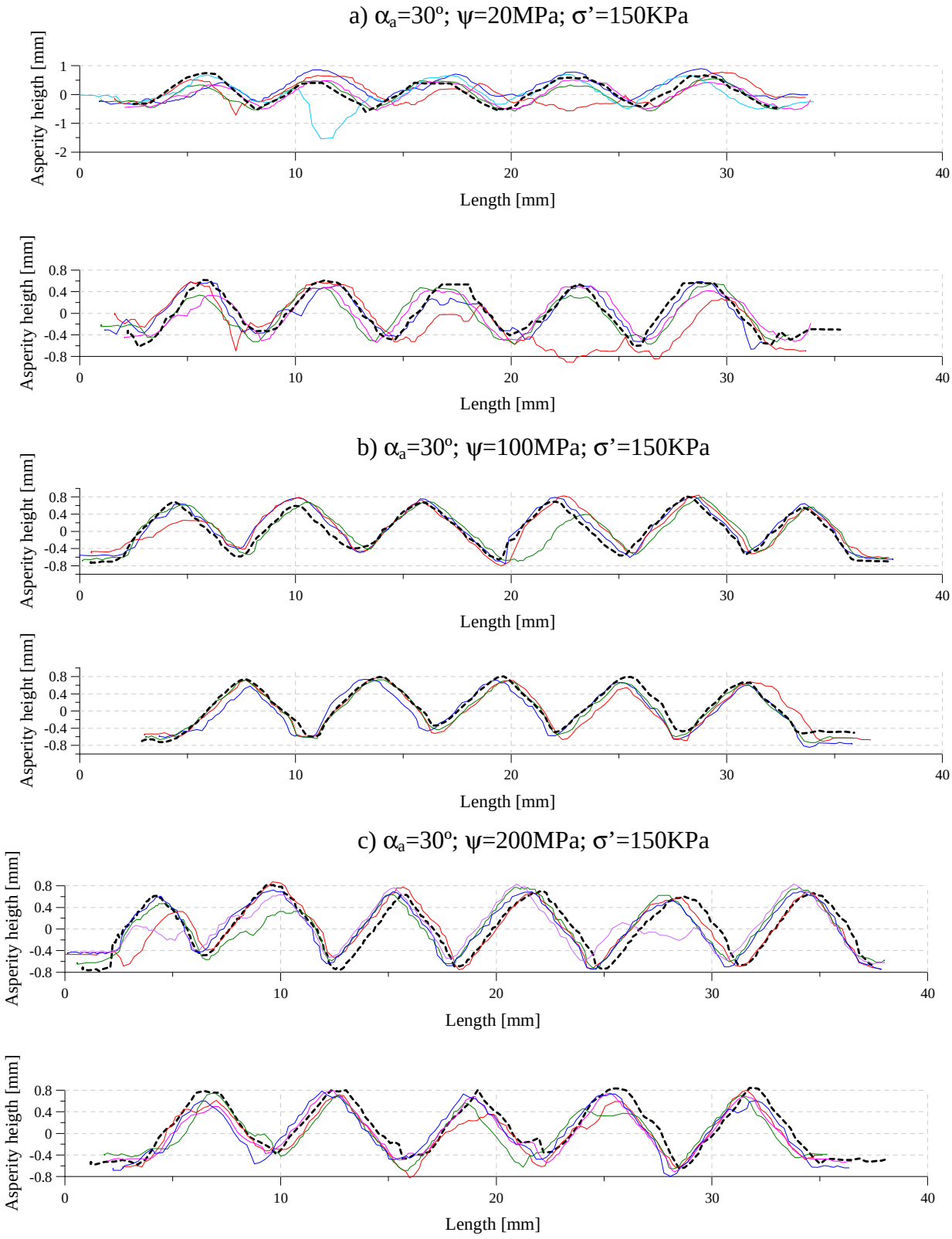

Figure 4.27: Topographical surface profile for rock joints with α_a = 30º and σ' = 150 kPa.

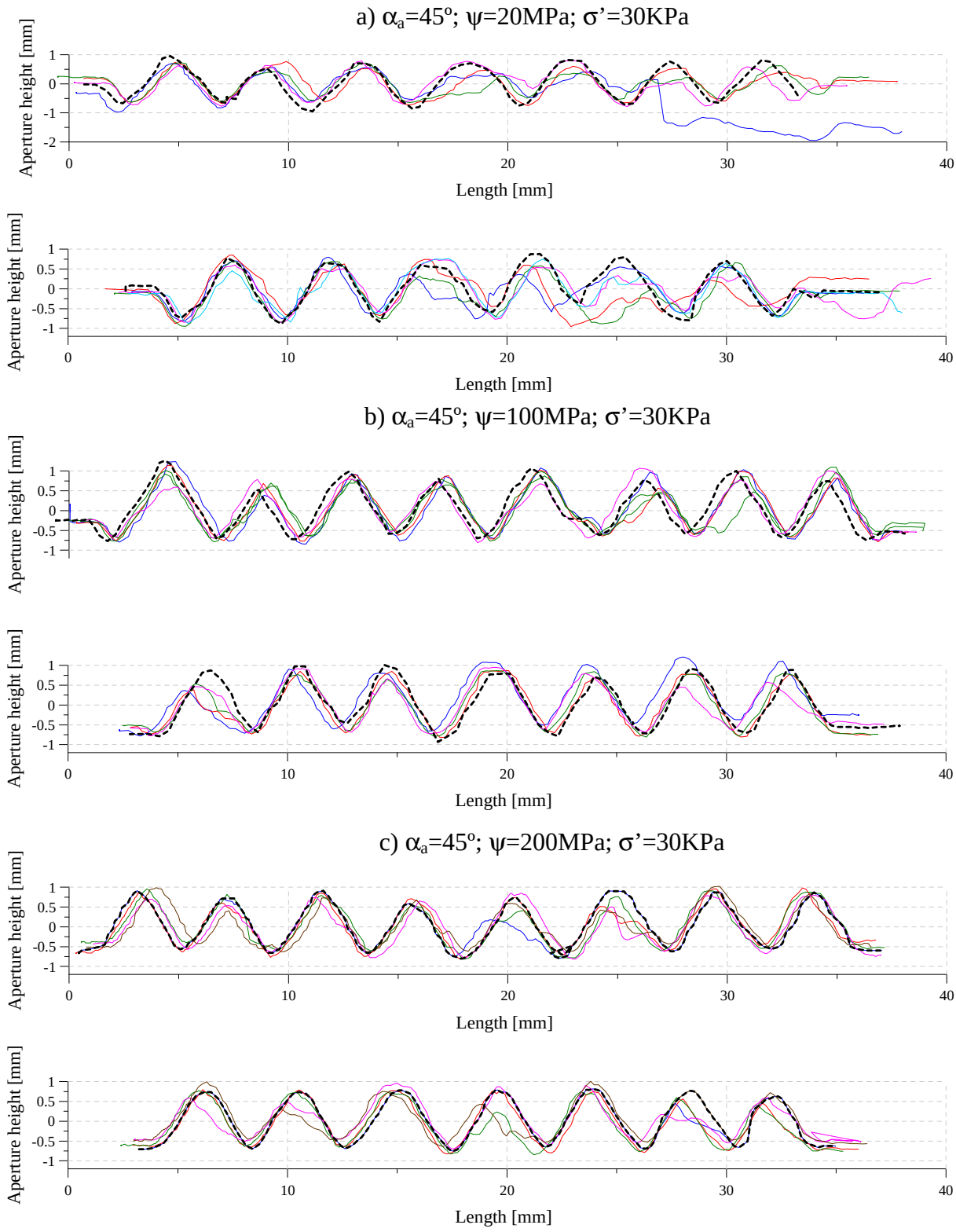

Figure 4.28: Topographical surface profile for rock joints with α_a = 45º and σ' = 30 kPa.

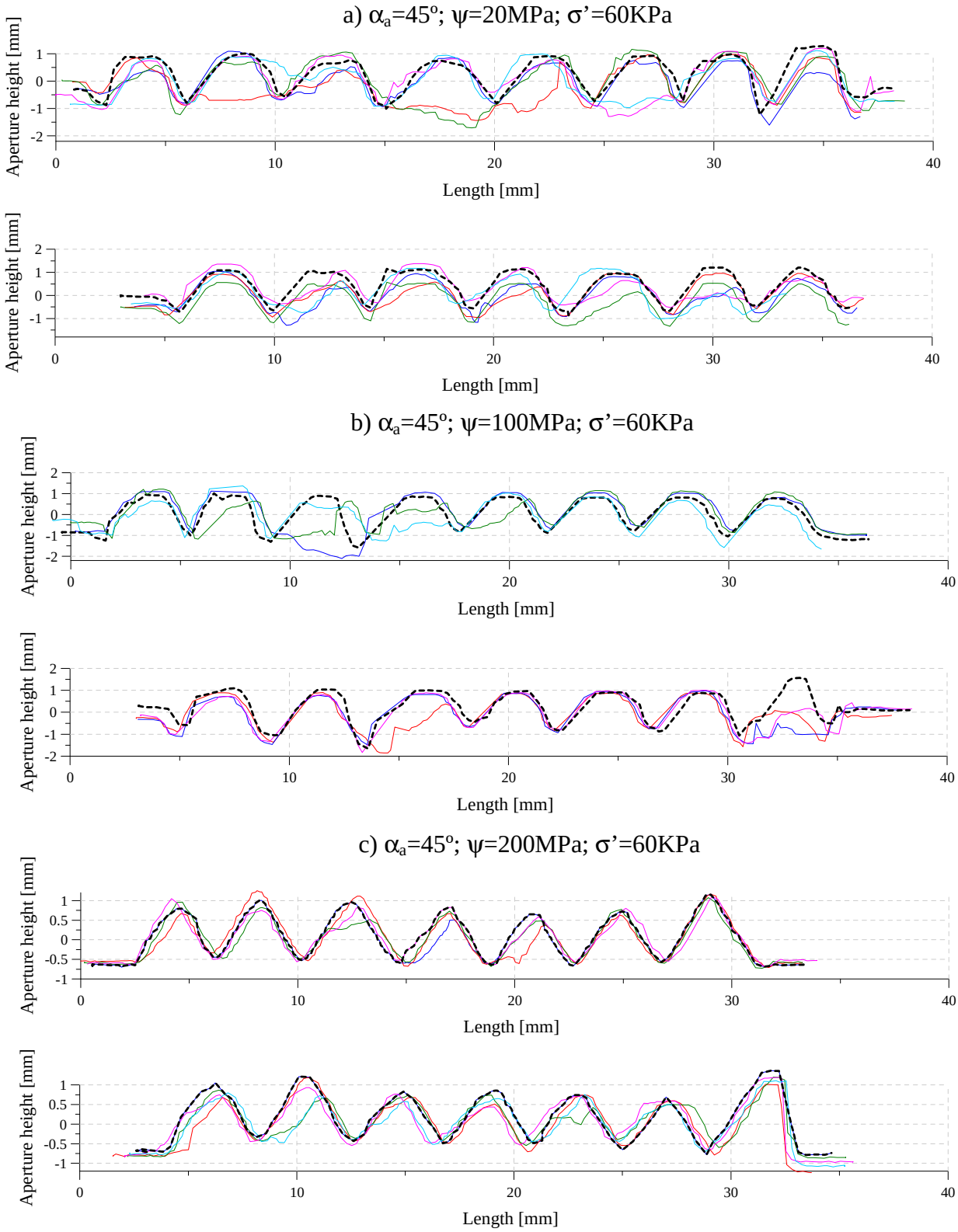

Figure 4.29: Topographical surface profile for rock joints with α_a = 45º and σ' = 60 kPa.

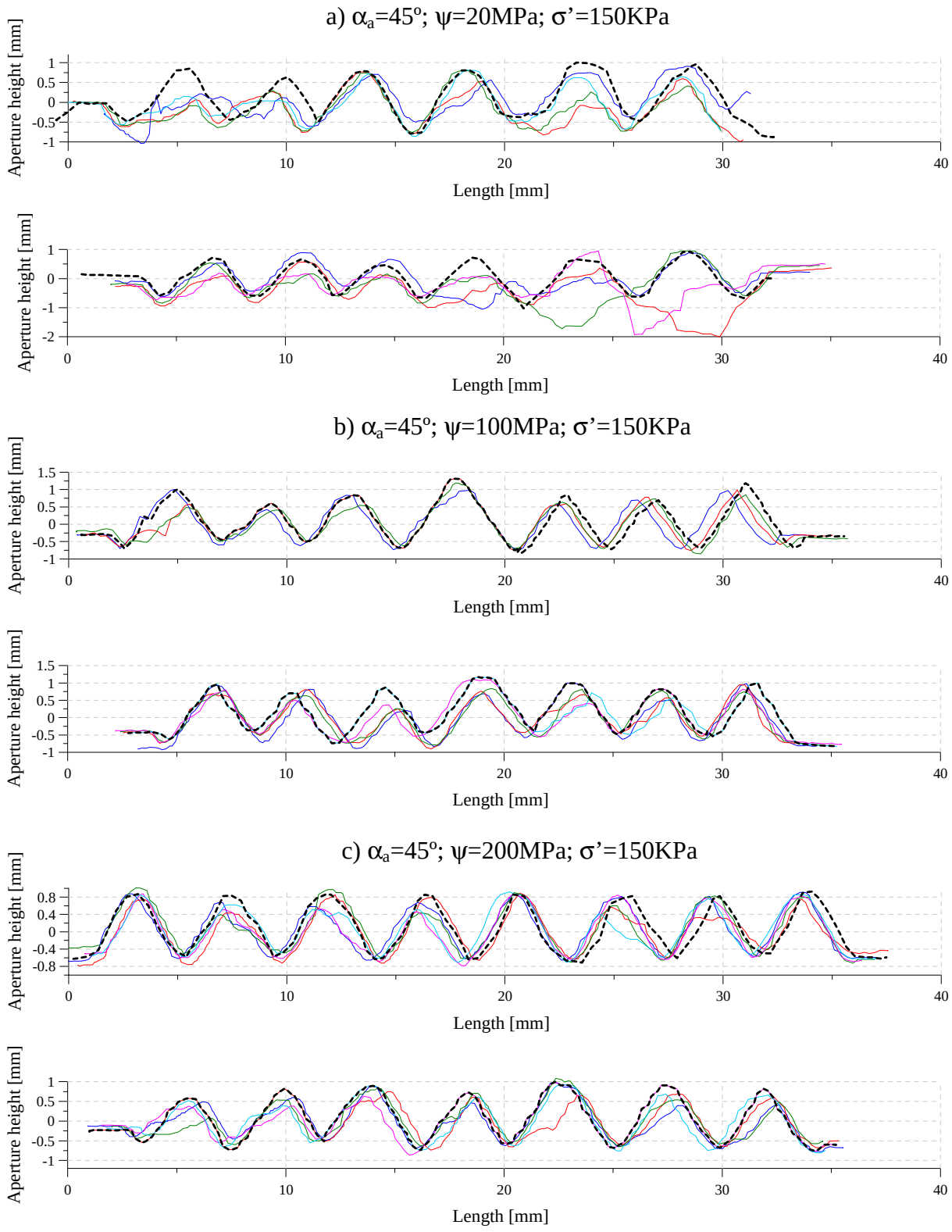

Figure 4.30: Topographical surface profile for rock joints with α_a = 45º and σ' = 150 kPa.

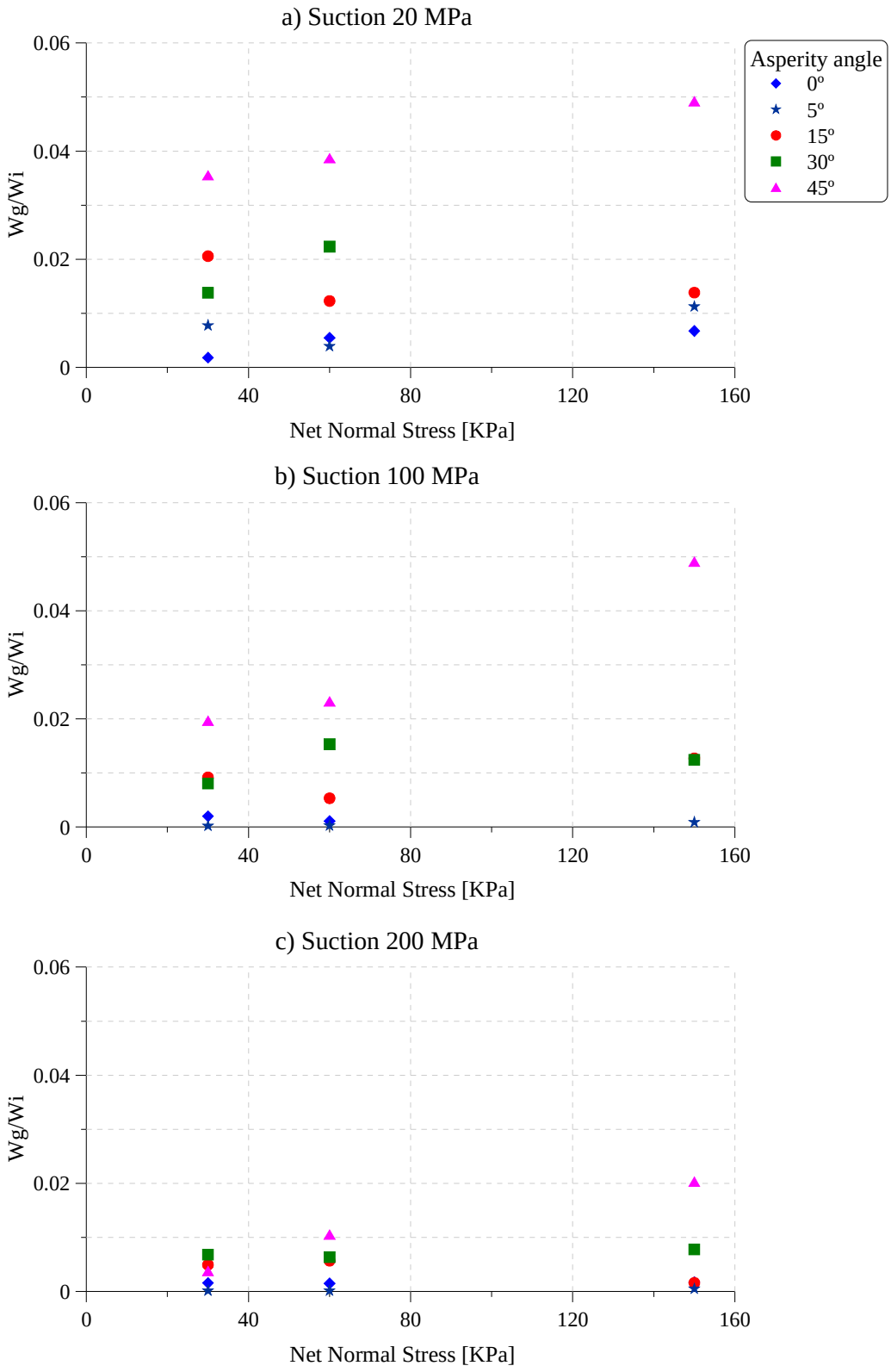

Figure 4.31. Ratio of the generated gouge weight vs. the specimen weight (Wg/Wi) with regards to initial net normal stress.

The photographs and topographical profiles show that in the case of joints with a roughness angle equal to 15º, damage is neglected. Only in the case in which suction is lower, damage can be observed, but only in a specific area, maybe a weaker zone of the rock. Nevertheless, the increase in the asperity angle causes a greater damage. In these cases, the effect of a larger normal stress and greater relative humidity can be also more noticeable, and the damage can be observed throughout the surfaces. The greatest damage occurs in the cases in which the asperity roughness angle equals 45º and suction equals 20 MPa. This phenomenon can be quantified by measuring the gouge material generated during shear testing. Figure 4.31 shows a maximum calculated Wg/Wi of 5.9% (for an asperity roughness angle equal to 45º, suction of 20 MPa and net normal stress of 150 kPa) and a minimum Wg/Wi of 0.15% (for an asperity roughness equal to 0º and 5º, suction of 200 MPa and net normal stress of 30 kPa).

Considering the comparison described above, it is possible to conclude that generally, rougher joints under a larger normal stress and larger relative humidity will show greater damage and produce more gouges. Greater damages imply minor strength and dilatancy of rock joints, which agrees with shear test results.

In Figures 4.32, 4.33 and 4.34 the damage ratio (Wg/Wi) is plotted in terms of shear work, dilatancy work and total work, respectively. In all cases, a maximum shear displacement of 2.5 mm was considered to calculate the work. Comparing figures 4.32 and 4.33 it is observed that the dilatancy work is one order of magnitude smaller than shear work. Therefore the total work is essentially the shear work. In order to determine a relationship between joint damage and the work applied to the joint during shearing, the ratio Wg/Wi is plotted against total work (shear plus volumetric) in Figure 4.34. The plot shows that suction is also a controlling factor not fully accounted for by the work. The trend lines plotted in the figure (dash blue, green and red line) indicate that the degradation of joints increased with the work exerted, in all cases. In addition, the higher the suction, for a given value of total work, the lower the joint degradation.

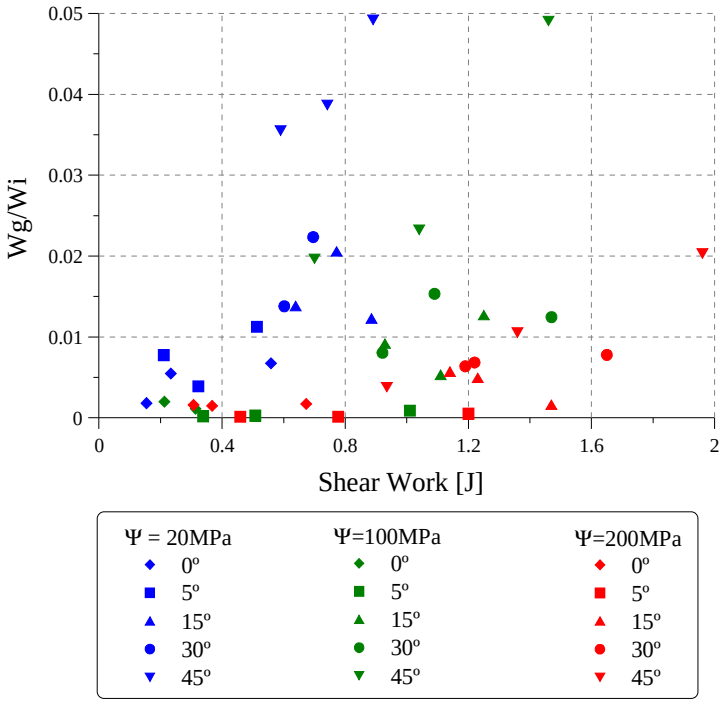

Figure 4.32. Wg/Wi against shear work.

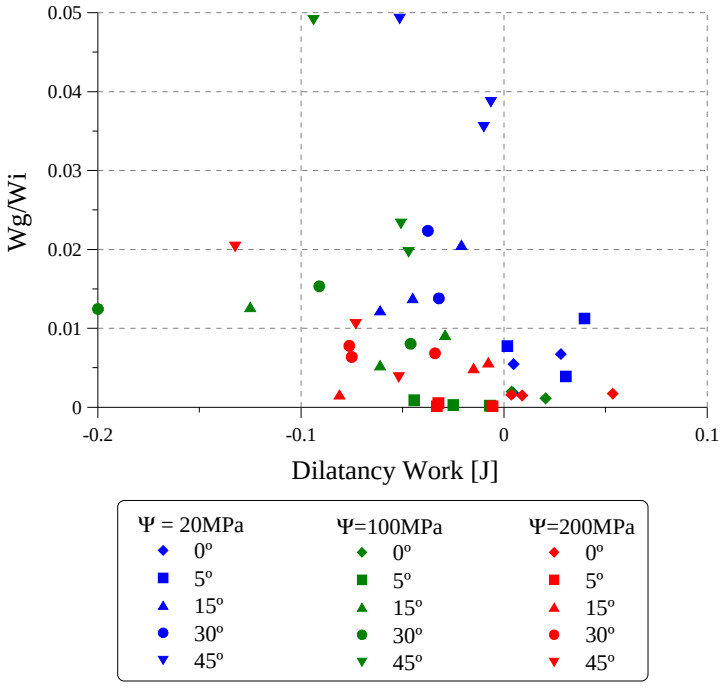

Figure 4.33. Wg/Wi against dilatancy work. Negative values correspond to dilatant behaviour and positive to contractant behaviour.

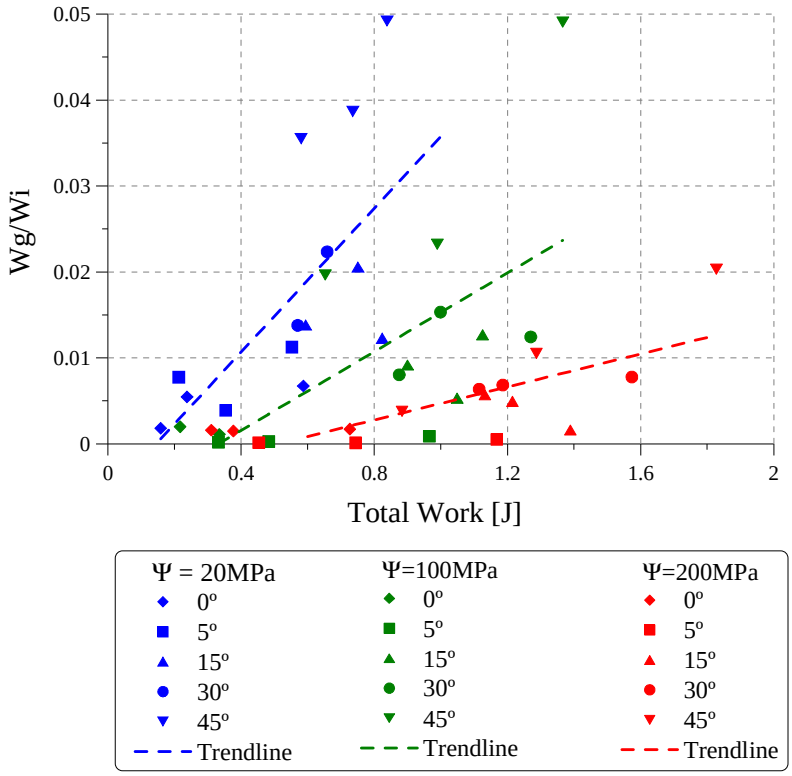

Figure 4.34. Relationship between Wg/Wi, total work and suction

4.7. Concluding remarks

A direct shear device was successfully adapted to test rock joints controlling the relative humidity of the specimens. Modifications included the addition of a vapour circulation system and the improvement of data acquisition by incorporating an analogue data acquisition device. The vapour circulation system allows studying the influence of suction on the mechanical behaviour of joints.

The carving process adopted to construct different roughness angles allowed exploring its effects on shear strength and dilatancy of joints.

The shear test results obtained not only showed the well-known dependency of shear strength on net normal stress, but also a marked dependency on suction and roughness. A decrease on shear strength and dilatancy was observed when inducing a decrease on suction (increment of RH ≅

86%). Furthermore, it was concluded that greater roughness implies greater shear strength. However, the comparison of the offset values of displacement, at which residual shear strength is reached, led to believe that the rougher the asperity, the smaller the values of shear displacement. This means, that a rougher joint implies a more brittle behaviour. This brittle behaviour causes higher damage on the joint surfaces. The amount of damage increase as α_a increase. In addition damage extent to a larger proportion of joint area. As a result of this extended damage, dilatancy is reduced in rougher surfaces.

The profilometry profiles plotted and the measurement of gouge material confirmed that the higher normal stresses higher relative humidity of rock joints and rougher asperities cause greater damage on joint surfaces. This translates in a maximum of Wg/Wi = 5.9% (for an asperity roughness angle of 45º, suction of 20 MPa and net normal stress of 150 kPa) and a minimum of Wg/Wi = 0.15% (for an asperity roughness angle of 0º, suction of 200MPa and net normal stress of 30kPa).

It was also concluded that the degradation of joints increased with the work in all cases. Nevertheless, the higher the suction, for a given value of total work, the lower the joint degradation

CHAPTER 5

Numerical modelling of rock joints considering suction and asperity roughness angle

5.1. Introduction

This chapter presents an analysis of the experimental results described in Chapter 4. Tests showed a significant effect of suction on peak shear strength conditions. Also, the degradation of asperities would differ depending on suction and on the geometrical angle of the joint.

The asymptotes of the experimental failure surfaces were determined, and their strength parameters calculated. Then it was possible to define mathematical expressions that consider the variation of cohesion and the tangent of the initial friction angle with suction and asperity roughness angle. These expressions were implemented in the visco-plastic constitutive law described in Chapter 3 and a simulation of the tests was performed.

Likewise it was necessary to redefine the model parameters that control the dilatancy of the model to better reproduce the test results.

The following sections described the analysis of the experimental results obtained. An explanation of the new expression for the strength is given. Fitting the new data requires also a new formulation of the dilatancy law. Finally the numerical simulation of the tests is compared with the experimental data.

5.2. Formulation of constitutive equations

In order to include the measured influence of suction and asperity roughness angle on strength parameters of the yield surface presented in Chapter 3, it was necessary to further analyse the test results.

5.2.1 Strength parameters

This analysis consists in calculating the asymptotic curves to yield surfaces from tests results. The asymptote for each suction and asperity roughness angle was obtained by plotting the maximum shear stress measured in the tests with respect to the net normal stress (see Fig. 5.1). Then, the initial effective cohesion (c'_0) and the tangent of the internal friction effective initial angle ($\tan\Phi'_0$) were calculated for each tangent curve. The values of maximum shear stress measured for the test and the resistance parameters of the yield surfaces were summarized in Table 5.1.

Values of effective cohesion and the values of the tangent of the internal friction effective angle were plotted with respect to the asperity roughness angle (α_a) and to suction to clarify the influence of these variables on the yield surface parameters (see Fig. 5.2a and b). Figure 5.2a shows minimum values of cohesion for $\alpha_a = 0^o$. It increases sharp up to $\alpha_a = 15^o$, and then it remains constant for the remaining asperities roughness angles. Figure 5.2b also shows that cohesion increases proportionally with suction. Therefore, the expression adopted to mathematically express the influence of suction and the asperity roughness angle is:

$$c'_{0(\Psi,\alpha_a)} = \left(c_0 + c_1\psi\right) + \left(b_0 + b_1\Psi\right)\left(1 - e^{-b_2 \tan\alpha_a}\right) \qquad 5.1$$

where $c'_{0\ (s,\alpha a)}$ is the effective initial cohesion that changes whith suction and the asperity roughness angle; ψ is the total suction; c_0 is the value of cohesion for a value of suction equal to zero and a value of $\alpha_a = 0^o$; c_1 is the slope of the cohesion-suction fit line for $\alpha_a = 0^o$; b_0 is an average value of cohesion for $\alpha_a = 15^o$, 30^o and 45^o and b_1 is a parameter of the model that controls the increment of cohesion with suction for $\alpha_a = 15^o$, 30^o and 45^o. The term

$\left(1-e^{-b_2 \tan\alpha_a}\right)$ controls the sharp increment of cohesion with α_a, and b_2 is a parameter that controls the shape of the cohesion-α_a curve.

Figure 5.3a and b presents the variation of $\tan\Phi'_0$ with α_a and suction respectively. Both curves show the $\tan\Phi'_0$ increase with α_a and suction. The equation proposed to calculate $\tan\Phi'_0$ is:

$$\tan\phi'_{0(\psi,\alpha_a)} = \left(t_0 + t_1\psi\right) + \left(d_0 + d_1\psi\right)\tan\alpha_a \qquad 5.2$$

where $\tan\Phi'_{0(\psi,\alpha a)}$ is the tangent of the internal friction effective initial angle that depends of suction and the asperity roughness angle; ψ is the total suction; t_0 is the value of $\tan\Phi'_0$ for $\psi = 0$ and $\alpha_a = 0^o$; t_1 is the slope of the $\tan\Phi'_0$-ψ fit line for $\alpha_a = 0^o$; d_0 and d_1 are model parameters that control the increment of $\tan\Phi'_0$ with suction for α_a = 5º, 15º, 30º and 45º, and $\tan\alpha_a$ is the geometric tangent of the asperity roughness angle.

Figures 5.2 and 4.3 present the fit of $c'_{0\,(\psi,\alpha a)}$ and $\tan\Phi'_{0(\psi,\,\alpha a)}$ with the equations proposed above. The values of the parameters are listed in Table 5.2.

Table 5.1: Summary of peak shear stress and resistance parameters of yield surfaces.

Asperity Roughness Angle 0º				
Suction 200MPa				
Net normal stress σ'[MPa]	Peak shear stress τ[KPa]	Initial effective cohesion c'_0[KPa]	Initial effective tangent of internal friction angle $\tan\Phi'_0$	Initial internal friction angle Φ'_0 [º]
30	77.24	58.69	0.69	34.61
60	103.31			
150	161.98			
Suction 100MPa				
30	57.03	28.42	0.84	40.03
60	73.98			
150	155.13			
Suction 20MPa				
30	37.80	9.22	0.86	40.70
60	57.36			
150	139.49			

Asperity Roughness Angle 5º				
Suction 200MPa				
Net normal stress σ'[MPa]	Peak shear stress τ[KPa]	Initial effective cohesion c'_0[KPa]	Initial effective tangent of internal friction angle $\tan\Phi'_0$	Initial internal friction angle Φ'_0 [º]
30	142.43	128.69	1.30	52.43
60	240.52			
150	315.49			
Suction 100MPa				
30	105.15	75.00	1.02	45.56
60	136.88			
150	264.65			
Suction 20MPa				
30	52.15	56.00	0.90	41.98
60	118.07			
150	211.25			

Asperity Roughness Angle 15º				
Suction 200MPa				
Net normal stress σ' [MPa]	Peak shear stress τ [KPa]	Initial effective cohesion c'_0[KPa]	Initial effective tangent of internal friction angle $\tan\Phi'_0$	Initial internal friction angle Φ'_0 [º]
30	376.46	307.60	1.81	61.08
60	396.90			
150	584.04			
Suction 100MPa				
30	274.79	225.0	1.10	47.72
60	314.74			
150	385.88			
Suction 20MPa				
30	243.34	184.00	0.90	41.98
60	216.09			
150	308.64			

Asperity Roughness Angle 30º				
Suction 200MPa				
Net normal stress σ' [MPa]	Peak shear stress τ[KPa]	Initial effective cohesion c'_0[KPa]	Initial effective tangent of internal friction angle $\tan\Phi'_0$	Initial internal friction angle Φ'_0 [º]
30	357.76	292.85	1.79	60.81
60	368.65			
150	565.14			
Suction 100MPa				
30	289.49	237.27	1.27	51.78
60	294.69			
150	432.55			
Suction 20MPa				
30	191.21	159.28	0.91	42.30
60	207.41			
150	296.91			

Asperity Roughness Angle 45º				
Suction 200MPa				
Net normal stress σ'[MPa]	Peak shear stress τ [KPa]	Initial effective cohesion c'_0[KPa]	Initial effective tangent of internal friction angle $\tan\Phi'_0$	Initial internal friction angle Φ'_0 [º]
30	288.43	296.00	2.40	67.38
60	465.28			
150	707.24			
Suction 100MPa				
30	256.50	244.38	1.39	54.27
60	366.87			
150	442.52			
Suction 20MPa				
30	203.37	168.00	0.90	41.98
60	216.41			
150	279.53			

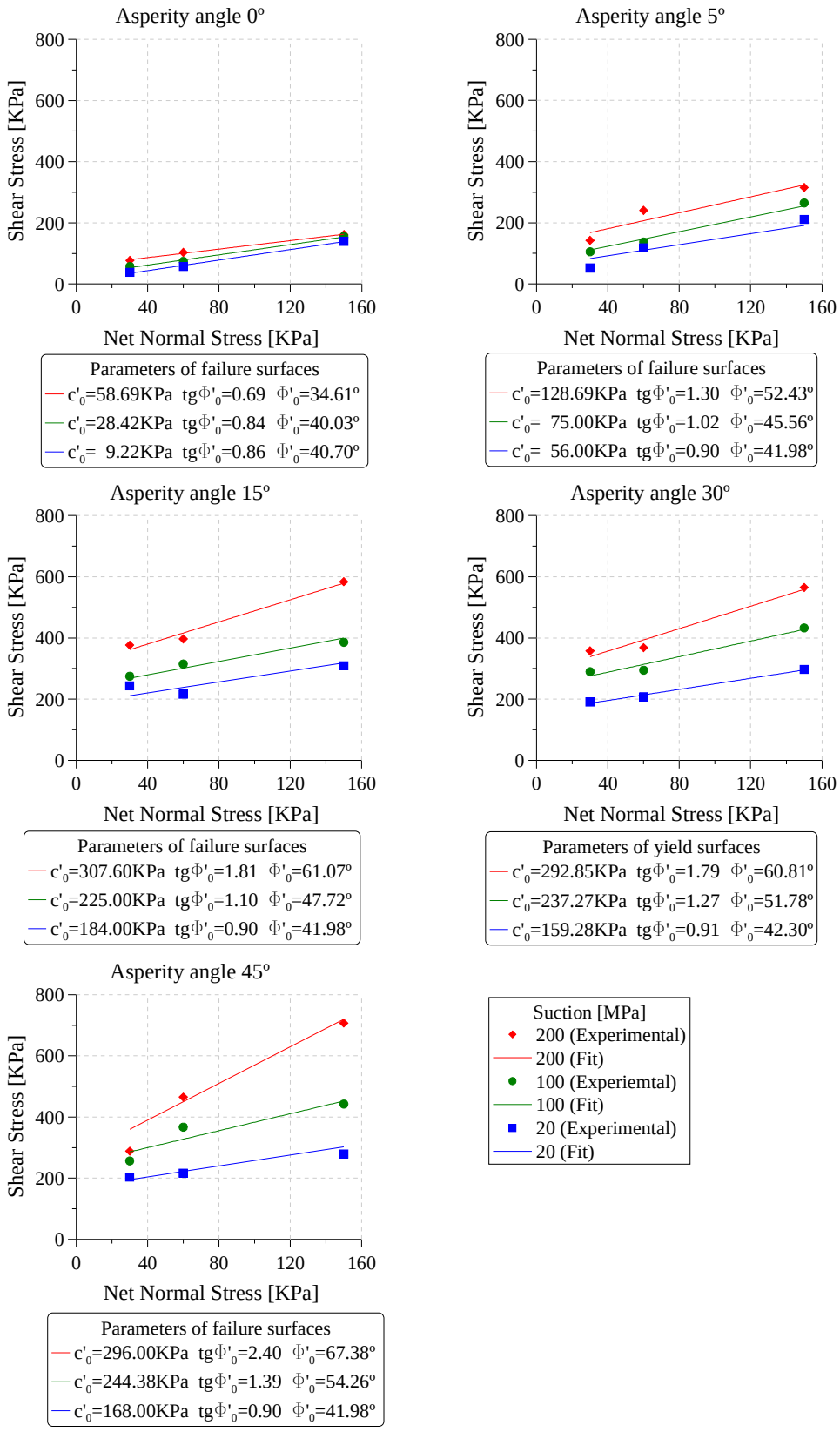

Figure 5.1: Peak shear stress vs. Net normal stresses. Strength parameters of the asymptote to failure surfaces considering the asperity roughness and the values of suction.

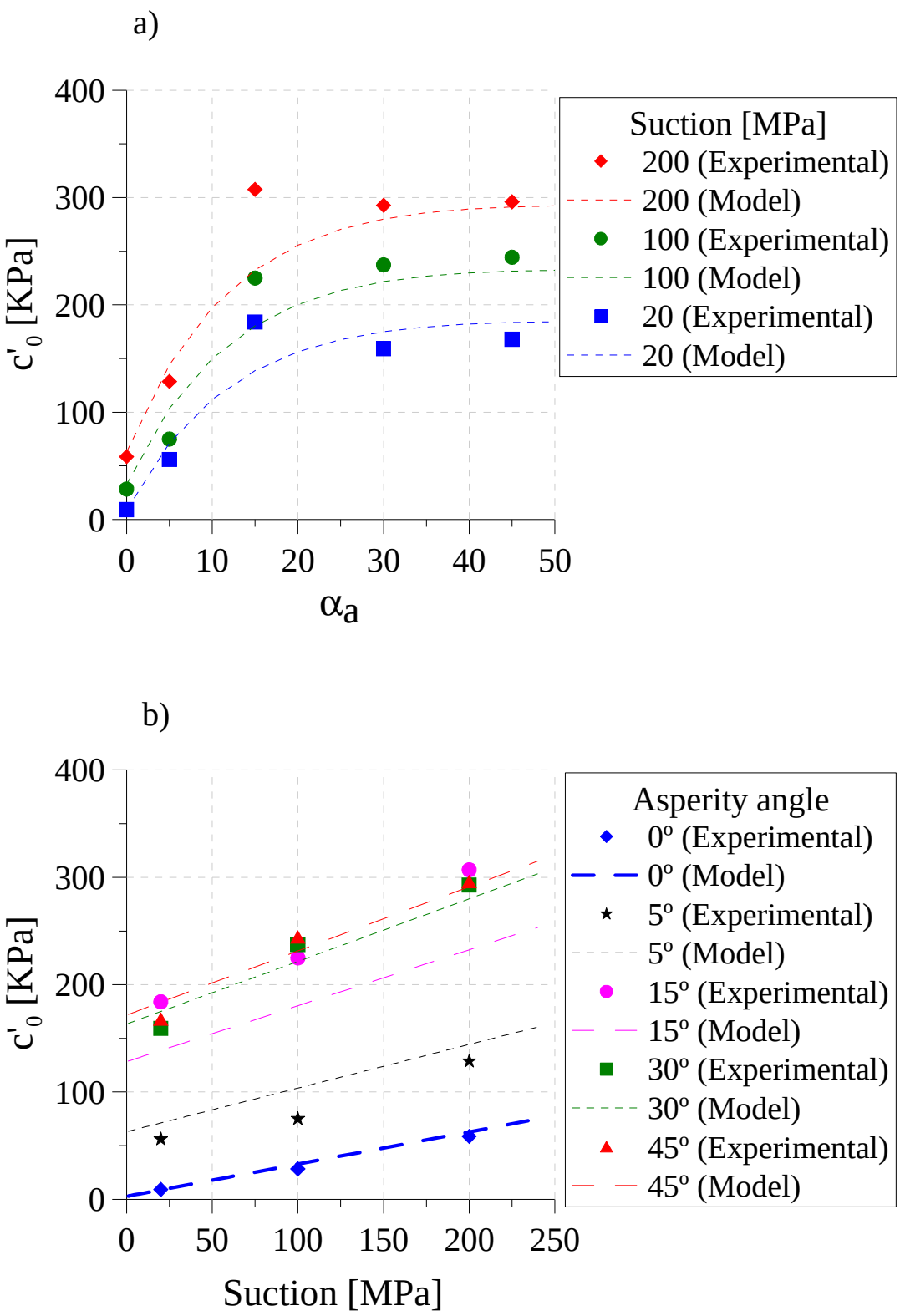

Figure 5.2 a) Effective cohesion vs. α_a and b) Effective cohesion vs. suction

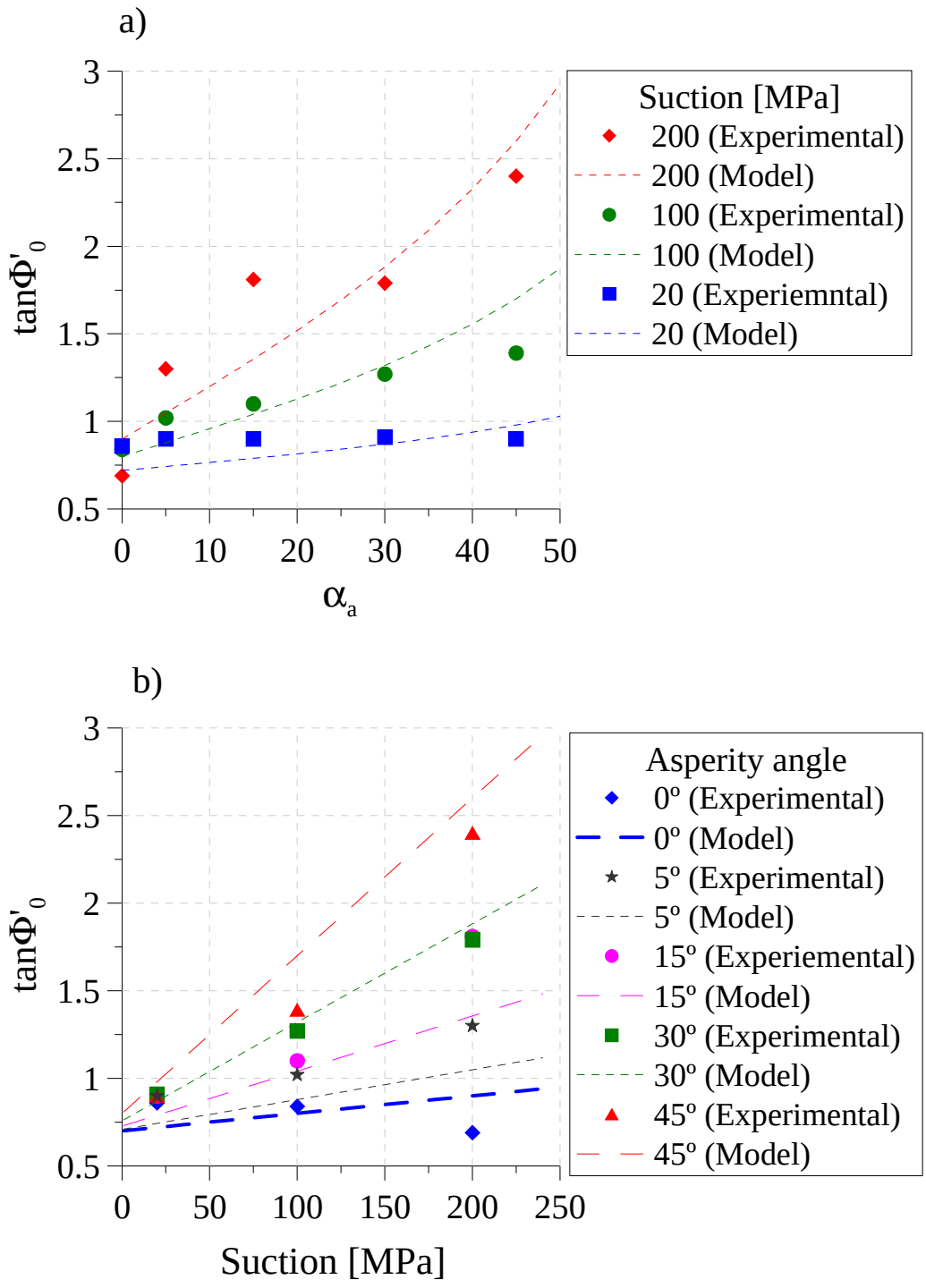

Figure 5.3 a) Effective tangent of the internal friction angle vs. α_a and b) Effective tangent of the internal friction angle vs. suction

Table 5.2: Parameters used to adjust the variation of $c_0'_{(\alpha a,s)}$ and tg $\Phi_{0\ (\alpha a,s)}$ with the asperity roughness angle and suction.

Parameter	Value
c_0	2.8 kPa
c_1	0.3
b_0	170.0 kPa
b_1	0.3
b_2	5.0
t_0	0.7
t_1	0.001
d_0	0.2
d_1	0.008

5.2.2. Dilatancy parameters

As it was mentioned in Chapter 3, the dilatant behaviour is considered using two model parameters, f_σ^{dil} and f_c^{dil}, that result in a non-associated rule. Parameter f_σ^{dil} is a function that controls the decrease of dilatancy considering that a compression stress, q_u, results in zero dilatancy. f_c^{dil} is proportional to the effective cohesion degradation. Moreover, in this case it was necessary to incorporate the asperity roughness angle and suction in both parameters to better reproduce the dilatant behaviour recorded in the tests. The following expressions were proposed:

$$f_\sigma^{dil} = \chi_d \sqrt{\tan \alpha_a} \left(1 - \frac{|\sigma'|}{q_u}\right) \exp\left(-\beta_d \frac{\sigma'}{q_u}\right) \quad 5.3$$

$$f_c^{dil} = \frac{c'_{(\psi,\alpha_a)}}{c'_{0(\psi,\alpha_a)}} \quad 5.4$$

where α_a is the asperity roughness angle; q_u is the uniaxial compression strength, and χ_d and β_d are model parameters.

5.3. Numerical simulation of rock joints under shear loads with suction control

The monotonic shear behaviour of rock joints were simulated using the expressions of the resistance parameters proposed above. These expressions were included in the constitutive law of the interface element implemented in Code_Bright (Ch. 3).

The geometry of the model is shown in Figure 5.2. The rock was considered as an elastic material and the joint as a viscoplastic interface element. The joint is discretised using 10 elements (red lines in the figure). The rate of displacement used in the test (0.05 mm/min) is applied to boundaries AC and BD. Boundaries EG and FH are horizontally fixed, while boundary GH is vertically fixed. The net normal stresses used in the test (30, 60 and 150 MPa) are applied to boundary AB. The initial stress is equal to 0.1 MPa and the initial liquid pressure is −20, −100 and −200 MPa, with respect to each test suction.

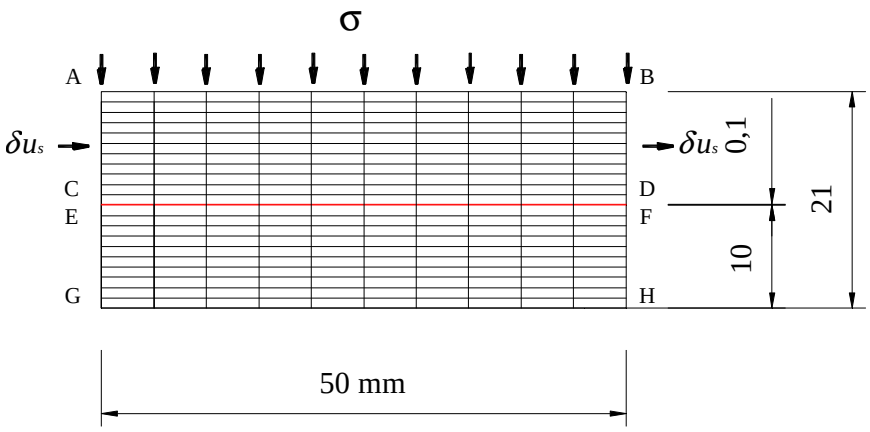

Figure 5.2: Geometry of the simple test model.

All simulations were performed using the same parameters, except for the critical values of shear displacements u^*_c and u^*_Φ that changed according to the strength softening of the shear stress and dilatancy of the joints. The parameters are listed in Tables 5.3 and 5.4.

The predictions of the numerical analysis are plotted alongside test measurements in Figures 5.5 to 5.9 for α_a = 0º, 5º, 15º, 30º and 45º respectively. In general the shear stress- shear displacement relation is well predicted, using the model proposed. Although it is not possible to

simulate the contractant behaviour of the flat joint, dilatancy could be reduced to zero by incorporating in Equation 5.3 the term $\sqrt{\tan \alpha_a}$, which considers the geometry of the joint. It was also necessary to calibrate parameters χ_d and β_d.

Table 5.3: Parameters of the materials.

Rock Matrix

Mechanical Properties	**Value**	**Unit**
Young's modulus [E]	27000	MPa
Poisson's ratio [υ]	0.29	

Joint Rock

Mechanical Properties	**Value**	**Unit**
Initial normal stiffness parameter [m]	100	MPa
Tangential stiffness [K_s]	500	MPa/m
Initial friction angle [Φ_0]	35º	
Residual friction angle [Φ_{res}]	8º	
Initial opening [a_0]	0.1	mm
Minimum opening [a_{min}]	0.01	mm
Viscosity [γ]	1×10^{-2}	s^{-1}
Stress power [N]	2.0	
Uniaxial compressive strength [q_u]	20	MPa
Model parameter [χ_d]	0.3	
Model parameter [β_d]	100	

Table 5.4: Parameters of the softening law used for different asperity roughness angles.

	0º	5º	15º	30º	45º
u^*_c [m]	1.0×10^{-2}	8.0×10^{-3}	8.0×10^{-3}	3.5×10^{-3}	2.0×10^{-3}
u^*_Φ [m]	1.5×10^{-2}	8.5×10^{-3}	8.5×10^{-2}	4.0×10^{-3}	2.5×10^{-3}

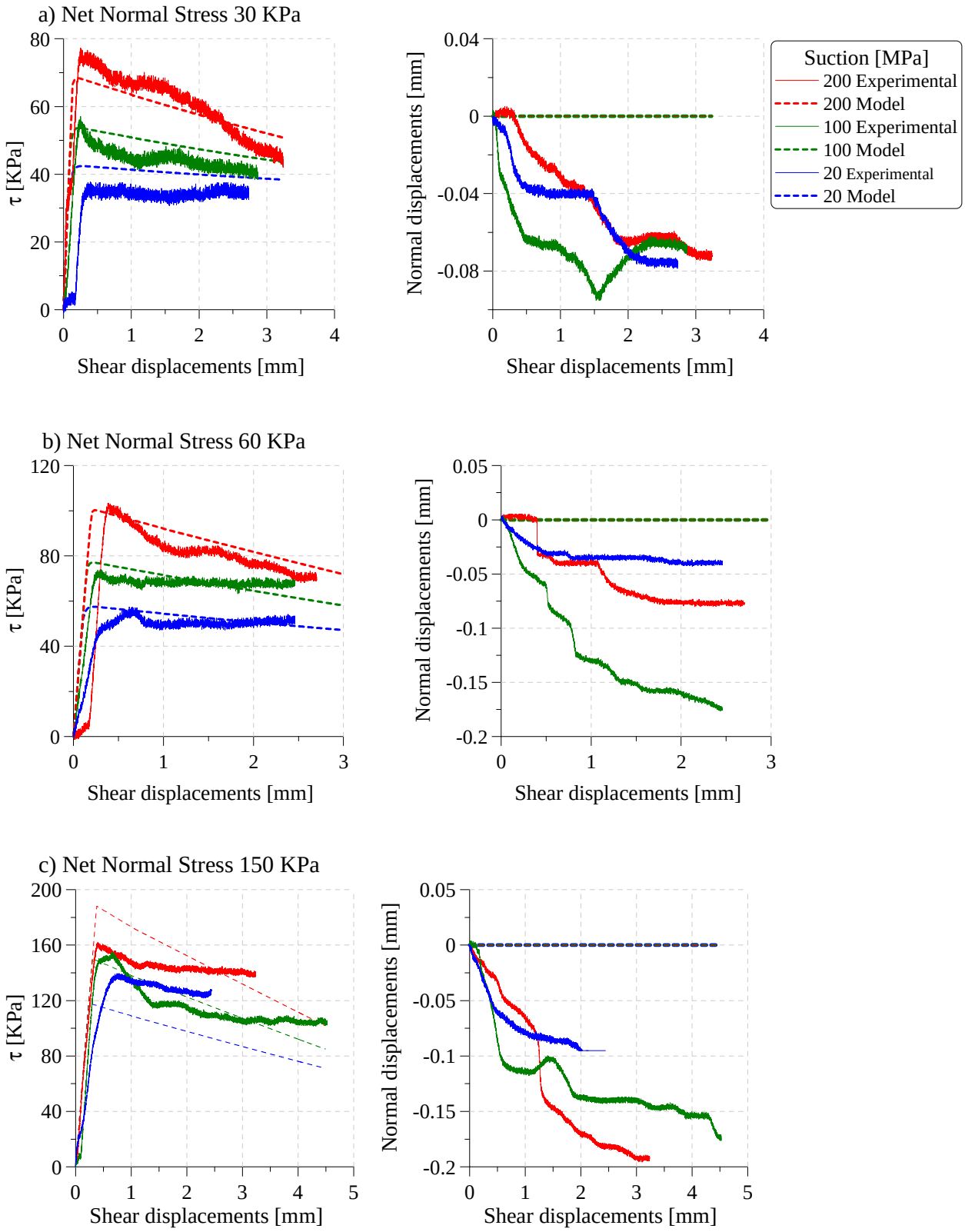

Figure 5.5: Comparison of shear stress vs. shear displacements and normal displacements vs. shear displacements from the experimental tests and simulation results (α_a = 0º).

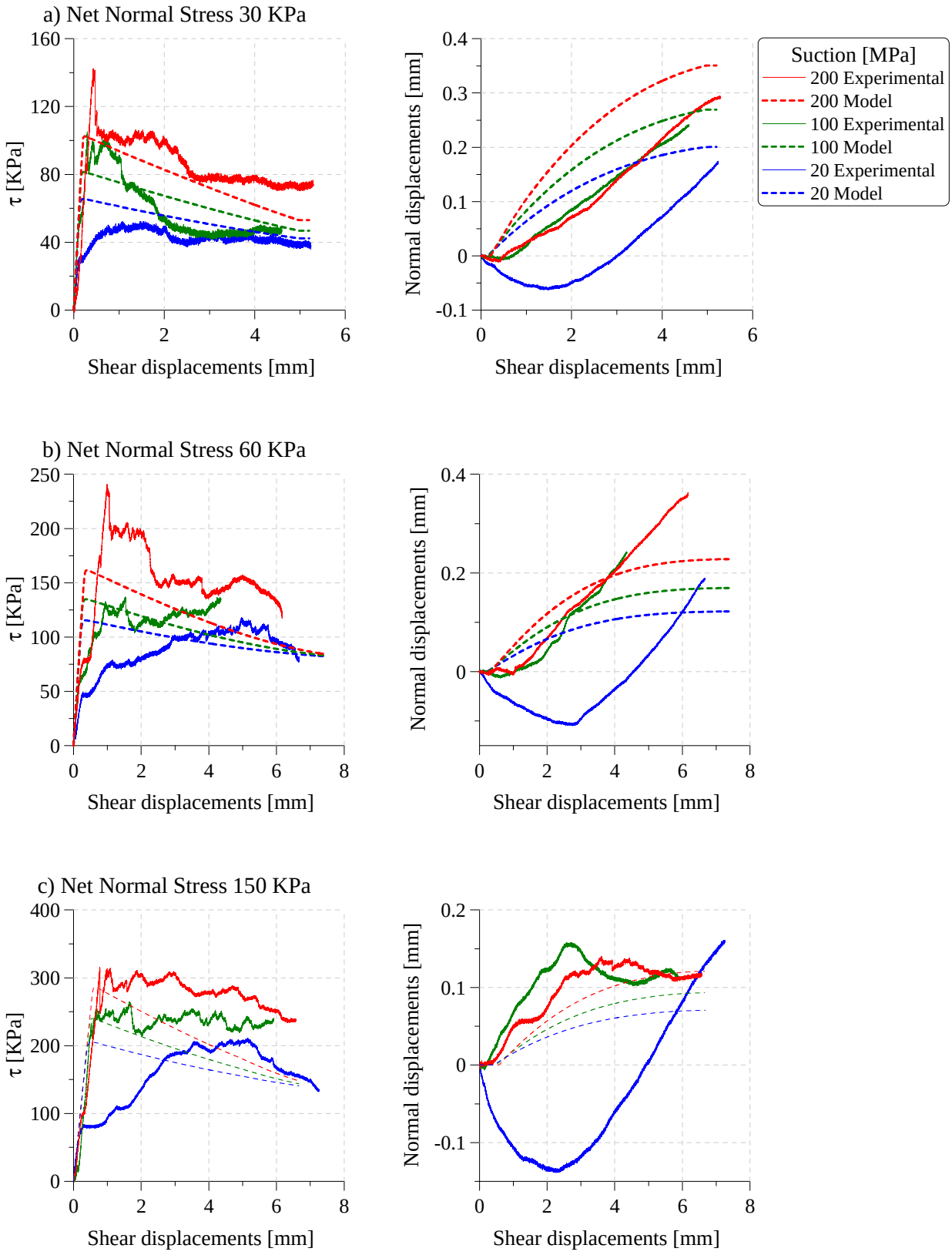

Figure 5.6: Comparison of shear stress vs. shear displacements and normal displacements vs. shear displacements from experimental tests and simulation results (α_a = 5º).

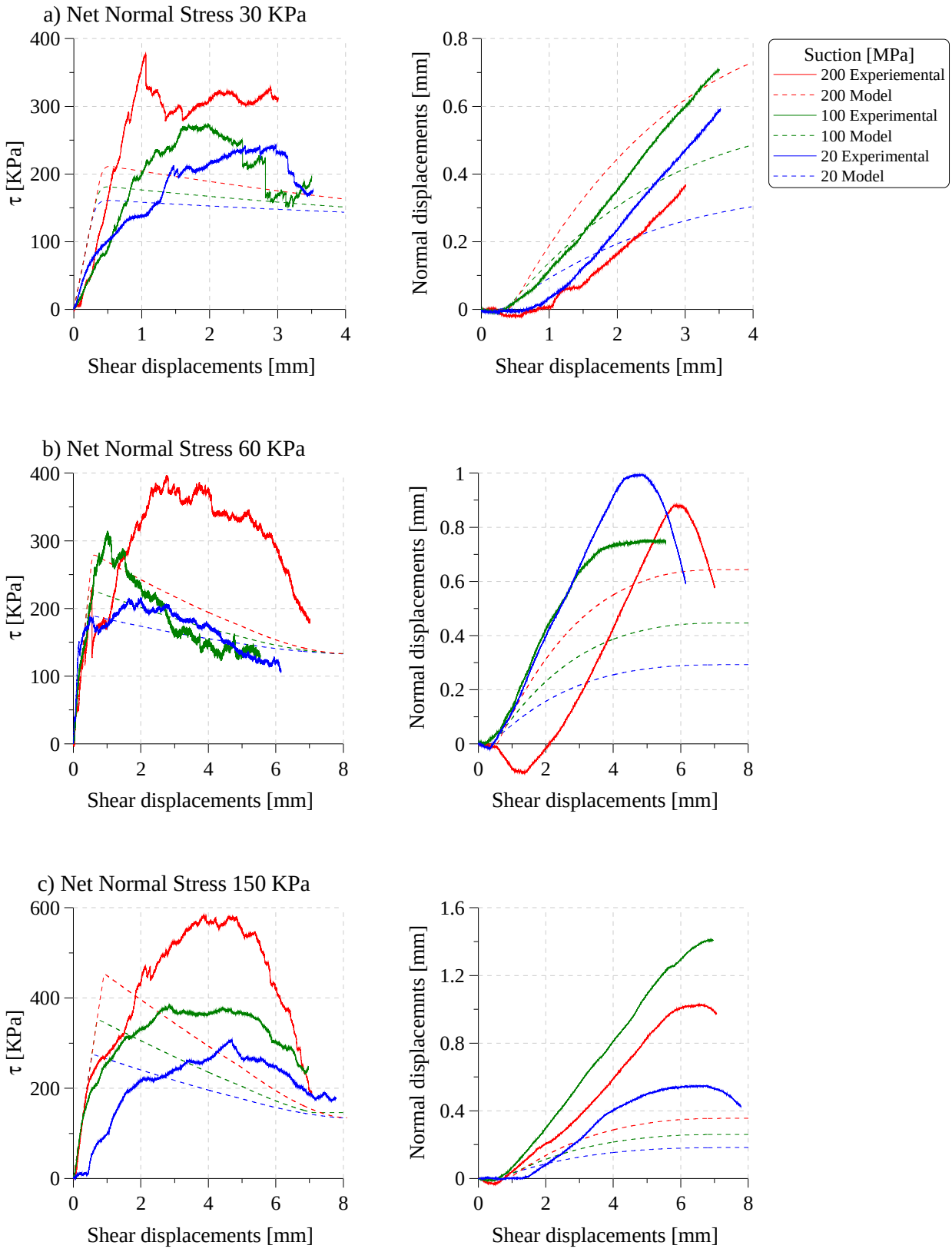

Figure 5.7: Comparison of shear stress vs. shear displacements and normal displacements vs. shear displacements from experimental tests and simulation results (α_a = 15º).

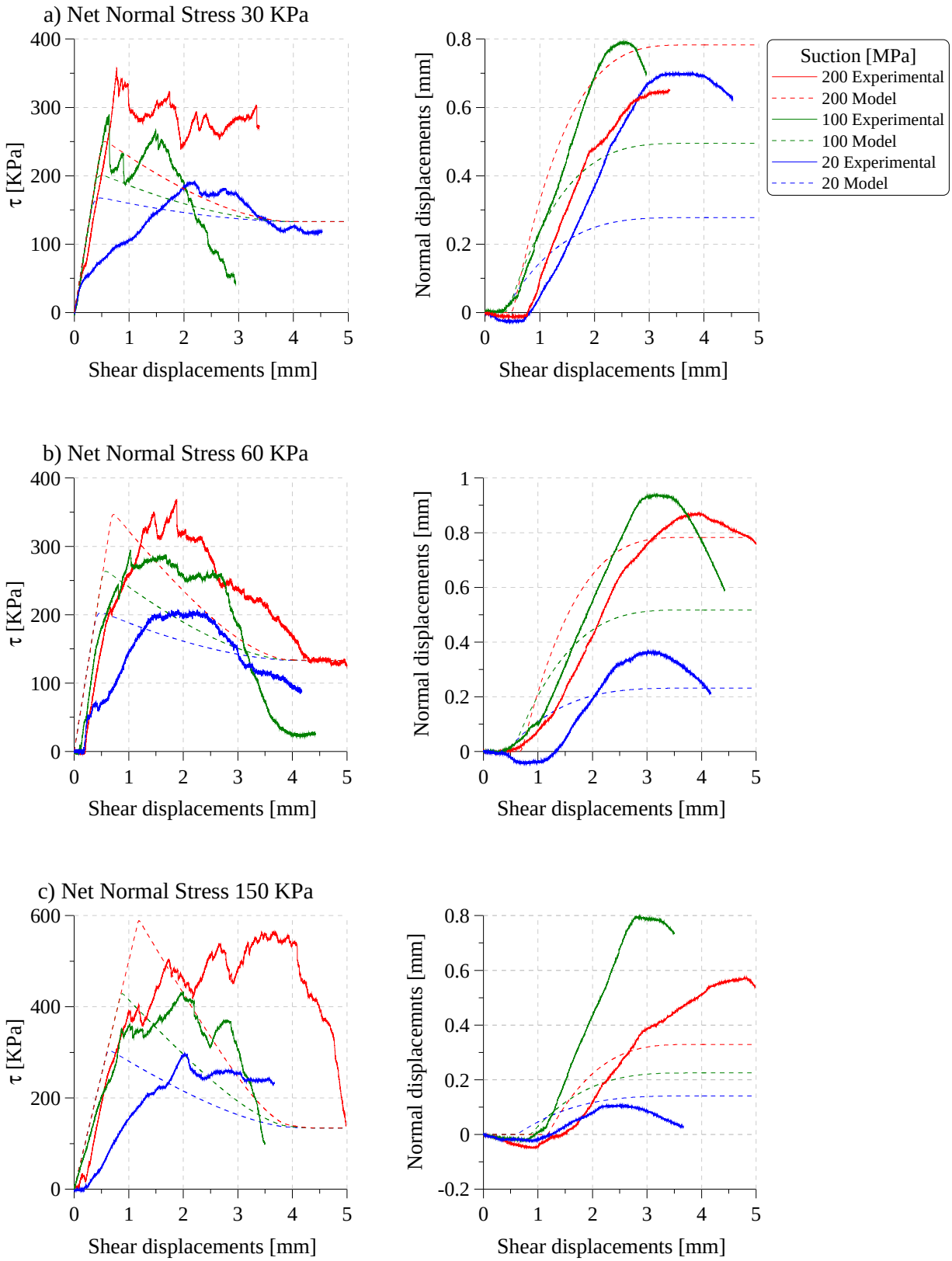

Figure 5.8: Comparison of shear stress vs. shear displacements and normal displacements vs. shear displacements from experimental tests and simulation results ($\alpha_a = 30^o$).

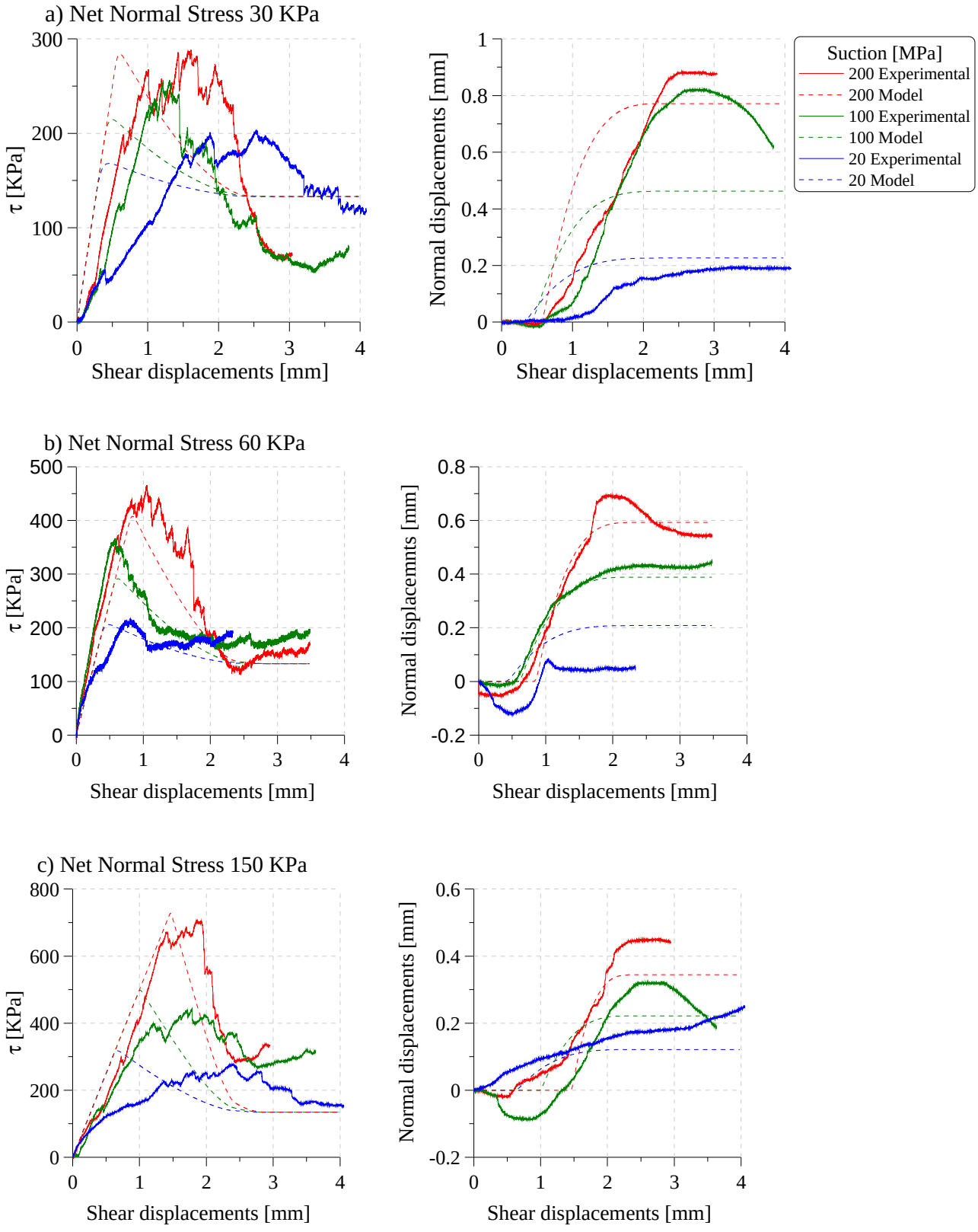

Figure 5.9: Comparison of shear stress vs. shear displacements and normal displacements vs. shear displacements from experimental tests and simulation results ($\alpha_a = 45^o$).

5.4. Concluding remarks

New mathematical expressions are proposed for the strength parameters (initial effective cohesion (c_0') and initial effective tangent of the internal friction angle (tanΦ'_0) of the yield surface asymptote). These expressions consider the effects of suction and the asperity roughness angle on strength parameters. The dilatancy parameters were also modified taking into account suction and the asperity roughness angle. Both modifications were introduced in the constitutive law of the interface element implemented in Code_Bright.

The results from the numerical simulation closely reproduce the experimental features of rock joints. The shear stress-shear displacements evolution is well predicted and the dilatancy trend is captured.

CHAPTER 6

Application of Interface Elements in a Thermo-Hydro-Mechanical model of a nuclear waste geological repository

6.1. Introduction

The Canister Retrieval Test (CRT) was performed to demonstrate the capability to retrieve deposited nuclear waste if a better disposal solution is found. The overall objective of the CRT was to demonstrate to specialists and to the general public that retrieving the canisters is technically feasible at any stage of the operating phase.

The CRT experiment was also used to carefully record THM processes in the Swedish KBS-3V deposit technique, besides proving the possibility of retrieving the canisters. This makes it very suitable for modellers to investigate theories, used in their simulations, since the calculated results can be checked against experimental data.

This experiment was numerically modelled within the European Project entitled “Coupled Thermo-Hydrological-Mechanical-Chemical Processes For Application In Repository Safety Assessment (THERESA)”. The project focused on THM behaviour of interfaces present between canister and engineered buffer and on the homogenization of the engineered barrier formed by bentonite blocks and pellets.

Then, in order to model the interface between the canister and the engineered buffer the interface formulation described in Chapter 2 was used. In this example a coupled T-H-M formulation is considered for the interface. The mechanical model only takes into account the elastic constitutive law.

The following section contains a description of the geometry and protocol of the CRT. The mathematical model adopted to perform the simulation and the determination of T-H-M

parameters of the model materials are fully explained in the following sections. After that, numerical results are compared with experimental data, and finally, the discussion and conclusions on the results obtained are presented.

6.2. Description of the CRT

The CRT is a full-scale in situ heating test that involved the placement of a full-scale canister in vertical drifts surrounded by an engineered barrier. A view of the experimental geometry is given in Figure 6.1 extracted from the CRT-Specifications (Börgesson L., 2007).

The experimental deposition tunnel is located at level 420 m and was excavated by conventional drill and blast. It is approximately 6 × 6 m and has a horseshoe-shaped profile. Two deposition boreholes were bored with a full-face tunnel boring machine modified to drill vertical boreholes. The deposition borehole is 8.55 metres deep and has a diameter of 1.76 metres. The surrounding rock at the upper part of the borehole consists mainly of greenstone and the lower part of Äspö diorite. One of the boreholes was used for the CRT (the other borehole was used to perform the Temperature Buffer Test (TBT)). The experiments, CRT and TBT, were placed approximately at the tunnel centreline. The centre-to-centre distance between the two deposition boreholes is 6 m, which is the spacing that was considered for the deep repository.

In the CRT borehole a 0.15 m thick concrete foundation was built to prevent water leaking from the rock from reaching the bentonite blocks and thereby to reduce the risk of tilting the stack of bentonite rings. Slots were cut in the rock wall to prevent cables from being damaged. Also 16 filter mats with a width of 10 cm were installed, uniformly spaced at 0.15 m, from the borehole bottom up to a height of 6.25 m.

The bentonite used as buffer material is SKB's reference material, MX-80. The buffer consists of highly compacted bentonite blocks and rings with an initial density of 1,710 and 1,790 kg/m^3, respectively. The initial water content of the bentonite was 17%. The bentonite buffer was installed as blocks and rings. The blocks have a diameter of 1.65 m and a height of 0.5 m. Ring-shaped or cylindrical bentonite blocks were placed in the borehole. When the stack of blocks was

6 m high, the canister, equipped with electrical heaters, was lowered down in the centre of the borehole and the cables to the heaters and instruments were connected.

A canister obtained from SKB's Encapsulation Project was used for the CRT. The outside diameter of the canister is 1,050 mm, its height is 4.83 m and its weight, 21.4 tonnes.

At the top of the canister MX-80 bentonite bricks filled up the volume between the top surface of the canister and the top surface of the upper ring (R10). The height difference between the two surfaces was 220 – 230 mm. The space between the bentonite blocks and the borehole wall was filled with bentonite pellets and water. Additional blocks were emplaced until the borehole was filled to a distance of 1 m from the tunnel floor.

The top of the borehole was sealed with a retaining structure formed by a plug made of concrete, a steel lid and rock anchors. The aim of the structure is to prevent the blocks of bentonite from swelling uncontrollably.

An impermeable rubber mat was installed between bentonite block C4 and the concrete plug. On top of the plug the steel lid was placed. The plug and lid can move vertically and are attached to the rock by nine rock anchors. Each of the nine rock anchors consists of 19 steel wires with a nominal area of 98.7 mm^2 and a fixed and free length of 5 m. The inclination of the anchors is 2.5:1 or ≈ 22 ° (Fig. 6.1) (Thorsager et al., 2002; Börgesson L., 2007).

A large number of instruments was installed to monitor the test as follows:

- Canister - temperature and strain
- Rock mass - temperature and stress
- Retaining system - force and displacement
- Buffer - temperature, relative humidity, pore pressure and total pressure.

The instrumented sections are indicated in Figure 6.2. The positions of the instruments in the buffer are indicated as: bentonite ring or cylinder number counted from the bottom /direction A(180º), B (0º), C (270º) or D (90º)/ radial distance from centre line in mm. The identification of

the sensors in the rock is the following: distance in meters from the bottom/ direction according to Figure 6.2/ distance in meters from the hole surface.

The temperature was measured using thermocouples. Relative humidity was determined using Wescor psychrometers and capacitive transducers manufactured by Vaisala. Total pressures were recorded using Geokon transducers (Börgesson L., 2007).

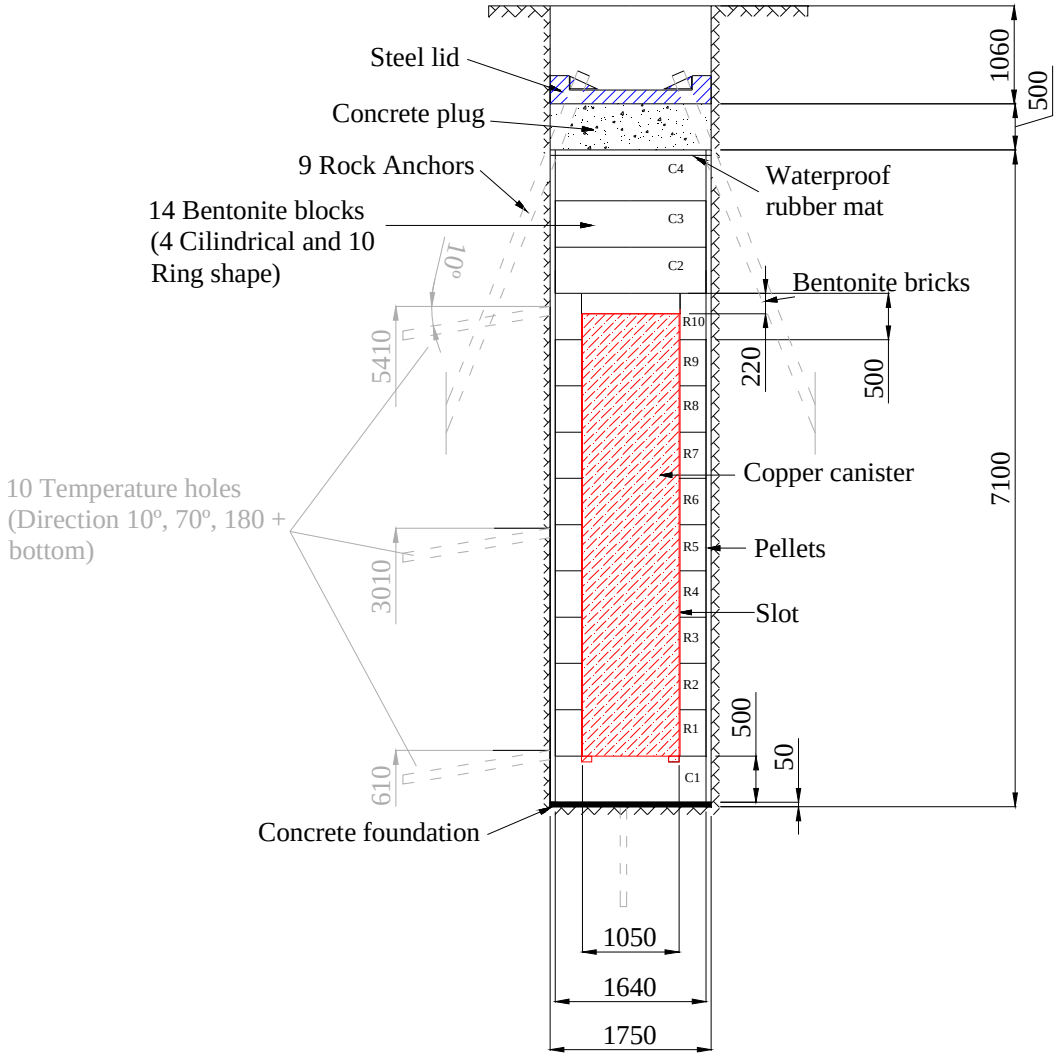

Figure 6.1: Canister Retrieval Test geometry (Börgesson L., 2007).

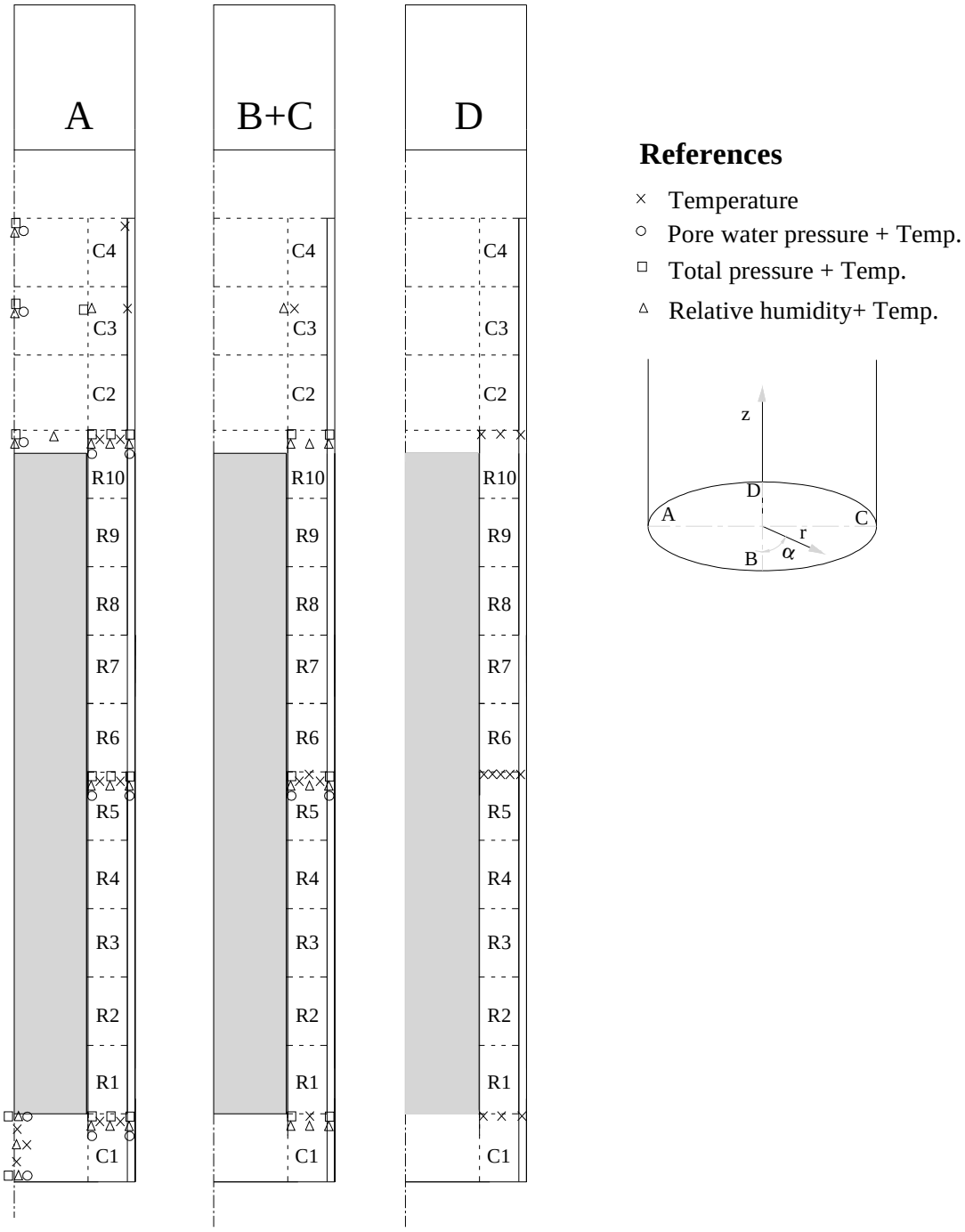

Figure 6.2: Schematic view of the position of the sensor at the CRT (Börgesson L., 2007).

6.3 Test protocol

1. The starting date of the experiment was October 26th 2000, when the buffer-rock interface was filled with pellets. Afterwards, water was pumped into the gap and filter mats.
2. Once pellets were hydrated, the concrete plug was casted and heating started. Heating began with an initially applied constant power of 700 W on day 1.
3. When the concrete plug rose 13 mm, due to bentonite swelling, three rock anchors were locked on day 5. The initial force in each anchor was 20 kN.
4. The canister heating power was raised twice, on day 18, to 1700 W, and on day 110, to 2600 W.
5. When the total force exceeded 1500 kN, the remaining six anchors were fixed. This procedure took place on days 46 to 48 .The total force was equally distributed between all anchors, i.e. the force was ≈ 170 kN/anchor.
6. The water pressure at filter mats was increased gradually up to 0.8 MPa from day 679 to 714 (02-09-05 to 02-10-10). On day 770 the water pressure was decreased to 0.1 MPa. Then it was increased again up to 0.8MPa on day 819 (03-01-23) and remained constant until day 1598 (05-03-12), when the water pressure was removed.
7. Heating of the TBT started on day 881 (03-03-26). This heating affected somewhat the temperature of the CRT buffer.
8. The heating was switched off on day 1811 (05-10-11).
9. After the end of the test, during dismantling, several samples from the buffer were drilled and tested to measure their dry density and degree of saturation (Börgesson, 2007).

Tables 6.1, 6.2, 6.3 and 6.4 and Figure 6.3 present a summary of the protocol followed in the test.

Table 6.1: CRT heater power protocol.

Date	Day	Heater Power [kW]	Comment
00-10-26	0	0	
00-10-27	1	0.7	
00-11-13	18	1.7	
01-02-13	110	2.6	
01-11-05	375	0	
01-11-06	376	2.6	
02-03-04	494	0	
02-03-11	501	2.6	
02-09-10	684	2.1	
03-12-04	1134	1.6	
05-03-10	1596	1.15	
05-10-11	1811	0	
06-03-28	1979	2	Testing the heaters
06-04-20	2002	0	

Table 6.2: TBT heater power.

Date	Day	Heater Power [kW]
00-10-26	0	0
03-03-26	881	0.9
03-04-03	889	1.2
03-04-10	896	1.5
06-06-09	2052	1.6

Table 6.3: CRT filter water pressure protocol.

Date	Day	Water pressure [MPa]	Comment
00-10-26	0	0	
02-09-05	679	0	Started to increase water pressure gradually
02-10-10	714	0.8	
02-12-05	770	0.1	
03-01-09	805	0.4	
03-01-23	819	0.8	
05-03-12	1598	0	
05-12-16	1877	0	Air flushed

Table Nº 6.4. Overview of rock anchor history.

Date	Day	Comment
2000-10-31	5	Three pre-stress anchors were attached to the lid. The initial force in each anchor was 20 kN
2002-12-12 2002-12-14	46-48	The remaining six anchors were attached to the lid when the total force exceeded 1.5 MN. The total force was distributed evenly between the anchors, which equals ~170 kN/anchor. The force in three of the anchors was measured.
2006-01-16 2006-01-18	1908-1910	Rock anchors were removed and the steel lid and concrete plug were lifted up from the deposition hole.

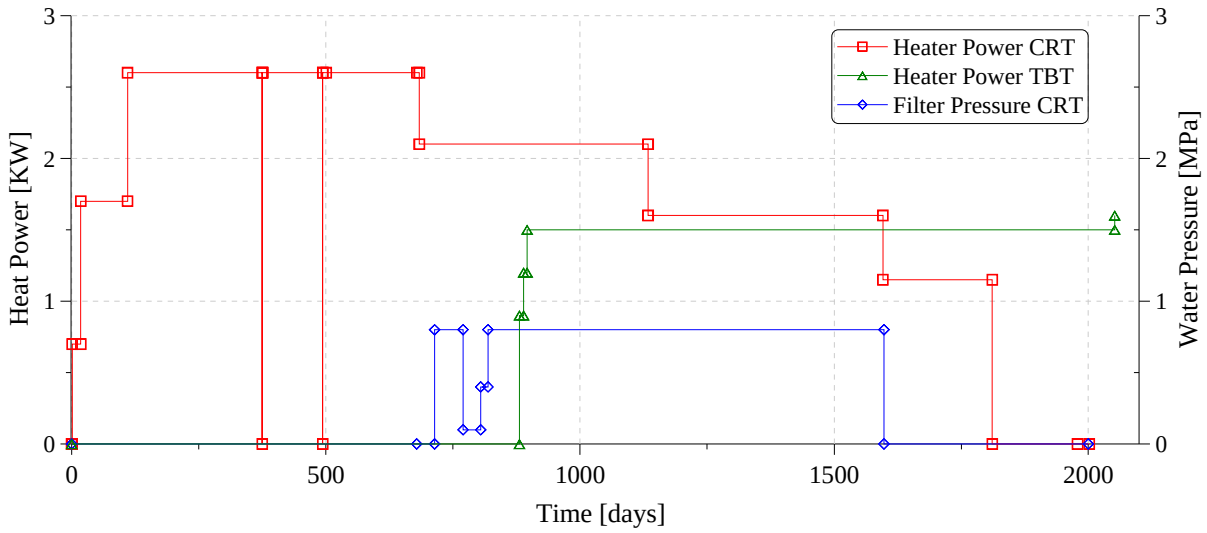

Figure 6.3: Heater power and filter pressure protocol at CRT and Heater protocol of TBT (Börgesson L., 2007).

6.4. Features of the analysis and material parameters

The analysis has assumed axi-symetric conditions using the mesh shown in Figure 6.4. The materials considered in the model are bentonite, cylinders, rings and bricks; pellets, the interface between bentonite and canister, canister, the concrete plug, the steel lid and the air in the gallery.

The geometry is discretized by 4-noded quadrilateral elements, and the mesh includes 1449 elements and 1540 nodes; 80 elements correspond to interface elements (indicated in red in Fig. 6.4).

The initial porosity, temperature and degree of saturation of bentonite, pellets and interface were obtained from Johanneson (2007) (see Tab. 6.5). The initial temperature for the air gallery equals 15 ºC while for the other materials it equals 20 ºC. Initial liquid pressures were calculated considering the retention curves of the materials and the saturation degrees measured in the test. The initial stress of the materials is assumed to be isotropic and equal to 0.11 MPa. A constant gas pressure was assumed to be equal to atmospheric throughout the test. The initial conditions of materials are summarized in Table 6.5

The heater power was applied on the canister volume according to the test protocol, except for the case in which heat power falled to zero on days 375 and 494 (Fig. 6.5). A special boundary conditions was prescribed in the host rock wall to allow some energy flux. The energy flux is expressed as an outflow rate given by:

$$j_e = j_e^0 + \gamma_e\left(T^0 - T\right) + E_g^w(j_g^w) + E_l^w\left(j_l^w\right)$$

where γ_e is a leakage coefficient, i.e. a parameter that allows a boundary condition of the Cauchy type. This parameter was calibrated to obtain at host rock wall the temperature measured by sensors. Likewise, this boundary condition allows considering the influence of heating from the TBT experiment.

Filter pressures were applied at the host rock wall according to the test protocol (see Fig. 6.5). The bottom boundary of Cylinder 1 and the top of Cylinder 4 were considered impervious because of the presences of concrete foundation and a rubber mat respectively.

The force applied on the steel lid by the anchors was considered as point load acting on the steel lid (Fig. 6.4).

Table 6.5: Initial conditions of materials.

Material	Initial porosity n_0	Dry density ρ_d [kg/m^3]	Initial degree of saturation Sr [%]	Liquid Pressure [MPa]
Bentonite Cylinder	0.39	1699	75.1	-43.1
Bentonite Ring	0.36	1782	85.9	-28.6
Bentonite Bricks	0.42	1616	63.7	-42.6
Pellets	0.64	1001	89.5	-3.4
Gap	-	1000	100.0	-0.1
Canister	0.001	8000	-	-0.1
Concrete plug	0.001	2400	-	-
Steel lid	0.001	7840	-	-
Air	0.98	1000	-	-

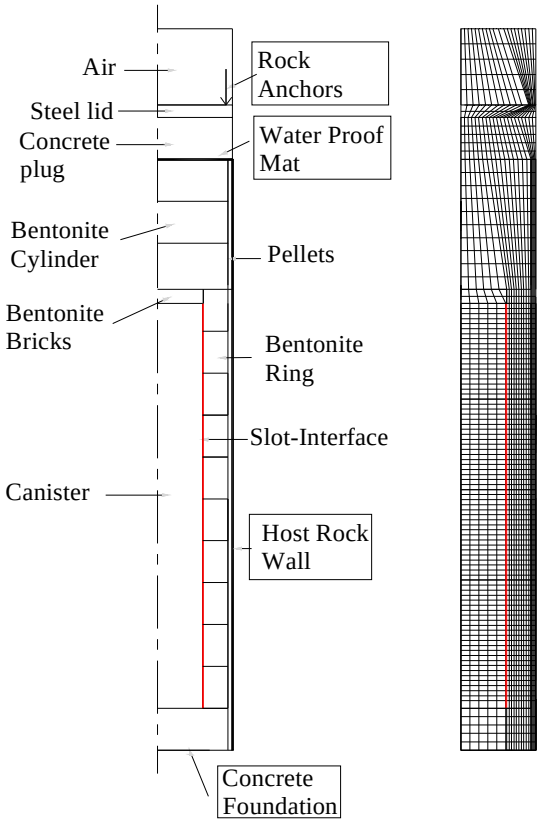

Figure 6.4: Geometry of the CRT model. Description of material and finite element mesh used in the numerical simulation.

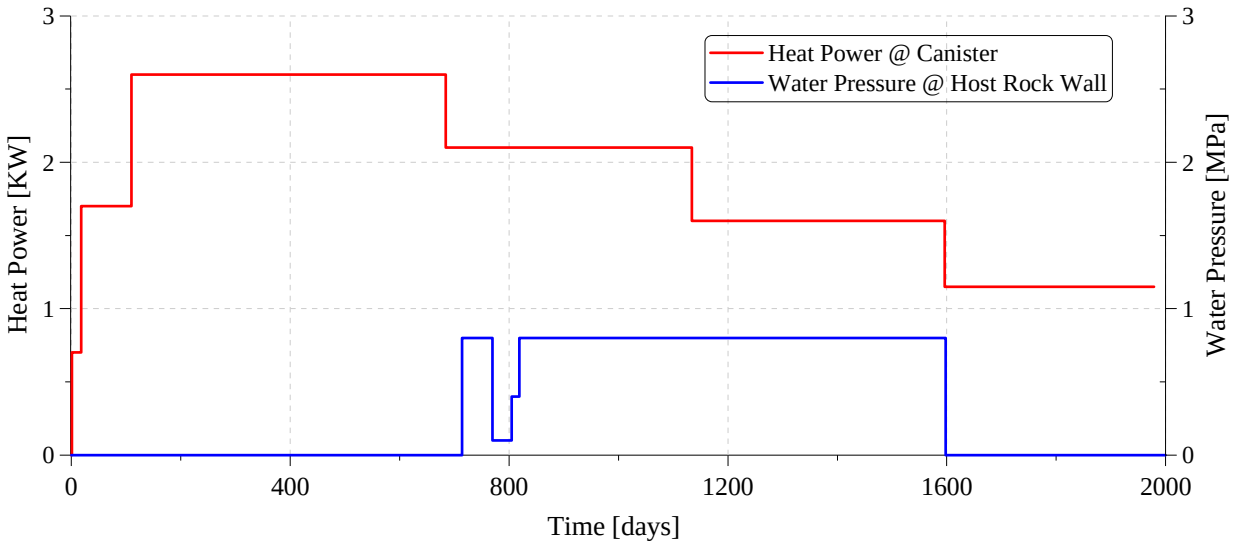

Figure 6.5: Heater power applied at canister and filter water pressure applied at host rock wall according to test protocol.

6.5. Materials parameters

The thermal, hydraulic and mechanical properties of the different materials of the CRT are extracted from several reports (Börgesson L., 2007)

6.5.1. Thermal properties

Thermal conductivity is given by:

$$\lambda = \lambda_{sat}\sqrt{S_l} + \lambda_{dry}\left(1-\sqrt{S_l}\right) \qquad 6.1$$

where: λ_{sat} is the thermal conductivity for a degree of saturation S_l = 1, and λ_{dry} is the thermal conductivity for S_l = 0.

Parameters λ_{sat} and λ_{dry} for bentonite and pellets were determined by adjusting experimental data to Equation 6.1 (Figure 6.6a and b). The thermal conductivities of the canister, concrete plug and steel lid were given in Börgesson et al. (1994), Börgesson et al. (1995), Börgesson &

Johannesson, (1995) and Sugita et al. (2003). For the interface, the conductivities adopted were similar to those of bentonite, because during the test bentonite expands filling the interface space. Besides the specific energy of the solid phase and the thermal expansion coefficients of bentonite and pellets are given in Börgesson et al. (1995). The properties of the canister, concrete and steel lid are given in Börgesson et al. (2007). Thermal parameters are summarized in Table 6.6.

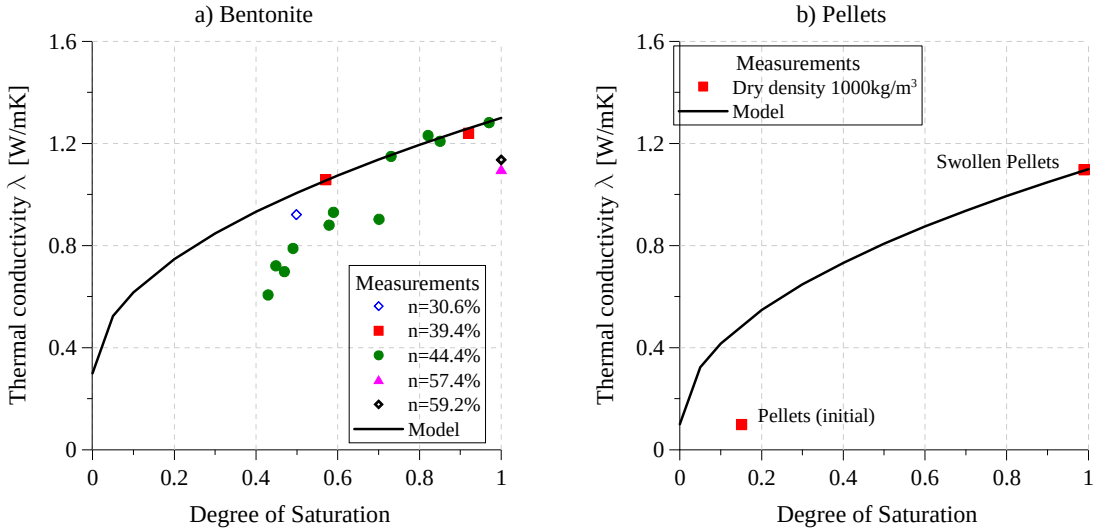

Figure 6.6: Variation of bentonite and pellets thermal conductivity with degree of saturation. Experimental results and model fitted. (Börgesson et al., 1995, Börgesson & Johannesson, (1995) and Sugita et al., 2003)

Table 6.6: Thermal parameters.

Material	Dry thermal conductivity λ_{dry} [W/mK]	Saturated thermal conductivity λ_{sat} [W/mK]	Solid phase specific heat c [J/kg K]	Linear thermal expansion coef. [$^oC^{-1}$]
Bentonite (Cylinder-Ring and Bricks)	0.3	1.3	800	$3.2x10^{-6}$
Pellets	0.1	1.1	800	$3.2x10^{-6}$
Gap	0.1	1.3	800	-
Canister	100	100	450	$12x10^{-6}$
Concrete plug	2.7	2.7	770	$10x10^{-6}$
Steel lid	47	47	460	$12x10^{-6}$
Air	0.03	0.03	-	-

6.5.2. Hydraulic properties.

The hydraulic conductivity of the materials is given by:

$$\mathbf{K}_l = \frac{\mathbf{k} k_{rl} \rho_l g}{\mu_l} \qquad 6.2$$

where k is the intrinsic permeability; k_{rl} is the relative permeability; ρ_l is the liquid density; μ_l is the viscosity of the liquid and g is the gravitational force.

The intrinsic permeability depends on porosity according to:

$$\mathbf{k} = k_0 \frac{n^3}{(1-n)^2} \frac{(1-n_0)^2}{n_0^3} \mathbf{I} \qquad 6.3$$

where k_0 is the reference intrinsic permeability at reference porosity n_0.

The intrinsic permeabilities at different porosities of MX-80 bentonite and pellets were experimentally measured by Pusch (2001), Villar (2002), Börgesson et al. (1999), Imbert et al. (2004) and Lajunie et al. (1994). Figure 6.7 shows the values of the intrinsic permeability adopted for bentonite cylinders, rings, bricks and pellets. For the interface element, a constant permeability several orders of magnitude higher was adopted. On the other hand, very low permeabilities were adopted for the rest of materials.

The relative permeability of the liquid phase is given by:

$$k_{rl} = S_{el}^{\ n} \qquad 6.4$$

where S_{el} is the effective degree of saturation and n is a parameter of the model. In this case a value $n = 3$ was adopted. The effective degree of saturation is evaluated as:

$$S_{el} = \frac{S_l - S_{lr}}{S_{ls} - S_{lr}} \tag{6.5}$$

where S_{lr} is the residual saturation; S_{ls} is the maximum saturation and S_l is the liquid degree of saturation, which is calculated by the retention curve.

The retention curve adopted in the analysis for MX-80 bentonite and pellets is a modification of van Genutchen's expression (1980) proposed by Sanchez et al. (2004):

$$\begin{aligned} S_l &= \left[1+\left(\frac{\psi}{P}\right)^{\frac{1}{1-\lambda}}\right]^{-\lambda} f_d \\ f_d &= \left(1-\frac{\psi}{P_d}\right)^{\lambda_d} \end{aligned} \tag{6.6}$$

where Ψ is the total suction; P is the capillary pressure; λ is a model parameter and f_d is a function included to properly fit the high-suction range of experimental data obtained. P_d and λ_d are model parameters.

The parameters of the retention curve of MX-80 bentonite and pellets were determined fitting the experimental data obtained by Eurogeomat (Dang & Robinet, 2004), CIEMAT (Villar, 2002) and Clay Technology (Hökmark & Fälth, 2003). Given that the retention curve depends on the dry density of the materials, the parameters for the cylinder, ring, bricks and pellets were determined considering their dry density values (Fig. 6.8).

The rest of materials followed the original expression proposed by van Genutchen (1980):

$$S_l = \left[1+\left(\frac{\psi}{P}\right)^{\frac{1}{1-\lambda}}\right]^{-\lambda} \tag{6.7}$$

The values of P and λ for interface elements were adopted to cause a fast drying of those elements (see Fig. 6.9). The values used for the canister, concrete and steel lid do not affect the hydraulic behaviour of the model.

The hydraulic parameters of the materials are summarized in Table 6.7

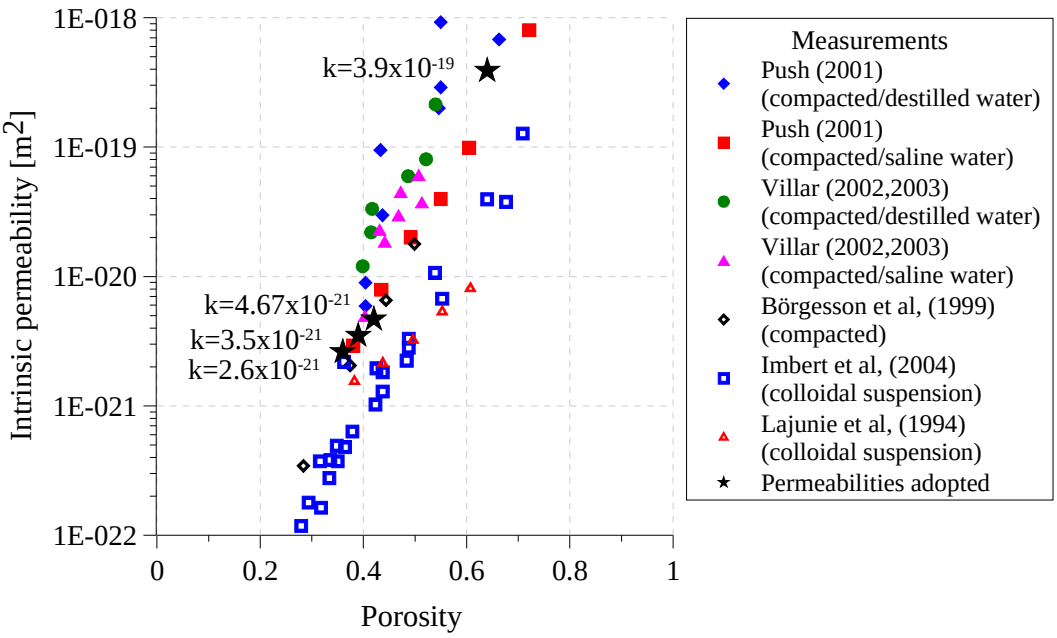

Figure 6.7: Variation of intrinsic permeability with porosity for MX-80 bentonite. Experimental results and values adopted.

Table 6.7: Hydraulic parameters of the materials.

Material	Intrinsic permeability k_0 [m^2]	Retention Curve			
		P_0 [MPa]	λ	P_d [MPa]	λ_d
Bentonite Cylinder	$3.50x10^{-21}$	30	0.2	500	1.1
Bentonite Ring	$2.60x10^{-21}$	50	0.3	600	1.1
Bentonite Bricks	$4.67x10^{-21}$	20	0.22	300	1.1
Pellets	$3.90x10^{-19}$	5	0.2	600	1.1
Gap	$1.00x10^{-16}$	1	0.3	-	-
Canister	$1.00x10^{-30}$	1000	0.5	-	-
Other materials	$1.00x10^{-30}$	$1x10^{-6}$	0.5	-	-

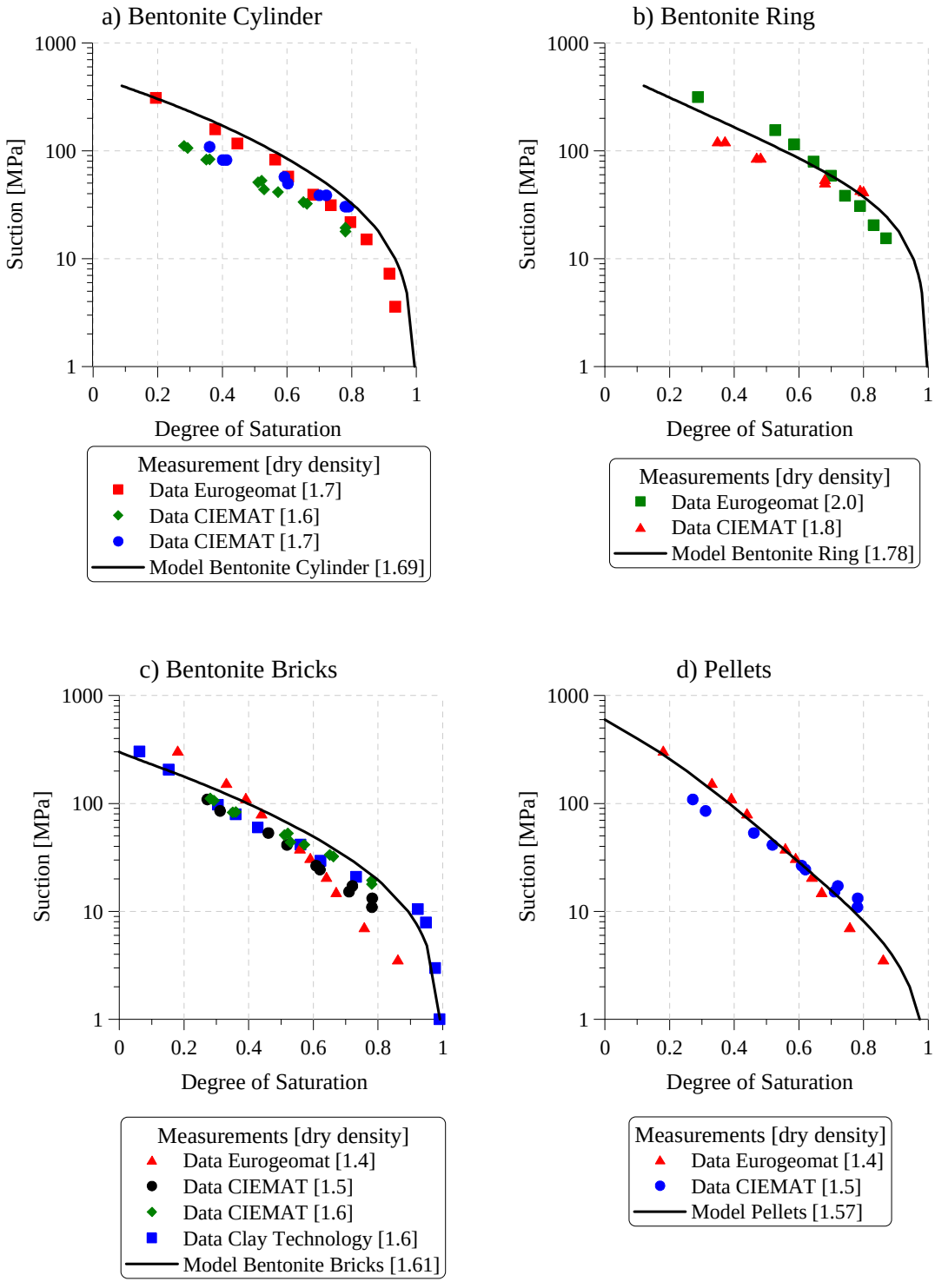

Figure 6.8: Retention curves adopted for bentonite cylinder, ring, bricks and pellets used in the numerical model and experimental data obtained for different dry densities of MX-80 bentonite. Data provided by Eurogeomat were found in Dang & Robinet (2004), by Clay Technology in Hökmark & Fälth (2003) and by CIEMAT in Villar (2002).

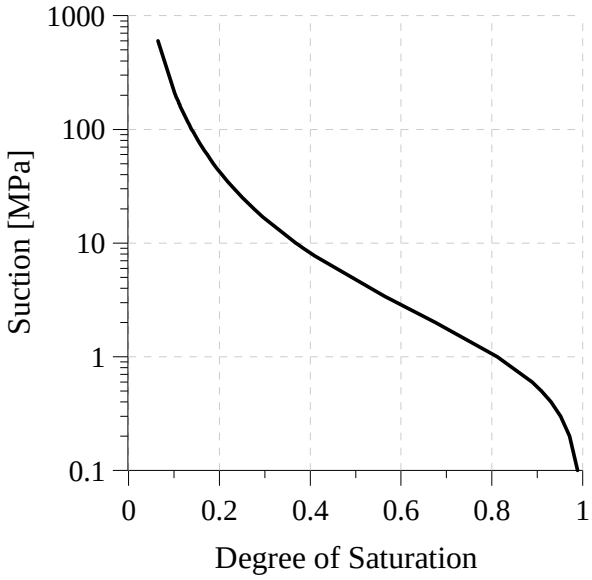

Figure 6.9: Retention curve adopted for the interface between the canister and the bentonite ring.

The vapour diffusion is calculated using Fick's law:

$$D_g^{vapour} = \tau D^v \left[\frac{(273.15 + T)^{2.3}}{P_g} \right] \qquad 6.8$$

where τ is the tortuosity coefficient. A tortuosity τ= 0.8 is adopted for bentonite; τ= 0.9 for pellets and τ= 1.0 for the interface. D^v is the coefficient of diffusion (5.9×10^{-6} $m^2/s/K$).

6.5.3 Mechanical properties

6.5.3.1 Continuum elements

The mechanical constitutive model adopted for MX-80 bentonite and pellets is a modified form of the Barcelona Basic Model; BBM (Alonso et al., 1990). The total strain of the model is calculated by adding elastic and viscoplastic strains. The original elastic formulation of BBM is modified to reproduce the expansive behaviour of the bentonite. The elastic model adopted is:

$$\dot{\varepsilon}_v^e = \frac{\kappa_i(\Psi)}{1+e}\frac{\dot{p}'}{p'} + \frac{\kappa_s(p')}{1+e}\frac{\dot{\Psi}}{\Psi + p_{at}} \qquad 6.9$$

$$\dot{\varepsilon}_s^e = \frac{\dot{J}}{G} \qquad 6.10$$

where ε_v^e and ε_s^e are the volumetric and deviatoric components of the elastic strain respectively; κ_i and κ_s are the elastic stiffness for changes in net mean stress and suction respectively; *p'* is the mean net stress; Ψ is the suction; *e* is the void ratio, *J* is the square root of the second invariant of deviatoric stress tensor ($J = \frac{1}{2} trace(\mathbf{s}:\mathbf{s}) = \frac{1}{3} q^2$; $\mathbf{s} = \sigma' - p'\mathbf{I}$) and G is the shear modulus.

The elastic stiffness for net mean stress depends on suction:

$$\kappa_i(\Psi) = \kappa_{i0}(1 + \alpha_i \Psi) \qquad 6.11$$

where κ_{i0} is the elastic stiffness under saturated conditions and α_i is a model parameter.

The elastic stiffness for suction changes depends on mean stress:

$$\kappa_s(p') = \kappa_{s0}\left[1 + \alpha_{sp} \ln\left(\frac{p'}{p_{ref}}\right)\right] \qquad 6.12$$

where κ_{s0} and α_{sp} are model parameters, and p_{ref} is the pressure reference.

Viscoplastic strains ($\dot{\varepsilon}^{vp}$) are calculated as:

$$\dot{\varepsilon}^{vp} = \Gamma\langle\Phi(F)\rangle\frac{\partial G}{\partial \sigma'} \; ; \; \Phi(F) = \left(\frac{F}{F_0}\right)^N \qquad 6.13$$

where Γ is the viscosity; N is the power of stress; F_0 is a value of reference; F is the failure surface, and G is the viscoplastic potential.

The failure surface is defined by:

$$F = 3J^2 - M^2(p + p_s)(p_0 - p) = 0 \qquad 6.14$$

and the viscoplastic potential is:

$$G = 3J^2 - \alpha M^2(p + p_s)(p_0 - p) = 0 \qquad 6.15$$

where M is the slope of the critical state; p_0 is the apparent unsaturated preconsolidation pressure; p_s considers de dependency of shear strength with suction, and α is a non-associative parameter.

p_0 is considered dependant on suction:

$$p_0 = p^c \left(\frac{p_0^*}{p^c} \right)^{\frac{\lambda(0)-\kappa_{i0}}{\lambda(\Psi)-\kappa_{i0}}} \qquad 6.16$$

The variation of compressibility with suction is given by:

$$\lambda(\Psi) = \lambda(0)\left[(1-r)\exp(-\beta\Psi) + r\right] \qquad 6.17$$

where $\lambda(0)$ is the compressibility under saturated conditions; r and β are the model parameters that define the shape of the LC failure surface.

The hardening law is expressed as a rate relation between the volumetric viscoplastic strain (ε_v^{vp}) and the saturated isotropic preconsolidation stress (p_0^*) according to:

$$\dot{p}_0^* = \frac{1+e}{\lambda(0)-\kappa} p_0^* \dot{\varepsilon}_v^{vp} \qquad 6.18$$

Elastic stiffness κ_{i0} and α_i; and parameters of compressibility $\lambda(0)$ r and β for MX-80 bentonite were determined fitting the experimental data obtained by Tang (2005) and Villar (2005) (see Fig. 6.10). The rest of parameters were determined from back calculation.

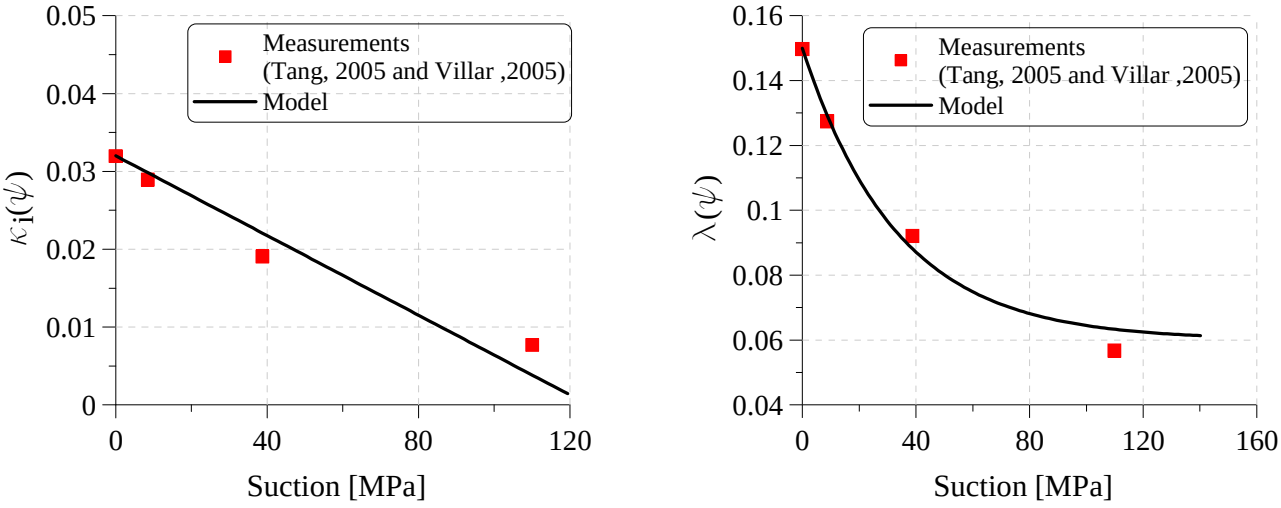

Figure 6.10: a) Variation of MX-80 bentonite elastic stiffness with suction. b) Variation of compressibility with suction (Tang, 2005; Villar, 2005).

The parameters of pellets were adopted taking as a framework the experimental values reported by Hoffman et al. (2006).

6.5.3.2 Interface elements

The mechanical behaviour of the interface, which was modelled using a non-linear elastic behaviour with the stiffness dependant on interface aperture, is described in Chapter 3.

A linear elastic behaviour was assumed for the canister, concrete plug and steel lid and their parameters were given in Börgesson (2007).

The mechanical parameters are listed in Table 6.8

Table 6.8: Summary of the mechanical parameters used in the model.

Material	Elastic parameter		Plastic parameter	
Bentonite	κ_{i0}	0.032	Γ_0 [s^{-1}]	$1x10^{-4}$
	κ_{s0}	0.072	N	5.0
	α_i	-0.008	F_0 [MPa]	1.0
	α_{sp}	-0.0016	$\lambda(0)$	0.15
	p_{ref} [MPa]	0.1	r	0.4
	G [MPa]	2.48	β	0.03
			M	1.0
			p_0^*	4.0
			p_c	0.1
			α	0.3
Pellets	κ_{i0}	0.074	Γ_0 [s^{-1}]	$1x10^{-4}$
	κ_{s0}	0.003	N	5.0
	α_i	-0.003	F_0 [MPa]	1.0
	α_{sp}	-0.006	$\lambda(0)$	0.15
	p_{ref} [MPa]	0.1	r	0.425
	G [MPa]	1.05	β	0.03
			M	1.0
			p_0^*	0.3
			p_c	0.095
			α	0.3
Interface	m [MPa]	1.0		
	K_t [MPa/m]	$1.0x10^6$		
	a_0 [m]	0.01		
Canister	E [MPa]	$130x10^3$		
	υ	0.25		
Concrete plug	E [MPa]	$30x10^3$		
	υ	0.15		
Steel lid	E [MPa]	$206x10^3$		
	υ	0.3		
Air	E [MPa]	0.02		
	υ	0.25		

6.6. Test and model results

In this section test observations (Gourdazi et al., 2006) are compared to the predictions of the numerical analysis.

6.6.1 Thermal

The temperature at MX-80 bentonite barrier and host rock wall is recorded by means of thermocouple sensors. The evolution of temperature at Cylinder 3, Ring 5 and Ring 10 is shown in Figure 6.11a, while the temperatures on the host rock wall are plotted in Figure 6.11b. The analysis reproduces the observation quite well. The agreement of temperatures indicates that the value of the thermal conductivity of the materials, especially in the interface between canister and bentonite is well captured.

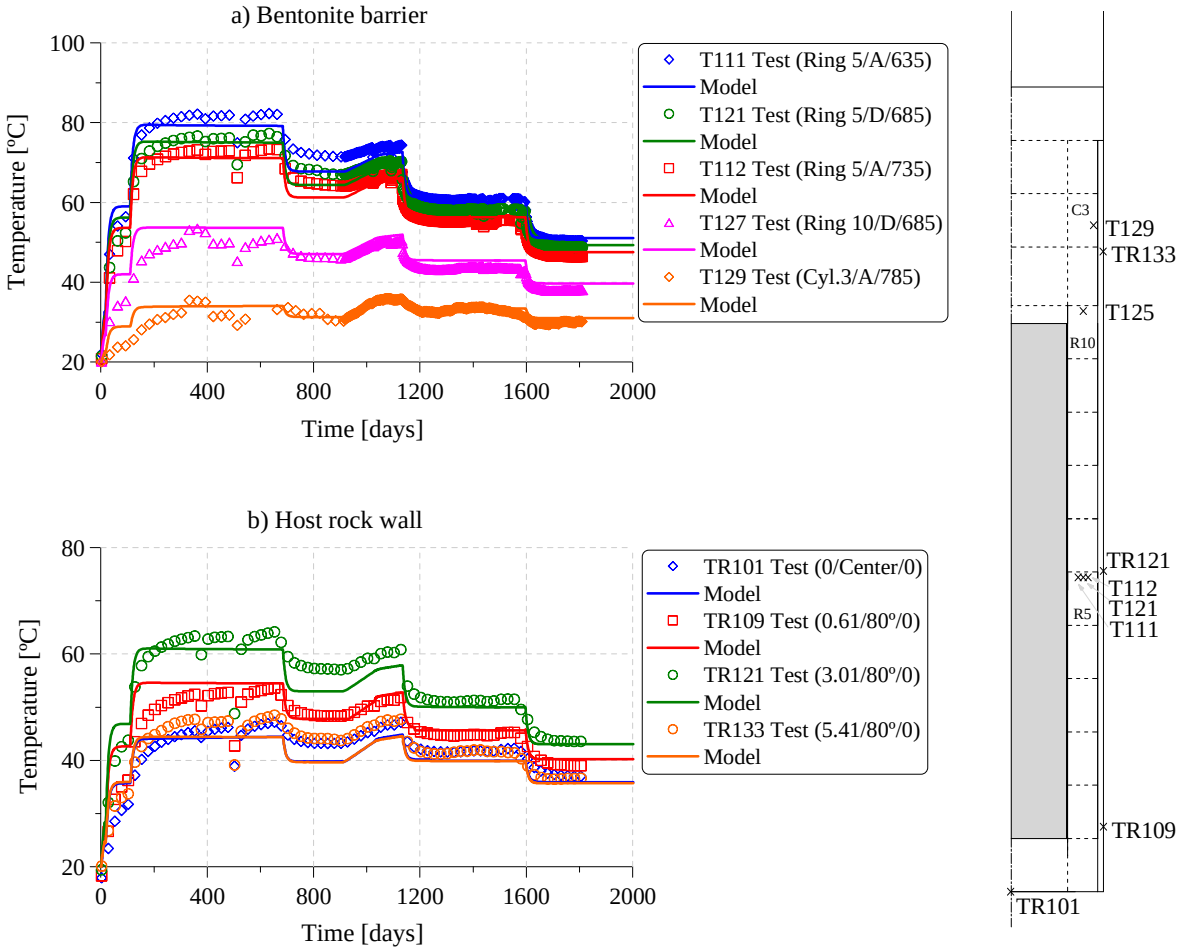

Figure 6.11: Evolution of temperatures in the bentonite barrier and host rock wall. Measured data and model results.

6.6.2 Hydraulic

Figures 6.12a, b and d show the variation with time of relative humidity measured by capacitive sensors. The relative humidity from the numerical simulation is calculated using Kelvin's equation:

$$RH = \exp\left[\frac{\Psi M_w}{R(273+T)\rho_l}\right] \qquad 6.19$$

where $\Psi = P_g - P_l$ is the total suction; M_w is the molecular weight of water; R is the ideal constant of the gas; T is the temperature and ρ_l is the liquid density.

In the cooler section of the barrier (Cylinder 3) and in the bentonite close to the host rock wall (W137, W142, W119 and W120) a monotonic increase of relative humidity is recorded. This is due to the condensation of the vapour that came from the heated zones, to the water inflow from the rock and to the artificial hydration from filter mats (Fig. 6.12a).

However the bentonite barrier closer to the canister exhibits an increase of relative humidity due to the vapour front driven by heating. Then the barrier dries because of the evaporation caused by the increment of temperature. And finally, the barrier hydrates and its relative humidity increases due to the water pressure inflow from the filter mats and rock (Sensor W134-Ring 10) (Fig. 6.12b). Nevertheless, at Ring 5, drying is followed by a fast increment of relative humidity. This may be attributed to the presence of water in the interface (see Fig. 6.12c-sensor W119). This water migrates in vapour form and hydrates the barrier. In general, it is observed that the predictions from the numerical model are quite satisfactory.

The evolutions of suction, measured with psycrometers, and the values calculated are plotted in Figure 6.13. There is no a good match between experimental and calculated results; however the decreasing trend of suction with the increment of water content of the buffer is predicted. The calculated suction decreased throughout the test; in contrast, the measured suctions kept constant at 2 MPa from day 800 up to the end of the test, perhaps due to osmotic effects not considered in the analysis.

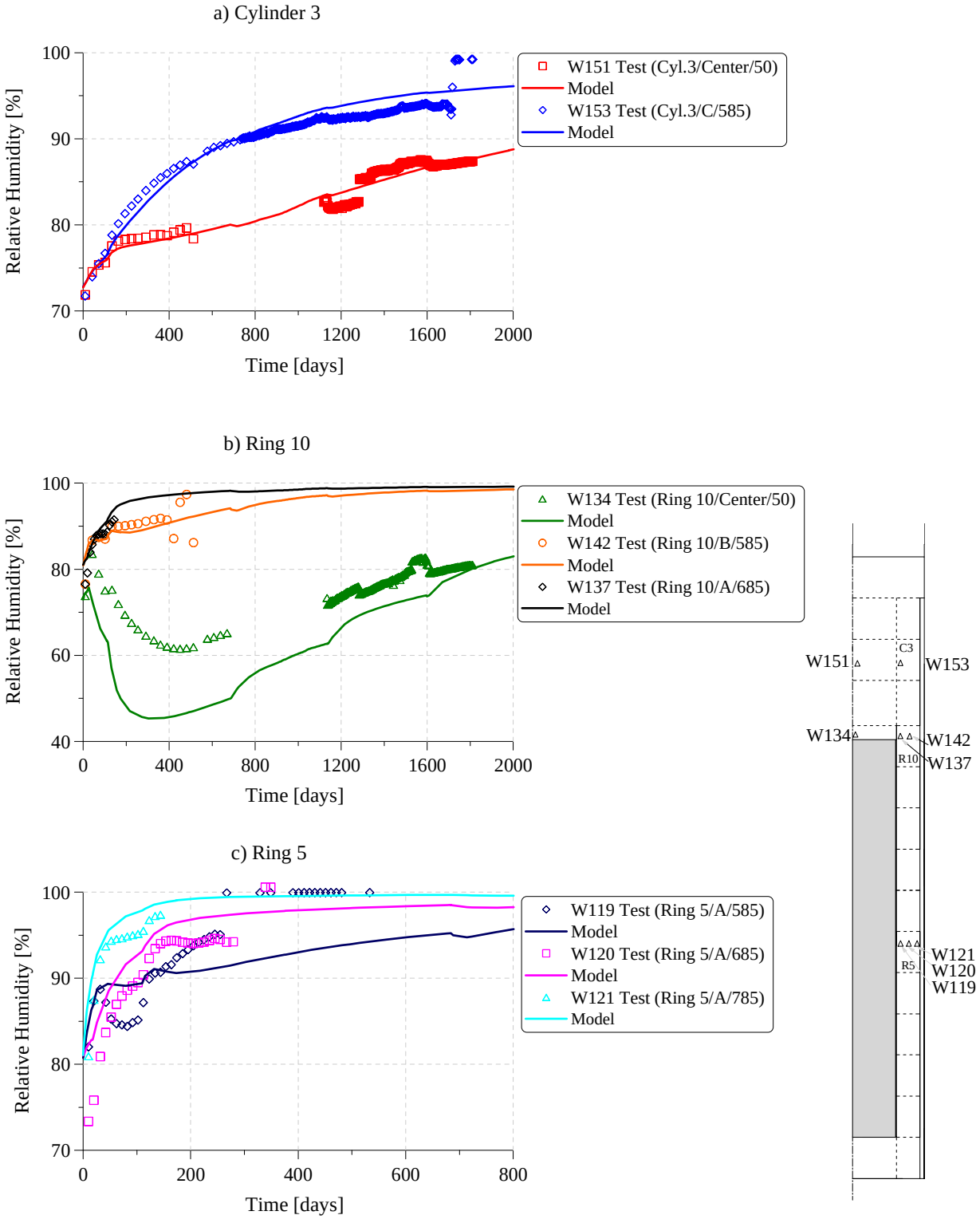

Figure 6.12: Evolution of relative humidity in bentonite barrier. a) Cylinder 3, b) Ring 10 and c) Ring 5. Test observation and numerical results.

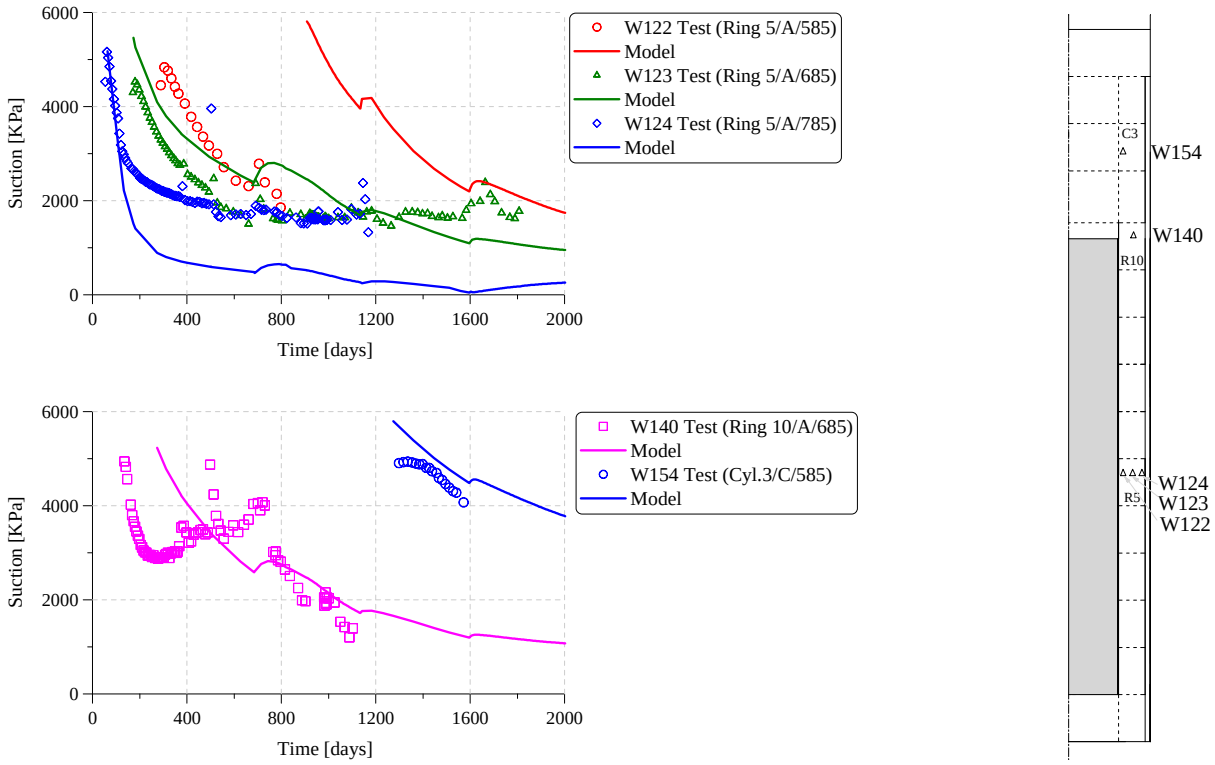

Figure 6.13: Evolution of suction in bentonite barrier Ring 5, Ring 10 and Cylinder 3. Test observation and numerical results.

6.6.3 Mechanical

The total vertical pressure (vertical stress) for the bentonite barrier is plotted in Figure 6.14. The swelling of bentonite causes stresses to increase up to 3.0 and 4.5 MPa. Although numerical results underestimated the magnitude of the stresses, they followed their trend.

Figure 6.15 shows the evolution of opening and normal stress at the interface. The interface closes while stress increases as bentonite swells. The final opening of the interface is approximately 0.2 mm and the maximum normal stress is 2.8 MPa corresponding to the stress calculated in the bentonite barrier next to the interface (Fig. 6.14-radial distance 585 mm).

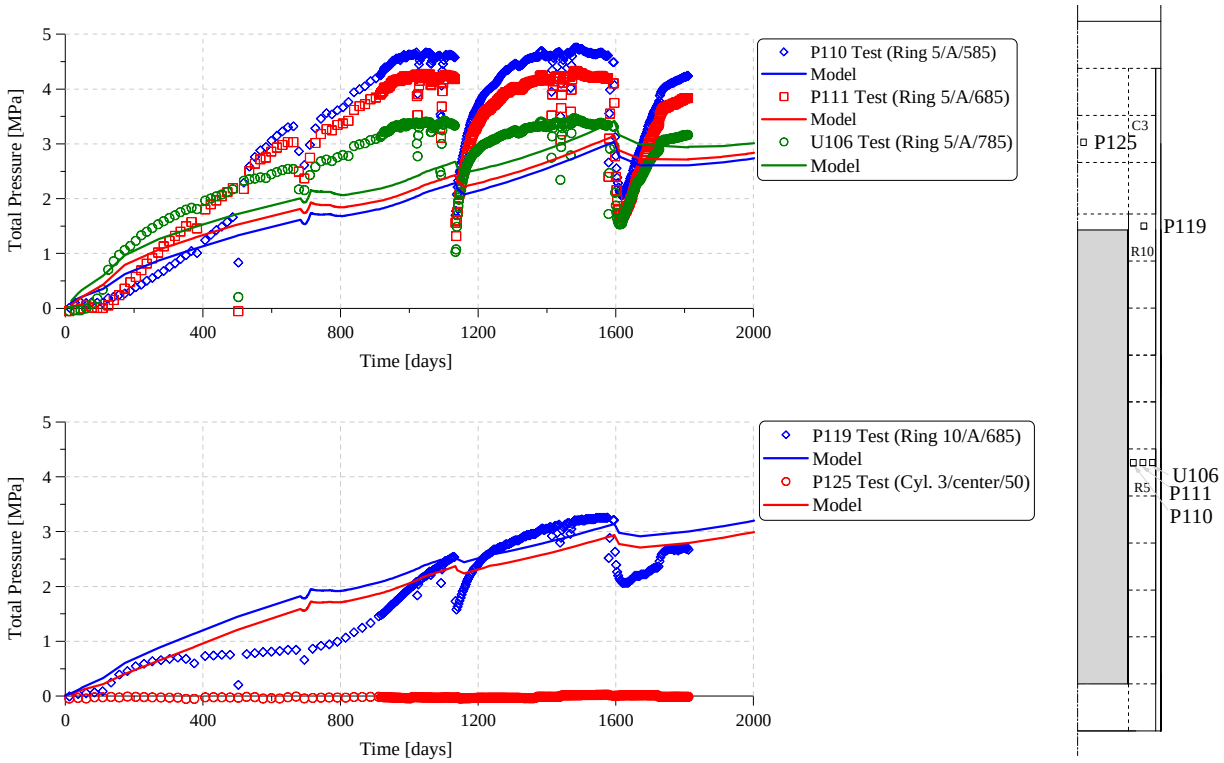

Figure 6.14: Evolution of total pressure in bentonite barrier. Experimental data against numerical results.

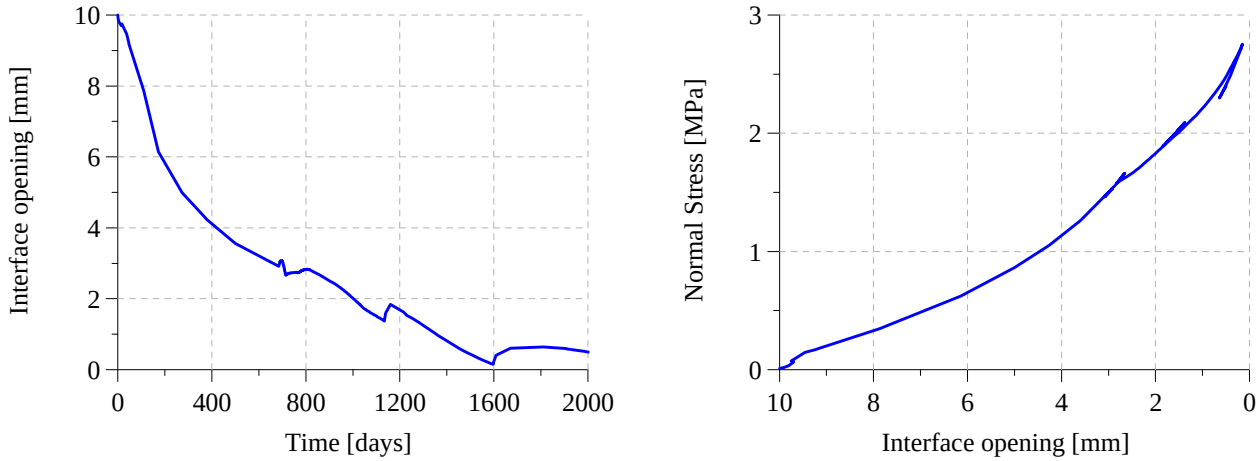

Figure 6.15: Evolution of opening and normal stress of the interface between canister and bentonite barrier.

6.7. Test dismantling

After the dismantling of the test, the samples at the selected section were cored from bentonite and pellets. In Cylinder 3, samples were extracted at different depths (50, 150, 250, 350 and 450 mm) measured from the top of the block. In Ring 10, samples were extracted at depths of 50, 110 and 175 mm. Finally in Ring 6, samples were taken from a depth of 50mm and directions α = 45º, 135º, 225º, 315º (see Fig. 6.2). The dry density and water content of samples were measured in the laboratory and the corresponding degree of saturation was then calculated (Johannesson, 2007). The values for the degree of saturation and dry density in Cylinder 3, Ring 10, Ring 7 and Ring 6 are shown in Figures 6.16, 6.17, 6.18 and 6.19 respectively.

The figures show that the final degree of saturation throughout the bentonite barrier is higher than the initial one, even in the zone closest to the canister. The degree of saturation is higher near the host rock wall, as a consequence of natural and artificial hydration.

The figures also show the decrease in dry density of bentonite blocks (cylinder and rings) due to their swelling. Given that the swelling of bentonite depends on its hydration, the dry density of the bentonite decreases further in the zones situated near the borehole wall. However, due to the low degree of hydration and compression from bentonite rings when swelled, the dry density of bentonite bricks increased. Furthermore, bentonite swelling caused the compaction of pellets and, consequently, an increase of their dry density.

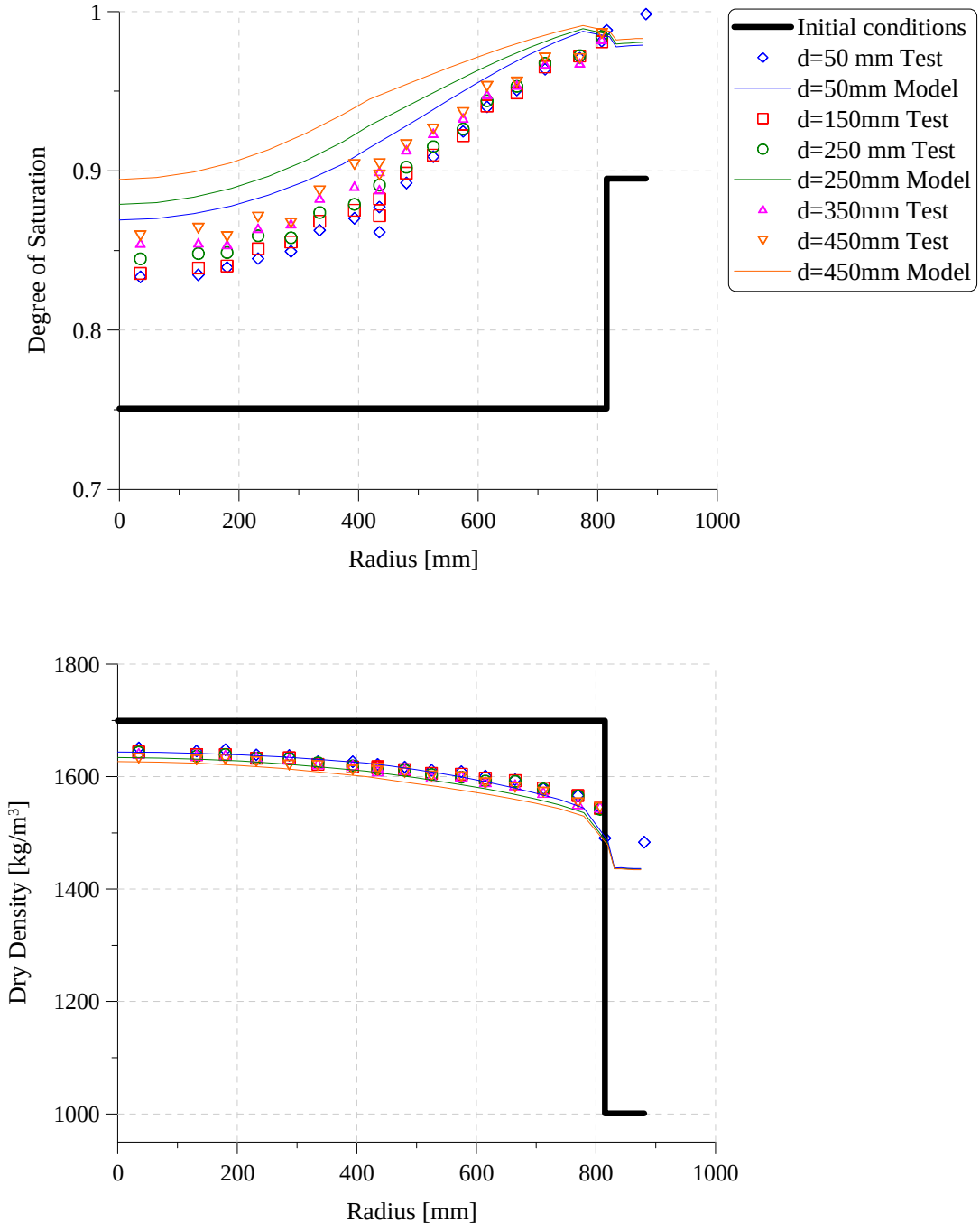

Figure 6.16: Degree of saturation and dry density of Cylinder 3 after test dismantling. Experimental and model results.

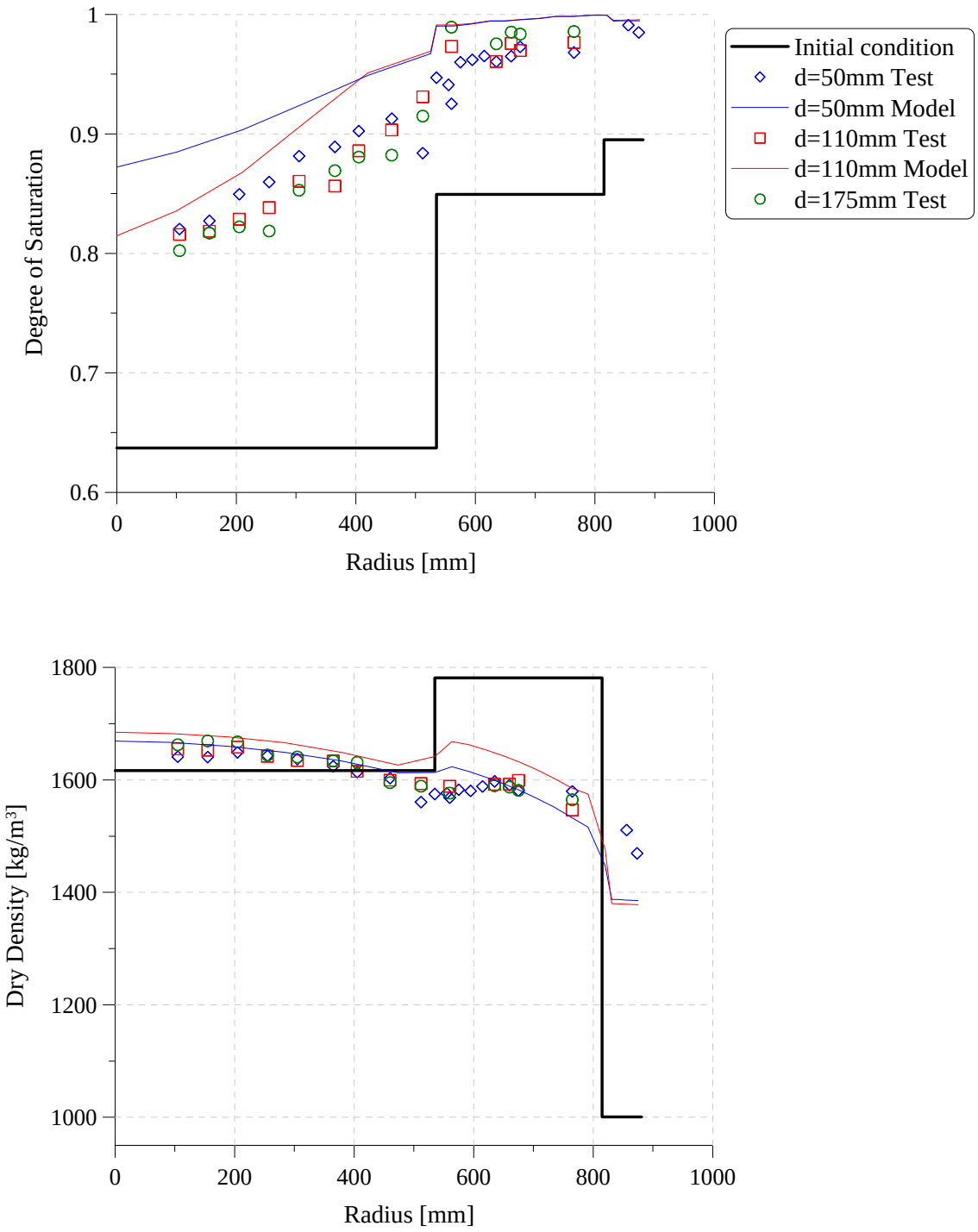

Figure 6.17: Degree of saturation and dry density of Ring 10 after test dismantling. Experimental and model results.

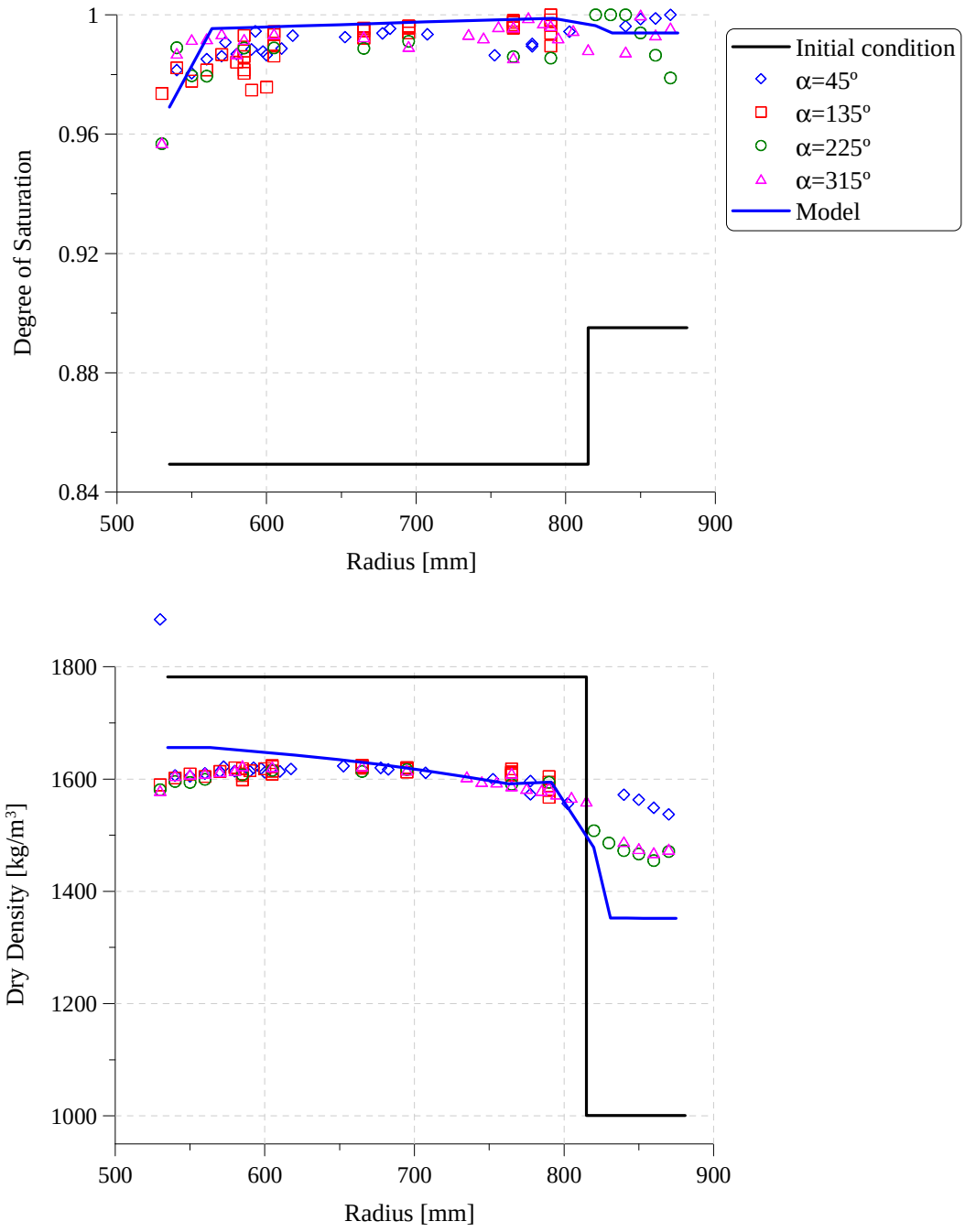

Figure 6.18: Degree of saturation and dry density of Ring 7 after test dismantling. Experimental and model results.

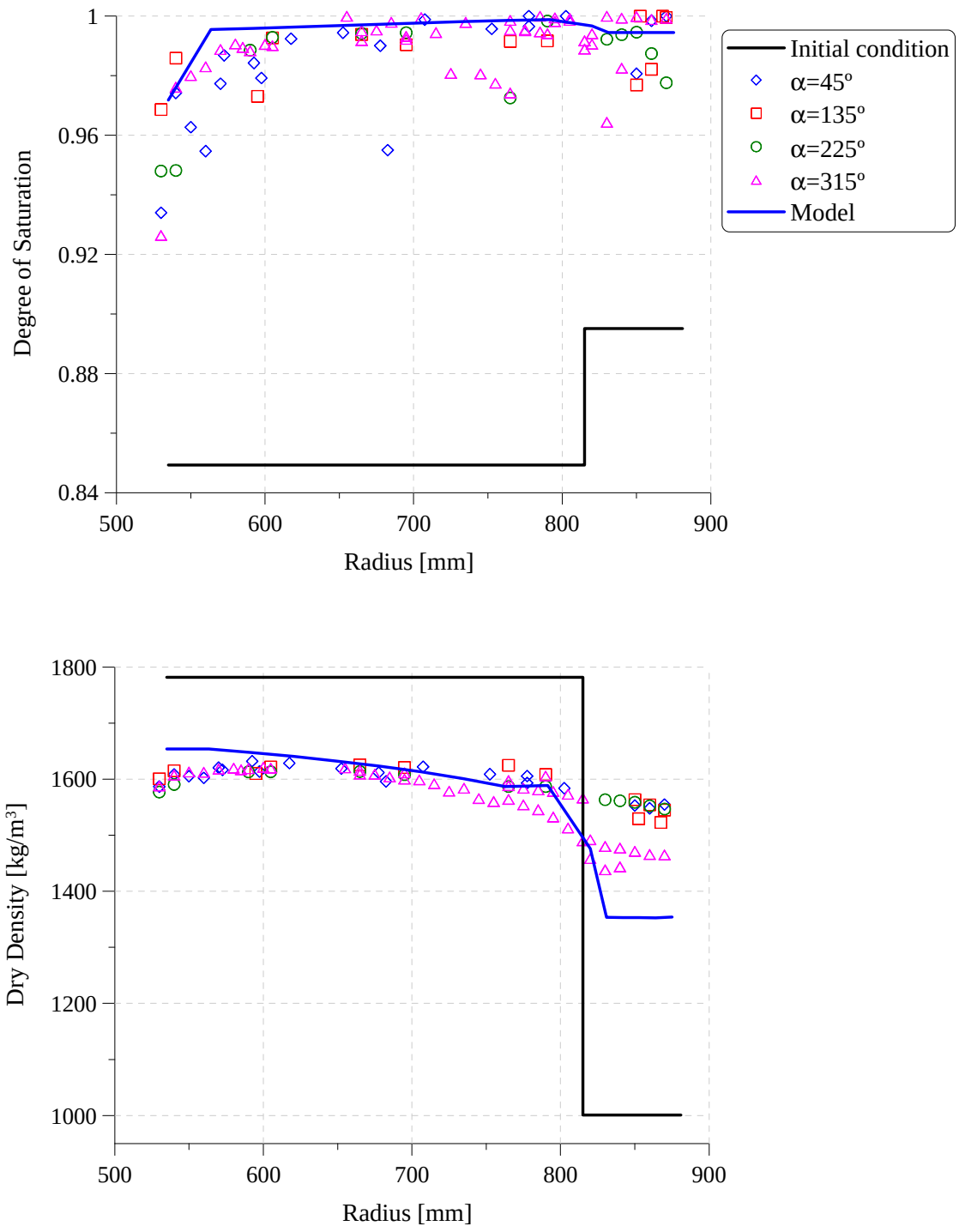

Figure 6.19: Degree of saturation and dry density of Ring 6 after test dismantling. Experimental and model results.

6.8. Concluding remarks

A coupled THM numerical simulation of a nuclear waste repository was satisfactorily performed. The required material parameters were mostly determined using data from laboratory tests; while others were estimated from back analysis.

To model the interface between canister and bentonite a specific mechanical formulation of this element was implemented in Code-Bright. The mechanical formulation is expressed at the mid plane of the element and relates the relative displacements of the mid plane with the normal and tangential stress through normal and shear stiffness respectively. In particular, a normal stiffness dependent on interface opening allows capturing the non-linear behaviour under normal stress. The hydraulic and thermal behaviour were modelled according to Darcy's and Fick's laws, respectively, as used in the code. The parameters of the interface were fitted by back calculation.

Comparing the results measured in situ with the results of numerical analysis shows that the formulation used is able to adequately reproduce the phenomena involved in the test, as well as their interactions. Moreover, the model was able to capture the final state of the bentonite and pellets showing the high degree of homogenization of their dry density achieved during the test.

Also, it was possible to verify from the results that the model implemented for interfaces is able to satisfactorily simulate interface behaviour. The evolution of its opening and stress development is mainly controlled by the progress of bentonite swelling.

CHAPTER 7

Analysis of thermo-hydro-mechanical coupling of the interface properties.

And study of gas flow through interface

7.1 Introduction

This chapter presents two studies. The first one is a sensitivity analysis, which focuses on the effects of considering the coupling of the hydro-mechanical properties of the interface. The other study centres its attention on the gas flow through the interface.

The first analysis consists in five simulations of the middle section of the Canister Retrieval Test (explained in Ch. 6). The middle section was modelled with a 1-D axisymmetry geometry. Five simulations were run considering different normal stiffness and hydraulic properties of the interface. In one case the hydraulic properties were maintained constant during the test, while in the rest these properties change with the interface opening. These examples allow studying the changes on degree of saturation of bentonite caused by the different hydraulic properties of the interfaces.

The study of the gas flow through the interface was carried out by simulating a gas generation due to the corrosion of the canister. The entire geometry of the CRT was considered. Four simulations were run in order to study the influence of gas permeability of bentonite, and of the different hydraulic and mechanical properties of the interface on the increment of gas pressure within the interface and gas flow through it.

The next two sections present a description of geometries and material properties adopted to perform each case. Furthermore the numerical results are described and discussed. The last section draws the conclusions obtained from the analysis.

7.2 Analysis of thermo-hydro-mechanical coupling of interfaces

The objective of this study is to evaluate the effects of considering variable stiffness of the interface element. This analysis mainly evaluates the effects of changes in permeability and the air entry pressure of the retention curve of the interface on the degree of saturation of the bentonite buffer.

7.2.1 Geometry of the model

This sensitivity analysis was performed by modeling the middle section of the CRT described in Chapter 6. The section was modeled using a one-dimensional axi-symmetric geometry. The materials considered in the model are the interface, the bentonite ring and pellets located between the buffer and the host rock wall. The section was discretised by 4-noded quadrilateral structured elements, and the mesh includes 50 continuum elements and 1 interface element (Fig. 7.1).

7.2.2 Initial and boundary conditions

Thermal boundary conditions were defined for the canister surface (AB) and for the rock host wall (CD). The thermocouple located near the canister registered temperatures up to day 1063. Then the temperatures were calculated for the rest of the test considering different values for the thermal conductivity of the rock, λ=1.0 and λ=1.2 (Börgesson, 2007 - Fig. 7.2a). The temperatures calculated with λ=1.2 were adopted as the thermal boundary conditions at surface AB (red line - Fig. 7.2a). The temperature measured by Sensor TR125, located at host rock wall, was considered to be at CD boundary (red line - Fig. 7.2b).

A hydraulic boundary condition equal to P_w = 0.1 MPa was applied at CD boundary to consider the water supplied by the rock. Since day 679 the water filter pressure protocol applied at filter mats (Fig. 7.2b) was followed. The other boundaries were defined as impervious. Gas pressures for all materials remained constant and equal to P_g = 0.1 MPa.

Finally, AC and BD boundaries were vertically fixed while AB and CD boundaries were horizontally fixed.

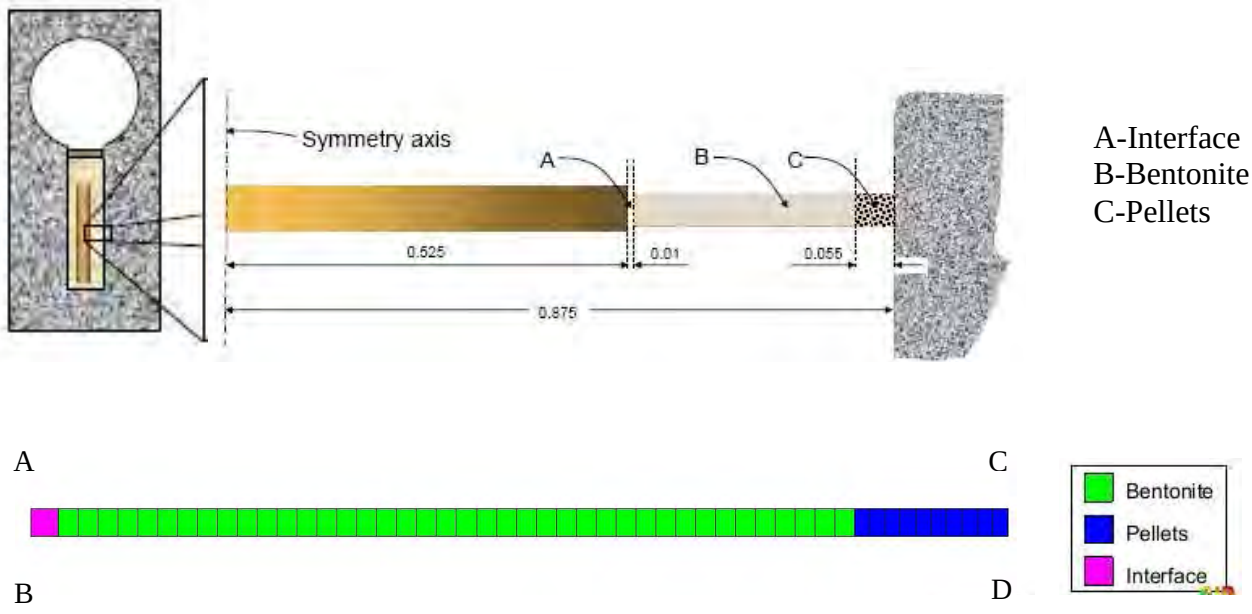

Figure 7.1: a) Middle section of the CRT extracted from Börgesson (2007b). Geometry of model and finite element mesh used for numerical simulation.

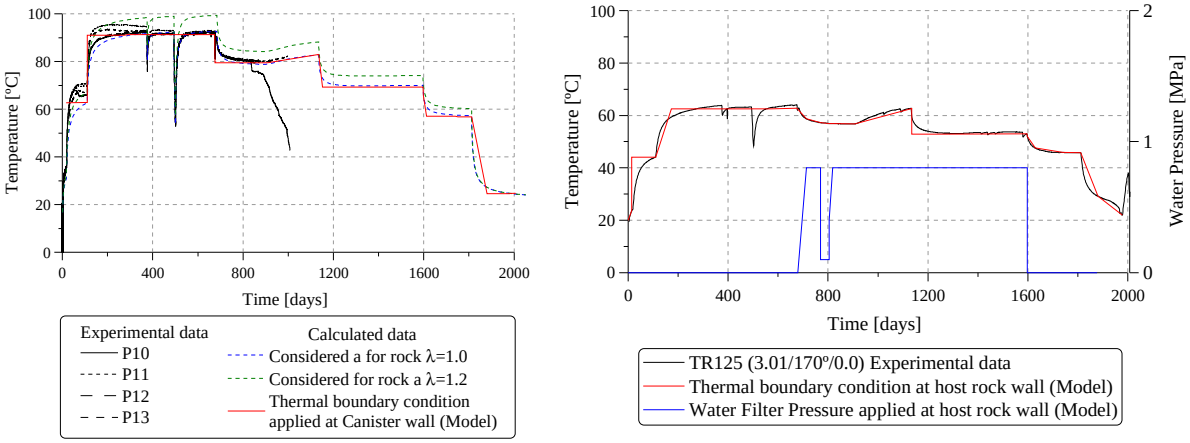

Figure 7.2: a) Temperatures measured and calculated at canister wall. b) Temperatures registered in sensor TR125, located at host rock wall, and water pressure protocol applied at filter mats.

7.2.3 Material parameters

The mathematical models and thermo-hydro-mechanical parameters of the bentonite ring and pellets are the same as the ones used in Chapter 6.

However, five cases were run considering different properties for the interface. The base case considered an interface with an initial stiffness of k_n = 100 MPa/m, which would vary with interface aperture. A constant intrinsic permeability of k = 1.0 × 10^{-6} m^2 and the constant air entry pressure of the van Genutchen retention curve P_0 = 1 MPa (namely the Base Case) were also used. The other four cases considered an initial normal stiffness for the interface of k_n = 100 MPa/m (Case 1), 50 MPa/m (Case 2), 20 MPa/m (Case 3) and 10MPa/m (Case 4), together with an initial value of intrinsic permeability, k = 1.0 × 10^{-6} m^2, and the initial air entry pressure, P_0 = 0.1 MPa. Therefore the normal stiffness, intrinsic permeability and the air entry pressure change with the interface aperture according to Equations 3.24, 3.37 and 3.39 respectively (Ch. 3).

7.2.4 Results and discussions

The evolution of the interface aperture and changes of horizontal stress with interface aperture is drawn in Figure 7.3a and b respectively. Comparing the results obtained for the cases analyzed, it is observed that as interface stiffness decreases, closure is higher during bentonite swelling and horizontal stress is lower. Consequently, when the water pressure supply is switched off and temperature remains high (since day 1598), the interface begins to open due to the contraction of bentonite. The opening of the interface depends on the maximum stiffness reached during the closure. Then, as the interface has a lower stiffness, it experiences a greater aperture.

Figure 7.3 plots the results obtained for the Base Case (black dash line). Note that the interface shows the same mechanical behavior for Case 1 (k_n = 100 MPa/m with hydraulic properties dependant on the interface opening results represented with a continuous red line).

The evolution of intrinsic permeability and the air entry pressure are given in Figures 7.4a and b. The figures show that as the interface closes, its permeability decreases while air entry pressure

increases, according to the constitutive laws (Eq. 3.37 and 3.39 – Ch. 3) proposed to calculate them. Therefore when the interface begins to open, permeability increases and air entry pressure decreases again.

The main consequence of permeability and air entry pressure changes is the alteration of the degree of saturation of the interface and the bentonite (Fig. 7.5a, b and c). During the heating phase (time interval from day 0 to day 500), the interface with the lowest permeability and highest air entry pressure has the greatest degree of saturation (Case 4). This is due to the following phenomena: the fact that higher air entry pressure implies less desaturation when temperature increases, and that lower permeability results in lower water flow towards bentonite. All these phenomena cause a lower degree of saturation of the bentonite during heating (see Fig. 7.5b and c).

During the water pressure supply (time interval between days 674 and 1598) the interface with lowest permeability and highest air entry pressure (Case 1) experiences a faster increment of the degree of saturation than the interfaces of the rest of cases. This is because a more impervious interface implies a higher liquid pressure gradient from bentonite towards interface. This higher degree of saturation of the interface causes an increment of its thermal conductivity that origins a higher desaturation of adjacent bentonite (Fig. 7.5b and c).

However observing the degree of saturation of bentonite at different radial distances from the interface (Figs. 7.5b, c and d), it can be concluded that the differences on the hydraulic conditions of the interface only affect the hydration of the bentonite close to the interface and up to a radial distance of 70 mm.

Figures 7.5a, b, c and d compare the degree of saturation calculated for the Base Case (black dash line - hydraulic properties that remain constant during the test) to other cases. Note that in the Base Case the interface has a higher degree of saturation at the beginning because its initial air entry pressure is higher. And if this case is compared to Case 1, which has the same normal stiffness, the difference in the degree of saturation of the interface remains unchanged during the entire example. Nevertheless, the degree of saturation of the bentonite does not significantly change in both Cases. A possible explanation of this is that the hydraulic properties of the

interface in Case 1 do not differ very much from the ones in the Base Case and they tend to adopt values from the Base Case.

Finally, note that in order to obtain changes on the degree of saturation of bentonite it is necessary for the hydraulic properties of the interface to change considerably. For instance, comparing the degree of saturation obtained for the Base Case and for Case 4 (Fig. 7.5 b and c), it is necessary that the interface permeability decreases five orders of magnitude and that the air entry pressure increases one order of magnitude to cause a small reduction of the degree of saturation of bentonite.

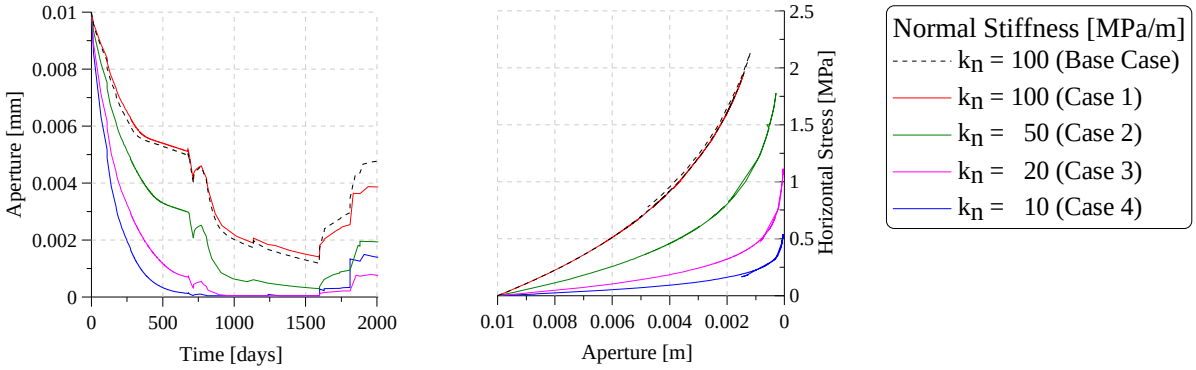

Figure 7.3: a) Evolution of the interface aperture with time. b) Evolution of the horizontal stress of the interface with its aperture.

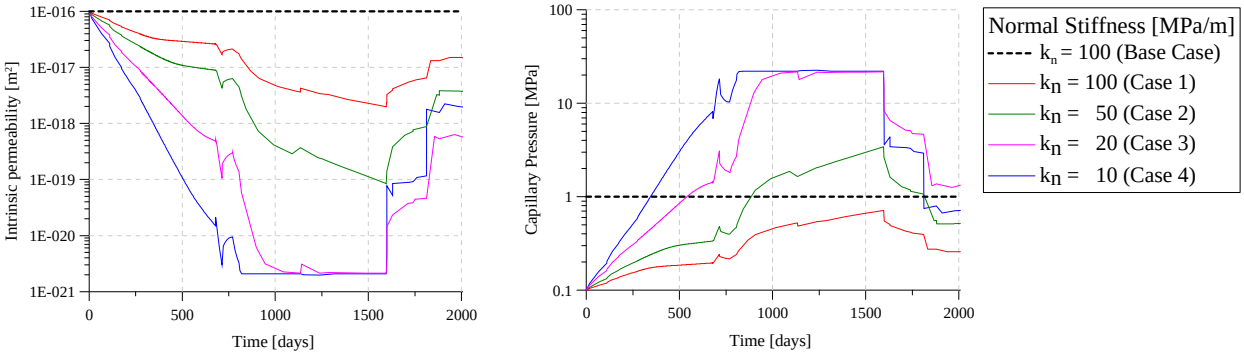

Figure 7.4: a) Evolution of the intrinsic permeability of the interface. b) Evolution of the air entry pressure of the retention curve of the interface.

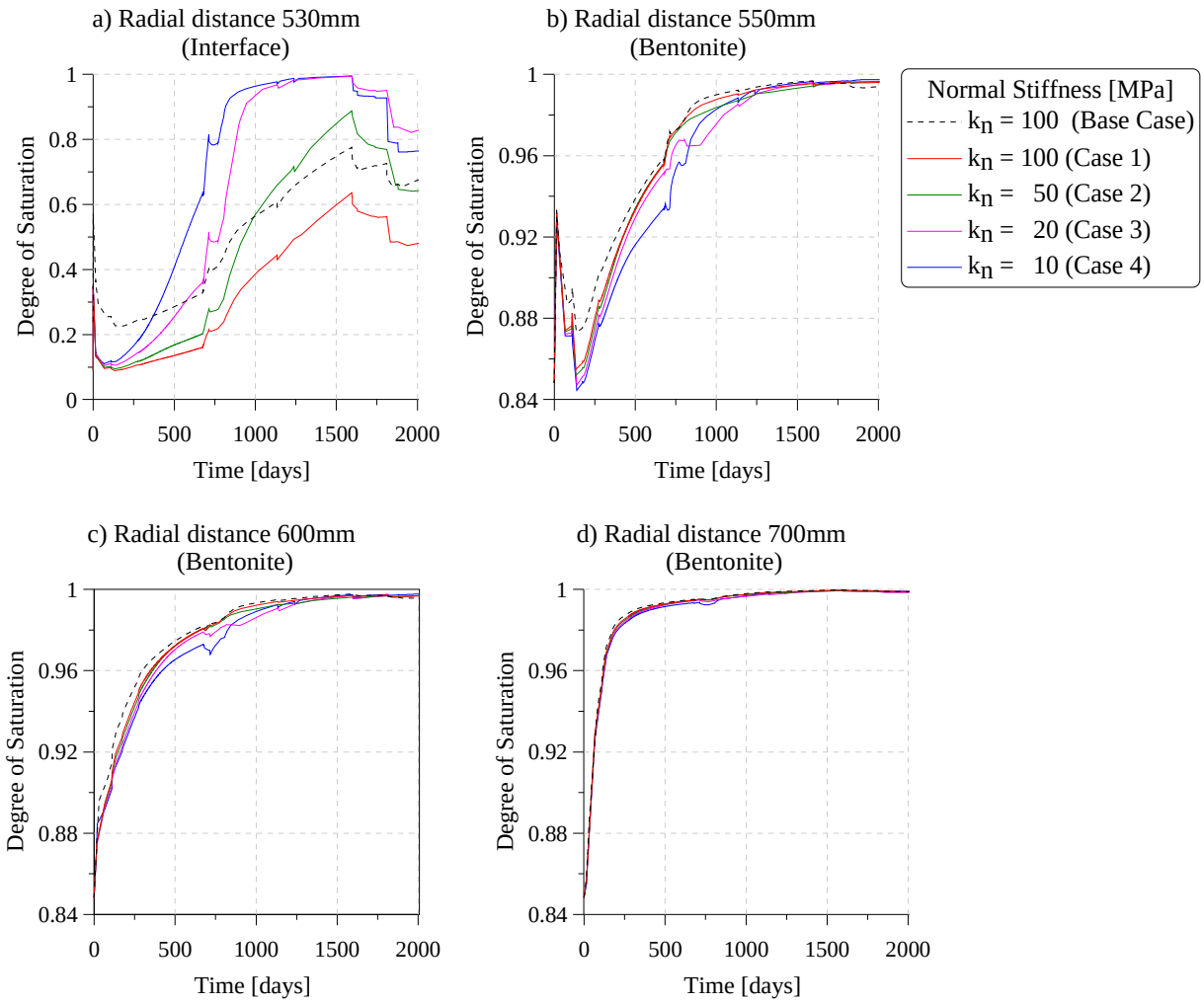

Figure 7.5: Evolution of the degree of saturation at different radial distances. a) Interface element (radial distance of 530 mm) b, c and d) MX-80 bentonite buffer (radial distances of 550, 600 and 700 mm respectively).

7.3 Study of the gas flow trough canister-bentonite interface

This study was performed to evaluate the gas flow behaviour of the interface element under thermo-hydro-mechanical conditions. The motivation of these examples is the fact that gas generation takes place in radioactive waste repositories due to the corrosion of canister.

Even though the example modelled is very simple, because only one point on the middle depth of canister is considered as a gas flow source, it allows performing some calculations to evaluate the gas pressure generation and the gas fluxes regarding different interface and bentonite properties.

7.3.1 Model description

The geometry of the model and the mesh used in the simulation are the same as the ones used in Chapter 6 for the CRT.

The thermal boundary condition consists in applying a heat flux on the canister volume (see Fig. 7.6).

The hydration of the buffer was possible by applying a water pressure of P_w = 0.8 MPa to the host rock wall (Fig. 7.6) and a constant gas pressure of P_g = 0.1 MPa. These conditions are applied during the 4000 days that lasts the simulation.

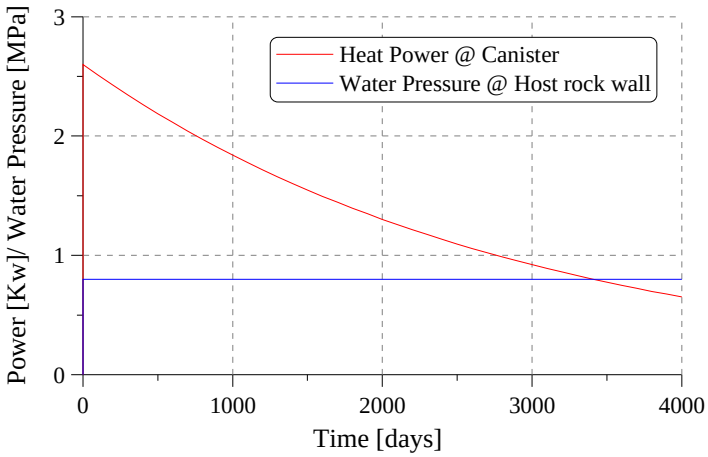

Figure 7.6: Boundary conditions. Heat power applied to the canister volume and water pressure applied to the host rock wall.

Since day 2000 a gas injection of 10^{-7} kg/s was impoused at a nodal point belonging to the middle length of the canister surface.

The number of materials in the simulation is the same as in the CRT analysis, as well as the type of constitutive models and parameters of the materials. Moreover, the following gas relative permeability for the materials is adopted:

$$k_{rg} = AS_{eg}{}^{\lambda}$$

where k_{rg} is the relative permeability of the gas, A is a constant equal to 1, $\lambda = 3$ and S_{eg} is the effective degree of saturation.

Four cases were simulated to study how the changes of hydraulic properties of the interface and the gas permeability of bentonite could affect gas flux. The cases performed are described in the following sections indicating the properties of bentonite and interface adopted in each case.

7.3.2 Sensitivity to intrinsic gas permeability of bentonite buffer

Two cases were compared in this section. Case 1 adopted a relation between gas and liquid permeability of $k_g/k_l = 1.0 \times 10^{+5}$. Given that the liquid permeability equals $k_l = 2.62 \times 10^{-20}$ m^2, the initial gas permeability in this case is $k_g = 2.62 \times 10^{-15}$ m^2. In Case 2, $k_g/k_l = 1.0 \times 10^{+3}$, and $k_g = 2.62 \times 10^{-17}$. These kg/kl ratios are selected taking into account that the gas permeability of clays is several orders of magnitude higher than liquid permeability. Then the relations used in these examples agree with the permeabilities measured experimentally in Febex bentonite and Boom Clay (Fig. 7.7).

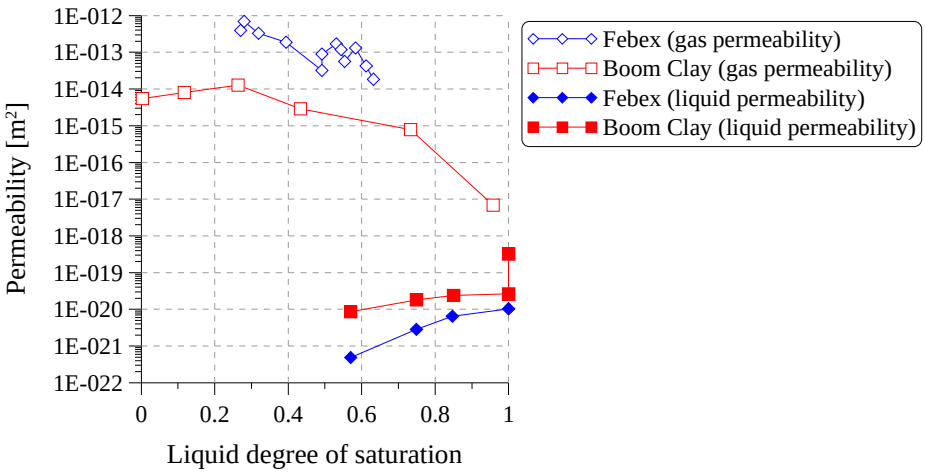

Figure 7.7: Data compiled on the permeability (in m^2) of clays to gas and water. Febex Clay (Villar, 1998) and Boom Clay (Volkaert et al., 1994).

The properties adopted for the canister-bentonite interface in both cases are k_n = 100 MPa/m, initial liquid and gas permeability k_l = kg = 1×10^{-16} and initial air entry P_0 = 1.0.

The permeability of bentonite changes due to swelling or contracting deformation. The permeability and air entry pressure of the interface change with its aperture.

The results obtained for Case 1 are plotted in Figures 7.8, 7.9, 7.10 and 7.11. The results for Case 2 are shown in Figures 7.12, 7.13, 7.14 and 7.15.

During the thermo-hydraulic phase both cases present the same behaviour: there is a desaturation of the interface and bentonite due to the increase in the heat flux followed by a hydration phase caused by the water pressure applied to the host rock wall. The bentonite begins to swell and consequently the interface closes. The difference between examples appears when the gas is injected.

In Case 1 the initial gas permeability of the bentonite is one order of magnitude higher than the interface permeability. Figure 7.8 shows that gas pressure increased during injection and reached a maximum value of 2.23 MPa in the interface at day 4000. The increment of gas pressure concentrated around the injection point (Fig. 7.8). The gas begins to flow trough the

interface, but it also flows trough the bentonite due to its high gas permeability (Fig. 7.9). The increase in gas pressure causes desaturation of the interface and also of the bentonite (Fig. 7.10). Figure 7.11 shows that during gas injection the interface is first opened, although this is only recorded for the length of the interface affected by the increment of gas pressure. Figure 7.11 also suggests that at a depth of 2 m the interface continues closing. Later, when gas begins to flow trough bentonite, the interface before opened begins to close again due to the swelling of bentonite, which is hydrated at all times by the water pressure applied to the host rock wall. Figure 7.11 also presents the evolution of interface permeability and air entry pressure. The decrease of aperture and the increment of air entry pressure also collaborated to increase the degree of saturation of the interface.

In Case 2 the gas permeability of bentonite is one order of magnitude lower than the initial gas permeability of the interface. Figure 7.12 shows that gas pressure increases up to 4.81 MPa and that it extends all throughout the interface. Furthermore, gas pressure is high in bentonite, and the gas flux concentrates also along the interface (Fig. 7.13). Both phenomena are a consequence of the low permeability adopted for bentonite. High gas pressures lead to an increased desaturation of the interface and bentonite buffer compared to the desaturation observed in Case 1 (Fig. 7.14). Moreover this desaturation extends to the entire zone affected by high gas pressure. Figure 7.15 depicts the evolution of the interface opening and highlights a sudden increase in the opening, when the gas is injected, due to the large increase in gas pressure. The opening continues but at a very slow rate because the gas begins to flow through the interface, the gas pressure extends to the whole interface and its aperture increases along its length (Fig. 7.15). The figure also shows abrupt changes in permeability (increases) and air entry pressure (decreases), which causes a very low rate of increment in the degree of saturation of the interface.

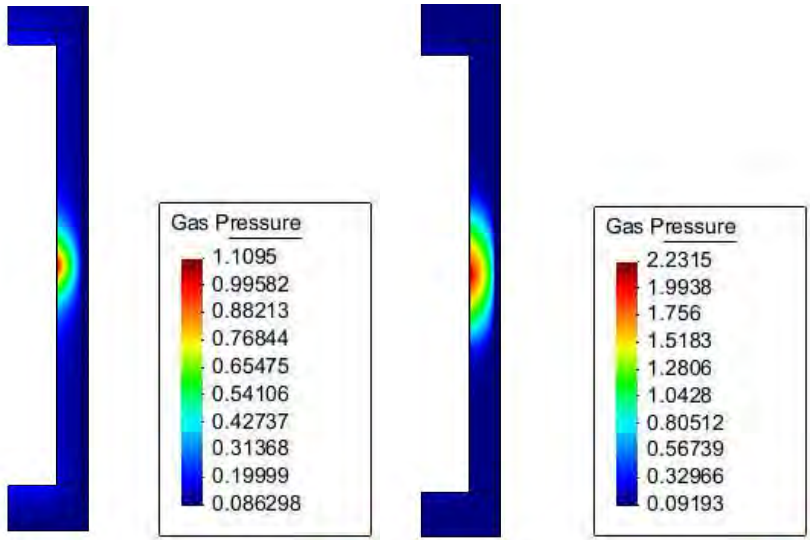

Figure 7.8: a) Gas pressure at day 2033 (after gas injection), b) Gas pressure at day 4000 (end of the test).

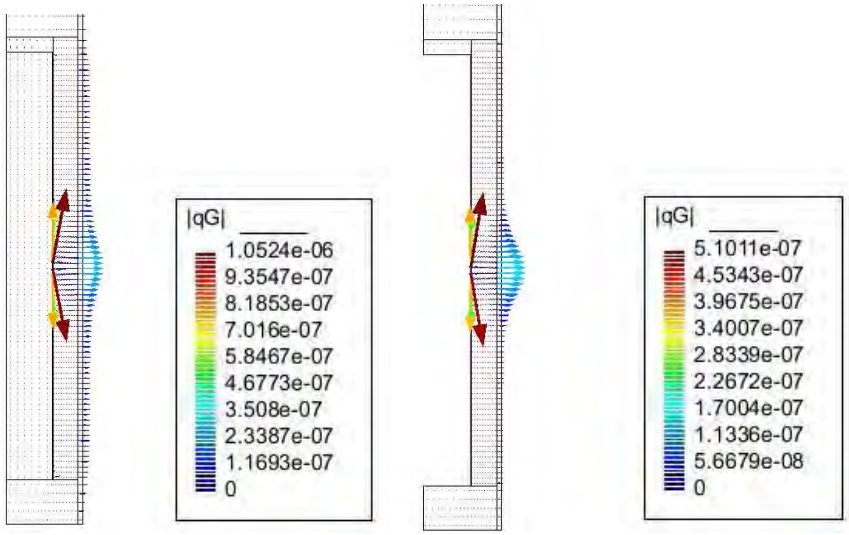

Figure 7.9: a) Gas flow at day 2033 (after gas injection), b) Gas flow at day 4000 (end of the test).

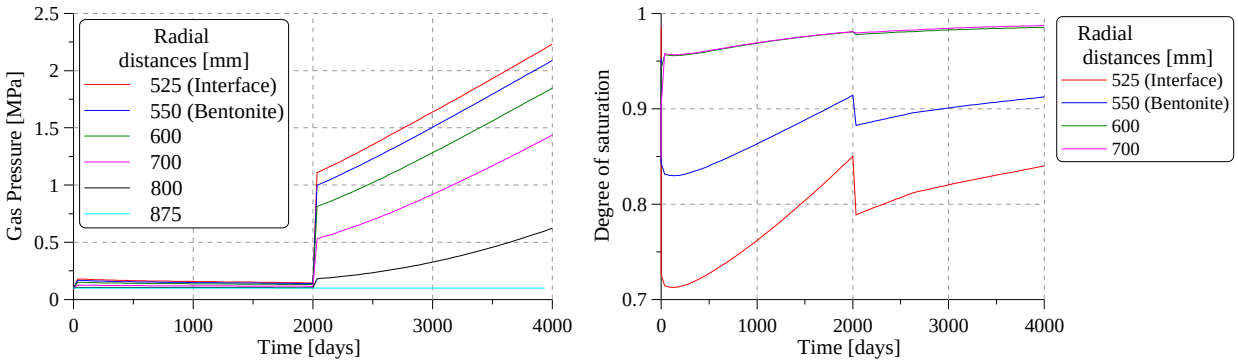

Figure 7.10: a) Evolution of gas pressure at the interface and bentonite buffer for different radial distances, b) Evolution of degree of saturation for the interface and bentonite buffer. Case 1.

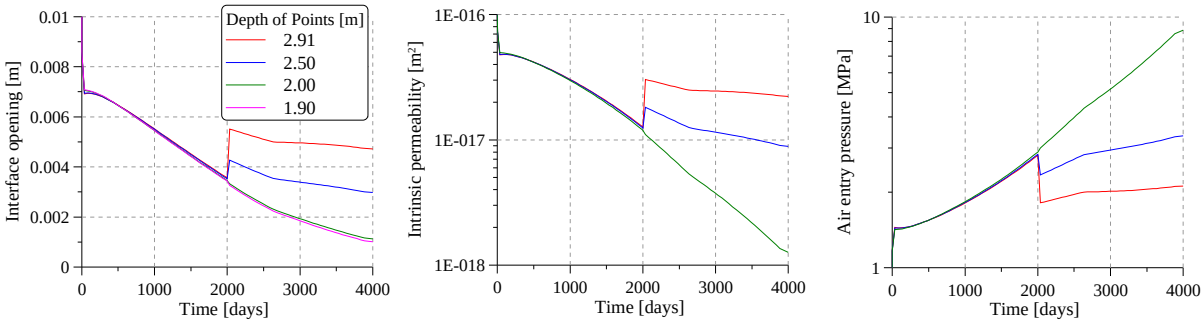

Figure 7.11: Evolution of the interface opening along its length before and after gas injection. Case 1.

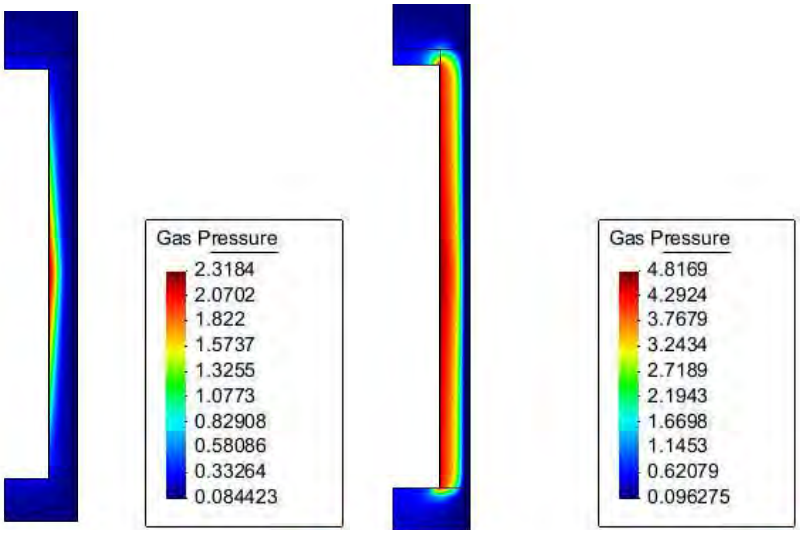

Figure 7.12: a) Gas pressure at day 2033 (after gas injection), b) Gas pressure at day 4000 (end of the test). Case 2.

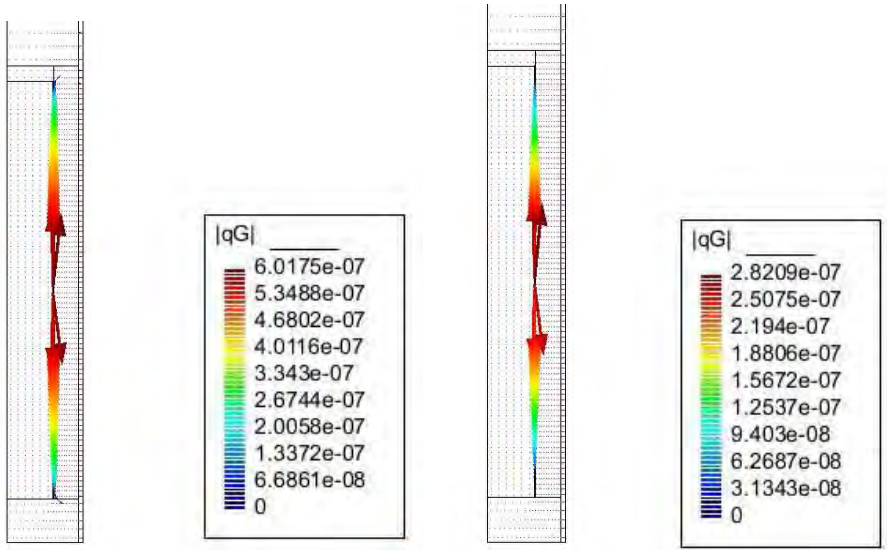

Figure 7.13: a) Gas flow at day 2033 (after gas injection), b) Gas flow at day 4000 (end of the test). Case 2.

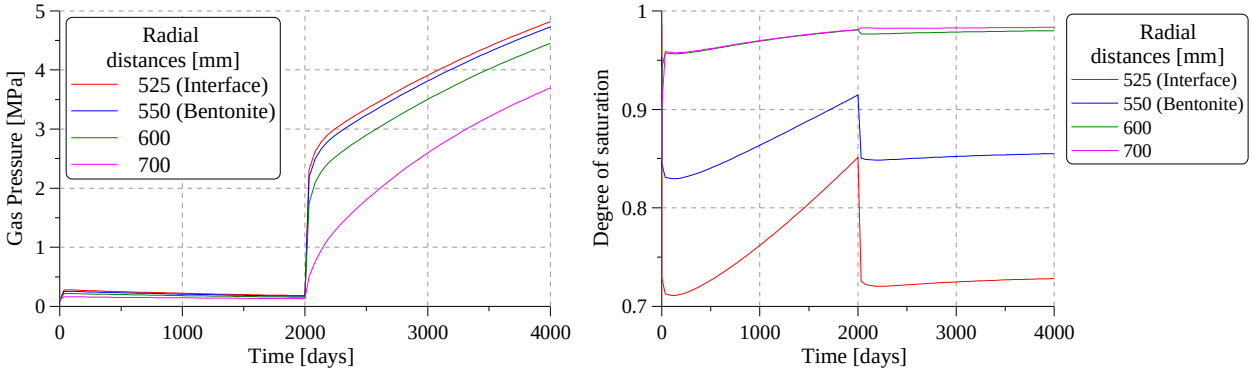

Figure 7.14: a) Evolution of gas pressure at the interface and bentonite buffer for different radial distances, b) Evolution of degree of saturation for the interface and bentonite buffer. Case 2.

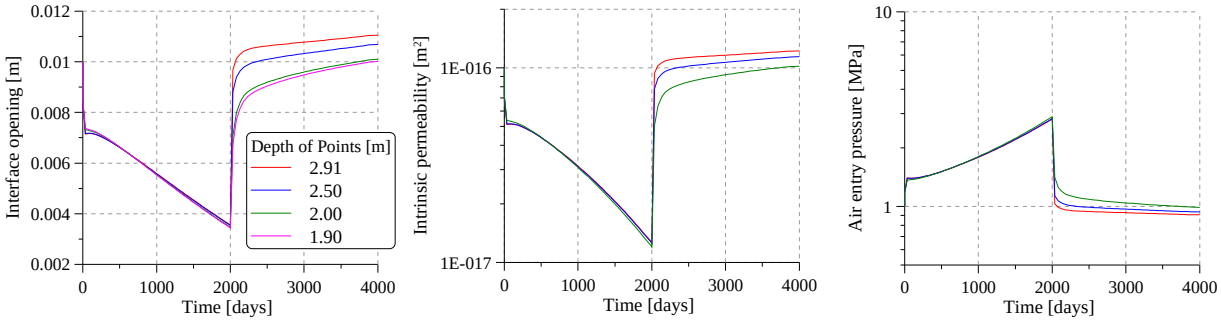

Figure 7.15: Evolution of the interface opening before and after gas injection. Case 2.

7.3.2 Effect of the air entry pressure of interfaces in the gas flow (Case 3)

In Case 3 the k_g/k_l ratio for bentonite is $1.0\times10^{+3}$ (the same as in Case 2). The normal stiffness (k_n = 100 MPa/m) and the initial intrinsic permeability ($k_l = 1.0\times10^{-16}$ m^2) of the interface are the same as the ones used in Case 2, but the initial air pressure for interface P_0 equals 0.1.

The results obtained for this case are shown in Figures 7.16, 7.17 and 7.18.

During the thermo-hydraulic phase, the degree of saturation of the interface showed to be lower than in Case 2. In this phase the degree of saturation of the interface is S_r = 0.65 while in bentonite it is S_r = 0.82. This is due to the lower P_0 of the interface, which implies a greater desaturation of the interface.

The gas pressure calculated in this case is lower than in Case 2 while the gas flux is greater. This is due to the lower degree of saturation that the interface has when the gas is injected. This lower degree of saturation causes a greater mobility of the gas through the interface, which is exemplified when comparing Figs 7.13 (gas flow – Case 2) and 7.17 (gas flow – Case 3). A consequence of the greater gas mobility is that the gas pressure increment is the same throughout the interface causing an extended increment of its aperture.

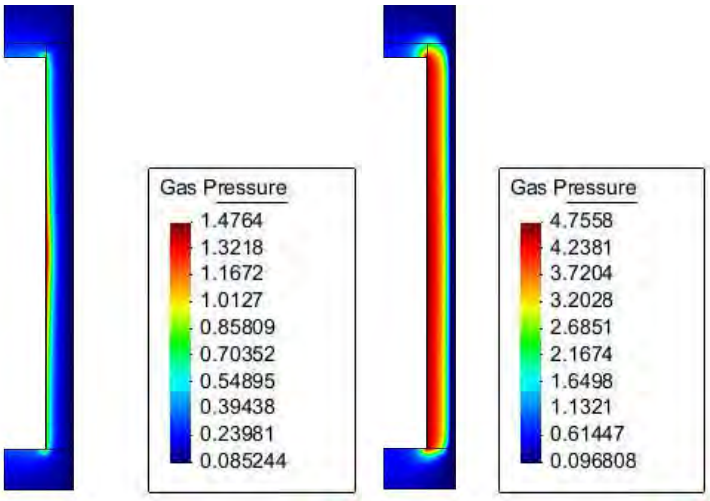

Figure 7.16: a) Gas pressure at day 2033 (after gas injection), b) Gas pressure at day 4000 (end of the test). Case 3.

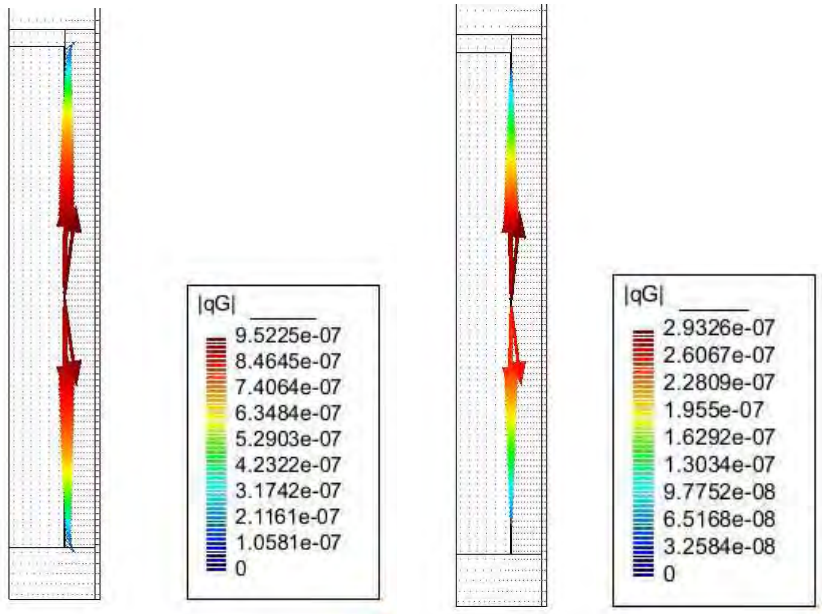

Figure 7.17: a) Gas flow at day 2033 (after gas injection), b) Gas flow at day 4000 (end of the test). Case 3.

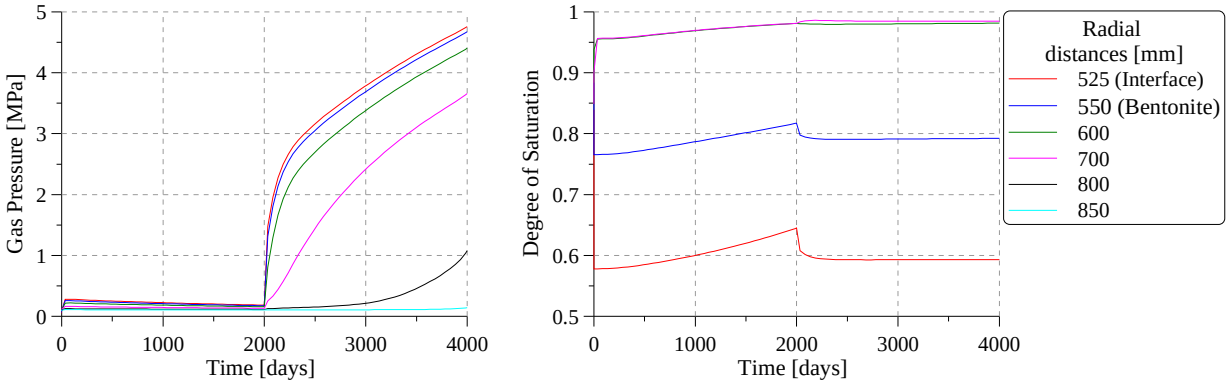

Figure 7.18: a) Evolution of gas pressure at interface and bentonite buffer for different radial distances, b) Evolution of degree of saturation for the interface and bentonite buffer. Case 3.

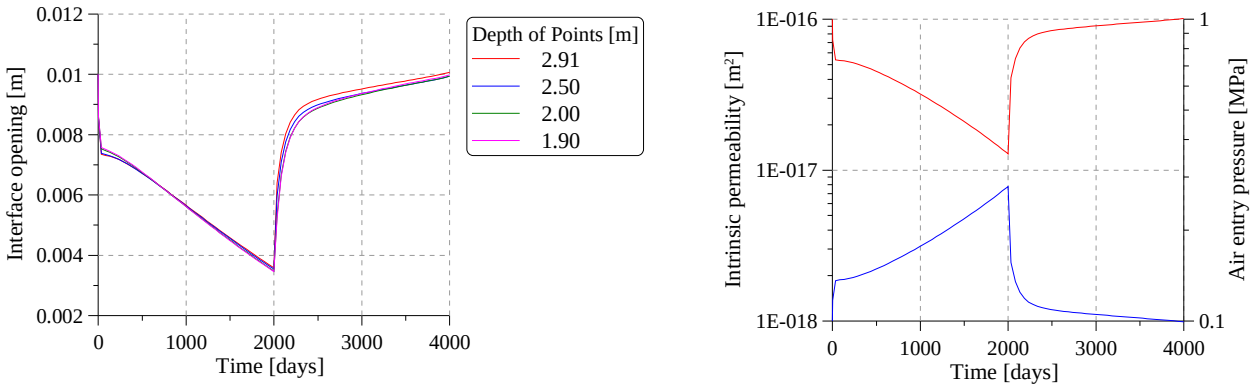

Figure 7.19: Evolution of the interface opening before and after gas injection. Case 3.

7.3.3 Effect of interface normal stiffness. Case 4

In Case 4 the initial normal stiffness of the interface was changed to k_n = 50 MPa/m. The objective of this example is to analyse the effect of normal stiffness on the interface hydraulic properties and on the gas pressure and flow.

In this case, during the thermo-hydraulic phase, the interface reached a higher degree of saturation than in Case 3. This is a consequence of a lower permeability and a higher air entry pressure because the lower normal stiffness is what causes a higher closure of the interface. Consequently, the gas pressure is higher than in Case 3. Then, the increment of gas pressure causes the aperture of the interface, and consequently its permeability to increase, its air entry pressure to decrease and the interface to desaturate.

But it is also observed that gas fluxes and the final degree of saturation of the interface and bentonite are very similar to those of Case 3.

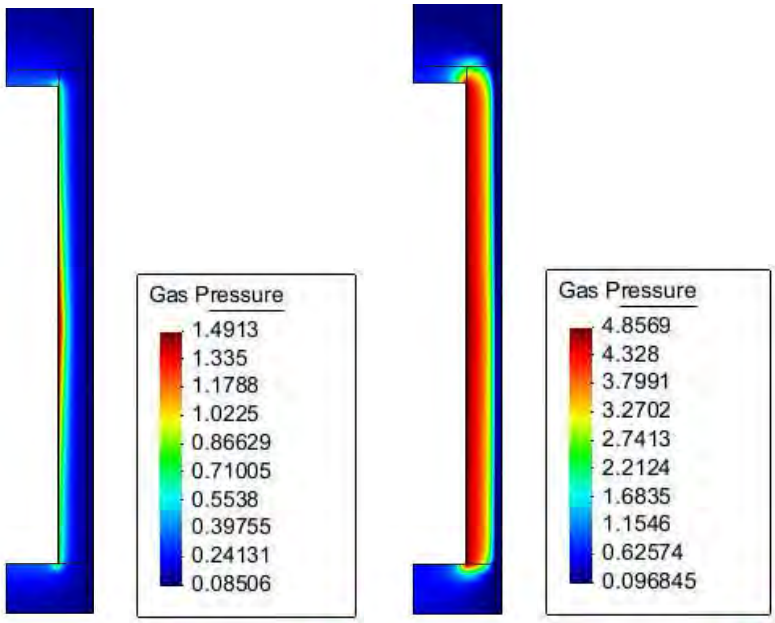

Figure 7.20: a) gas pressure at day 2033 (after gas injection), b) gas pressure at day 4000 (end of the test). Case 4.

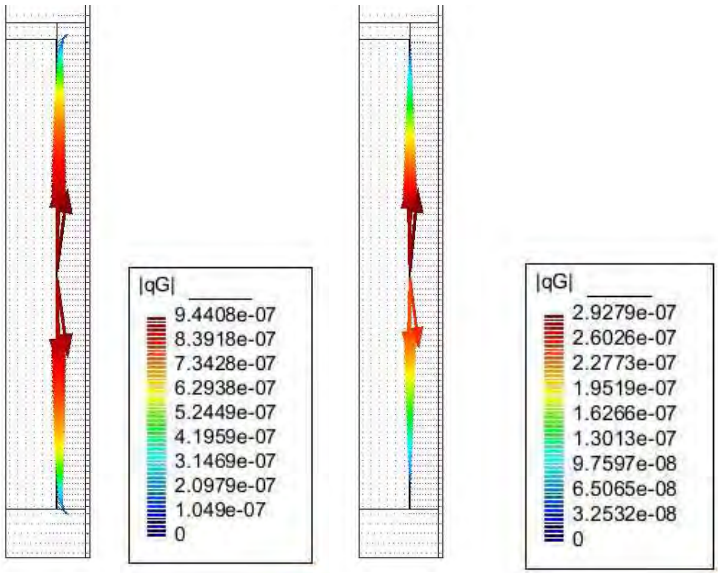

Figure 7.21: a) Gas flow at day 2033 (after gas injection), b) Gas flow at day 4000 (end of the test). Case 4.

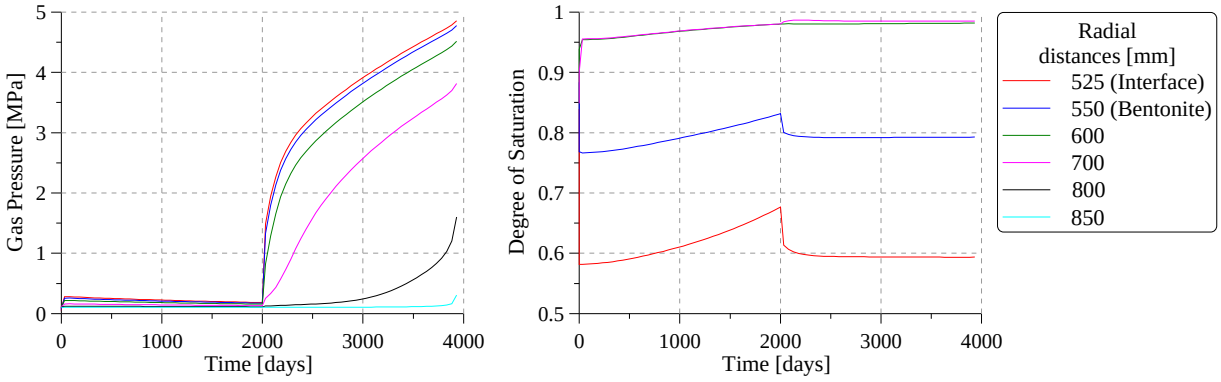

Figure 7.22: a) Evolution of gas pressure at the interface and bentonite buffer for different radial distances, b) Evolution of the degree of saturation for the interface and bentonite buffer. Case 4.

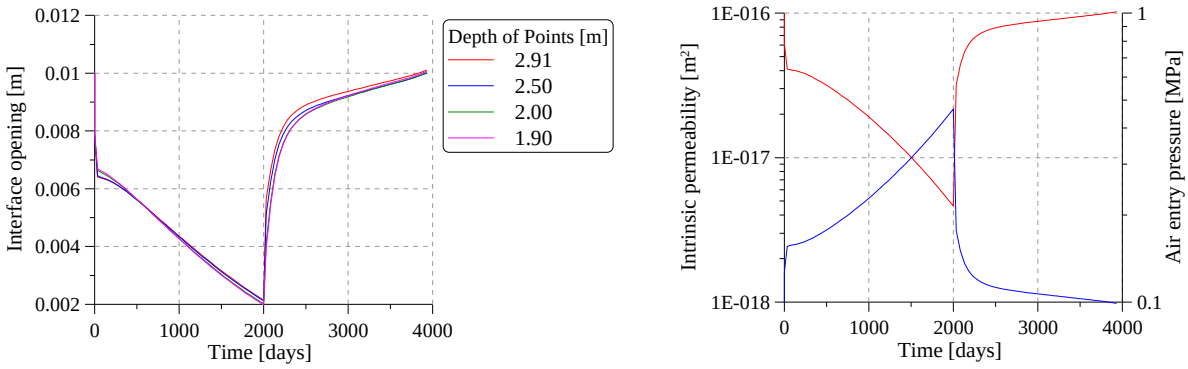

Figure 7.23: Evolution of the interface opening before and after gas injection. Case 4.

7.4 Concluding remarks

From the sensitivity analysis of the permeability and air entry pressure changes due to the opening evolution and considering the different normal stiffness of the interface, the following conclusions are drawn.

Lower permeability and higher air entry pressure are the consequence of considering the lower stiffness of the interface. These interfaces present a greater degree of saturation than stiffer interfaces. They also induce a lower degree of saturation of the bentonite.

However, the saturation of bentonite close to the interface (approximately up to a radial distance of 70 mm from the interface) is only dependant on the hydraulic conditions of the interface.
Note that in order to vary the degree of saturation of bentonite it is necessary that the hydraulic properties of the interface change considerably. This is confirmed by the fact that a small decrease of the degree of saturation of bentonite is observed when comparing the results obtained for an interface with a constant permeability of $k_l = 1.0 \times 10^{-16}$ m^2 and an air entry pressure of $P_0 = 1.0$ MPa and the results for the interface with variable hydraulic properties and a $k_n = 10$ MPa/m that reached a minimum value of $k_l = 2.0 \times 10^{-21}$ and a maximum value of $P_0 = 11.0$ MPa.

From the gas flow study it is possible to conclude that the increment on gas pressure and gas flow depends considerably on the gas permeability adopted for the bentonite with respect to the one adopted for the interface. A bentonite with gas permeability one order of magnitude higher than interface permeability implies a lower gas pressure. The gas flowed trough the interface causing a decrease of the degree of saturation of the bentonite. The gas pressure and the gas flow affected the area closest to the injection gas point. The interface is opened by the increment in gas pressure, but then, given that gas can flow through bentonite, the interface is able to close because the bentonite begins to swell again because its hydration is possible.

However, a bentonite having a gas permeability one order of magnitude lower than the interface implies for the interface and bentonite to exhibit a higher gas pressure. The gas flux concentrated only along the interface. High gas pressures lead to a faster desaturation of the interface and bentonite, compared to the case before-mentioned. Moreover this desaturation extends to the whole interface, which opens due to the increment in gas pressure and remains so during gas injection.

Then, the decrease in initial air pressure for interface P_0 equals 0.1, which in turn causes the degree of saturation of bentonite to be lower when gas injection starts. This allows the gas to move easily through the interface. That is why, in this case, the gas pressure is somewhat lower than in the case before-mentioned and, as a result, the increment of the interface aperture is also lower.

Finally, the fact of considering an interface with a stiffness twice as low has no significant effect on gas pressure and on the degree of saturation of the interface and bentonite.

CHAPTER 8

Conclusions and Future research

Summarizing, the thesis has included the following main developments:

1. The theoretical formulation of thermo-hydro-mechanical coupled behaviour of discontinuities and its discretization using the finite element method and the joint element with double nodes have been presented.

2. The hydraulic formulation is able to consider unsaturated joints. It also considers the possibility of a two-phase flow through the joint.

3. The mechanical behaviour of the joint was developed in the framework of viscoplasticity.

4. The experimental program allows studying the effect of moisture content and the roughness of rock joints under shear loads. It was possible to formulate a new mechanical constitutive law taking into account both effects.

5. The mathematical formulations before mentioned were implemented in Code_Bright.

8.1 Conclusions.

The hydro-mechanical behaviour of rock joints depends on their geometric properties and the level of stress applied to the joint. Regarding the geometric properties, it was experimentally proven that the wall roughness has a strong influence on strength and dilatancy. It was also demonstrated that joint permeability is affected by normal stress level, dilatancy and the damage of the joint walls roughness. Furthermore the degradation of roughness affects both residual strength and permeability.

Several mathematical models were formulated to numerically simulate the behaviour of joints. It is possible to make a distinction between models based on rock mechanics and on fracture mechanics. The former kind of models mentioned considers pre-existent joints, while the latter determines a joint initiation and its propagation. Models are formulated taking into consideration empirical observations. As an example of pre-existent joints models, the hydro-mechanical model proposed by Ollson & Barton (2001), and the mechanical elasto-plastic model proposed by Gens et al. (1990) were adopted as a general reference. Ollson & Barton's model is based on empirical measures such as JRC and JCS and on the empirical relation of geometry aperture and hydraulic aperture. The elasto-plastic model is based on the plasticity theory that defines a yield surface whose size depends on strength parameters. The evolution of the parameters is controlled by the plastic strain of the joint.

As an example of the fracture mechanics model, the formulation proposed by Carol et al. (1997) is mentioned. Fracture initiation and its propagation depend on a crack surface, whose evolution is controlled by the fracture energy dissipated in Modes I and II of fracture.

Although models of the roughness degradation of rock joints wall have recently been incorporated into mechanical models, this improvement was possible thanks to advanced techniques to measure the surface topography.

In general, all hydro-mechanical models predict satisfactorily the main characteristic of rock joints behaviour, i.e. the increase of normal stiffness with joint closure; the softening of shear strength and the decreasing dilatancy with shear displacements. Given that the evolution of the mechanical opening joint is related to its hydraulic aperture, permeability changes are also predicted.

The thesis involves two activities, one theoretical and another one experimental. The first one consisted in implementing in Code_Bright a joint element taking into account a coupled thermo-hydro-mechanical formulation using viscoplasticity. In addition, some examples were carried out to validate and evaluate the formulation. On the other hand, the second activity focused on performing an experimental program to test rock joints under shear load considering different values of suction and different values of asperity roughness. From the analysis of experimental

results, a new mechanical constitutive law was proposed. Then this new law was implemented in Code_Bright and the tests were simulated.

The theoretical formulation of the implemented joint element is based on the work by Goodman et al., (1968) and Segura (2008). They formulated the equilibrium of stress, the mass balance of water and air, and the energy balance equations.

The mechanical constitutive law is formulated on effective stress and is based on Gens et al. (1990). This law considers the elastic and plastic strain of the element. The elastic law is non-linear with normal stiffness dependant on the evolution of the opening of the joint element. The plastic behavior is defined by a hyperbolic failure surface, while the softening is based on a slip weakening model (Palmer & Rice, 1973). The equations theoretically developed were transformed to fit the viscoplastic framework.

The hydraulic constitutive laws adopted consisted in calculating the longitudinal flux by Darcy´s law and calculating the transversal flux by considering a pressure drop between interface surfaces (Segura, 2008). The cubic law was used to calculate the intrinsic permeability, which dependeds on joint opening. The air entry pressure of van Genutchen's retention curve was also calculated taking into account the joint aperture. The implementation of a retention curve to the joint element allowed studying cases in which the joint is under unsaturated conditions.

The non advective flux (vapour diffusivity) was calculated by Fick's law. On the other hand, the heat conduction through joint is given by Fourier's law.

Finally the nodal displacements, liquid pressure, gas pressure and temperature were obtained by solving simultaneously the balance equations.

Then, some numerical simulations were run to validate and evaluate the formulation of joint elements. One simulation involved the reproduction of the hydro-mechanical tests on granite joints under shear loads performed by Lee and Cho (2002). From the comparison between test and numerical results it was concluded that the formulation was able to reproduce the main

characteristic of coupled joint behavior. For instance, shear stress softening and dilatancy with shear displacements are well-captured as well as the increase of permeability with displacements.

Another simulation that considered the thermo-hydro-mechanical coupled behaviour of the material in a nuclear waste repository was satisfactorily performed. The simulation was carried out in the framework of the European Project THERESA. The main objective of this work was to take into account in the model of a large scale tests the interface between canister and bentonite. The large scale test modelled is the Canister Retrieval Tests (CRT). It was necessary to define the parameters of the materials used in the waste nuclear repository. Several parameters have been determined using data from laboratory tests; others were adopted by back analysis calculations. Specially, the parameters of the interface were fitted by back calculation analysis. Comparing the results measured in situ with the results of numerical analysis it can be concluded that the formulation used is able to reproduce well the phenomena involved in the test as well as their interactions. From the results it was possible to verify that the model implemented for the interface is able to capture its behaviour. This shows that the evolution of its opening and stress depends mainly on the bentonite swelling or contraction.

Laboratory activities involve modifying an available direct shear device, developing the sampling method and conducting a shear test program that would then define a constitutive law for rock joints with different suction. Moreover the damage to rock joints caused by the shear load was quantified, a profilometry of the joints walls was carried out, and the loss of mass of the samples was determined quantitatively.

The modification of the shear device included adding a vapor circulation system and improving the acquisition of data by incorporating an analogue data acquisition device. The vapor circulation system allows studying the influence of suction on the mechanical behaviour of rock joints.

Joint samples were carved into the rock using a drilling machine. The carving process adopted allows constructing different roughness angles. This effect was also studied on the shear strength and dilatancy of joints.

The shear test results obtained not only showed the well known dependency of shear strength with net normal stress, but also showed a marked dependency on suction and roughness. A decrease of shear strength and dilatancy was observed when inducing a decrease on suction. A greater roughness implies a greater shear strength. However, comparing the offset value of displacement, for which the residual shear strength is reached, it became clear that the rougher the asperity, the smaller the displacement required to reach residual conditions. This means that a rougher joint implies a more brittle behaviour. This brittle behaviour causes higher damage on joints surfaces, specially if this damage extends to all the surfaces. Consequently, rougher surfaces show lower dilatancy.

The profilometry profiles plotted and the gouge material measured confirmed that higher normal stresses, higher relative humidity of rock joints and rougher asperities causes greater damage to joint surfaces. A maximum of Wg/Wi = 5.9% is envisaged for an asperity roughness angle equal to 45º, a suction of 20 MPa and a net normal stress of 150 KPa. A minimum of Wg/Wi = 0.15% is asigned to an asperity roughness angle equal to 0º, a suction of 200 MPa and a net normal stress of 30 KPa.
It was also concluded that the degradation of joints increased with the work in all cases. Nevertheless, the higher the suction, for a given value of total work, the lower the joint degradation

From the analysis of test results it was possible to define new mathematical expressions for the strength parameters (initial effective cohesion (c_0') and initial effective tangent for the internal friction angle ($\tan\Phi'_0$) of the yield surface asymptote). These expressions consider the effects of the suction and asperity roughness angle on strength parameters. Likewise, dilatancy parameters were modified taking into account the suction and asperity roughness angle. Both modifications were introduced in the constitutive law of the interface element implemented in Code_Bright and then the tests were simulated.

The numerical results obtained using the suggested expressions closely reproduce the experimental features of rock joints. The results of the simulation have shown a good prediction of the evolution of shear stress with shear displacements. The dilatancy trend is also well-

captured. The differences between numerical and experimental data are due to the natural heterogeneity of the rock. Also the manual construction of the joints is a source of irregularities.

Other examples were carried out to evaluate the formulation of joint elements in other possible cases. For instance, a sensitivity analysis of their properties was carried out considering a simplified 1-D THM model of the CRT. These studies allow determining how the interface properties could affect the state of adjacent materials. The other examples consist in studying the gas flow through the interface taking into account different properties of the interface and bentonite. In these cases a 2-D model was used for the CRT.

From the sensitivity analysis of the permeability and air entry pressure changes, due to the evolution of openings considering different normal interface stiffness, the following conclusions were drawn.
Lower permeability and higher air entry pressure are a consequence of considering the lower stiffness of the interface. This interface presents a higher degree of saturation than stiffer interfaces. This is also the reason for the lower degree of saturation of the bentonite.

However, the saturation of bentonite close to the interface (approximately up to a radial distance of 70 mm from the interface) is only dependant on the hydraulic conditions of the interface.

In order to obtain changes on the degree of saturation of the bentonite, it is necessary for the hydraulic properties of the interface to change considerably. This is confirmed by the fact that a small decrease on the degree of saturation of bentonite is observed when the results obtained for an interface (with a constant permeability of $k_l = 1 \times 10^{-16}$ m^2 and an air entry pressure of $P_0 =$ 1.0 MPa) are compared to those of the interface with variable hydraulic properties and $k_n = 10$ MPa/m (which reached a minimum value of $k_l = 2 \times 10^{-21}$ m^2 and a maximum value of $P_0 = 11.0$ MPa).

From the gas flow study it is possible to conclude that the increment on gas pressure and gas flow depends considerably on the gas permeability adopted for the bentonite with respect to that adopted for the interface. A bentonite with gas permeability one order of magnitude higher than interface permeability implies lower gas pressure. The gas flow through the interface and

through bentonite causes a decrease of their degree of saturation. Gas pressure and gas flow affected the area closest to the injection gas point. The interface is opened by the increment in gas pressure, but then, given that gas can flow trough bentonite, the interface is able to close because bentonite begins to swell again because of hydration.
However, a bentonite with gas permeability one order of magnitude lower than the interface implies higher gas pressure for the interface and bentonite. Nevertheless, the gas flux concentrated only along the interface. High gas pressures lead to a faster desaturation of the interface and bentonite compared to the case mentioned before. Moreover this desaturation extends to the whole interface, which opens due to the increment in gas pressure and remains so during gas injection.

Then, the decrease in initial air pressure for interface P_0 equals 0.1, which, in turn, causes the degree of saturation of bentonite to lower when gas injection starts. This allows the gas to move easily trough the interface. That is why the gas pressure is a somewhat lower than in the case before-mentioned and consequently the increment of the interface aperture is also lower.

Finally, the fact of considering an interface with stiffness twice as low has no significant effect on gas pressure and on the degree of saturation of the interface and bentonite.

8.2. Future research

There are some aspects that should be further investigated, they are classified here in numerical and experimental developments.

Regarding the numerical developments the following is suggested:

- Implement of a 3-D joint element formulation. This development will be useful for different problems, for instance the study gas flow through a nuclear waste repositories and the study of the stability of geotechnical excavation.

- Improvement of the hydraulic constitutive law, by coupling permeability with gouge material generation.

Regarding the experimental work, the following is proposed:

- Performing a shear test with suction control on rock joints of sandstone or limestone to study the effects of moisture content on these joints.

- Evaluating the effects of suction on joints under normal stress.

- Carrying out a coupled hydro-mechanical test on rock joints with different suctions. These tests will allow studying the effect of the damage of the rock joint wall on the permeability of joints. And analysis if damage induced anisotropy in permeability.

- Performing a normal and shear test on mismatched joints with suction control, in order to evaluate the effect of the geometry of the joint on its strength and degradation.

REFERENCES

Alonso, E. E., Olivella, S. & Arnedo, A. (2006). *Mechanism of gas transport in clay barriers*. J. Iberian Geol. 32, No. 2, 175–196.

Alonso EE., Gens A. & Josa A. (1990), *A constitutive model for partially saturated soils,* Geotechnique 40(3), 405~430.

Bandis S.C., Lumsden A.C. & Barton N.R. (1983), *Fundamentals of rock joint deformation*. International Journal of Rock Mechanics and Mining Sciences & Geomechanics Abstracts, 20(6):249–268.

Bandis S.C., Lumsden A.C., & Barton N.R.(1981). *Experimental studies of scale effects on the shear behaviour of rock joints.* International Journal of Rock Mechanics and Mining Sciences & Geomechanics Abstracts, 18:1–21.

Barton, N.R. & Bandis, S.C. (1990), *Review of Predictive Capabilities of JRC-JCS Model in engineering practice.* Int. Rock Joints. Proc. Int. symp. On rock joints, Leon Norway, (eds N. Barot and O. Stephansson), pp. 125-140. Rotterdam: Balkema.

Barton N., Bandis S. & Bakhtar K. (1985), *Strength, deformation and conductivity coupling of rock joints*. International Journal of Rock Mechanics and Mining Science & Geomechanics Abstracts, 22(3):121–140,

Barton N. & Choubey V. (1977), *The shear strength of rock joints in theory and practice*. Rock Mech. 10, I 54.

Barton N.R.(1976), *The shear strength of rocks and rock joints*. International Journal of Rock Mechanics and Mining Science & Geomechanics Abstracts, 13:255–279.

Barton N.(1973), *Review of a new shear strength criterion for rock joints*. Engng Geology 7, 287-32.

Belem, T., Mountaka, S. & Homand F. (2007), *Modelling surface roughness degradation of rock joint wall during monotonic and cyclic shearing.* Acta Geotechnica 2: 227-248.

Berdugo, I.R, (2007) *Tunnelling in sulphate-bearing rocks expansive phenomena*. PhD Thesis. Department of Geotechnical Engineering and Geosciences, UPC.

Börgesson L., (2007). *Canister Retrieval Test,* Compilation made for the EBS Task Force.

Borgesson L, & Hernelind J. (1999), *Coupled thermo-hydro-mechanical calculations of the water saturation phase of a KBS-3 deposition hole*, Technical Report TR-99-41.

Börgesson L. Fredrikson A. & Johannesson L.-E. (1994), *Heat conductivity of buffer materials*, SKB Technical report 94-29

Börgesson L., Johannesson L.-E., Sandén T. & Hernelind J. (1995), *Modelling of the physical behaviour of water saturated clay barriers. Laboratory tests, material models and finite element application*, SKB Technical report 95-20.

Börgesson L. & Johannesson L.-E. (1995), *Thermo-hydro-mechanical modelling of water unsaturated buffer material,* SKB Work report 95-32.

Carol I., Prat P. & Lopez C.M.(1997), *A normal/shear cracking model. Application to discrete crack analysis*. ASCE Journal of Engineering Mechanics, 123(8):765–773.

Dang, K.D. & Robinet, J.-C., (2004). *Thermo-hydro-mechanical behaviour of MX80 bentonite for temperature ≥100ºC.* Final Report. ANDRA report C.RP.0EUG.02.008.

DIT-UPC. (2000).CODE_BRIGHT. *A 3-D program for thermo-hydro-mechanical analysis in geological media.* User's guide. Barcelona: Centro Internacional de Métodos Numéricos en Ingeniería (CIMNE).

Escario V. & Saez J. (1986) The shear strength of partly saturated soils, Geotechnique 36(3):453–456

Fredlund D.G. & Rahardjo H. (1993).*Soils mechanics for unsaturated soils.* New Wiley & Sons.

Gale, J. E. (1982), *The effects of fracture type (induced-versus natural on the stress-fracture closure-fracture permeability relationships*. Proc., 23rd U.S. Symp. on Rock Mechanics, Univ. of Calif., Berkeley, 290–298.

Gangi, A. F. (1978), *Variation of whole and fractured porous rock permeability with confining pressure.* Int. J. Rock Mech. Min. Sci. Geomech. Abstr. 15, 249–257.

Garcia-Castellanos, D., Vergés, J. Gaspar-Escribano, J. & Cloetingh, S. (2003*). Interplay between tectonics, climate, and fluvial transport during the Cenozonic evolution of the Ebro Basin (NE Iberia).* J. Geophys. Res., 108 (B7): ETG 8-1-8-18.

Gens A., Carol I. & Alonso E.E.(1990), *A constitutive model for rock joints; formulation and numerical implementation.* Computers and Geotechnics, 9:3–20.

Goodman R.E., Taylor R.L. & Brekke T.L. (1968) *A model for the mechanics of jointed rock.* ASCE Journal of the Soil Mechanics and Foundations Division, 94(SM3):637–659.

Goudarzi R., Börgesson L., Röshoff K. & Edelman M. (2006), *Sensors data report (Period: 001026-060501) Canister retrieval test*, Report no. 12.

Hakami E. (1995), *Aperture distribution of rock fractures*. Doctoral thesis, Division of Eng. Geol., Royal Institute of Technology, Stockholm, Sweden.

Hans J.(2002). *Etude expérimental et modélisation numérique multiéchelle du comportamente hydromécanique de répliques de joints rocheux. Thése de doctorant*- Université Joseph Fourier Grenoble.

Hoffman C., Alonso E.E. & Romero E. (2007). *Hydro-mechanical behaviour of bentonite pellet mixtures.* Physics and Chemistry of the Earth 32 832-849.

Hökmark H. & Fälth B. (2003). *Temperature Buffer Test. Predictive Modelling Programme. Äspö Hard Rock laboratory* internal report F12.1G 1012125.

Imbert C., Billaud P., Touze G & Dang K.D. (2004). *Comportement thermo-hydro-mécanique d'une argile gonflante méthodologique en situation de stockage.* CEA, Rapport RT-DPC/SCCME 04-677-A.

Jennings J.E. & Robertson A.MacG. (1969): *The stability of slopes cut into natural rock*. Conf. on Soil Mechanics and Foundation Engineering, Mexico, Vol. II, pp. 585-590.

Johannesson L.-E., (2007). *Testing of a retrieval technique, Dismantling and sampling of the buffer and determination of density and water ratio.*(to be published)

Lajudie A., Raynal J., Petit J.-C. & Toulhoat P. (1994). *Clay based materials for engineered barriers. A review*. Mat. Res. Soc. Symp. Proc. Vol. 353, pp. 221-230.

Lee H.S., Park Y.J., Cho T.F. & You K.H. (2001). *Influence of asperity degradation on the mechanical behaviour of rough joints under cyclic shear loading.* Int. Joural of Rock Mechanics & Mining Science 38 967-980.

Lee H.S. & Cho T.F.(2002). *Hydraulic Characteristics of Rough Fractures in Linear Flow under Normal and Shear Load.* Rock Mechanics and Rock Engineering,35(4),229-318.

López, C.M. (1999) *Análisis microestructural de la fractura del hormigón utilizando elementos finitos tipo junta. Aplicación a diferentes hormigones.* PhD thesis, ETSECCPB, UPC, Barcelona, España.

Lorefice R., Etse G. & Carol I. (2008). *Viscoplastic approach for rate-dependent failure analysis of concrete joints and interfaces.* International Journal of Solids and Structures 45, 2686-2705.

Olivella, S. & Alonso, E. E. (2008). *Gas flow through clay barrier.* Geotechnique **58** No. 3, 157–176.

Olivella, S., Gens, A., Carrera, J. & Alonso, E. E. (1995). *Numerical formulation for a simulator (CODE_BRIGHT) for the coupled analysis of saline media.* EngngComput. 13, No.7, 87–112.

Olsson R. & Barton N.(2001), *An improved model for hydromechanical coupling during shearing of rock joints.* International Journal of Rock Mechanics and Mining Sciences, 38:317–329.

Palmer A.C., & Rice J.R. (1973).*The growth of slip surfaces in the progressive failure of over-consolidated clay.* Proc. Roy. Soc. Lond. A 332, 527-548.

Perzyna P. (1963), *The constitutive equations for rate sensitive materials*, *Quarterly of Applied Mathematics.*, no. 20, 321-332.

Pineda, J.A., De Gracia, M. & Romero E. (2010). *Degradation of partially saturated argillaceous rocks: influence on the stability of geotechnical structures.* 4th Asia-Pacific Conference on Unsaturated Soils, Newcastle, Australia. Unsaturated soils-Buzzi,Fityus & Sheng (eds.). Taylor & Francis Group.

Plesha, M. E. (1987), *Constitutive models for rock discontinuities with dilatancy and surface degradation.* Int. J. Numer. Anal. Meth. Geomech. 11, 345–362.

Pusch, R., (2001). *Experimental study of the effect of high porewater salinity on the physical properties of a natural smectitic clay.* SKB Tech. Rep. TR 01-07.

Raven R.G. & Gale J.E.(1985), *Water flow in natural rock fracture as a function of stress and sample size.* Int J. Rock Mech. Min. Sci & Geomech. Abstr, vol22, Nº4: 251-261.

Romero, E.E. (2001). *Controlled suction techniques*. Proc 4º Simposio Brasileiro de Sols Nao Saturados. Gehling and Schnaid Edits. Porto Alegre, Brasil, pp 535-542.

Sánchez, M. (2004), *Thermo-hydro- mechanical coupled analysis in low permeability media.* Ph.D. Thesis. Universitat Politècnica de Catalunya (UPC). 281 pp. Barcelona.

Segura J. Ma. (2008). *Coupled HM analysis using zero-thickness interface elements with double nodes.* Tesis de Doctorado-Universidad Politécnica de Catalunya, Barcelona.

Sugita Y., Chijimatsu M. and Suzuki H. (2003), *Fundamental properties of bentonite pellet for prototype repository project, Advances in understanding engineered clay barriers, Large scale field tests in granite: Fundamental research*. Material behaviour and laboratory testing, pp 293-301.

Swan, G. (1983), *Determination of stiffness and other joint properties from roughness measurements*. Rock Mech. Rock Engng. 16, 19–38.

Tang A.M. (2005), *Effect de la temperature sur le comportement des barrieres de confinement*, PhD thesis, CERMES, ENPC, Paris, France.

Tarragó, D.(2005) *Degradación mecánica de argilitas sulfatadas y su efecto sobre la expansividad*. BSc dissertation. Universitat Politécnica de Catalunya, Barcelona

Thorsager P., Börgesson L., Johannesson L-E & Sandén T., (2002). *Canister retrieval test, Report on installation,* International progress report 02-30.

Van Genuchten, M. Th. (1980). *A closed-form equation for predicting the hydraulic conductivity of unsaturated soils*. Soil Sci. Soc.Am. J. 49, No. 9, 892–898

Villar M.V. (2005), *MX-80 bentonite, thermo-hydro-mechanical characterisation performed at CIEMAT in the context of the Prototype project*, CIEMAT Technical Report, Madrid, Spain.

Villar, M.V. (2002), *Thermo-hydro-mechanical characterisation of a bentonite from Cabo de Gata. A study applied to the use of bentonite as sealing material in high level radioactive waste repositories.* Publicación Técnica ENRESA 01/2002. 258 pp. Madrid.

Villar, M. V. (1998). *Ensayos para el proyecto FEBEX*, CIEMAT-report 70-IMA-L-5-51, prepared for ENRESA.

Volkaert G, Ortiz, L., De Cannière P., Put M., Horseman S. T., Harrington J. F., Fioravante V. & Impey M. (1994). *Modelling and experiments on gas migration in repository host rocks*, MEGAS Project, Final Report, Phase 1.

Zienkiewicz O.C. & Cormeau I. (1974). *Visco-Plasticity-Plasticity and Creeping Elastic Solids-A Unified Numerical Solution Approach.* International Journal for Numerical Methods in Engineering, Vol 8, 821-845.